



LUND UNIVERSITY

Design and Optimization of In-Cycle Closed-Loop Combustion Control with Multiple Injections

Jorques Moreno, Carlos

2021

Document Version:

Publisher's PDF, also known as Version of record

[Link to publication](#)

Citation for published version (APA):

Jorques Moreno, C. (2021). *Design and Optimization of In-Cycle Closed-Loop Combustion Control with Multiple Injections*. LTH, Lund University.

Total number of authors:

1

Creative Commons License:

Unspecified

General rights

Unless other specific re-use rights are stated the following general rights apply:

Copyright and moral rights for the publications made accessible in the public portal are retained by the authors and/or other copyright owners and it is a condition of accessing publications that users recognise and abide by the legal requirements associated with these rights.

- Users may download and print one copy of any publication from the public portal for the purpose of private study or research.
- You may not further distribute the material or use it for any profit-making activity or commercial gain
- You may freely distribute the URL identifying the publication in the public portal

Read more about Creative commons licenses: <https://creativecommons.org/licenses/>

Take down policy

If you believe that this document breaches copyright please contact us providing details, and we will remove access to the work immediately and investigate your claim.

LUND UNIVERSITY

PO Box 117
221 00 Lund
+46 46-222 00 00



Design and Optimization of In-Cycle Closed-Loop Combustion Control with Multiple Injections

CARLOS JORQUES MORENO

DIVISION OF COMBUSTION ENGINES | FACULTY OF ENGINEERING | LUND UNIVERSITY



Design and Optimization of
In-Cycle Closed-Loop Combustion
Control with Multiple Injections

Design and Optimization of In-Cycle Closed-Loop Combustion Control with Multiple Injections

by Carlos Jorques Moreno



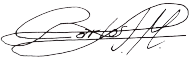
LUND
UNIVERSITY

Thesis for the degree of Doctor of Philosophy
Thesis advisors: Prof. Ola Stenlång, Prof. Per Tunestål
Faculty opponent: Prof. Ming Zheng, Windsor University

Doctorate Dissertation to be presented, with the permission of the Faculty of Engineering of
Lund University, Sweden, in the KC:A lecture hall at the KC-Building, on Friday, the 14th of
May 2021 at 10:15.

Organization LUND UNIVERSITY Department of Energy Sciences P.O. Box 118 SE-221 00 LUND Sweden		Document name DOCTORAL DISSERTATION	
Author(s) Carlos Jorques Moreno		Date of disputation 2021-05-14	
		Sponsoring organization Swedish Energy Agency, FFI program (22485-4) Scania CV AB	
Title and subtitle Design and Optimization of In-Cycle Closed-Loop Combustion Control with Multiple Injections			
<p>Abstract: With the increasing demand of transportation, biofuels play a fundamental role in the transition to sustainable powertrains. For the increased uncertainty of biofuel combustion properties, advanced combustion control systems have the potential to operate the engine with high flexibility while maintaining a high efficiency and robustness. For that purpose, this thesis investigates the analysis, design, implementation, and application of closed-loop Diesel combustion control algorithms. By fast in-cylinder pressure measurements, the combustion evolution can be monitored to adjust a multi-pulse fuel injection within the same cycle. This is referred to as in-cycle closed-loop combustion control.</p> <p>The design of the controller is based on the experimental characterization of the combustion dynamics by the heat release analysis, improved by the proposed cylinder volume deviation model. The pilot combustion, its robustness and dynamics, and its effects on the main injection were analyzed. The pilot burnt mass significantly affects the main combustion timing and heat release shape, which determines the engine efficiency and emissions. By the feedback of a pilot mass virtual sensor, these variations can be compensated by the closed-loop feedback control of the main injection. Predictive models are introduced to overcome the limitations imposed by the intrinsic delay between the control action (fuel injection) and output measurements (pressure increase). High prediction accuracy is possible by the on-line model adaptation, where a reduced multi-cylinder method is proposed to reduce their complexity. The predictive control strategy permits to reduce the stochastic cyclic variations of the controlled combustion metrics. In-cycle controllability of the combustion requires simultaneous observability of the pilot combustion and control authority of the main injection. The imposition of this restriction may decrease the indicated efficiency and increase the operational constraints violation compared to open-loop operation. This is especially significant for pilot misfire. For in-cycle detection of pilot misfire, stochastic and deterministic methods were investigated. The on-line pilot misfire diagnosis was feedback for its compensation by a second pilot injection. High flexibility on the combustion control strategy was achieved by a modular design of the controller. A finite-state machine was investigated for the synchronization of the feedback signals (measurements and model-based predictions), active controller and output action. The experimental results showed an increased tracking error performance and shorter transients, regardless of operating conditions and fuel used.</p> <p>To increase the indicated efficiency, direct and indirect optimization methods for the combustion control were investigated. An in-cycle controller to reach the maximum indicated efficiency increased it by $+0.42\%_{unit}$. The indirect method took advantage of the reduced cyclic variations to optimize the indicated efficiency under constraints on hardware and emission limits. By including the probability and in-cycle compensation of pilot misfire, the optimization of the set-point reference of CA50 increased the indicated efficiency by $+0.6\%_{unit}$ at mid loads, compared to open-loop operation.</p> <p>Tools to evaluate the total cost of the system were provided by the quantification of the hardware requirements for each of the controller modules.</p>			
Key words Diesel Combustion, Pilot-Main Injection, Pilot Mass Estimation, Cylinder Volume Estimation, Bayesian Estimation, In-Cycle Combustion Controllability, In-Cycle Combustion Control, Model Predictive Combustion Control, Stochastic Combustion Optimization, Hardware Quantification			
Classification system and/or index terms (if any)			
Supplementary bibliographical information		Language English	
ISSN and key title 0282-1990		ISBN 978-91-7895-827-6 (pint) 978-91-7895-828-3 (pdf)	
Recipient's notes		Number of pages 254	Price
		Security classification	

I, the undersigned, being the copyright owner of the abstract of the above-mentioned dissertation, hereby grant to all reference sources the permission to publish and disseminate the abstract of the above-mentioned dissertation.

Signature 

Date 2021-4-1

Design and Optimization of In-Cycle Closed-Loop Combustion Control with Multiple Injections

by Carlos Jorques Moreno



LUND
UNIVERSITY

Cover illustration front: Illustration of the analysis and control of a direct injection internal combustion engine, by Carlos Jorques Moreno.

Funding information: The thesis work was financially supported by the Strategic Vehicle Research and Innovation program (FFI) of the Swedish Energy Agency, grant number 22485-4, and Scania CV AB.

© Carlos Jorques Moreno 2021

Faculty of Engineering, Department of Energy Sciences

ISBN: 978-91-7895-827-6 (print)

ISBN: 978-91-7895-828-3 (pdf)

ISRN: LUTMDN/TMHP-19/1163-SE

ISSN: 0282-1990

Printed in Sweden by Media-Tryck, Lund University, Lund 2021



But still try, for who knows what is possible!

Michael Faraday

Abstract

For the increasing demand of transportation services, decoupling fossil fuels and energy demand is a must to reduce the effects of green-house gases on global warming. The uprise of alternative powertrains based on electricity relies heavily on long-term investments and technologies not yet available. Meanwhile, the demand of internal combustion engines for long-haul transportation is increasing due to their high output work, low cost of operation, high efficiency, and robustness. For these reasons, biofuels play a fundamental role in the sustainability of the transportation sector. With the increased uncertainty of biofuel combustion properties, advanced combustion control systems have the potential to operate the engine with high flexibility while maintaining a high efficiency and robustness. Pushed by the increasingly stringent emission legislations, operation of combustion engines requires an increasing number of sensors and actuators to operate with tighter margins over a wide range of operating conditions. This thesis investigates the analysis, design, implementation, and application of closed-loop Diesel combustion control algorithms. By fast in-cylinder pressure measurements, the combustion evolution can be monitored to adjust the multi-pulse fuel injection within the same cycle. This is referred to as in-cycle closed-loop combustion control. The measurements are processed in an FPGA for the computation of the control of a pilot-main fuel injection, at the scale of nanoseconds.

The design of the controller is based on the experimental characterization of the combustion dynamics by the heat release analysis. To increase its accuracy, a model to estimate the cylinder volume deviation was investigated. The pilot combustion, its robustness and dynamics, and its effects on the main injection were analyzed. The separation between the pilot combustion and main injection affects the combustion rate, which was described by the interaction modes. The pilot burnt mass significantly affects the main combustion timing and heat release shape, which determines the engine efficiency and emissions. These variations can be compensated by the in-cycle adjustment of the main injection.

The closed-loop architecture is followed for the design of the feedback combustion control. An in-cycle pilot mass virtual sensor is proposed to obtain feedback with an accuracy of $\pm 0.5mg$ already at the peak of the heat release. To overcome the low accuracy of highly uncertain short pilot on-times due to measurement noise, a Bayesian estimator based on the pilot misfire ratio was proved to reduce the uncertainty by 60% to $\pm 0.54mg/st$. The limitations imposed by the intrinsic delay between the control action (fuel injection) and

output measurements (pressure increase) were overcome by a predictive model. High prediction accuracy is possible by the on-line model adaptation, where a reduced multi-cylinder method is proposed to reduce its implementation complexity in the FPGA. The predictive closed-loop combustion control strategy permits to reduce the stochastic cyclic variations of the controlled combustion metrics by 50%, with a total dispersion of $\pm 0.4CAD$ and $\pm 0.3CAD$ for the pilot and main SOC respectively, $\pm 0.6mg$ pilot burnt mass and $\pm 0.2bar$ IMEP. In-cycle controllability of the combustion requires simultaneous observability of the pilot combustion and control authority of the main injection. The imposition of this restriction for closed-loop operation may reduce the indicated efficiency (by $-0.01\%_{unit}$ in 14% of the cases) and increase the operational constraints violation compared to open-loop operation. This is especially significant in the case of pilot misfire, with a penalty of $-1\%_{unit}$. For in-cycle pilot misfire detection, stochastic and deterministic methods were investigated, with 96% correct detection accuracy before the main SOI. The on-line pilot misfire diagnosis was feedback for its compensation by a second pilot injection, where the main SOC error was reduced from $+1.5 \pm 0.6CAD$ to $0 \pm 0.4CAD$ and the load error from $-0.5 \pm 0.4bar$ to $0 \pm 0.2bar$. High flexibility on the combustion control strategy was achieved by a modular design of the controller. A finite-state machine was investigated for the synchronization of the feedback signals (measurements and model-based predictions), active controller and output action. The experimental results showed an increased performance in the root mean-squared error of the reference tracking and shorter transients, regardless of operating conditions and fuel used.

To increase the indicated efficiency, direct and indirect optimization methods for the combustion control were investigated. An in-cycle controller to reach the maximum indicated efficiency under the operational uncertainty was developed. The efficiency was increased by $+0.42\%_{unit}$. The effectiveness was limited due to the controller linearization. The indirect method took advantage of the reduced cyclic variations to optimize the set-point reference for maximum indicated efficiency while fulfilling constraints on hardware and emission limits. The risk of pilot misfire requires wider tolerance margins, which can be reduced by the in-cycle controller. By embedding the reduced dispersion in the stochastic optimization, the closed-loop control of CA50 permits to increase the indicated efficiency by $+0.6\%_{unit}$ at mid loads and, up to $+1.8\%_{unit}$ at low loads, under maximum pressure rise rate constraints, compared to open-loop operation.

Finally, tools to evaluate the total cost of the system were provided by the quantification of the hardware requirements for each of the controller modules.

Populärvetenskaplig sammanfattning på svenska

Ett samhälle med ökande behov av transporttjänster och stort behov av minskade växthusgasutsläpp måste bryta sitt beroende av fossila bränslen. Introduktionen av alternativa, elektrifierade, fordonsdrivlinor kräver tekniska lösningar och långsiktiga ekonomiska investeringar som inte finns än. Samtidigt ökar efterfrågan på förbränningsmotorbaserade drivlinor, eftersom de på ett tillförlitligt och ekonomiskt sätt kan leverera det mekaniska arbete som behövs för tunga transporter. Biobränslen spelar alltså en nyckelroll i ett hållbart transportsystem. Allt hårdare utsläppslagstiftning ökar kraven på motorns styrsystem och kräver i sin tur fler och fler sensorer och ställdon. Ökad användning av biobränslen med varierande förbränningsegenskaper ställer ytterligare krav på styrsystem för att säkerställa låg bränsleförbrukning och hög driftsäkerhet. Avhandlingen behandlar analys, design, implementering och tillämpning av algoritmer för återkopplad dieselförbränningsreglering. Genom mätning av trycket i motorns cylindrar kan förbränningens övervakas snabbt nog för att styra flera bränsleinsprutningar i en och samma cykel. Detta koncept benämns "in-cycle closed-loop combustion control" vilket kan översättas med "återkopplad styrning under pågående förbränning". Pilot- och huvudinsprutning av bränsle analyseras och beräknas inom nanosekunder och sker baserat på det uppmätta cylindertrycket i en FPGA (Field Programmable Gate Array).

Vid små pilotbränslemängder måste bränsleinsprutarna aktiveras under kort tid vilket leder till stor osäkerhet i mängden bränsle som sprutas in. Samspelet mellan pilotinsprutning och huvudinsprutning studeras i avhandlingen och en strategi för hur huvudinsprutningen kan justeras för att kompensera för t.ex. utebliven pilotinsprutning beskrivs. En virtuell pilotbränslemängdssensor baserad på tryckmätningen anger bränslemängden med en noggrannhet på $\pm 0.5mg$. En prediktiv modell utvecklades för de fall då tidsfördröjningen var för stor.

I avhandlingen jämförs direkta och indirekta metoder för att minimera bränsleförbrukningen genom återkopplad styrning under förbränningen. Direkta metoder innebär att bränsleinsprutningen och förbränningen styrs så att den beräknade bränsle-förbrukningen blir så låg som möjligt medan indirekta metoder försöker bibehålla förkalibrerade förbränningsegenskaper (t.ex. förbränningstidpunkt) som ger lägsta bränsle-förbrukning. Med direkta metoder uppnåddes en ökning av verkningsgraden med 0.42% *enheter*. En begränsande faktor var lineariseringen i regulatorn som var nödvändig för att hantera regleringen i FPGA. Den indirekta metoden ledde till minskad förbränningsvariation och höjde verkningsgraden samtidigt som samtliga hårdvaru- och utsläpps begränsningar uppfyllades. Reglering i förbränningscykeln minskar känsligheten för pilotmisständning

och verkningsgraden ökas med 0.6% _{enheter} för motorlaster i mellanregistret och med 1.8% _{enheter} för låga laster genom att förbränningstidpunkten styrs under förbränningen till sitt kalibrerade värde.

Hårdvarukraven för den typ av styrning som beskrivs i avhandlingen analyserades och ett verktyg för utvärdering av systemkostnaderna togs fram.

Acknowledgements

The thesis you have in front of you would not have been possible without the guidance and support from my supervisors, Prof. Ola Stenlås and Prof. Per Tunestål. I want to thank both of them for given me enough freedom to get lost and explore, learn new lessons and get back on track with new ideas. The knowledge and expertise they have shared with me assisted and inspired me throughout this work. They really challenged and encouraged me to always seek a little bit further, which pushed forward the findings presented in this thesis. My greatest gratitude to both of you, as supervisors and colleagues.

The project was possible by the funding support of the Strategic Vehicle Research and Innovation (FFI) program, Scania CV AB and Lund University, to which I am indebted to. The experimental work was carried out at the facilities at Lund University, coordinated by the lab manager Dr. Marcus Lundgren, to whom I thank for his fast support when any problem aroused. I gratefully acknowledge the assistance of the lab technicians, who helped me to change the fuel injectors a countless number of times. I want to thank Dr. Gabriel Tureson and Dr. Lianhao Yin for introducing me to the lab facilities and teaching me how to run the engine. I also want to acknowledge the seniors at Lund University, Prof. Öivind Andersson, Prof. Martin Tunér and Prof. Sebastian Verhelst, and the rest of my colleagues at the Division of Combustion Engines for the good fika discussions and venting therapy when nothing seemed to work out.

The other half of this thesis has been done thanks to Scania, where I spent most of my time surrounded by incredibly experienced colleagues from whom I learned a lot. I very much appreciate the people who took their time to support and steer this project, Roger Hälleberg, Dr. Jonas Holmborn and Magnus Pelz, for their insightful suggestions and comments. Enourmous thanks to all my colleagues at NESC and NCFC throughtout the years. Special thanks to my previous managers, Patrik Ederstål, Thomas Colton and Sofie Jarelius, for their support and for signing the many train tickets. Great thanks to Dr. Stephan Zentner, for sharing great fika stories and his knowledge on how to model and control an engine, and Mikael Nordin for sharing his vast experience on engine development.

Finally, I must acknowledge my family, who inconditionally supported me from the very beginning ever since I dreamed of becoming an inventor, to when I moved to Sweden for my Masters and where I ended up coursing my PhD studies. *Os quiero*. And last but not least, it is an honour to have shared all these years with my expat familiy in Stockholm, and my good friends in Spain.

Nomenclature

Abbreviations

0D	Zero-Dimensional
AC	Alternative Current
AD	Analog to Digital
ADC	Analog to Digital Conversion
AFR	Air-Fuel Ratio
AHR	Accumulated Heat Release
ANOVA	Analysis of Variance
AO	Analog Output
AO/DIO	Analog-Output / Digital Input-Output
ASI	Application Specific Interface
ASIC	Application Specific Integrated Circuit
ATDC	After Top Dead Center
BDC	Bottom Dead Center
BP	Back Pressure
CA	Crank Angle
CA10	Crank Angle at 10% fuel mass burnt
CA50	Crank Angle at 50% fuel mass burnt
CA90	Crank Angle at 90% fuel mass burnt
CAD	Crank Angle Degree
CARB	California Air Resources Board
CFD	Computational Fluid Dynamics
CI	Compression-Ignited
CL	Closed-Loop
CLB	Configurable Logic Block
CLCC	Closed-Loop Combustion Control
CMRE	Controllable Maximum Reachable Efficiency
CO	Carbon Monoxide
COV	Coefficient of Variation
DBCC	Duration Before the Center of Combustion
DC	Direct Current
DEM	Discrete Event Model
DES	Disturbed Efficiency Set
DIO	Digital Input/Output
DOC	Diesel Oxidation Catalyst
DPF	Diesel Particulate Filter
EGR	Exhaust Gas Recirculation

EKF	Extended Kalman Filter
EOC	End of Combustion
EOI	End of Injection
EPA	Environmental Protection Agency
EU	European Union
EVO	Exhaust Valve Open
FAME	Fatty Acid Methyl Esters
FEM	Finite Element Model
FF	Feed-Forward
FPGA	Field Programmable Gate Array
FS	Full Scale
FSM	Finite-State Machine
FTM	Fast-Thermal Management
GDP	Gross Domestic Product
GHG	Greenhouse Gases
HC	Hydrocarbon
HCCI	Homogeneous Charge Compression Ignition
HDL	Hardware Describe Language
HLS	High-Level Synthesis language
HMI	Human-Machine Interface
HP	High Pressure
HR	Heat Release
HRR	Heat Release Rate
HT	Heat Transfer
HVO	Hydrotreated Vegetable Oil
HW	Hardware
ICE	Internal Combustion Engine
ID	Ignition-Delay
IIR	Infinite Impulse Response
IMEP	Indicated Mean Effective Pressure
IO	Input/Output
IP	Index Protocol
IS	Interconnection Switch
ITE	Indicated Thermodynamic Efficiency
IVC	Inlet Valve Closing
KF	Kalman Filter
LHV	Lower Heating Value
LP	Low Pressure
LU	Logic Unit
LUT	Look-Up Table
MBT	Maximum Brake Torque

MHRR	Mean Heat Release Rate
MPC	Model Predictive Control
MRE	Maximum Reachable Efficiency
MVM	Mean Value Modelling
NI	National Instruments
NO	Nitrogen Monoxid
PC	Personal Computer
PCI	Peripheral Component Interface
PD	Pilot Duration
PI	Proportional-Integral Controller
PM	Particulate Matter
PPC	Partially Premixed Combustion
PRR	Pressure Rise Rate
PXI	PCI Extensions for Instrumentation
RAM	Random Access Memory
RCCI	Reactivity Controlled Compression Ignition
RME	Rapeseed Methyl Ester
RMSE	Root Mean-Squared Error
RPM	Revolutions Per Minute
RTOS	Real Time Operating System
SCR	Selective Catalyst Reduction
SI	Spark-Ignited
SOC	Start of Combustion
SOI	Start of Injection
SOV	Start of Vaporization
TCP	Transmission Control Protocol
TDC	Top Dead Center
TUHC	Total Unburnt Hydrocarbons
UHC	Unburned Hydrocarbons
UMRE	Unconstrained Maximum Reachable Efficiency
VHDL	Virtual Hardware Description Language
VI	Virtual Instrument
VVA	Variable Valve Actuation
XPI	Extreme High-Pressure Injection System

Symbols

a	Acceleration
A	Cylinder surface area
A_p	Piston area
B	Bore
D	Detection event
$dQ/d\theta$	Heat release rate
dQ_{HR}	Net heat release
dQ_{HT}	Heat transfer
F	Force
$f(\cdot)$	General function
f_M	Measured output
h_{HT}	Heat transfer gain
I	Identity matrix
J	Model-error cost function
k	Gain
K	Kalman filter gain
l	Connecting rod length
L	Stroke
m	Mass
M	Misfire event
m_{air}	Fresh air mass
m_{inj}	Injected fuel mass
m_{IVC}	Mass at IVC
m_{main}	Main fuel mass
m_{O_2}	Oxygen mass
m_{pilot}	Pilot fuel mass
m_{pilot}^{burnt}	Burnt pilot mass
m_{res}	Residual gas mass
m_f	Fuel mass
n	Number of cycles
N	Total number of cycles
n_{cyl}	Number of cylinders
N_{eng}	Engine speed
p	Cylinder pressure
p_m	Motoring cylinder pressure
P	Probability density function
p_{exh}	Exhaust pressure
p_{rail}	Rail pressure
Q	Measurement covariance matrix

q_{inj}	Fuel injection flow
q_{prem}	Premixed combustion rate
q_{diff}	Diffusive combustion rate
q_{decay}	Decay combustion rate
Q_{comb}	Combustion heat
Q_{HT}	Heat transfer
Q_{LHV}	Lower heating value
r	Crank radius
R	Ideal gas constant
R^2	Coefficient of determination
r_{comb}	Unitary combustion progress
r_m	Misfire ratio
s	Linear cylinder speed
t_{inj}	Injection on-time
T	Cylinder temperature
T_{SOI}	In-cylinder temperature at SOI
T_q	Instantaneous torque
u	Input vector
V	Cylinder Volume
V_c	Clearance volume
V_d	Displaced volume
V_t	Total volume
w	Gas mean velocity
$W_{c,i}$	Indicated work
W_g	Gross Indicated work
x	System internal states
Y	Logarithmic pressure evolution
z	Measurement
α	Pilot misfire rate gain
β	Pilot misfire rate offset
χ	Combustion completion state
δ	Binary pilot misfire variable
Δp	Pressure sensor offset
$\Delta\theta_{ID}$	Ignition-delay
$\Delta\theta_{pilot-main}$	Pilot-main injection separation
δ_{comb}	Combustion trigger
δ_{inj}	Active injection variable
\dot{m}_{inj}	Fuel mass injection rate
ϵ	Non-dimensional normal strain
ϵ_u	Input error
ϵ_z	Measurement error

η_{comb}	Combustion efficiency
η_{max}	Maximum indicated efficiency
η_{th}	Thermodynamic efficiency
Γ	Robustness metric
γ	Specific heat ratio
\hat{m}	Estimated mass
κ	Polytropic coefficient
λ	Lambda
\mathbb{E}	Expected value
\mathbf{x}	Measured variable
$\mathcal{B}_{\mathcal{N}}$	Binomial distribution
\mathcal{H}_0	Null hypothesis
\mathcal{H}_1	Alternative hypothesis
\mathcal{N}	Normal distribution
\mathcal{R}	Space of reachable states
\mathcal{U}	Space of inputs
μ	Mean value of normal distribution
μ_{comb}	Combustion rate gain
μ_b	Bearing radial clearance
ν	Measurement error uncertainty
ω	Angular velocity
\overline{HR}	Mean heat release rate
Φ	Dynamic system
$\phi(\mathbf{x})$	Detection function
Ψ_u	Space of input disturbances
Ψ_x	Space of state disturbances
ρ_i	Correlation coefficient
σ	Standard deviation
τ	Combustion rate time constant
θ	Crank angle degree
θ_{SOI}	Start of injection
θ_{EOI}	End of injection
θ_{SOC}	Start of combustion
v	Parameter uncertainty
ε	Disturbances
ϑ	Parameter set
ψ	Parameter vector
φ	Common-cylinder parameter vector
ξ	Individual-cylinder parameter vector
(x, y, z)	Cartesian coordinates
$[O_2]$	Oxygen concentration

List of publications

This thesis is based on the following publications:

- I **Investigation of Small Pilot Combustion in a Heavy-Duty Diesel Engine**
Jorques Moreno, C., Stenlång, O. and Tunestål, P.
SAE Int. J. Engines 10(3):1193-1203, 2017
- II **Influence of Small Pilot on Main Injection in a Heavy-Duty Diesel Engine**
Jorques Moreno, C., Stenlång, O. and Tunestål, P.
SAE Technical Paper 2017-01-0708, 2017
- III **Cylinder Pressure-Based Virtual Sensor for In-Cycle Pilot Mass Estimation**
Jorques Moreno, C., Stenlång, O. and Tunestål, P.
SAE Int. J. Engines 11(6):1167-1182, 2018
- IV **In-Cycle Closed-Loop Combustion Controllability with Pilot-Main Injections**
Jorques Moreno, C., Stenlång, O. and Tunestål, P.
Thiesel 2018, Conference on Thermo-and Fluid Dynamics Processes in Direct Injection Engines, Valencia, Spain, 2018
- V **In-Cycle Closed-Loop Combustion Control with Pilot-Main Injections for Maximum Indicated Efficiency**
Jorques Moreno, C., Stenlång, O. and Tunestål, P.
IFAC-PapersOnLine, Volume 51, Issue 31, 2018, Pages 92-98
- VI **Internal Combustion Engine Cylinder Volume Trace Deviation**
West, I., Jorques Moreno, C., Stenlång, O., Jönsson, O., Haslestad, F.
SAE Int. J. Engines 11(2):195-214, 2018

- VII **Cylinder Pressure Based Method for In-Cycle Pilot Misfire Detection**
Jorques Moreno, C., Stenlång, O. and Tunestål, P.
SAE Int. J. Adv. & Curr. Prac. in Mobility 2(2):488-502, 2020
- VIII **Bayesian Method for Fuel Mass Estimation of Short Pilot Injections based on its Misfire Probability**
Jorques Moreno, C., Stenlång, O. and Tunestål, P.
2020 American Control Conference (ACC), Denver, CO, USA, 2020, pp. 1507-1513
- IX **Predictive In-Cycle Closed-Loop Combustion Control with Pilot-Main Injections**
Jorques Moreno, C., Stenlång, O. and Tunestål, P.
IFAC-PapersOnline, Volume 53, Issue 2, 2020, Pages 14000-14007
- X **Multi-Cylinder Adaptation of In-Cycle Predictive Combustion Models**
Jorques Moreno, C., Stenlång, O. and Tunestål, P.
SAE Technical Paper 2020-01-2087, 2020
- XI **In-Cycle Closed-Loop Combustion Control for Pilot Misfire Compensation**
Jorques Moreno, C., Stenlång, O. and Tunestål, P.
SAE Int. J. Adv. & Curr. Prac. in Mobility 3(1):299-311, 2021
- XII **Stochastic Set-Point Optimization for In-Cycle Closed-Loop Combustion Control Operation**
Jorques Moreno, C., Stenlång, O. and Tunestål, P.
SAE Technical Paper 2021-01-0531, 2021
- XIII **Modular Design and Integration of In-Cycle Closed-Loop Combustion Controllers for a Wide-Range of Operating Conditions**
Jorques Moreno, C., Stenlång, O. and Tunestål, P.
Accepted for publication in *2021 American Control Conference (ACC)*, New Orleans, LA, USA, 2021

XIV Quantification of FPGA Requirements for Closed-Loop Combustion Control Implementation

Jorques Moreno, C., Stenlång, O. and Tunestål, P.

Submitted to *ICE2021, International Conference on Engines and Vehicles*, Capri, Italy, 2021

XV Efficiency Optimization by In-Cycle Closed-Loop Combustion Control

Jorques Moreno, C., Stenlång, O. and Tunestål, P.

Submitted to *Control Engineering Practice*, 2021

Contents

Abstract	i
Populärvetenskaplig sammanfattning på svenska	iii
Acknowledgements	v
Nomenclature	vii
List of publications	xiii
1 Introduction	1
1.1 Global Context and Motivation	1
1.2 Diesel Engine Challenges	5
1.3 Outline and Contributions	8
2 Fundamental Engine Principles	15
2.1 The Diesel Engine	15
2.2 Cylinder Geometry	22
2.3 Fuel Characteristics	23
2.4 Operating Parameters	24
2.5 Combustion Supervision	27
3 Experimental Setup	31
3.1 The Scania D13 Engine	31
3.2 Calibration	35
3.3 Signal Processing	36
3.4 Control-System Architecture	36
3.5 Fuels	40
4 Experimental Combustion Characterization	41
4.1 Pilot and Main Injections	41
4.2 Pilot Injection	44
4.3 Main Injection	50
5 Combustion Modeling	57
5.1 Modeling Approaches	57
5.2 Stochastic Simulation Models	60
5.3 Predictive Models	78
5.4 Model Calibration	81

6	Estimation Methods	85
6.1	Cylinder Volume Estimation	85
6.2	Specific Heat Ratio Estimation	92
6.3	Pilot Misfire Detection	95
6.4	Start of Combustion Detection	103
6.5	In-Cycle Pilot Mass Estimation	105
6.6	Misfire Ratio Based Pilot Mass Estimation	112
7	On-line Model Adaptation	117
7.1	Model Adaptation	117
7.2	Multi-Cylinder Adaptation	119
7.3	Adaptation of Predictive Combustion Models	122
8	Closed-Loop Combustion Controller Design	129
8.1	In-Cycle Controller Design	129
8.2	In-Cycle Controllability	132
8.3	Cascade Multi-Loop Interaction	142
9	In-Cycle Closed-Loop Combustion Control	145
9.1	Variance Reduction	146
9.2	Pilot Misfire Compensation	153
9.3	Controller Management	163
10	Efficiency Optimization	173
10.1	Direct Efficiency Optimization	174
10.2	Indirect Efficiency Optimization	183
11	Implementation Requirements	193
11.1	Signal Processing Requirements	193
11.2	Algorithm Implementation	195
11.3	Hardware Requirements	200
12	Summary and Conclusions	203
13	Future Work	209
	References	215

1.1 Global Context and Motivation

Transportation is a key component of economic development and human welfare, as they are intrinsically linked (Kahn Ribeiro et al., 2007). The increase in the gross domestic product (GDP) over the last decades correlates directly with the expansion of road freight transportation (IEA, 2017a), see Figure 1.1a. The primary energy source for transportation has been the internal combustion engine (ICE), due to their simplicity, durability, reliability, low power-to-weight ratio, high power controllability and reasonable efficiency (Heywood, 1988). The benefits of the ICE on transportation are offset by the greenhouse gases (GHG) they produce, as fossil fuels still supply 95% of the energy they require (Kahn Ribeiro et al., 2007). GHG, primarily CO₂ from combustion, absorb long-wave radiative energy that results in temperature increase i.e., global warming. Human activity is responsible for the drastic increase in GHG over the last decades (IPCC, 2014) and the consequent temperature rise, as can be visualized in Figure 1.1b.

In Europe, the transport sector accounts for 27% of the total GHG, 74% of which from road freight transport (EIA, 2005; IEA, 2020c). Altogether, road freight alone accounts for 7% of global energy-related CO₂ emissions. From

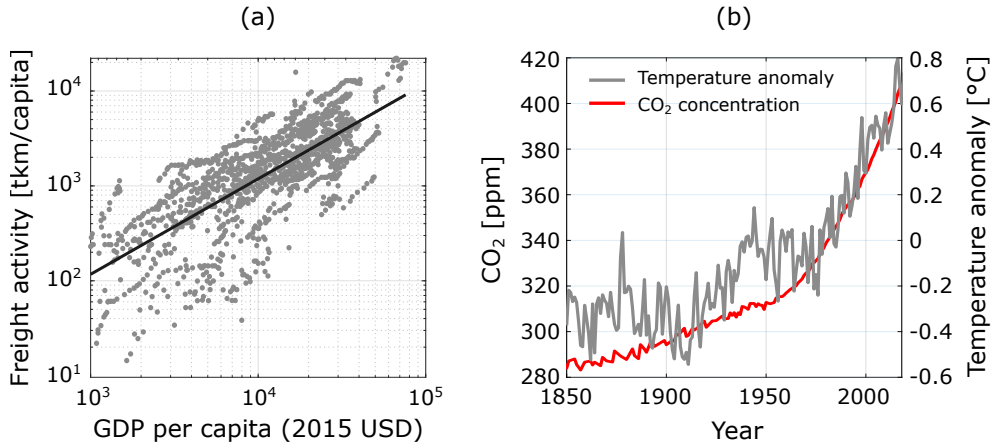


Figure 1.1: (a) Road freight activity in tonne kilometer per capita plotted against GDP per capita for different countries between 1971 and 2014 (Source: IEA (2017a)) (b) Land-surface temperature anomaly relative to the average between 1951 and 1980 and yearly average of atmospheric CO₂ concentration (Sources: Berkeley Earth, IEA (2020c) and Scripps Institution of Oceanography, Sims et al. (2014)).

2000, transport emissions reached a 7.0Gt CO₂ eq (Sims et al., 2014), increasing by 2.6% annual (IEA, 2020b), and more than doubled by 2010 compared to 1970 levels. In non-OECD countries, the transport sector accounts for 36% of total emissions, and are expected to increase to 46% by 2030 if current trends continue (Kahn Ribeiro et al., 2007).

With an expected 2% of increase demand on energy for transportation every year (Kahn Ribeiro et al., 2007), emissions need to half by 2050, compared to 1990 levels, to meet the long-term 80% GHG reduction target (EIA, 2005) and 50% reduction in petroleum use by 2030. For road freight transportation, Diesel ICE represents more than 90% of powertrains, and even as late as 2050, most trucks in the global fleet are still expected to use Diesel ICE (IEA, 2017b). Trucks contribute to more than one third of total transport-related emissions of NO_x, and half of the particulate matter (IEA, 2017b), whose emissions levels were legislated in EU and US EPA regulations since 2014.

During the past 20 years, the increasingly stringent EU I-VI and CARB regulations have driven the research and development of efficient ICE for transportation to fulfill emissions levels (European Union, 2007). While the total oil demand in the car population has already started to decline in developed countries (IEA, 2020b, 2017a), the heavy-duty fleet still have a global net increase in Diesel demand. Therefore, the historical link between economic growth, energy demand and GHG emissions must be decoupled to guarantee a sustainable future, considering the increasing demand of passenger and freight activity (Sims et al., 2014).

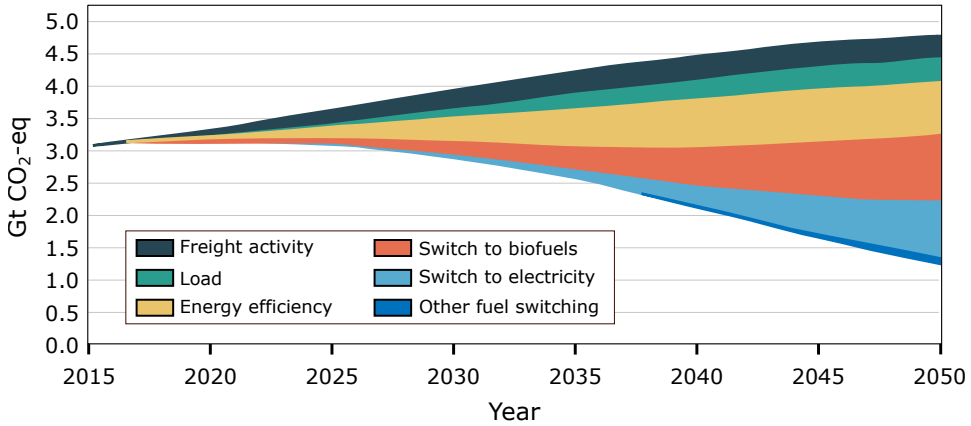


Figure 1.2: Contribution to GHG emissions reduction by measure in the Modern Truck Scenario, relative to the Reference Scenario (IEA, 2017a)

1.1.1 Decarbonization of transportation

Decoupling transport from GDP growth will require the development and deployment of appropriate measures, advanced technologies, and improved infrastructure (Sims et al., 2014). The cost-effectiveness of these opportunities may vary by region and over time (Sims et al., 2014) which will require infrastructure investments simultaneously with more efficient vehicle technologies (Sims et al., 2014). The decarbonization of the road freight transportation sector requires long-term planning and support, as more than 60% of the emissions reduction in 2070 come from technologies not commercially available today (IEA, 2020a). To achieve this goal, an increase in energy efficiency and a full transition from fossil fuels combustion-based energy generation to renewable energy is mandatory (IEA, 2020a).

In the Modern Truck Scenario (IEA, 2017a) energy efficiency and alternative fuels, including electrification, account for a 34% energy reduction in 2050, see Figure 1.2. Together with improvements in logistics and road freight operation, a total reduction of 75% of CO₂ emissions can be achieved. The path towards this scenario requires a broad mix of technologies, such as electrification via battery, plug-in and hydrogen fuel-cell electric vehicles, advanced biofuels, and synthetic fuels, together with a renewable production of electricity (IEA, 2020b,a). In the Modern Truck Scenario, the projected fuel demand of these technologies is summarized in Figure 1.3.

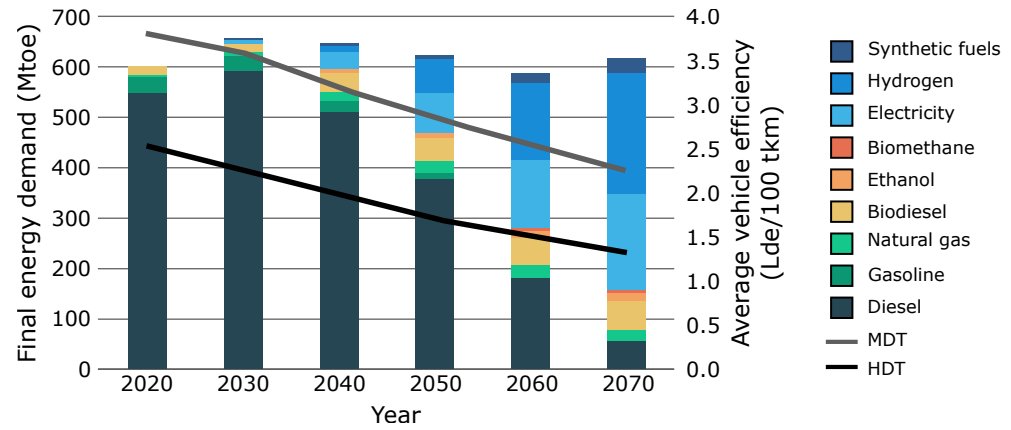


Figure 1.3: Global heavy-duty trucking energy demand by fuel in equivalent Diesel liters (Lde) and average vehicle efficiency for medium-duty trucks (MDT) and heavy-duty trucks (HDT) in the Sustainable Development Scenario (IEA, 2020a).

Batteries

Electric heavy-duty vehicles driven by electric motors have so far a limited market penetration due to short driving range, short battery life and high cost (Kahn Ribeiro et al., 2007). This is especially significant for heavy-duty transportation, where the gravimetric and volumetric energy densities, specific power, durability, and number of discharge cycles limit the applicability of batteries. In the Sustainable Development Scenario, the equivalent to 33 Tesla Gigafactories will be needed by 2070 to equip heavy-duty trucks (IEA, 2020a).

Hydrogen

Hydrogen is a flexible energy carrier and extends electricity's reach (IEA, 2020a), but today's energy system is still heavily dependent on fossil fuels that require a transition for hydrogen to become a sustainable fuel (IEA, 2017a) and are crucially dependent on the development of supporting infrastructure (IEA, 2020a).

Biofuels

Alternatives such as electricity and hydrogen can help on the decarbonization of transportation, but the full cycle carbon reduction depends on the generation of electricity and hydrogen (Kahn Ribeiro et al., 2007). The uptake of hydrogen and electricity-based trucks is very uncertain and the balance of long-term

technology uptake will depend on the progress of relevant technologies (IEA, 2020a). This is why biofuels play a crucial role for the decarbonization of the long-haul sector (IEA, 2017b). Biofuels are projected to supply a 17% of final energy demand by 2060 in the 2°C IEA scenario, providing almost a 20% of the CO₂ savings (IEA, 2017b). Consequently, ICE powertrains using a mix of biofuels with low or negative lifecycle GHG emissions will be crucial in the Sustainable Development Scenario (IEA, 2020a). This thesis aims to ease the transition towards ICE efficient and clean operation with biofuels.

1.2 Diesel Engine Challenges

The increasingly stringent emission legislation promoted the research and development of engines during the past decades, aiming for fuel consumption reduction while limiting emissions of CO₂, NO_x, PM and HC. The accomplishment of current CARB and EURO VI legislation levels requires the use of high pressure fuel injection, compression and cooling of inducted air, and costly after-treatment systems (Majewski and Khair, 2006). The resulting engine technology advancement to fulfill emissions legislation led to an increase in the number of sensors and actuators, which promoted the advance of engine-control systems.

Closed-loop engine control is an enabler to realize the requested torque with minimal fuel consumption, high performance and robustness, under varying real-world operating conditions, while meeting constraints related to emissions, noise, and safety, despite the operational uncertainties (Willems, 2018; Kolbeck, A., 2011; Schnorbus et al., 2008). Furthermore, the smart engine operation by closed-loop engine-control systems permits to reduce the development time and cost of the engine design and operation.

Advanced closed-loop engine control has also promoted the development of new, clean and efficient combustion concepts, such as HCCI (Olsson and Johansson, 2001), PPC (Manente, 2010) and RCCI (Reitz and Duraisamy, 2015). These low temperature combustion concepts require the closed-loop control of its combustion to ensure the stability and robustness over a wide range of operating conditions. While this is not required for Diesel combustion operation, closed-loop combustion control eases the engine calibration and operation with tighter margins for increased efficiency under operational uncertainties. This thesis is focused on the development of Diesel closed-loop combustion control algorithms.

1.2.1 Closed-loop combustion control

Traditionally, combustion in compression ignition engines has been operated in open-loop, where the fuel amount was determined by the accelerator pedal position, engine speed and air-fuel ratio to reach the torque demand. Fuel injection timings for the combustion control were calibrated from maps (Guzzella and Onder, 2004). Forthcoming EURO VII legislation is expected to include standards for GHG emissions levels considering real driving conditions (Regulation (EU) 2019/1242, 2019). Moreover, the wide range of different properties that biofuels cover affect the ICE performance and emissions (Kumar et al., 2014). These are major challenges for the design, calibration, and operation of ICE over their whole life span, considering the different operating conditions (engine speed, load, oxygen concentration, humidity, rail pressure, etc.), fuel properties, production tolerances, aging and stochastic normal variations (Saracino et al., 2015; Willems, 2018).

To address these challenges, closed-loop combustion control comprises all the technologies to automatically respond to changes, disturbances and random variations of the combustion process. The design of the automatic control of the combustion establishes which variable to actuate, in order to influence the engine state, information which can be obtained by an output measurement. Closed-loop controllers have the advantage of making the system more resilient to the external disturbances and variations in system components. Notwithstanding, a trade-off between system performance and robustness is imposed by the addition of possible dynamic instabilities and the introduction of sensor noise into the system (Åström and Murray, 2008).

Depending on the specified system-performance requirements to be fulfilled in the short-, mid- and long-term applications, different measurements and variables are selected for the closed-loop combustion control, following a hierarchical architecture. This is illustrated in Figure 1.4, where some of the most important subsystems are indicated.

A fundamental variable for the combustion supervision in an internal combustion engine is the cylinder pressure, which is available for direct measurement (Shahroudi, 2008). Piezoresistive or piezo-capacitive transducers are commonly used for a fast, accurate and reliable pressure measurement (D’Ambrosio et al., 2015). In this thesis, piezoelectric pressure transducers, mounted in the cylinder head, utilize the piezoelectric effect to measure the charge generated when a piezoelectric crystal is exposed to the pressure force. The in-cylinder pressure is commonly used to estimate indicated engine work, temperature, heat release rate, NO_x formation (Muric et al., 2013b) and soot (Yang et al., 2017) by virtual

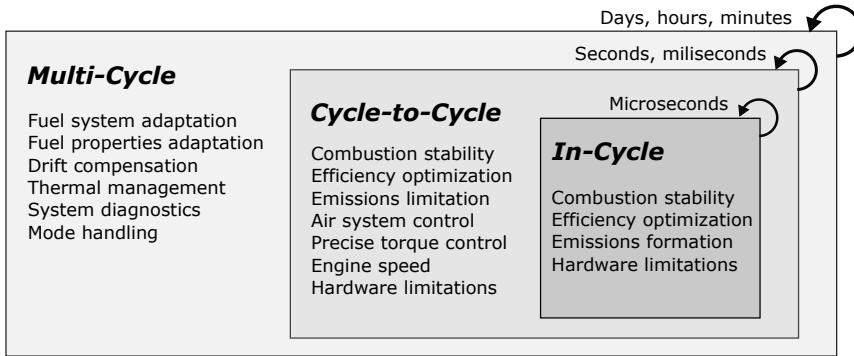


Figure 1.4: Engine closed-loop control hierarchy attending to the time horizon of the control problem. Some examples of control targets are listed. This thesis focuses on the in-cycle time scale.

sensors. Although pressure sensors are commonly used in engine research, development and calibration (Powell, 1993), their high technical demands and associated costs have hindered their widespread use in production vehicles. However, the potential use for pressure sensors in engine control and diagnostics (Iorio et al., 2003; Eriksson and Thomasson, 2017) still motivate that cylinder pressure sensing might be widely implemented in future production vehicles.

The main combustion control variable is the injected fuel amount. The actuation is provided by a solenoid injector, connected to a common-rail fuel system. The injected fuel quantity is determined by the common-rail pressure and the opening duration of the injector nozzle, commanded by the current pulses sent to the injector's solenoid. Details of the working of a solenoid injector can be found in (Bosch, 2011). The possibility to divide the fuel among several injection events within the same cycle gives additional degrees of freedom for the combustion control.

1.2.2 In-cycle combustion control

At the fastest time scale, the combustion is controlled in the same cycle, intra cycle or in-cycle. For in-cycle control, the combustion monitoring is provided by the in-cylinder pressure sensors synchronized with the crank angle degree for the cylinder volume estimation. Additional sensors for referencing the in-cylinder pressure measurements and estimating the inlet charge are also required. This is commonly provided by inlet manifold pressure and temperature sensors.

Strategies for in-cycle closed-loop control are designed for the direct or indirect regulation of the combustion. The strategies attend to different objectives, tar-

getting the reduction of different disturbances effect on the combustion. Some examples of external disturbances are intake air mass (Steffen et al., 2012), EGR variations (Yang et al., 2014), fuel mass injected (Zander et al., 2010b), or pilot misfire (Jorques Moreno et al., 2020a). Examples of control targets are the combustion stabilization (Wick et al., 2019), efficiency optimization (Jorques Moreno et al., 2018); reduction of cyclic dispersion of the accumulated heat release (Zander et al., 2010b), the exhaust pressure (Yang et al., 2014), or the combustion metrics (Jorques Moreno et al., 2020b); constraint fulfillment (Steffen et al., 2012); limitation (Muric et al., 2013b) and reduction of emissions formation (Muric et al., 2013a).

Direct methods use different combustion metrics as the set-point reference, such as the start of combustion (Jorques Moreno et al., 2020b), the center of combustion (Yang et al., 2014) or the exhaust temperature (Zheng et al., 2009). Indirect methods use the trace evolution of some combustion-related variable, such as the pressure (Steffen et al., 2012), temperature (Asad and Zheng, 2008), heat release (Zander et al., 2010b) or pollutant formation (Muric et al., 2013b).

The actuation on the combustion progress is mainly regulated by the multiple fuel injections. Additional degrees of freedom can be provided by variable valve timing actuators and supplementary injectors, for the injection of fuel, water (Wick et al., 2019) or emissions reductant such as urea (Muric et al., 2013a).

1.3 Outline and Contributions

The author was the foremost contributor to the publications the thesis is based on, except for Publication VI (*ICE Cylinder Volume Trace Deviation*, West, I. et.al., *SAE Int. J. Engines* 11(2):195-214, 2018.), where the author contributed as a co-author with analysis of experimental results. The author was responsible for the related work on system description, modeling, control and experimental evaluation. That covers the problem formulation, development, implementation, testing and evaluation of the control strategies and designs. The author wrote the papers with feedback and input from the co-authors.

The present thesis summarizes the research conducted by the author between 2016 and 2021. This thesis investigates the analysis, design, implementation, and application of closed-loop Diesel combustion control algorithms, based on in-cylinder pressure measurements, for the in-cycle adjustment of multiple fuel injections. This work is limited to compression ignition combustion engines. Only a single injector per cylinder is used. The injectors can perform a discrete number of injection pulses. In the scope of this work, only a pilot-main injection

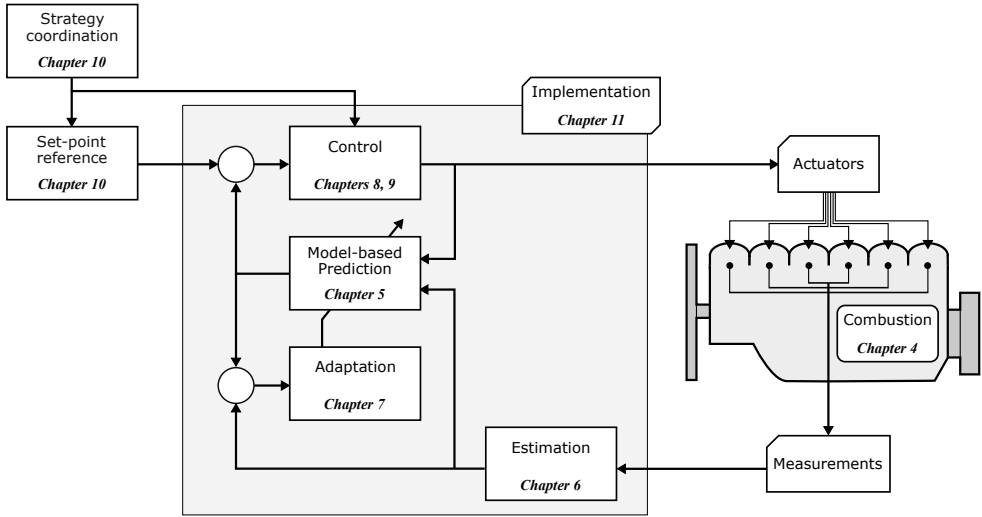


Figure 1.5: Closed-loop architecture for in-cycle combustion control, together with the outline of the thesis chapters.

is considered. The fuels investigated were limited to conventional Diesel and biodiesel fuels with high cetane number.

The thesis outline is illustrated in Figure 1.5, following the closed-loop control structure. It starts with the introduction of the basic concepts of internal combustion engines, in Chapter 2 and, the experimental setup in Chapter 3. Chapter 4 describes the experimental characterization of the pilot and main injections' combustion, which sets the base for the in-cycle controller design. Chapter 5 focuses on combustion modeling for system simulation and model-based control development. For the supervision of the combustion progress, estimation methods are provided in Chapter 6. The on-line adaptation of the models is covered in Chapter 7. Chapter 8 revises the closed-loop combustion control architecture, the observability and the controllability limitations of in-cycle control algorithms. The central topic of this thesis is in Chapter 9, where different in-cycle combustion control strategies are introduced and discussed. The coordination and handling of the different strategies are also investigated. The potential of in-cycle closed-loop combustion control is explored by direct and indirect efficiency optimization approaches in Chapter 10. The hardware requirements for the implementation of the algorithms are quantified in Chapter 11. Finally, the thesis results and main conclusions are summarized in Chapter 12. Future work is suggested in Chapter 13. A detailed description of the chapters, along with the related publications, is given below.

Previous research published in the authors licentiate thesis contributed to the content of the chapters:

Jorques Moreno, C. (2018). *In-Cycle Closed-Loop Diesel Combustion Control with Pilot and Main Injections*. Licentiate Thesis. Dept. of Combustion Engines, Lund University, Lund, Sweden.

Chapter 4

The thesis starts with the analysis of the system to be controlled i.e., the Diesel combustion. This chapter presents the experimental characterization of pilot and main fuel injections combustion. It first covers the robustness and combustion parameters of the pilot injection. Its effect on the main injection, both from the combustion parameters and engine-out parameters perspective, is described by the pilot-main interaction modes conceptual model.

Related Publications

Jorques Moreno, C., Stenlås, O. and Tunestål, P. (2017) “Investigation of Small Pilot Combustion in a Heavy-Duty Diesel Engine”, *SAE Int. J. Engines* 10(3):1193-1203, 2017

Jorques Moreno, C., Stenlås, O. and Tunestål, P. (2017) “Influence of Small Pilot on Main Injection in a Heavy-Duty Diesel Engine”, *SAE Technical Paper* 2017-01-0708, 2017

Chapter 5

The simulation combustion models and the in-cycle predictive models are introduced in this chapter. The stochastic modeling approach for the Monte Carlo simulation is presented along with the models. The requirements of the predictive models considering the implementation limitations for real-time execution are discussed.

Chapter 6

This chapter provides the estimation techniques of the combustion relevant variables for its supervision and control. The methods cover the cylinder volume estimation, combustion detection, pilot mass and heat capacity ratio estimation, which is necessary for the pressure trace prediction as a polytropic compression process.

Related Publications

- West, I., Jorques Moreno, C., Stenlås, O., Jönsson, O., Haslestad, F.(2018) “Internal Combustion Engine Cylinder Volume Trace Deviation”, *SAE Int. J. Engines* 11(2):195-214, 2018
- Jorques Moreno, C., Stenlås, O. and Tunestål, P.(2020) “Cylinder Pressure Based Method for In-Cycle Pilot Misfire Detection”, *SAE Int. J. Adv. & Curr. Prac. in Mobility* 2(2):488-502, 2020
- Jorques Moreno, C., Stenlås, O. and Tunestål, P.(2018) “Cylinder Pressure-Based Virtual Sensor for In-Cycle Pilot Mass Estimation”, *SAE Int. J. Engines* 11(6):1167-1182, 2018
- Jorques Moreno, C., Stenlås, O., and Tunestål, P., (2020) “Bayesian Method for Fuel Mass Estimation of Short Pilot Injections based on its Misfire Probability”, *2020 American Control Conference (ACC)*, Denver, CO, USA, 2020, pp. 1507-1513

Chapter 7

Due to the limitations on the predictive models implementation, the required simplifications compromises the prediction accuracy. To increase the model accuracy, the models can be adapted on-line. This chapter presents a novel adaptation formulation for a trade-off between the total number of adaptation variables and individual cylinder adaptation accuracy.

Related Publications

- Jorques Moreno, C., Stenlås, O. and Tunestål, P.(2020) “Multi-Cylinder Adaptation of In-Cycle Predictive Combustion Models”, *SAE Technical Paper* 2020-01-2087, 2020

Chapter 8

An overview of the architecture for closed-loop combustion control algorithms is provided in this chapter. For the architecture design of in-cycle control algorithms, the limitations on observability and controllability are studied. The interaction of the cascade multi-loop effects on the error dispersion and stability are considered.

Related Publications

Jorques Moreno, C., Stenlås, O. and Tunestål, P.(2018) “In-Cycle Closed-Loop Combustion Controllability with Pilot-Main Injections”, *Thiesel 2018, Conference on Thermo-and Fluid Dynamics Processes in Direct Injection Engines*, Valencia, Spain, 2018

Chapter 9

In this chapter, different in-cycle closed-loop combustion controllers are investigated for the reduction of the combustion metrics dispersion and the compensation of pilot misfire. To handle the available feedback and the different control strategies, a controller manager is proposed and studied.

Related Publications

Jorques Moreno, C., Stenlås, O. and Tunestål, P.(2020) “Predictive In-Cycle Closed-Loop Combustion Control with Pilot-Main Injections”, *IFAC-PapersOnline*, Volume 53, Issue 2, 2020, Pages 14000-14007

Jorques Moreno, C., Stenlås, O. and Tunestål, P.(2021) “In-Cycle Closed-Loop Combustion Control for Pilot Misfire Compensation”, *SAE Int. J. Adv. & Curr. Prac. in Mobility* 3(1):299-311, 2021

Jorques Moreno, C., Stenlås, O. and Tunestål, P.(2021) “Modular Design and Integration of In-Cycle Closed-Loop Combustion Controllers for a Wide-Range of Operating Conditions”, Accepted for publication in *2021 American Control Conference (ACC)*, New Orleans, LA, USA, 2021

Chapter 10

This chapter evaluates how the indicated efficiency can be optimized by the in-cycle closed-loop combustion control. A direct method based on a specifically designed in-cycle regulator is investigated. Due to its limitations, an indirect approach reviews how the reduced dispersion of the previous controllers can be exploited to maximize the indicated efficiency. This is achieved by optimizing the set-point reference.

Related Publications

Jorques Moreno, C., Stenlås, O. and Tunestål, P.(2018) “In-Cycle Closed-Loop Combustion Control with Pilot-Main Injections for Maximum Indicated Efficiency”, *IFAC-PapersOnLine*, Volume 51, Issue 31, 2018, Pages 92-98

Jorques Moreno, C., Stenlås, O. and Tunestål, P.(2021) “Stochastic Set-Point Optimization for In-Cycle Closed-Loop Combustion Control Operation”, *SAE Technical Paper 2021-01-0531*, 2021

Chapter 11

This chapter is dedicated to the hardware requirements and their quantification for the implementation of the previous algorithms.

Related Publications

Jorques Moreno, C., Stenlås, O. and Tunestål, P.(2021) “Quantification of FPGA Requirements for Closed-Loop Combustion Control Implementation”, Submitted to *ICE2021, International Conference on Engines and Vehicles*, Capri, Italy, 2021

Chapter 12

The methods developed throughout this investigation, together with the main conclusions and results, are summarized in this chapter.

Related Publications

Jorques Moreno, C., Stenlås, O. and Tunestål, P.(2021) “Efficiency Optimization by In-Cycle Closed-Loop Combustion Control”, Submitted to *Control Engineering Practice*, 2021

Fundamental Engine Principles

This chapter introduces the fundamental concepts to understand the principles of reciprocating internal combustion engines, specifically the Diesel engine. The fundamental concepts are linked with the challenges addressed in this thesis for the Diesel combustion control, the efficiency maximization and emissions limitation.

2.1 The Diesel Engine

2.1.1 Heat engines

A heat engine converts the thermal energy of a working fluid to mechanical work. The working fluid goes through a thermodynamic cycle, where it takes energy from a high-temperature reservoir, produces work, and transfers waste heat to a low-temperature sink. By this working principle, their maximum efficiency is limited by Carnot's theorem (Wu, 2007). An example of a heat engine is the Stirling engine (Wu, 2007).

In a combustion engine, the thermal energy is transformed from the chemical energy of the fuel, such as in a steam engine (Wu, 2007).

In an internal combustion engine (ICE), the working fluid is the mixture of

fuel with the oxidant (typically air) and their combustion products. A flow of fresh fuel-oxidant mixture must be supplied continuously, which generates a continuous exhaust. An example of an internal combustion engine is the gas turbine (Wu, 2007).

A reciprocating internal combustion engine uses a crank-piston mechanism to drive the thermodynamic cycle. For each cycle, the piston brings a fresh mixture, whose combustion with the fuel generates the pressure that produces work on the piston, and then the piston expels the exhaust gases out. The most common examples are the Otto engine (spark-ignition) and the Diesel engine (compression-ignition) (Heywood, 1988). Reciprocating ICE's are commonly classified by the number of strokes required to complete the thermodynamic cycle. This thesis is focused on modern heavy-duty Diesel engines, which commonly use four strokes, high pressures and medium engine speeds.

2.1.2 Thermodynamic cycle in Diesel engines

In a four-stroke Diesel engine, two crankshaft revolutions are required to complete a full thermodynamic cycle. The four strokes of a conventional Diesel engine are illustrated in Figure 2.1. The cycle starts with the intake stroke, where the intake valves open to induct the fresh charge due to downward motion of the piston. The intake valves close to compress the charge as the piston moves upwards. When the piston approaches top-dead-center (TDC), fuel is injected into the combustion chamber. The high pressure and temperature of the mixture auto-ignites the fuel jet. The expansion of the gas mixture pushes the piston downwards to generate work on the crankshaft. Finally, the exhaust valves open to expel the combustion products with the upward piston movement.

The working principle of the Diesel engine provides several advantages over the Otto engine. The Diesel engine controls the fuel auto-ignition by its direct fuel injection. The risk of fuel auto-ignition (knocking) present in spark-ignition engines is not a limitation on the compression ratio and air-fuel ratio for Diesel engines. Furthermore, throttling is avoided to regulate the engine-out power. As a consequence, Diesel engines provide higher conversion efficiencies than Otto engines, however at the expense of higher complexity (and cost). This trade-off sets the common use of Diesel engines for heavy-duty applications, where the fuel consumption is a key factor.

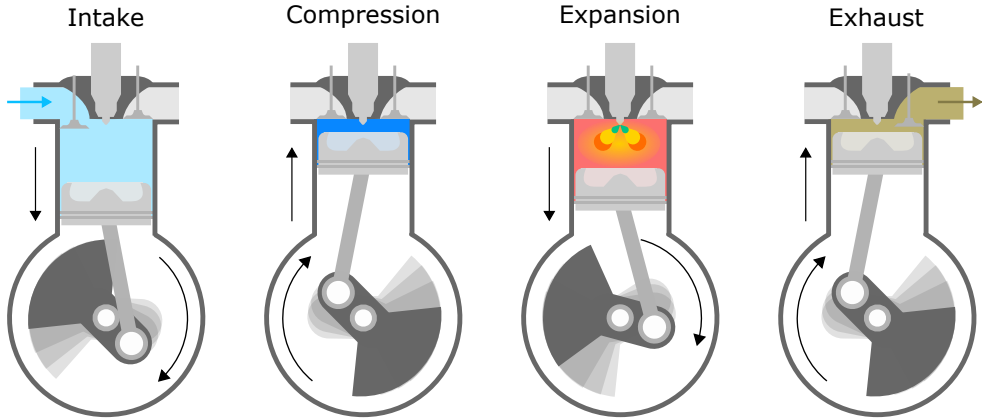


Figure 2.1: Illustration of the thermodynamic cycle of a four-strokes conventional Diesel engine.

2.1.3 Fuel injection

In Diesel combustion engines, the fuel is directly injected inside the combustion chamber. Modern Diesel engines use common-rail high pressure systems to achieve high engine-out power, high efficiency and low emissions with improved control of the injected fuel mass. The high injection pressures permit higher compression ratios for increased efficiency, while the emissions are reduced due to the enhanced fuel atomization and air entrainment (Dingle, 2010). This represents an advantage of Diesel engines compared to Otto engines, however, at the expense of increased system complexity and cost.

Multiple fuel injection is achieved by fast piezoresistive or piezocapacitive injectors with high pressure common-rail systems. The multi-pulse injection allows a better control of the combustion timing and shape, in the short, middle- and long-terms (Shahrودي, 2008). This improves the engine indicated efficiency while reducing the emissions (Badami et al., 2002; Johansson, 2012). Depending on the duration and timing of the commanded pulses, they are classified as pilot injections, main injection (the longest) and post-injections. The main injection can furthermore be split in two or more pulses (Johansson, 2012). The multi-pulse injection is illustrated in Figure 2.2. In this thesis, one or more pilot injections and a main injection were used for the control of the combustion (both highlighted in Figure 2.2).

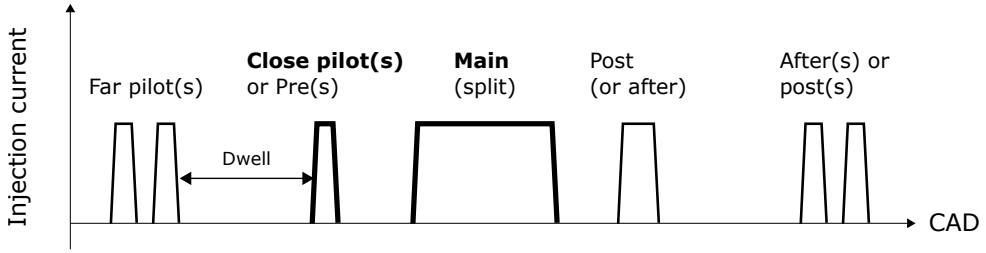


Figure 2.2: Definition of various injection events (multi-pulse fuel injection), adapted from Johansson (2012). The work developed in this theses is based on the pilot and main injection pulses, both highlighted.

2.1.4 Diesel combustion

The combustion process is fundamentally the exothermal reaction of the hydrocarbons oxidation into the exhaust species. The combustion in an internal combustion engine starts towards the end of the compression stroke and finishes during the expansion stroke, when most of the fuel has oxidized. The process includes also the fluid dynamics, starting with the fuel injection spray. The process is therefore a complex three-dimensional multi-phase turbulent process, occurring at high pressure and temperature. The standard conceptual model describing combustion in Diesel engines was provided by Dec (1997). Later improvements by Kosaka et al. (2005) and Pickett and Siebers (2004) extended the basic model for further understanding.

Following Dec's conceptual model, the process of the Diesel combustion starts with the liquid fuel jet. Air is entrained downstream the fuel jet, where fuel gases mix with liquid-fuel droplets. As the fuel is injected, it expands until it vaporizes. When auto-ignition conditions are reached at high pressures, temperatures and the fuel is mixed with the oxygen inside the combustion chamber, the combustion starts. The location of the initial combustion is not well defined spatially or temporally due to the stochastic nature of the process.

The initial fast combustion phase is referred to the premixed combustion, which burns rapidly due to the rich air-fuel mixture with $\lambda = 2-4$. The products of the fuel-rich premixed flame at the periphery start reacting with the surrounding air, until the reaction surrounds completely the diffusion flame, and extends downstream to the tip of the liquid fuel penetration i.e., lift-off length.

This phase is followed by the diffusive combustion. The combustion rate of this phase is limited by the mixing-controlled combustion, kept towards the leading edge of the diffusion flame, and extended until the end of the injection. The diffusive combustion phase is a quasi-steady process, where the relatively uniform mixture of the turbulent air entrainment is sufficient to vaporize all the

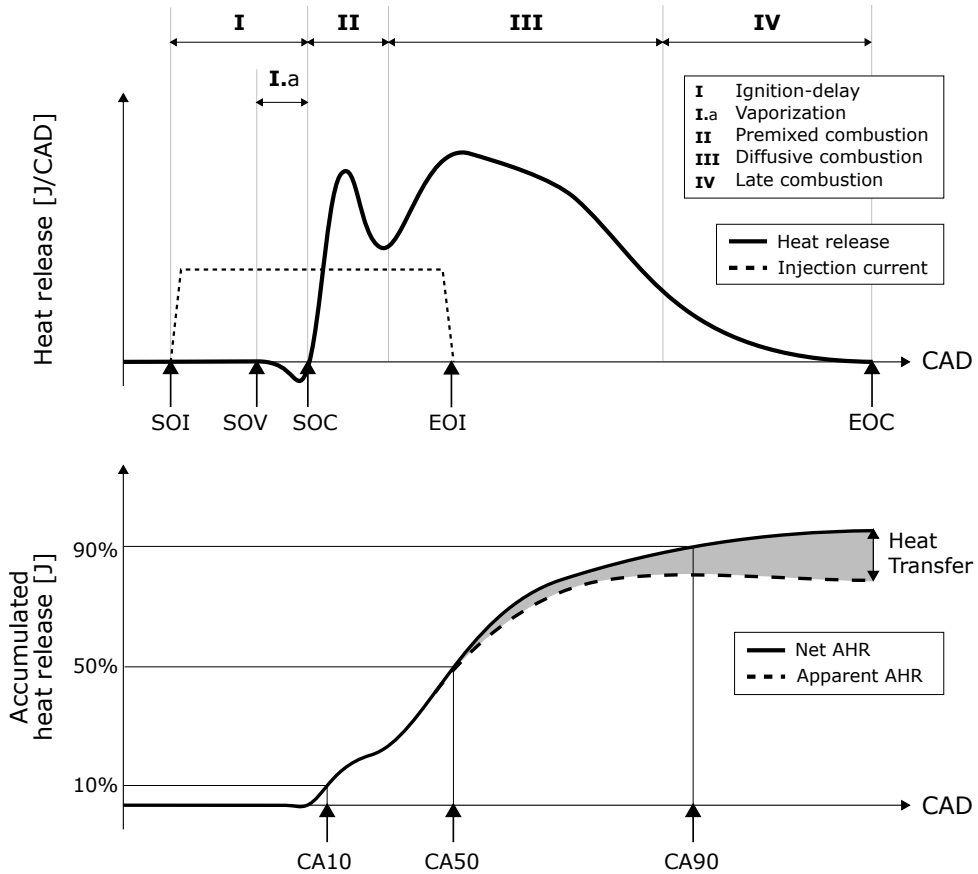


Figure 2.3: Typical heat release rate and accumulated heat release of Diesel combustion, adapted from (Heywood, 1988). The injection current events (start of injection, SOI; and end of injection, EOI) determine the rate of the heat release shape. Different phases are identified, determined by the driving mechanism of the combustion. These are, the ignition-delay (I), which includes the vaporization (I.a), the premixed combustion (II), mixed-controlled or diffusive combustion (III) and late combustion (IV). Based on the combustion phases, the discrete events of the start of vaporization (SOV), the start of combustion (SOC) and the end of combustion (EOC) are defined. The common metrics for the progress of the combustion are indicated in the lower plot. These are, the crank angle degree of the 10% accumulated heat release (CA10), the center of combustion (CA50) and the crank angle degree of the 90% accumulated heat release (CA90).

fuel at the lift-off length of the spray tip, and whose shape suffers only moderate changes. Most of the emissions are formed during this phase due to the high local temperatures, which facilitates the formation of NO_x , and fuel rich zones, which creates soot (Dec, 1997).

The last phase after the end of the injection is the late mixing controlled phase, where the remaining fuel in the chamber is burned until the combustion ends. The four phases are illustrated in Figure 2.3. Details of the associated heat release and metrics for each phase are introduced later in Section 2.5.4.

The Diesel combustion timing is regulated to achieve the maximum brake torque (MBT) for a given injected fuel mass (Johansson, 2012). However, when the associated emissions from Diesel combustion are considered, the combustion timing is calibrated for lower emissions levels, at the expense of lower efficiency. Furthermore, other factors such as hardware constraints due to maximum pressure also impact the final calibration of the combustion timing (Johansson, 2012).

2.1.5 Emissions of Diesel combustion

The main exhaust emissions in heavy-duty Diesel engines are the carbon monoxide (CO), unburnt hydrocarbons (HC), nitrogen oxides (NO_x) and particulate matter (PM) (Reşitoglu et al., 2014). These are also the main pollutants limited by EURO and CARB regulations. A brief description of them is given below:

- **CO:** carbon monoxide results from the incomplete combustion of the fuel, when the oxidation process is not completed. CO emissions are minimal for Diesel combustion due to the lean fuel-air mixtures ($\lambda > 1$). However, transient operation, large fuel droplets, insufficient time or, insufficient turbulence of the charge mixture inside the combustion chamber may increase the CO emissions (Demers D, 1999).
- **HC:** insufficient temperature for the complete fuel combustion results in unburnt fuel, which composes the hydrocarbons emissions. This occurs near the cylinder wall at low loads. In general, unburnt hydrocarbons is not an issue of conventional Diesel engines. However at low loads, the flame speed may not suffice to complete the combustion during the power stroke (Zheng et al., 2008).
- **PM:** particulate matter is composed of heavy HC, metal fragments (from the engine wear), various salts (e.g., ashes from lubricating oil and residues of urea by-products), and soot. Soot is the main component of particulate matter of Diesel engines, which is considerably higher than for Otto engines. Soot is originated from the combustion process. It may be from small particle agglomeration of partly burnt fuel, partly burnt lube oil, ash content of fuel oil, and cylinder lube oil or sulfates and water (Demers D, 1999). Soot is formed through the full length of the burning spray at fuel-rich zones, where small particles exist upstream and grow in size (Dec, 1997), as well as oxidized during combustion. The soot oxidation is the main driver for post injections in Diesel engines (Majewski and Khair, 2006).

- **NO_x**: in a Diesel engine, the thermal NO_x formation is the dominating mechanism. By this chemical mechanism, nitrogen oxides are formed due to the reaction between the oxygen and nitrogen of the intake air at the high temperatures inside the combustion chamber via the Zeldovich mechanism (Heywood, 1988), starting at values between 1600°C and 1800°C, depending on the criteria. The total formed NO_x is a function of the maximum temperature inside the cylinder, the oxygen concentration and residence time (Dec, 1997). Diesel engines are the most important source of road NO_x emissions, primarily on the form of NO (Wang et al., 2012).

As the emissions legislation advanced, a number of techniques has been used for the reduction of exhaust emissions of Diesel engines (Reşitoglu et al., 2014), along with after-treatment systems since EURO IV. To reduce the system cost, exhaust gas recirculation together with common-rail injectors achieved Euro V NO_x levels, with a consumption penalty, however. With the introduction of the Euro VI normative, the use of after-treatment systems could not be avoided. For Diesel engines, Selective Catalyst Reduction systems (SCR) were necessary for NO_x reduction, as the three-way catalyst requires stoichiometric conditions. The SCR requires of a minimum exhaust temperature for efficient conversion. The solution uses urea injection for the reduction of NO_x. The Diesel Particulate Filter eliminates the particulate matter with efficiencies close to 100%. The Diesel Oxidation Catalyst (DOC) is responsible for the reduction of CO and PM, but also fundamental to achieve higher conversion efficiencies in the Diesel Particulate Filter (DPF) and SCR.

An additional regulated engine-out emission is the noise. Noise is produced from the combustion, the engine mechanical moving elements and the structural resonances generated during the engine operation (Heywood, 1988). The combustion noise has a significant impact on the final noise emissions, and it can be reduced by an adequate combustion rate shaping using multiple fuel injections (Denny, 2019).

With the introduction of the after-treatment system to handle the exhaust emissions, the previous solutions' penalty on efficiency were removed, and the combustion can be optimized for MBT. However, the operational cost of the after-treatment system (conversion efficiency and urea consumption), has to be considered together with the fuel consumption. The regulation of the combustion to achieve this is not straight-forward, and heavy calibration efforts are required to consider all the engine operation variables and uncertainties.

Advanced combustion concepts with low exhaust emissions, such as HCCI, PPC and RCCI, gained popularity among the engine research community to avoid

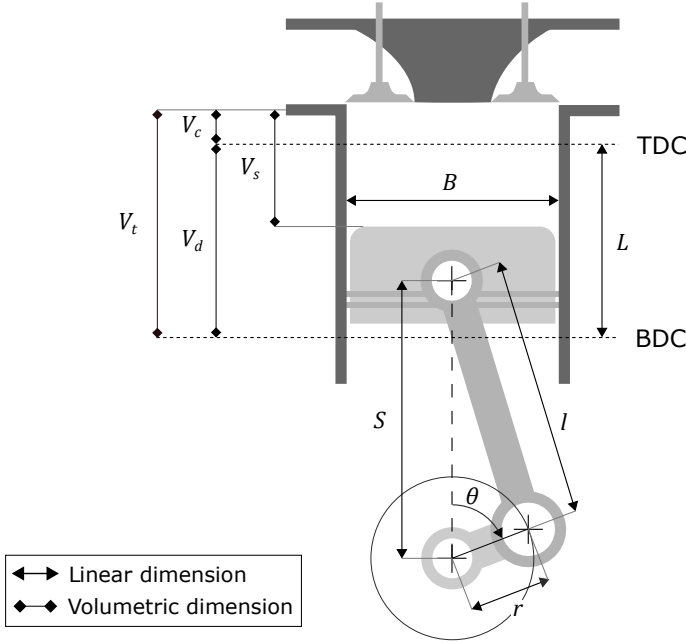


Figure 2.4: Basic cylinder geometry. The parameters are the bore (B), stroke (L), connecting rod length (l), crank angle degree (θ), crank radius (r), displaced volume (V_d), clearance volume (V_c), total volume (V_t). The top dead center (TDC) and bottom dead center (BDC) where the cylinder moves are indicated.

the costly after-treatment systems. These concepts require of advanced closed-loop controllers to guarantee the combustion stability (Johansson, 2012), which need additional sensors, actuators and computational power, increasing again the total system cost and complexity.

2.2 Cylinder Geometry

The cylinder volume evolution determines the resulting thermodynamic cycle. The volume trace is computed by the crank mechanism and the cylinder geometry. The main volumetric and longitudinal dimensions are defined in Figure 2.4. The piston area A_p is approximated as:

$$A_p = \frac{\pi B^2}{4} \quad (2.1)$$

The instantaneous cylinder velocity is in Eq.(2.2):

$$\frac{ds(\theta)}{d\theta} = r \sin(\theta) \left(1 + r \frac{\cos(\theta)}{\sqrt{l^2 - r^2 \sin^2(\theta)}} \right) \quad (2.2)$$

The minimum volume of the combustion chamber is the clearance volume (V_c). The clearance volume is the result of the tolerance distance between the piston, the cylinder head, and the piston bowl shape (not represented in Figure 2.4). The total displaced volume (V_d) is the difference between the maximum and minimum combustion chamber volumes. It is computed as:

$$V_d = LA_p \quad (2.3)$$

The instantaneous volume is computed as a function of the crank angle degree (θ) by Eq.(2.4):

$$V(\theta) = V_c + A_p \left(l + \frac{L}{2} (1 - \cos(\theta)) + \sqrt{l^2 - \frac{L^2}{4} \sin^2(\theta)} \right) \quad (2.4)$$

The instantaneous volume derivative is calculated in the same manner by Eq.(2.5):

$$\frac{dV(\theta)}{d\theta} = \frac{V_d}{2} \sin(\theta) \left(1 - \frac{L}{2} \cos(\theta) \left(l^2 - \frac{L^2}{4} \sin^2(\theta) \right)^{-\frac{1}{2}} \right) \quad (2.5)$$

For more details in the derivation of these equations, see Heywood (1988).

The production tolerances, aging and high pressures inside the cylinder result in deviations of the actual cylinder volume, which differs from a perfect cylinder. This results in deviations from the nominal thermodynamic cycle. The quantification of these deviations and modeling for on-line implementation are summarized in Section 6.1.

2.3 Fuel Characteristics

The relevant parameters of the fuels used in Diesel engines are described below:

- **Density:** it is the fuel mass per volume. This is relevant for the injection timing regulation. The injectors establish the fuel volume injected, but the engine load is determined by the fuel mass injected and fuel lower heating value.

- ***Cetane number***: it indicates the tendency of auto-ignition, used for Diesel-like fuels. A high number indicates a stronger tendency to self ignite. The injection timing has to be adjusted to compensate differences in the combustion auto-ignition properties due to different cetane number of the fuel.

- ***Lower heating value***: it measures the energy content per weight unit. This parameter is used to determine the energy injected. The fuel amount injected has to be adjusted to compensate for engine load differences due to the different lower heating value of the fuel.

- ***Stoichiometric air/fuel ratio***: it indicates how much air is necessary for complete combustion of the fuel. This is set by the chemical composition. The operational parameter lambda (λ) expresses the relative air/fuel ratio to the stoichiometric ratio:

$$\lambda = \frac{AFR}{AFR_{st}}$$

In relation to the stoichiometric air/fuel ratio, the mixture can be lean (excess of air, $\lambda > 1$) or rich (excess of fuel, $\lambda < 1$). Compression-ignition engines are typically run with a lean mixture.

- ***FAME Content***: the Fatty Acid Methyl Esters (FAME) content indicates the amount of these biofuels in the fuel mixture, measured in percentage.

The diverse origin of biofuels result in a high variability on their properties. For example, FAME and other biofuels can be produced from renewable processes, or also synthesized from different non-fat based sources, with a total carbon neutral result. High dispersion in the cetane number, lower heating value and air/fuel ratio will on their counterpart have an impact on the combustion characteristics. Namely the ignition-delay, combustion rate and energy release (Zander et al., 2010a). This thesis is focused on the design of controllers to automatically adjust the engine operation for compensation of the fuel properties variations.

2.4 Operating Parameters

The operating parameters used throughout this thesis for the description of the engine and control algorithms performance are introduced below.

Indicated work

The work exerted by the combustion gases on the piston over one thermodynamic cycle is defined as the indicated work:

$$W_{c,i} = \oint p(\theta) dV(\theta) \quad (2.6)$$

When the integral is computed only over the compression and expansion strokes, it is referred as the *gross indicated work*. When it is computed over all four strokes, it is referred as the *net indicated work*.

Indicated mean effective pressure

The indicated mean effective pressure (IMEP) is defined as the work per displaced volume:

$$IMEP = \frac{W_{c,i}}{V_d} \quad (2.7)$$

This is the necessary constant pressure over the expansion stroke to obtain the same work. The advantage in using IMEP instead of work is its independence of engine size. The IMEP can be computed over the compression and expansion strokes to obtain the *gross IMEP*, or the whole cycle for the *net IMEP*.

Efficiency definitions

The related energy efficiencies to the combustion control are the combustion efficiency and indicated thermal efficiency. The combustion efficiency is the conversion ratio from the fuel energy to heat:

$$\eta_{comb} = \frac{Q_{comb}}{m_f Q_{LHV}} \quad (2.8)$$

The overall combustion efficiency in Diesel engines is close to the unity. However, the individual fuel injections, such as pilot injections, may burn with lower combustion efficiencies.

The thermodynamic efficiency is the conversion from heat to piston work. The indicated thermal efficiency is computed by the energy conversion from the fuel energy to the gross indicated work:

$$\eta_{th} = \frac{W_g}{Q_{comb}} \quad (2.9)$$

Cylinder balancing

In a multi-cylinder engine, variations of the pressure evolution throughout the cycle may result in variations of the torque produced by each of the cylinders. Torque variations increase the stress on the crank shaft and causes engine speed variations, which increase the vibrations (Heywood, 1988). To quantify the cylinder unbalance, the instantaneous torque is estimated from the pressure trace signal (van Nieuwstadt and Kolmanovsky, 2000). The cycle-average torque is computed as the reference to calculate the magnitude of the torque deviation for each of the cylinders in that cycle. The instantaneous torque is computed by the momentum from the in-cylinder pressure excerpt on the piston area and the instantaneous cylinder speed:

$$T_q(\theta) = p(\theta)A_p \frac{ds(\theta)}{d\theta} \quad (2.10)$$

The total cycle-average torque for a cylinder i is the integral of the instantaneous torque:

$$\bar{T}_q^i = \int T_q^i(\theta) d\theta \quad (2.11)$$

The cylinder-average of the cycle is:

$$\bar{T}_q^{cycle} = \frac{1}{n_{cyl}} \sum_{i=1}^{n_{cyl}} \bar{T}_q^i \quad (2.12)$$

The cylinder balancing is computed as the deviation of each cylinder cycle-average to the cylinder-average torque:

$$\Delta \bar{T}_q^i = \bar{T}_q^i - \bar{T}_q^{cycle} \quad (2.13)$$

2.5 Combustion Supervision

The combustion in most Diesel engines for heavy-duty applications are operated in open-loop, due to its stability and robustness. However, efficient and low exhaust emission operation with tighter margins benefits by the closed-loop control of the combustion. Closed-loop combustion control reduces the impact of external disturbances, actuators tolerances and transients on the combustion. Moreover, the automatic regulation on the combustion allows for a reduced calibration effort. The combustion supervision monitors its progress, where information for its control is obtained. The complexity of the combustion process in a Diesel engine makes its supervision a difficult task. Combustion supervision requires fast and accurate measurements, which can be challenging considering the dispersion and tolerances of the sensor transducers. For the closed-loop combustion control, the measurement rate is typically in the range of few crank angle degrees to a fraction of a crank angle degree.

For on-line combustion supervision, the in-cylinder pressure provides valuable information about its progress and the thermodynamic cycle. In-cylinder pressure measurement has been used for many decades in the study of engine combustion diagnostics and control (Powell, 1993). Piezoresistive or piezocapacitive transducers are commonly used for a fast, accurate and reliable pressure measurement (d'Ambrosio et al., 2015). Furthermore, they provide a relevant signal for the in-cycle supervision of the combustion (Shahroudi, 2008). Alternatives to in-cylinder pressure measurements still try to estimate its value by e.g., acceleration transducers (knock sensor), but their accuracy is under investigation (Rugland and Stenlaas, 2018).

The study of the combustion process is commonly aided by indirect measurements of the heat release, computed by e.g., the approach described in (Gatowski et al., 1984). Furthermore, it can be used for the supervision and estimation of other variables and parameters (Eriksson and Thomasson, 2017), which are otherwise hard or impossible to be measured directly, or without a prohibitive time-delay. Some examples are knock detection, air/fuel ratio (Tunestål, 2001), NO_x (Muric et al., 2013b) or soot formation (Yang et al., 2017).

2.5.1 Pressure pegging

The commonly employed piezoelectric or piezoresistive transducers for in-cylinder pressure supervision measure the relative pressure but not the absolute. The signal characteristic of the pressure transducers has the form:

$$p_{meas} = kp + \Delta p \quad (2.14)$$

An absolute pressure reference is necessary to relate the relative pressure measurement to the absolute pressure estimation. This process is called *pressure pegging*. Methods to estimate k and Δp were introduced by (Randolph, 1990). Different methods can be found in the literature (Lee et al., 2008), such as those based on intake pressure (Randolph, 1990) or assuming a polytropic compression (Tunestål, 2009a). In this work, k was calibrated and Δp was obtained by referencing the measurement to the absolute inlet pressure p_{intake} at inlet valve closing (IVC).

2.5.2 Heat release analysis

The heat release is obtained by applying the first law of thermodynamics to the combustion chamber. With the assumption of a constant mass fuel-air mixture in gas phase with an homogeneous composition, pressure and temperature i.e., single zone, the conservation of energy yields the expression in terms of the crank angle degree (θ), as derived in (Heywood, 1988):

$$\frac{dQ}{d\theta} = \frac{\gamma}{\gamma - 1} p \frac{dV}{d\theta} + \frac{1}{\gamma - 1} V \frac{dp}{d\theta} + \frac{dQ_{HT}}{d\theta} \quad (2.15)$$

The specific heat ratio (γ) can be estimated only as a function of the temperature (Gatowski et al., 1984), or include the chemical composition to significantly improve the heat release estimation (Tunestål, 2001). In case additional accuracy on the composition and temperature is necessary (for example for NO_x estimation, Muric et al. (2013b)), multiple-zone temperature and composition are used (Egnell, 1998).

2.5.3 Heat transfer

The heat transfer is difficult to measure directly and it is often estimated indirectly. When the heat transfer is included in the heat release, it is referred as the *gross heat release*. If the heat transfer term is not considered, it is referred as the *net heat release*. In this work, the heat transfer is estimated by the method proposed by (Woschni, 1967), but more complex methods for the heat transfer estimation are available in the literature (Zak et al., 2016; De Cuyper

et al., 2017). The empirical correlation for the heat transfer (h) estimation by (Woschni, 1967) in $[WK^{-1}m^{-2}]$ is:

$$h_{HT} = 3.26 \cdot B^{-0.2} p^{0.8} T^{-0.55} w^{0.8} \quad (2.16)$$

$$\dot{Q}_{HT} = h_{HT} A (T - T_{wall}) \quad (2.17)$$

Where (w) is the gas mean velocity and (T) the bulk gas temperature. The heat transfer (Eq. (2.17)) is a function of the cylinder surface area (A) and cylinder wall temperature (T_{wall}). The gas mean-velocity is modeled according to:

$$w = C_1 S_p + C_2 \frac{V_d T_{IVC}}{p_{IVC} V_{IVC}} (p - p_m) \quad (2.18)$$

The first term relates to the mean piston speed (S_p), and the second term captures the charge-density variation during combustion, where p_m is the pressure of the motoring cycle. Non-linear estimation methods for these parameters can be found in (Turesson, 2018).

2.5.4 Combustion metrics

Several combustion metrics are used to globally described the combustion. The metrics used throughout the thesis are defined below. Note that crank angles are referred to top dead center.

Injection

- ***Start of injection (SOI)***: defined as the crank angle position the injector energizing starts, at the start of the current command. Note that some published studies use the opening of the injector's tip instead.
- ***End of injection (EOI)***: defined as the crank angle position at the end of injector energizing, at the end of the current command.

Combustion timing

- ***Start of vaporization (SOV)***: defined as the crank angle position when the measurable fuel vaporization inside the cylinder chamber starts.

- ***Start of combustion (SOC)***: defined as the crank angle position the fuel combustion starts. It is determined when the heat release derivative becomes positive after the measurable fuel vaporization.
- ***End of combustion (EOC)***: defined as the crank angle position where the total gross heat released is maximal.
- ***Ignition-delay (ID)***: crank angle interval between the start of injection and the start of combustion.
- ***CA_x***: crank angle degree in which $x\%$ of the total heat has been released during the combustion process.

Due to their correlation to engine performance and emissions, the most commonly used metrics are the SOC (CA10), the center of combustion (CA50) and EOC (CA90). CA50 is used to place the combustion phasing. The big slope in the AHR at that point makes it less sensitive to noise perturbations. CA10 and CA90 represent the combustion duration (CA10-90). CA10-50 is used as an indicator of the premixed combustion. In premixed combustion, a large share of the fuel burns in a short time due to its fast combustion rate. The combustion timing metrics are indicated in Figure 2.3.

Combustion dispersion

- ***Coefficient of variation (COV)***: computed for the gross indicated mean effective pressure, it is the main indicator of the combustion stability (COV_{IMEP}), defined as:

$$COV_{IMEP}(\%) = \frac{\sigma_{IMEP}}{\mu_{IMEP}} \times 100 \quad (2.19)$$

where σ_{IMEP} and μ_{IMEP} are the standard deviation and mean value of the IMEP over the measured cycles, respectively.

- ***95% confidence interval***: it is used for the study of the dispersion of the combustion parameters. It represents the range where 95% of the measurements are. For non-symmetric distributions, the 2.5% and 97.5% percentiles are instead used to compute the 95% confidence interval.

Experimental Setup

The experimental facility for the development and evaluation of the combustion control algorithms is presented in detail in this chapter. It consisted of a test cell bed, with a Scania D13 multi-cylinder engine, together with the appropriate measurement and data acquisition equipment. It was located at the laboratories of the Division of Combustion Engines at Lund University.

3.1 The Scania D13 Engine

3.1.1 Engine specifications

The experiments were performed on a modified six-cylinder Scania D13 engine. The geometrical specifications of the engine are listed in Table 3.1. The injection system was the Scania common-rail Extreme High-Pressure Injection System (XPI), where the injectors used were previously calibrated. A picture of the engine test cell is in Figure 3.1. The engine layout is illustrated in Figure 3.2.

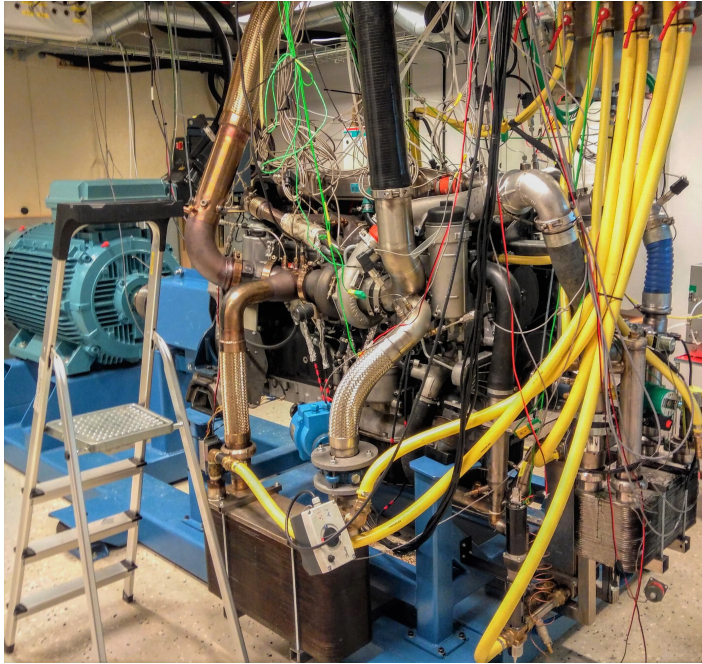


Figure 3.1: Scania D13 Engine test cell, located in Lund University, used for the experiments.

Table 3.1: Engine geometrical specifications.

Parameter	Value
Cylinder number	6
Displaced volume	12.74L
Stroke	160mm
Bore	130mm
Compression ratio	18:1
Number of valves	4
Intake valve closing timing (IVC)	-151CAD ATDC
Exhaust valve opening timing (EVO)	146CAD ATDC

3.1.2 Instrumentation

Sensors

The engine operation was monitored by directly measured sensor signals and indirectly estimated virtual sensor variables. The location of the measured variables and sensing techniques are briefly described in this section. The sensor

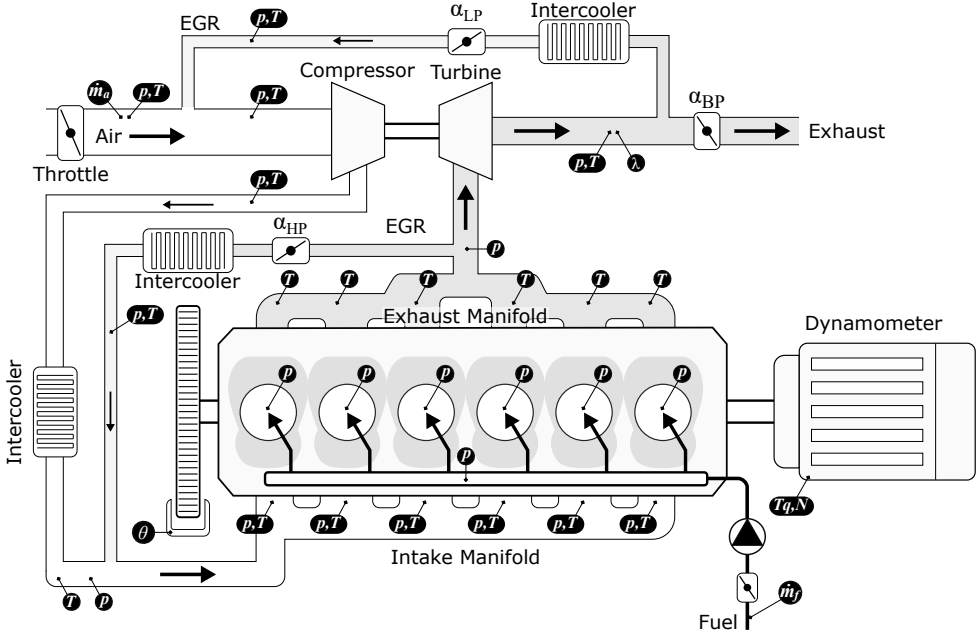


Figure 3.2: Schematic diagram of the Scania D13 engine used in the experiments. The measurements and position of the sensors are indicated in the diagram. p - pressure sensor, T - temperature, N - engine speed, T_q - Torque, θ - crank angle position, \dot{m}_a - air mass flow, \dot{m}_f - fuel mass flow, λ - relative air/fuel ratio. The valves are indicated with α , used for exhaust gas recirculation (EGR) through the low pressure (LP) and high pressure (HP) routes, and for the back pressure (BP).

specifications used for the data acquisition in the engine are summarized in Table 3.2. The sensor and actuator locations are indicated in Figure 3.2.

Crank angle position The crank angle position was measured by a Leine- & Linde encoder, emitting 5 pulses per CAD i.e., 0.2CAD resolution. The injection current, cylinder pressure and engine torque were synchronized with the pulses. The absolute position was used to estimate the in-cylinder volume for the heat release processing.

In-cylinder pressure It was measured by water cooled Kistler 7061B relative pressure piezoelectric transducers. The measured pressure acts through the diaphragm of a quartz crystal measuring element, which transforms the pressure into an electrostatic charge. This measurement technique can handle the extreme temperatures and pressures in the cylinder chamber, while providing good linearity and high cut-off frequency. The pressure signal was sampled every 0.2CAD, synchronized with the crank angle encoder.

Rail pressure The standard Scania absolute pressure sensor was used for the rail pressure measurements.

Table 3.2: Specifications summary of the sensors.

Sensor	Model	Measurement Range	Precision
CA encoder	Leine & Linde RSI503	0-6000RPM	± 0.02 CAD
Cylinder pressure	Kistler 7061B	0-250bar	$\pm 0.5\%$
Torque	HBM T40B	0-110kN·m	$\pm 0.05\%$
Generic pressure	Keller PAA-23S	0-5bar	$\pm 0.05\%$ FS
Generic temperature	Pentronic 8105000	0-1100°C	$\pm 2.5^\circ\text{C}$
Air flow meter	Bronkhorst F106CI	0-900kg/h	$\pm 0.1\%$ FS
Fuel flow meter	Bronkhorst CORI-FLOW M15	0.2-300kg/h	± 0.05 FS
CO/CO ₂	Horiba MEXA-9400	0-1/16%	$\pm 1\%$ FS
CO ₂ EGR		0-25%	$\pm 1\%$ FS
NO _x		0-5000ppm	$\pm 1\%$ FS
TUHC		0-10000ppm	$\pm 1\%$ FS
O ₂		0-25%	$\pm 1\%$ FS
HC ₄	AVL AMA i60	0-10000ppm	
Soot	MSS ^{plus} AVL MicroSoot	0-25mg/m ³	$\pm 5\text{g/m}^3$
λ	Bosch LSU 4.9	0.65 to air	4.2%

Torque The brake torque after the fly-wheel was measured by a HBM T40B torque sensor, integrated in the electrical motor (dynamometer).

Engine speed The internal speed measurement of the electrical motor (dynamometer) was used.

Fuel flow A Bronkhorst mini CORI-FLOW M15 mass-flow meter measured the fuel-mass flow, mounted prior to the fuel system.

Air flow It was measured by a Bronkhorst hot-film air-mass flow meter at the compressor's intake.

Pressure and temperature Keller PAA-23S absolute pressure sensors measured the pressure at different locations of the gas-exchange system (see Figure 3.2). The response time of these sensors is in the order of milliseconds. The temperature was measured by K-type thermocouples, with a response time of seconds. The mounting locations of the pressure and temperature sensors were:

- Intake manifold, individually next to the intake valves of cylinders 1-6.

- Exhaust manifold. Individual temperature sensors mounted at the exhaust valves of cylinders 1-6, and a single mounted pressure sensor at the center of the exhaust manifold.
- Downstream the turbine.
- Upstream and downstream the compressor.
- Downstream the inter-cooler.
- Downstream the low pressure EGR valve.
- Downstream the high pressure EGR valve.

Exhaust gas A broadband λ -sensor, mounted at the turbine exhaust, measured the oxygen concentration. The exhaust gas emissions used a Horiba MEXA-9100E for measurements of the intake and exhaust CO₂, NO_x, HC, CO and O₂. The soot was measured by an AVL micro-soot sensor.

Actuators

The actuators locations are illustrated in Figure 3.2. The main actuators are:

Fuel injection Scania common-rail XPI injectors were used for the fuel injection inside the cylinder chamber. The current-pulse timings and durations were commanded from LabVIEW and actuated by the Drivven direct-injection drivers. More details can be found in (Källkvist, 2011).

Gas flow For the gas flow control, the Scania standard throttle valve and waste gate were used.

Engine speed The engine speed was regulated by the controller included in the dynamometer.

3.2 Calibration

3.2.1 Fuel injectors

The fuel injectors were calibrated for an accurate reference in the combustion characterization experiments and the estimation methods. The calibration was conducted in a spray rig. A sweep of on-times at different rail pressures and three repetitions was performed. The fuel volume was measured individually for each injector. The data was used to generate individual maps with the injectors' characteristics.

3.2.2 TDC offset

The pressure sampling must be synchronized with the crank angle degree. The sensor might be mounted with an offset and the thermodynamic top dead center not be aligned with the geometric top dead center. Hence, the offset must be calibrated. Cylinder pressure measurements under engine motoring were collected for the TDC offset calibration with the method described in (Tunestål, 2009b).

3.3 Signal Processing

3.3.1 Signal filtering

The measurement noise in the cylinder pressure signal, of high frequency content, was attenuated with a zero-phase digital filter. Namely, a Butterworth filter calibrated for an adequate noise attenuation. To avoid phase-shifting, the filter is run two times, forward and backwards. This technique can only be used once the whole cycle is completed. Therefore, this technique cannot be applied for on-line in-cycle control. A different method is necessary for the low-pass filtering of the pressure signal. The method chosen was a IIR filter calibrated for a satisfactory trade-off between signal shifting and noise attenuation.

3.3.2 Heat release

For the on-line estimation of the heat release in Eq.(2.15), the specific heat ratio (γ) was estimated as a function of the temperature (Gatowski et al., 1984). For off-line analysis of the experimental results, the NASA polynomials were used to estimate the specific heat ratio (Tunestål, 2001). For on-line computations, only the apparent heat release was computed due to computing limitations. The net heat release was estimated for the off-line data analysis.

3.4 Control-System Architecture

The control system is responsible for the sampling, processing and command of the signals monitoring and actuating the test cell. The structure of the data acquisition and control systems is illustrated in Figure 3.3. The archi-

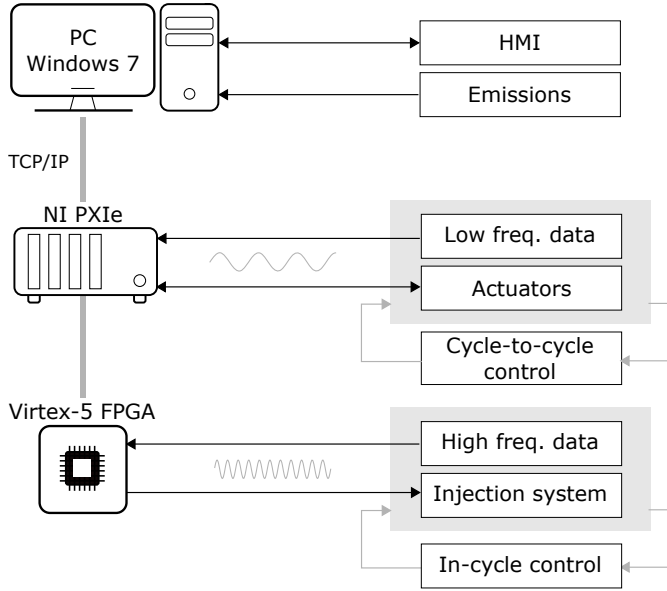


Figure 3.3: Test cell hardware and system architecture for the data acquisition and control.

architecture for the control system is structured according to the signal acquisition sampling frequency. The set-point reference handling and model adaptation are implemented for their cycle-to-cycle execution in the low-frequency hardware i.e., NI PXI. The in-cycle closed-loop combustion control is implemented in the high-frequency hardware i.e., Virtex-5 FPGA. The hardware and software specifications are detailed in the following subsections.

3.4.1 Hardware

The high frequency signals were processed by two FPGA boards NI PXI-7854/7854R. The FPGA was used as a flexible reconfigurable AO/DIO hardware for AD acquisition, triggered by the crank angle encoder. More details about the FPGA are given in the next section. The ADC resolution was 16-bits. For the handling of the low frequency signals, a PXI chassis (NI PXIe-8135 2.3GHz quad-core processor) was executed at 100Hz. For the data display and actuation interface, a PC with Windows 7 was used as the HMI. It communicated with the PXI via the TCP/IP protocol.

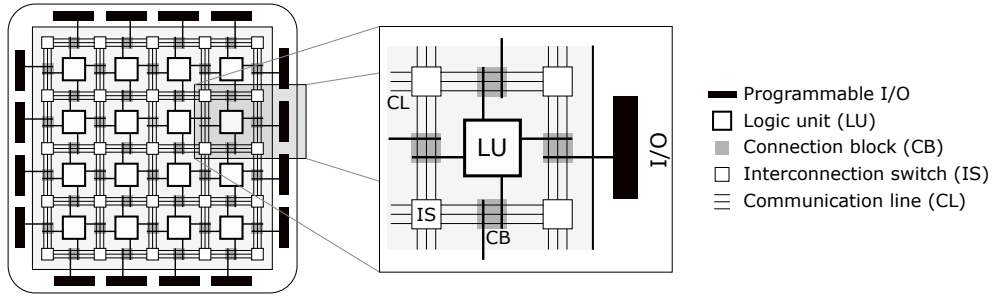


Figure 3.4: Illustration of the FPGA logic blocks diagram implemented with a generic island architecture.

Field Programmable Gate Array (FPGA)

The sampling time of the controller is synchronized with the crank angle encoder. All the operations must be completed every 0.2CAD . At 1200RPM , this means that only $27\mu\text{s}$ are available for all the computations. With a Field Programmable Gate Array (FPGA), the computations can be performed in parallel, contrary to a common sequential processor. This allows for the high computational throughput that is required for the in-cycle closed-loop combustion control. An FPGA is a reconfigurable I/O hardware platform that can be programmed as an Application Specific Integrated Circuit (ASIC). The re-programming avoids the disadvantages of the long design time and cost of producing a fixed-function ASIC (Kuon et al., 2008). FPGAs have been used for many complex control systems (Monmasson and Cirstea, 2007), including the control of internal combustion engines (Wilhelmsson et al., 2006).

The flexibility of the FPGA is achieved by the reconfigurable interconnection of a number of predefined computational resources, which are digitally programmed. The basic components of an FPGA are the logic units, the connection units and the I/O. An illustration of the common blocks of an FPGA is plotted in Figure 3.4. The configurable logic blocks (CLBs) implement a number of digital functions commonly based on look-up tables (LUTs) and flip-flops. Since the introduction of current FPGA architectures and technologies by Xilinx in 1984 (Farooq U., 2012), their complexity has increased enormously.

The FPGAs used for this project were two Virtex-5 LX110/LX30 FPGA's, included in the NI PXI-7854/7854R. The cylinder pressure signal processing and in-cycle controllers were implemented in the Virtex-5 LX110. Its hardware specifications are summarized in Table 3.3. The basic computing unit in the Xilinx architecture is a slice register, comprised of LUTs and flip-flops. Xilinx defines

Table 3.3: Virtex-5 LX110 FPGA hardware specifications (Xilinx, 2015).

Bus/Form factor	PXI
Analog inputs (16-bit)	8
Max sampling rate per input channel	750kS/s
Analog outputs (16-bit)	8
Max update rate per output channel	1MS/s
Digital I/O	96
Number of flip-flops	69120
Number of 6-input LUTs	69120
Number of DSP48 slices	64
Embedded block RAM	4,608kbits
Timebase	40MHz

the number of LUTs and flip-flops to make up a single slice based on the family of the chip. A slice in the Virtex-5 family is composed of 4 flip-flops and 4 LUTs. The hardware requirements for the controller implementation are analyzed in Chapter 11.

3.4.2 Software

The programming of an FPGA consists of the description of how all the components must be wired. The engine control was implemented using the graphical high-level synthesis (HLS) LabVIEW environment (G. W. Johnson, 2006). The Xilinx Compilation Tools package compiles the code and generates the bit-files for the FPGA programming. In the LabVIEW environment, code is programmed in blocks connected with wires. Each block represents an individual operation with multiple inputs and outputs. Programming blocks can be packed in a single I/O block called a Virtual Instrument (VI). The interaction with the user is executed in a front panel with a graphical interface. Detailed considerations when working with LabView for real-time control of combustion engines can be found in (Zander, 2011).

The software architecture was distributed in three levels, as shown in Figure 3.3, ensuring the real-time execution of the code. The least demanding instructions were left at the PC, where the user interface was run under Windows 7. The most time critical instructions were downloaded to a target computer (PXI) running a real-time operating system (RTOS). The real-time execution of the instructions guaranteed the synchronization with the engine cycles and the control of the actuators at the right time. The target computer communicated via the TCP/IP protocol with the PC to receive instructions and show relevant information for the user. The base code for the project was developed by (Borgqvist, 2013).

Finally, the FPGA was responsible for the in-cycle executed instructions.

LabVIEW FPGA

The FPGA was programmed with the functions provided by the NI FPGA module. The main difference to the real-time code is the true parallel execution of the code instructions. To reduce the FPGA memory usage and over-mapping, the VI can be configured as non-reentrant. With this configuration, only one single physical block will be implemented in the FPGA. Therefore, only one instance of the block can be called simultaneously. A trade-off between memory mapping and fast computation needs to be selected.

Only integer arithmetic logic is provided by this FPGA. Intermediate operations were scaled adequately before performing the arithmetic. The scaling used powers of 2, due to their fast implementation by bit-shift operations. The scale factor has to be selected to provide enough resolution of the magnitude despite the rounding loss (Yates, 2007). Detailed analysis of the modules implementation is described Chapter 11.

3.5 Fuels

Fuels with different properties were used in the experiments. All were high cetane number Diesel-like fuels. Standard Swedish Diesel MK1 fuel was used as the reference for comparison with two biodiesel fuels, Rapeseed Methyl Ester (RME) and Hydrotreated Vegetable Oil (HVO). The different properties of the fuels were used to test the robustness of the control methods presented in the thesis. The fuel properties are detailed in Table 3.4:

Table 3.4: Summary of the fuel properties used in the experiments.

Parameter	Diesel MK1	RME	HVO
Cetane number	53.2	56	80-99
Density @ 15°C[Kg/m ³]	835.9	880	780
Lower heating value [MJ/kg]	42.9	37-39	34-44
Air/Fuel ratio [-]	14.5	12.7	15.2
FAME [%]	0-10	100	0
Viscosity @ 40°C[mm ² /s]	2.746	6.9-8.2	2.3-5
Oxygen [%]	0	11	0

Experimental Combustion Characterization

This chapter is a review of the Diesel combustion from the phenomenological point of view, where the pilot and main fuel injections are experimentally characterized. The qualitative and quantitative descriptions of the pilot and main combustion will later be used to support the controller strategy design, requirements, architecture and specifications, as well as the set-point optimization. The chapter starts with the analysis of the pilot injection and combustion, where its robustness, uncertainty and timing are studied. The second part focuses on the pilot effects on the main fuel injection. Finally, the overall impact of the pilot and main injections on the engine operation parameters and emissions is considered.

4.1 Pilot and Main Injections

Multiple injections are typically used in heavy-duty Diesel engine applications (Johansson, 2012). A common combination is the pilot and main fuel injections this thesis focuses on, illustrated in Figure 4.1. Pilots are short injections, smaller than half of the total fuel mass (Johansson, 2012), which improve the performance at low loads (MacMillan et al., 2009) and cold-start (Osuka et al., 1994) and, reduce emissions and engine-out noise (Kiencke and Nielsen, 2000).

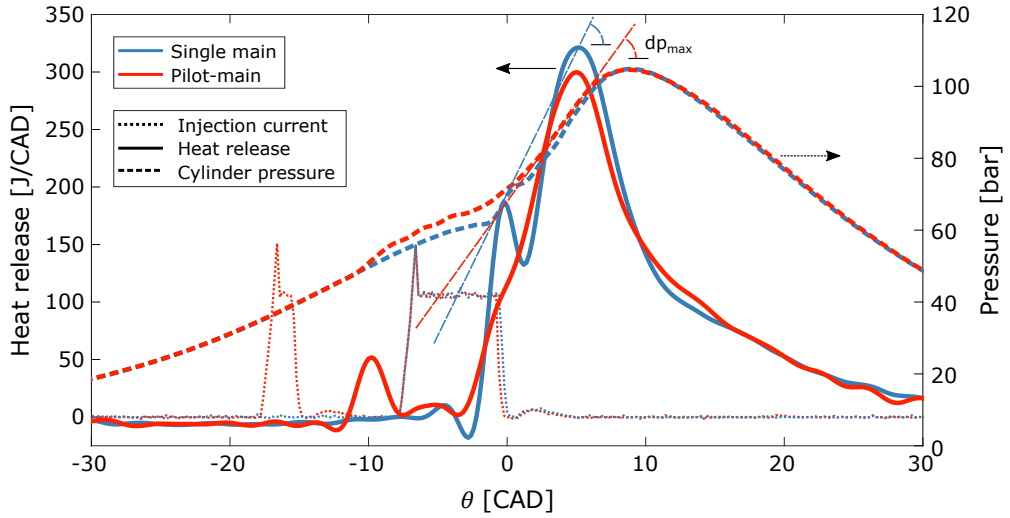


Figure 4.1: In-cylinder data illustrating the effects of the pilot injection (red) compared to single main injection (blue). The heat release of the pilot combustion increases the chamber temperature, reducing the main ignition-delay and its premixed combustion. This reduces the maximum pressure rise rate, indicated by the tangent lines. The engine was operated at 10bar IMEP, 1200RPM and 1200bar rail pressure. The injection current is plotted without scaling.

Pilot injection reduces the ignition-delay of the main injection by increasing the chamber pressure and temperature. The shorter ignition-delay of the main injection increases its stratification and lowers its combustion rate (Solsjö, 2014). The lowered premixed main combustion reduces the fast rise of the in-cylinder pressure. High pressure rise rates cause loud audible engine-out noise and may also produce engine damage (Heywood, 1988). Despite not as significant in conventional Diesel engines, it was found in Tsurushima et al. (2002) that the pressure oscillations due to the abrupt combustion can break the insulating gas boundary layers in the cylinder, increasing the heat flux and losses. With a single main fuel injection, similar noise levels as for a pilot-main injection are obtained for later combustion timings with associated efficiency penalty. Hence, pilot and main fuel injections achieve higher indicated efficiencies while limiting engine-out noise and maximum in-cylinder pressure. Furthermore, due to the change of the fuel mixture process and chemical reaction, the soot and NO_x emissions can also be reduced by the pilot injection (Badami et al., 2001; Minami et al., 1995; Tanaka et al., 2002; Zhang, 1999).

Pilot injections are commonly placed before TDC. Hence, its combustion reduces the indicated efficiency, as the cylinder pressure is built against the cylinder upwards movement during the compression stroke. To increase the indicated efficiency, the trade-off is between the benefit from the advancement of the main combustion and the penalty from the pilot combustion. The penalty of pilot

combustion is directly correlated with the burnt pilot mass. To reduce this penalty, short pilot injections can be placed either early with limited combustion efficiency, or later, with limited work against the piston movement. The optimization problem is discussed in Chapter 10. Despite the fact short pilot injections can increase the indicated efficiency, the combustion of small pilot masses presents controllability and robustness challenges, as will be discussed in this chapter. The design of the experiments run to obtain the data for the analysis is described in the following subsection.

4.1.1 Design of experiments

The pilot injection parameters investigated were the pilot mass, the rail pressure, the pilot-main SOI separation and the global combustion phasing, set by the main HRR-peak through the regulation of CA50. This experimental setup was selected to keep constant the main combustion phasing, which affects more significantly the operating conditions. The approach is focused on the pilot-main injection necessary to obtain a given operating condition. In this manner, the interdependence of the pilot injection and its effects on the main injection can be studied. This provides insights on how the pilot injection should be designed, and the main injection adjusted, to maintain the engine operating condition at the set-point reference.

The extensive experimental design for the pilot and main combustion study followed a full matrix design with different levels of the engine operating variables, listed in Table 4.1. The central matrix design in Table 4.2 was followed for the combination of engine speed and load. All the combinations of HRR-peak, pilot-main injection separation and pilot mass in Table 4.1 were tested. The rail pressure range was limited depending on the engine load (due to minimum opening time). The central point is number #18 in Table 4.2, at 10 bar IMEP and 1200RPM.

Table 4.1: Engine operating conditions for the extensive experimental design.

Parameter	Value
Engine speed	600, 900, 1200, 1500, 1800 [RPM]
Load (IMEP)	2.5, 5, 7.5, 10, 12.5, 15 [bar]
Rail pressure	900, 1050, 1200, 1350, 1500 [bar]
HRR-Peak	0, 5, 10 [CAD]
Pilot-main injection separation	5, 7.5, 10 [CAD]
Pilot mass	6, 8, 10, 12 [mg/st]

Table 4.2: Central design matrix for the extensive experimental design. The central set-point was number #18.

Engine Speed (RPM)	Engine Load (IMEP, bar)						
	Motoring	2.5	5	7.5	10	12.5	15
600	#1	#6	#9	#12	#16		
900	#2	#7	#10	#13	#17		
1200	#3	#8	#11	#14	#18	#21	#24
1500	#4			#15	#19	#22	#25
1800	#5			#20	#23	#26	

4.2 Pilot Injection

For a heavy-duty Diesel engine, small pilot masses range from masses of the injector's minimum opening time, around $6mg/st$, to masses less than half of the main injection at low loads, around $20mg/st$. However, injectors are designed optimally to handle the main injection masses, ranging from $30mg/st$ to over $300mg/st$ at high loads. In the low region of the on-time, the resulting injected mass is not as linear nor stable as for the high region of the on-time. The short opening times result in high sensitivity to rail-pressure oscillations. Furthermore, the small pilot masses injected are also more sensitive to variations of the combustion chamber conditions i.e., pressure, temperature, air mass, turbulence, EGR, etc.

The pilot injection and its combustion were investigated in Publication I. The focus was to determine and understand the robustness and variability of the pilot combustion to different injection parameters and operating conditions. The analysis is structured as follows. The injection and operating parameters impact on the pilot combustion robustness i.e., misfire probability, is first studied. The pilot combustion metrics are quantified as a function of the input and operating variables. Finally, the impact of the initial chamber conditions on the pilot combustion, set by the previous cycle's combustion, is considered.

4.2.1 Pilot misfire

Pilot misfire is its lack of combustion, when its auto-ignition is not triggered. The pilot combustion has the effect of reducing the main ignition-delay and its premixed peak (presented in Section 4.3). Due to the lack of combustion, pilot misfire increases the premixed fuel mass and combustion rate of the main injection. Consequently, pilot misfire is defined in this work as the lack of

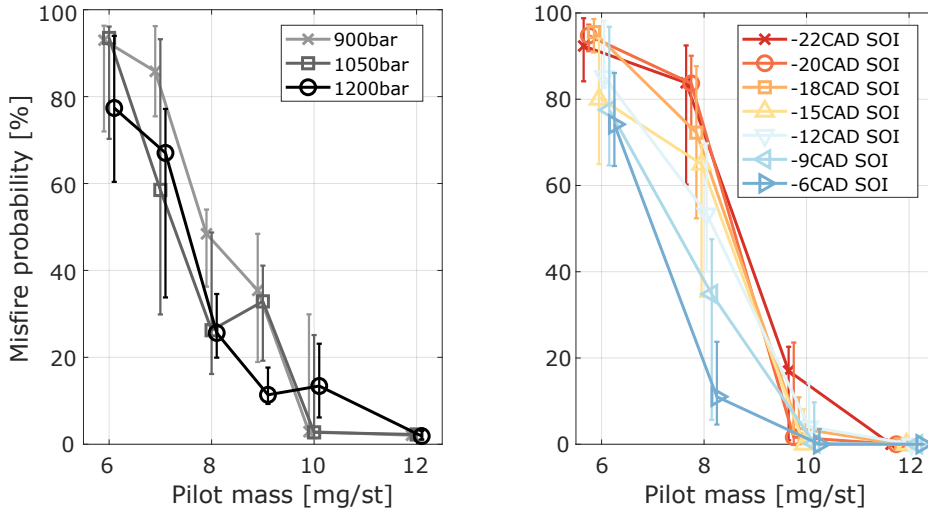


Figure 4.2: Pilot misfire probability for different rail pressures (left) and pilot SOI (right) as a function of the pilot mass. The engine was operated at 10bar IMEP, 1200RPM, no EGR for 300 cycles. The central operating point was 1200bar rail pressure, 5CAD HRR-peak, 7.5CAD pilot-main separation. The bars represent the 95% confidence interval over the six cylinders.

enough pilot combustion resulting in an increase of the premixed peak of the main injection combustion. Therefore, the lack of measured pilot heat release, due to locally bounded combustion or small cylinder pressure change, does not imply its classification as misfire.

Pilot misfire is a stochastic process. The probability of obtaining a misfire cycle, interpreted as the frequency or ratio, represents the pilot combustion robustness. Its sensitivity varies as a function of the injected fuel mass, the injection pressure (rail pressure), chamber temperature and pressure. The pilot misfire probability is plotted in Figure 4.2 for different rail pressures (left) and for different SOI (right) as a function of the pilot mass. The percentage was computed over 300 cycles and the bars represent the 95% confidence interval.

Larger pilot masses reduce the misfire probability significantly. There is a transition, at around 8mg/st, from full pilot misfire for masses under 6mg/st to full pilot combustion for masses over 12mg/st at this operating condition. For the smallest pilot masses of 6mg/st, there is the possibility the detected pilot misfire is due to the lack of the opening of the injector nozzle because of the short on-time. To discard this hypothesis, it was observed that the pressure rise rate increased, compared to single main injection, when the pilot injection was commanded. This revealed the injected pilot mass burned together with the main injection during its premixed combustion phase, increasing it. The experiment confirmed that for 6mg/st the pilot misfire was not due to its lack of injection.

The rail pressure and SOI shift the transition curve. For higher rail pressures, the misfire risk is reduced, more significantly at low loads and low engine speeds, see Publication I for details. However, the higher the rail pressure, the shorter the on-time, resulting in higher sensitivity to rail pressure oscillations, which increases the cylinder-to-cylinder variability of the misfire probability. The effect of the SOI has a more significant impact on the pilot misfire than the rail pressure. Early pilot injections increases the pilot misfire probability. This is due to the lower in-cylinder pressure and temperature, where the pilot auto-ignition is more sensitive to the chamber conditions (Heywood, 1988), increasing the misfire stochasticity i.e., cylinder-to-cylinder dispersion. Consequently, the exact pilot misfire probability sensitivity to SOI is a function of the engine load, due to the higher in-cylinder pressures and temperatures. This result highlights the possibility of controlling the auto-ignition robustness by adjusting the pilot SOI. Furthermore, the correlation between the pilot mass and misfire probability is stronger than the correlation between the pilot on-time and the pilot misfire probability. This is exploited to estimate the pilot mass based on the pilot misfire probability, as will be presented in Chapter 6.

The cross-correlation analysis between the cylinders showed that the risk of pilot misfire is independent of the current cycle conditions. In other words, if a pilot misfire is obtained for one cylinder, it does not imply the pilot injections of the other cylinders may misfire.

4.2.2 Pilot combustion

Short pilot injections burn in premixed mode due to the long ignition-delay. The combustion timing, efficiency and metrics are reviewed in this section. The previous cycle combustion did not affect the next cycle pilot combustion. The gas residuals are essentially constant for steady operating conditions, since combustion efficiency in Diesel engines is close to the unity. The other stochastic variables had a more significant effect on the pilot combustion variability, as discussed in Publication I. These variables are the fuel injection parameters and engine operating conditions, reviewed in this section.

Ignition-delay

The premixed combustion of short pilot injections follows an Arrhenius reaction rate. The ignition-delay of the pilot is therefore mostly sensitive to the temperature at the SOI. Other variables such as the pilot mass, engine speed and rail

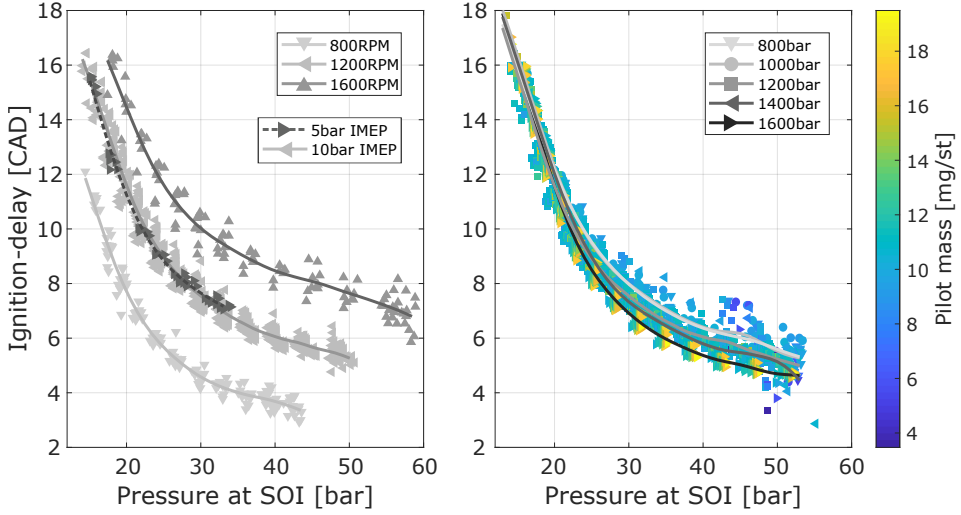


Figure 4.3: Pilot ignition-delay as a function of the pressure at the pilot SOI, for different engine speeds and loads (left), pilot masses and rail pressures (right). The lines represent the data smoothing by a polynomial spline.

pressure have a limited effect on the pilot ignition-delay. The intake pressure and engine load have an indirect effect on the ignition-delay, by determining the in-cylinder temperature. This can be observed from Figure 4.3, where the ignition-delay is plotted as a function of the in-cylinder pressure at SOI.

The in-cylinder temperature, hence the pressure for a closed system, reduces exponentially the ignition-delay as it increases. In the CAD domain, the ignition-delay is proportional to the engine speed. The engine speed increases the dispersion, due to the higher turbulence, but also the higher signal noise and uncertainty when detecting the SOC. The engine load shifts the range of in-cylinder pressures reached within the scope of pilot SOI, but not the overall exponential trend of the ignition-delay. The pilot mass has no significant impact on the ignition-delay. Higher rail pressure reduces linearly the ignition-delay to a limited extent, in the range of $-0.0012 \text{ CAD}/\text{bar}$. This is only significant for short ignition-delays at high temperatures i.e., late SOI, where the higher rail pressure increases the fuel-air mixing. These observations are based on the results of Publication I, and supported by previous work (Ishida et al., 1994; Carlucci et al., 2003).

Combustion efficiency

Although Diesel combustion reaches efficiencies close to the unity (Heywood, 1988), the pilot injection alone has lower combustion efficiency. The pilot

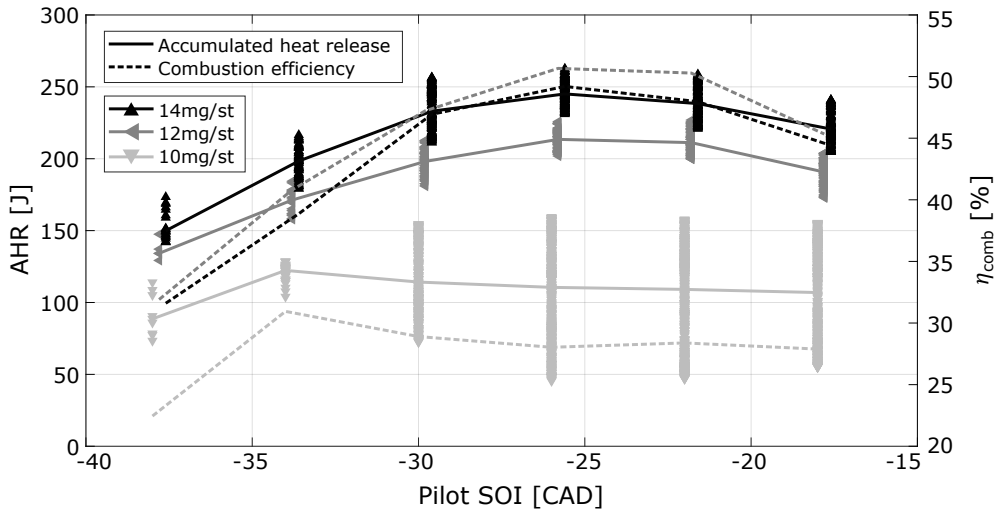


Figure 4.4: Accumulated heat release and combustion efficiency as a function of pilot SOI for different pilot masses. The engine was operated at 10bar IMEP, 1200RPM, 1200bar rail pressure, no EGR.

combustion efficiency is a function of the pilot mass and the ignition-delay. The burnt fuel is estimated from the accumulated heat release measurements, between the pilot SOI and the main SOC. The AHR and combustion efficiency are plotted in Figure 4.4 as a function of the pilot SOI for different injected pilot masses.

The pilot combustion efficiency increases as the injection is retarded. The shorter ignition-delay prevents the diffusion of the fuel mass and the reduction of local temperatures, which increases the combustion efficiency. However, as the pilot approaches the main injection, the overlap of the heat release results in an apparent measured AHR reduction, as it is only computed before the main SOC. Small pilot masses have higher stochasticity on its fuel mass burnt. However, for early injections, the higher misfire probability results in a smaller dispersion of the AHR from pilots whose combustion is triggered. The total pilot mass fuel burnt saturates as the injected pilot mass increases. This translates into a reduced pilot combustion efficiency. For pilot masses with high ignition-delay sensitivity to engine speed and load, around 10mg/st, the relation between the pilot and main ignition-delays determines the final pilot AHR. In these cases, the longer pilot and main ignition-delays at low loads and low engine speeds resulted in a higher AHR from pilot combustion. A main conclusion is that the AHR is a non-linear function of the pilot mass and injection timing, which must be considered for pilot mass estimation algorithms based on this metric.

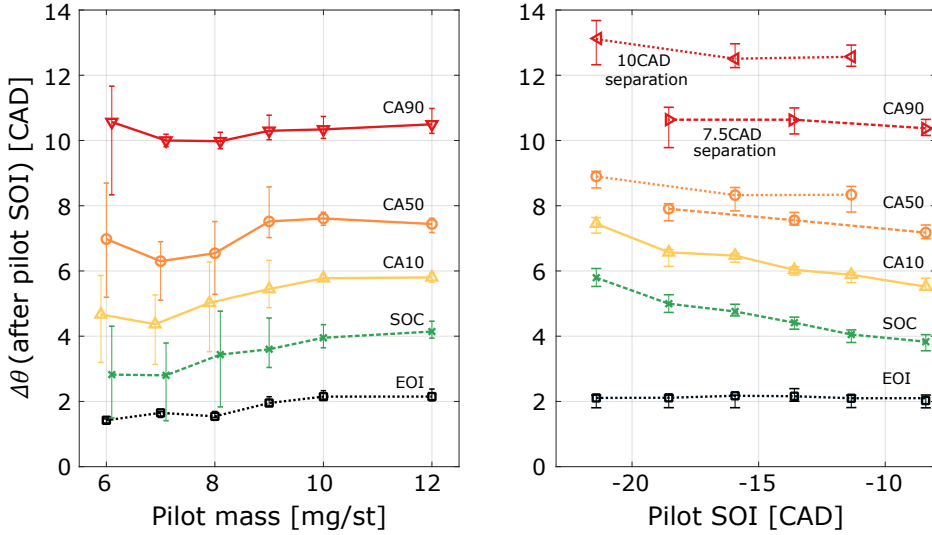


Figure 4.5: Pilot combustion dynamics quantified by the elapsed CAD from the pilot SOI until the combustion metrics (SOC, CA10, CA50 and CA90) as a function of the pilot mass at 5CAD main HRR-peak and 7.5CAD pilot-main separation (left) and pilot SOI for 12mg/st pilot mass (right). The engine was operated at 10bar IMEP, 1200RPM, no EGR. The bars represent the 95% confidence interval over the six cylinders.

Combustion metrics

The combustion metrics for the pilot combustion are computed considering the AHR only before the main SOC. For short pilot-main separations, there may be an overlap between their combustion. For the computation of the metrics, this results in an apparently lower AHR for short pilot-main separations. The results are plotted in Figure 4.5 for 10bar IMEP and 1200RPM. The elapsed CAD from the pilot SOI is plotted as a function of the pilot mass (left) and pilot SOI (right).

The elapsed CAD from the pilot SOC to CA10, CA50 and CA90 is essentially constant. This is because the pilot combustion shape does not change significantly as a function of the pilot mass or injection parameters. In Figure 4.5, the dependence of the pilot SOC with the pilot mass is because the pilot injection was advanced to maintain the pilot-main separation and the combustion phase constant. It was observed that only for early pilot injections, around $-35CAD$, the lower temperature was significant to extend the combustion duration, retarding CA50 and CA90. For small pilot masses of 6mg/st, the higher misfire probability and larger ignition-delay stochasticity enlarges the variance of the combustion duration metrics. Larger pilot masses increase the robustness of the combustion shape, resulting in a smaller variance of the combustion metrics.

The engine load and engine speed do not impact the shape of the pilot heat release significantly. Higher rail pressure reduces the combustion duration linearly, with around $-0.0025 CAD/bar$. These observations will be later exploited for the design of the in-cycle pilot mass estimation, presented in Chapter 6.

4.3 Main Injection

This section presents the experimental results of the pilot combustion effects on the main injection and overall engine performance, based on Publication II. The sensitivity analysis of the main combustion to the pilot injection sets the basis to build a conceptual combustion model. The conceptual model introduces the *pilot-main interaction modes*. The model aids to explain the pilot effects on the main combustion behavior, the engine performance and emissions.

4.3.1 Sensitivity of main combustion to pilot injection

The sensitivity of the main combustion to the pilot injection is studied by a sweep of pilot SOI and masses. The main combustion metrics are plotted in Figure 4.6 as a function of the pilot mass (left) and pilot-main separation (right) for different engine loads and speeds.

Pilot injection reduces the main ignition-delay when its auto-ignition is triggered, for pilot masses over $8 mg/st$ at these operating conditions (see the lower plot in Figure 4.6). The magnitude of the reduction holds constant once the pilot mass is large enough to ensure its combustion. For very short pilot-main separations, the high local temperatures and the interaction of the main spray fuel jet with the pilot combustion aids the trigger of the main injection auto-ignition (Denny, 2019), reducing further the main ignition-delay. These trends are observed regardless engine load and speed.

The premixed combustion is inversely correlated to the pilot mass, as its effects on the reduction of the main ignition-delay reduces also the premixed combustion. Therefore, the same trends of the main ignition-delay are obtained for the duration of the premixed combustion (CA50-10). For high loads and engine speeds, the premixed combustion is less sensitive to the pilot injection, due to the shorter main ignition-delay time duration. The pilot-main separation does not affect the premixed combustion. The only exception is observed at high loads, where for large pilot-main separations, the additional remaining fuel from the pilot injection increases the premixed combustion.

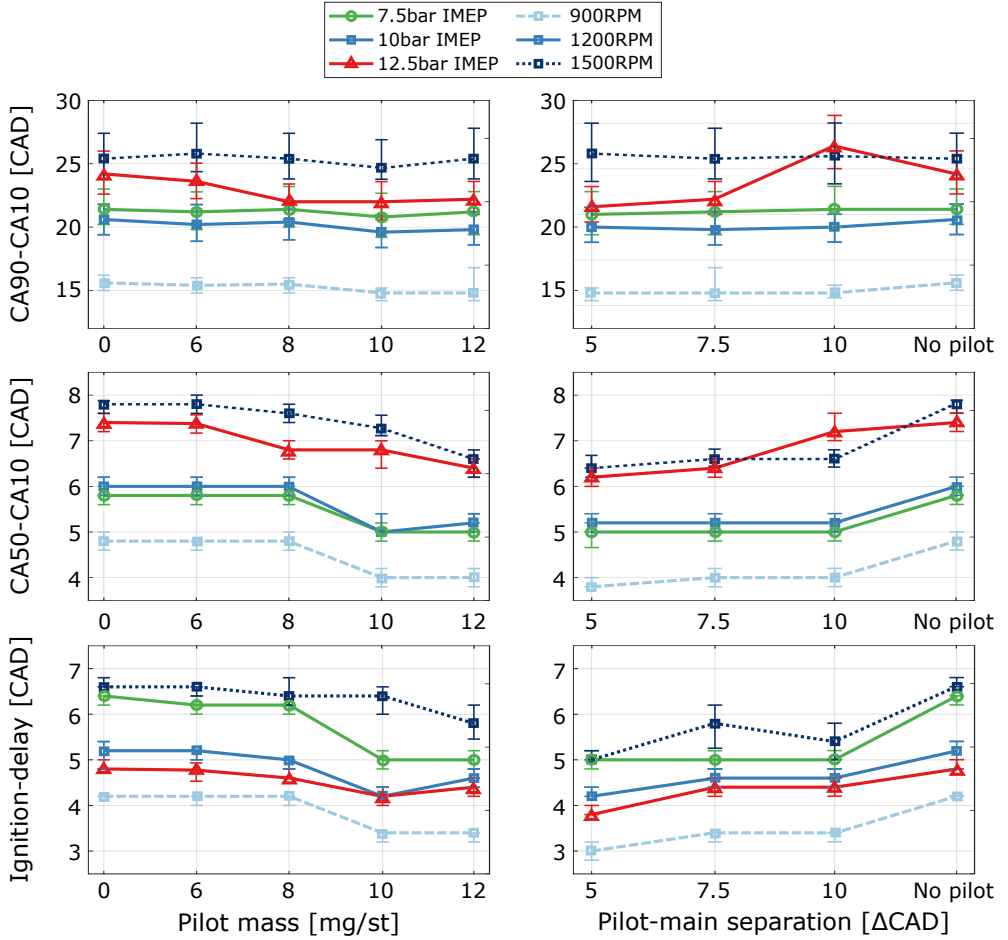


Figure 4.6: Main combustion metrics (combustion duration, measured by CA90-10 (top); premixed combustion duration, measured by CA50-10 (middle); and ignition-delay (bottom)) as a function of the pilot mass (left) and pilot-main separation (right) for different engine loads and speeds. The central operation point was $7.5CAD$ pilot-main separation and $12mg/st$ pilot mass, no EGR. The bars represent the 95% confidence interval over the six cylinders.

The total combustion duration follows the previous trends, with a reduced magnitude. However, the reasoning is different. Larger pilot masses reduce the total share of the fuel mass from the main injection at constant load, despite the lower indicated efficiency. The pilot-main separation has a limited effect on the main combustion duration, except at high loads. Large pilot-main separations are obtained for early pilot combustions, which reduces the efficiency. This is compensated by a larger main injection.

From this sensitivity analysis, it was observed that the effects of the pilot combustion on the main injection were not directly related to the pilot *injection*

parameters but to the pilot *combustion* parameters, i.e., in which phase of the pilot combustion the main injection starts. The interaction modes are introduced to describe the pilot combustion effects on the main combustion metrics, engine operation and emissions.

4.3.2 Pilot-main interaction modes

The pilot-main interaction modes facilitate the description of the pilot combustion effects on the main injection, regardless pilot injection parameters, rail pressure, engine load and speed. The theoretical simplification is based on how the pilot combustion develops in relation to the main injection, which determines the effects. The interaction modes, illustrated in Figure 4.7, are defined by the pilot combustion phase at which the main injection starts:

- In *mixing interaction mode*, the main injection starts during the mixing phase of the pilot injection. The in-cylinder charge has an additional concentration of fuel that has been mixed and vaporized, close to the conditions for auto-ignition. This interaction mode is obtained for large pilot ignition-delays, including pilot misfire, small pilot masses, short pilot-main separations, low engine speeds or low engine loads. The main injection window is between the minimum pilot-main separation, imposed by hardware constraints, and the pilot SOC.
- In *premixed interaction mode*, the main injection starts during the initial premixed combustion phase of the pilot combustion. The main injection window is limited between the pilot SOC and the maximum premixed combustion duration, $2CAD$ after pilot SOC (Publication I).
- In *diffusive interaction mode*, the main injection starts during the diffusive combustion of the pilot injection. This mode is obtained for large enough pilot masses that reach the diffusive combustion, over $10mg/st$ (Publication I), at early pilot injections, large enough pilot-main separations, low engine speeds or high engine loads.
- In *completed combustion interaction mode*, the main injection starts after the pilot has burned completely. This interaction mode is obtained for early pilot injections, short pilot ignition-delays, late main injections, large pilot-main separations, low engine speeds or high engine loads. Therefore, the indicated efficiency is reduced for this interaction mode.

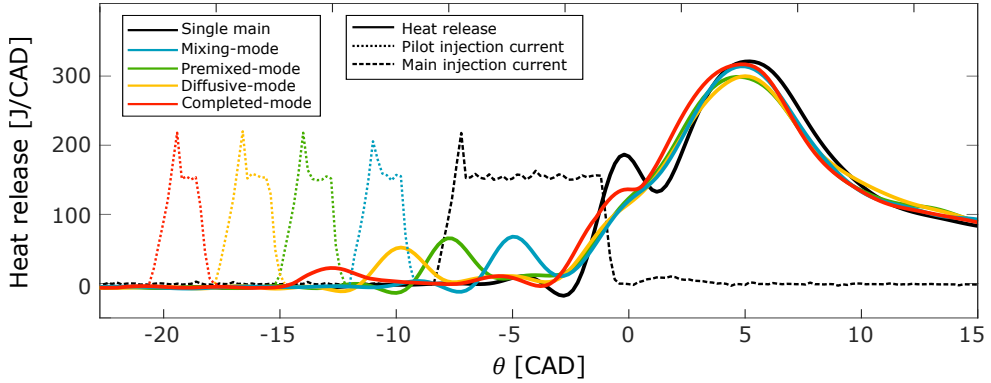


Figure 4.7: Pilot-main interaction modes for different pilot injections. The heat release of the pilot combustion determines the resulting interaction mode when the main injection is kept constant.

4.3.3 Main combustion metrics

The main combustion metrics are plotted for the different interaction modes at 10bar IMEP, 1200RPM, 1200bar rail pressure in Figure 4.8, together with the pilot SOC. The analysis is based on the results of Publication II. The main injection was adjusted to obtain a constant combustion phase, at 5CAD HRR-peak, which results in a constant CA50. With pilot and main injections, the pilot-main separation determines the transition from mixing-mode to completed-mode. However, pilot misfire may result in mixing-mode despite the main fuel is injected after the virtual pilot SOC (computed with an ignition-delay model), even for large pilot masses. Therefore, there is a wide range of pilot SOC that result in mixing-mode. Similarly, the range of pilot injections for diffusive mode is larger, compared to premixed and completed-modes.

For single main injection, the larger premixed combustion reduces the duration between the main SOC and CA10. As the pilot burnt mass increases (from premixed-mode to completed-mode), the smaller premixed combustion enlarges CA10-SOC but reduces more significantly CA50-10. Hence, the main SOI is retarded to maintain constant the combustion phase. The combustion duration (CA90-SOC) is reduced from premixed-mode onwards due to the additional fuel injected from the pilot, despite the lower premixed main combustion. These trends can be deduced from Figure 4.8, see Publication II for details.

The trends are similar for different engine loads and speeds. However, some cases require special attention. At low loads (2.5bar IMEP), mixing mode from pilot misfire may increase the main ignition-delay. The lower bulk temperature increases the pilot ignition-delay enough to overlap with the main SOI, resulting

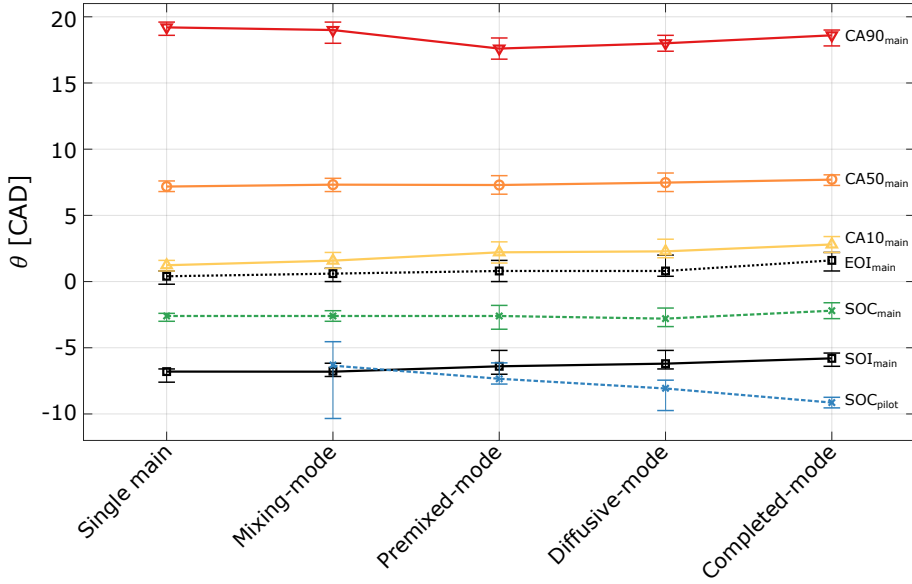


Figure 4.8: Combustion metrics (SOC, CA10, CA50 and CA90) as a function of the interaction modes. The pilot SOC and main injection are also indicated. For pilot misfire cases, the SOC was computed with a pilot ignition-delay model. The engine was operated for $5CAD$ HRR-peak, at $10bar$ IMEP, $1200RPM$, $1200bar$ rail pressure, no EGR. The bars represent the 95% confidence interval over the six cylinders.

in an even longer ignition-delay altogether. Furthermore, the pilot-main ratio is higher at low loads and the main premixed combustion more sensitive to the main ignition-delay. This results in a significant reduction of the premixed combustion (CA50-10) and an increase of the combustion duration (CA90-10) from premixed-mode onwards, opposite to the trend at higher loads, see Publication II for details.

4.3.4 Engine performance and emissions

The engine performance is quantified by the indicated efficiency, maximum in-cylinder pressure and exhaust temperature. The emissions are the engine-out noise (quantified by the maximum pressure rise rate) and NO_x . Soot and UHC emissions are excluded in this section as they are limited, either from the measurement equipment range or their low values, more details can be found in Publication II. The engine performance and emissions are plotted in Figure 4.9 for three combustion phases at $10bar$ IMEP, $1200RPM$ and $1200bar$ rail pressure.

The indicated thermal efficiency decreases as the interaction mode advances (i.e., more pilot mass is injected) from mixing-mode to completed-mode, compared to single main injection. The particular case of mixing-mode requires special

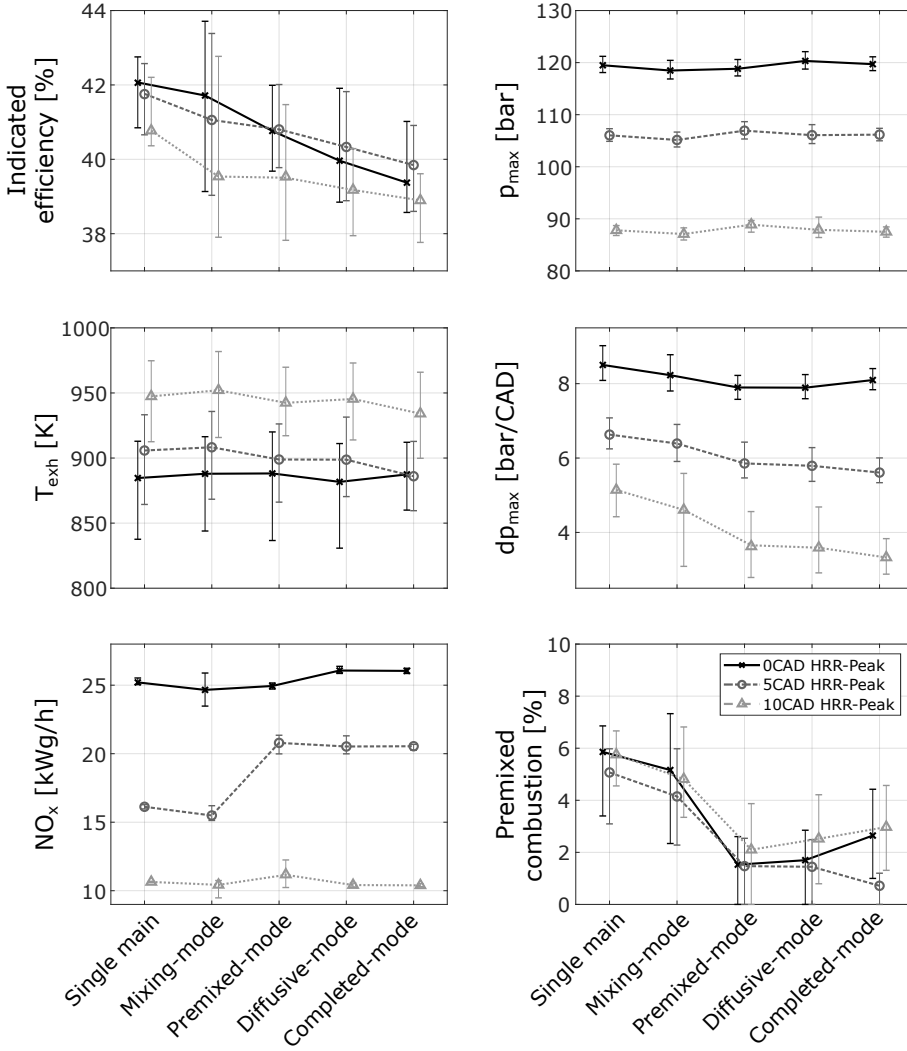


Figure 4.9: Engine-out parameters and emissions (indicated efficiency, maximum pressure, exhaust temperature, maximum pressure rise rate, NO_x and premixed AHR) as a function of the interaction modes for different HRR-peaks. The engine was operated at 10 bar IMEP, 1200 RPM, 1200 bar rail pressure, no EGR. The bars represent the 95% confidence interval over the six cylinders.

attention. For mixing-mode, the indicated efficiency range is wider, as small pilot masses resulting in misfire are included. For those cases, the indicated efficiency may be increased due to the additional premixed combustion. This can be observed in the bottom right plot, where the premixed AHR was computed with the fit of multiple Wiebe functions (see Publication II). On the other hand, mixing-mode with pilot combustion reduces the indicated efficiency as much as for completed-mode. The later the combustion timing, the lower the indicated

efficiency. However, there is a transition for 5CAD HRR-peak. From premixed-mode onwards, the indicated efficiency is larger than for earlier combustion timings. This is due to the same interaction modes as for 0CAD HRR-peak are obtained for later pilot combustions, with a lower penalty on the indicated efficiency.

The engine-out emissions are more significantly correlated with the combustion phase than the interaction mode. The interaction mode has an impact mostly on the maximum pressure rise rate. As the pilot burnt mass increases, the maximum PRR decreases, more significantly for later combustion timings. From premixed-mode onwards, the reduction is saturated. NO_x is also affected by the interaction modes for 5CAD HRR-peak, where the reduced premixed combustion increases after premixed-mode. This is a combination of the higher maximum pressure, which facilitates the NO_x formation due to higher temperatures, but shorter reaction (see Figure 4.8) that freezes the reactions, with higher net NO_x emissions. For earlier or later combustion timings, NO_x is not as sensitive to this trade-off.

The trends are similar for different engine operating conditions. However at low loads, the combustion is mostly premixed with single main injection. Therefore, the pilot injection only reduces the indicated efficiency. At low loads, the soot levels are also increased due to the pilot combustion, from premixed mode onwards (see Publication II). Therefore, following the soot- NO_x trade-off, the NO_x levels are reduced at low loads for increasing pilot burnt masses, from premixed-mode onwards. The maximum PRR is more heavily reduced at low loads when pilot burns, from premixed-mode onwards. As the load increases, the sensitivity to pilot combustion reduces, hence the pilot combustion impact on the reduction of the maximum PRR.

Combustion Modeling

Model-based design aids the optimization, development, testing and verification of control algorithms in a systematic manner. This approach can reduce the development effort and time, considering the increasing engine complexities. Furthermore, model-based system simulation and development has the advantage of reducing the experimental work-load. The models introduced in this chapter can be used for the off-line stochastic simulation, for the set-point optimization and, for the design and validation of estimation methods and controller performance. The models can also be used on-line to aid the controller by predicting the system behavior in real-time. Stochastic and predictive modeling approaches for the model-based controller design were adopted in this thesis. The methodologies and models are presented in this chapter.

5.1 Modeling Approaches

The system dynamics in a reciprocating engine have different time scales (Höckerdal et al., 2018). A common modeling approach for engine control-oriented models is the mean value modeling (MVM)(Guzzella and Onder, 2004). MVM is able to describe the deterministic effect of the inputs on the outputs, by continuous-time lumped parameters. This approach is suitable to capture slower dynamics,

assuming the fast combustion characteristics as static effects. Faster dynamics are modeled by discrete event models (DEM) that take explicitly into account the reciprocating behavior of the engine (Guzzella and Onder, 2004). In DEM the independent variable is the crankshaft angle, often assuming a constant engine speed. The crank angle resolved DEM methodology is followed in this work, which is a common approach for the modeling of the in-cylinder processes.

For the combustion modeling, the fluid mechanics, chemical kinetics and thermodynamics of Diesel combustion are of high complexity, making its modeling and simulation a challenging task (Lakshminarayanan and Aghav, 2010). The most detailed modeling approach is Computational Fluid Dynamics (CFD). CFD utilizes numerical algorithms to solve partial differential equations describing the fluid dynamics, together with the chemical processes with up to hundreds of species and reactions. The spatial and temporal resolution are selected for a satisfactory trade-off between computation time and detailed results. In CFD simulation, the volume of the cylinder is meshed into finite small elements with homogeneous properties. A detailed review of these methods can be found in (Shi and Reitz, 2010). Simulations require from hours to months, which limits the application of CFD methods for control-oriented modeling. Examples of applications of CFD methods are the design of combustion chamber geometry, the study of fuel-spray properties and detailed analysis of in-cylinder flow patterns, as a complement to experimental testing (Han et al., 2002; Szekely et al., 2004; Shi and Reitz, 2010).

As an alternative, lower complexity is achieved by zero-dimensional (0D) models. In this approach, the model represents average variables over large thermodynamical homogeneous regions (Jung and Assanis, 2001). A number of zones can be used to represent the evolution of different average variables, such as the in-cylinder pressure and temperature. A common approach to account for the temperature gradient is a two-zone model, for the burnt and unburnt fuel (Heider and Zeilinger, 1998). On the other hand, single-zone models assume the whole cylinder volume has homogeneous thermodynamic properties (Foster, 1985). These models are typically derived from first principles, where sub-models with empirical parameters represent the fuel injection, fuel/air mixing and combustion. Examples of such models are presented in (Egnell, 1998; Kiencke and Nielsen, 2000; Eriksson and Nielsen, 2014; Isermann, 2016). Despite the loss of spatial resolution, zero-dimensional models can accurately describe engine-out data with high temporal resolution (Kiencke and Nielsen, 2000; Chmela et al., 2007; Widd et al., 2012).

The zero-dimensional modeling approach for the combustion is adopted in this thesis. The sub-models for the stochastic simulation, controller design, para-

meter estimation and in-cycle prediction, were selected based on the trade-off requirements between model accuracy and computational complexity. The modeling approaches and detailed equations are presented and discussed in the following sections.

5.1.1 Simulation modeling

The simulation of in-cycle controllers requires an adequate description of the stochastic cyclic variations of the combustion (Willems, 2018), which must be included in the combustion model. A stochastic modeling approach is followed in this work to capture the many degrees of freedom, complexity and uncertainty of the combustion. This approach models the effects of the input dispersion on the parameters and output dispersion, instead of all the detailed fluid mechanics, chemistry and thermodynamic processes. The reduced complexity of the model permits to describe the stochastic cyclic variations with reduced simulation times. The cyclic stochasticity is explicitly modeled by the correlation of the inputs dispersion to the parameters and outputs dispersion. Therefore, for the stochastic model calibration, each cycle must be fitted individually. In this manner, the dispersion of the identified parameters can be included in the stochastic model parametrization. The stochastic modeling permits to simulate the reduction of the stochastic cyclic variations using the in-cycle controllers. The reduction of the cyclic variations is exploited for the set-point optimization, discussed in Chapter 10.

5.1.2 Predictive modeling

To overcome the inherent delay between the control action (fuel injection) and the measured effects (in-cylinder pressure) within the same cycle, highly accurate, fast, predictive models are required (discussed in Chapter 8), as the prediction accuracy affects the controller performance (discussed in Chapter 9). Additionally, the models require real-time execution, under $0.2CAD$ for the current engine setup. For the fast, parallel execution, the predictive models are implemented in an FPGA. This imposes limitations on the complexity of the model expressions, as some mathematical operations are not natively supported, and require a few clock cycles for their computation (see Chapter 11). To overcome these limitations and still achieve accurate in-cycle predictive regulation of the combustion, the approach taken in this thesis is to use simplified models. The models provide accurate predictions locally around the nominal operating conditions where the engine is to be regulated. The low complexity of the mod-

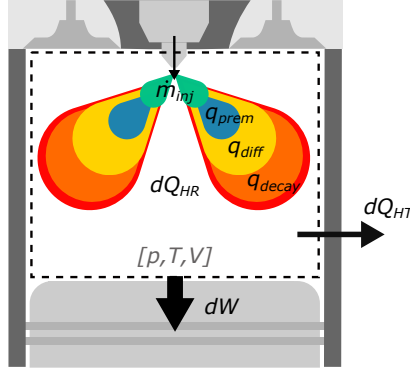


Figure 5.1: Control volume for mass and energy balance of the combustion chamber. Arrows indicate the energy and mass flows. The cylinder is considered as a closed system with no material losses i.e., no blow-by, no crevices. The net heat release (dQ_{HR}) is the combination of the premixed combustion (q_{prem}), diffusive combustion (q_{diff}), combustion decay (q_{decay}) and heat transfer (dQ_{HT}).

els ensures their implementability in the FPGA. The accuracy is improved by the on-line adaptation of the model parameters, presented in Chapter 7. The predictive models are selected considering the requirements for an accurate and robust on-line adaptation.

5.2 Stochastic Simulation Models

For the simulation of the heat release and in-cylinder pressure, the models describe the pressure at the start of the compression stroke, the fuel injection, the pilot combustion, the ignition-delay, the shape of the heat release rate (composed of the premixed, diffusive and decay combustion rates) and, the pressure evolution by the charge thermodynamics.

Some simplifications and assumptions are adopted for the combustion model. The injected mass is neglected compared to the air mass inside the cylinder, the chamber has no mass losses, the heat transfer to the injected mass up to the vaporization temperature is neglected, and the work due to the fuel gas expansion is neglected. The injections do not overlap in time i.e., there is only one injector. The control volume with the mass and energy flows is illustrated in Figure 5.1.

The parameters and model accuracy is quantified by the coefficient of determination (R^2) and the root mean-squared error. A chi-squared hypothesis test of normality was used to validate the assumption of the normal distribution of the model parameters. See the appendix of Publication XII for more details.

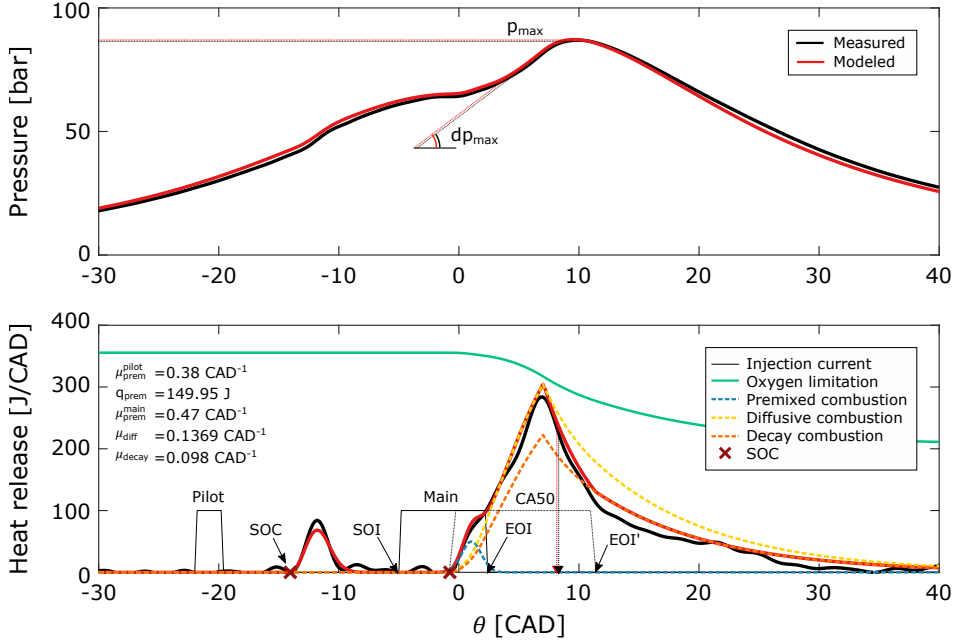


Figure 5.2: In-cylinder pressure (upper plot) and heat release rate (lower plot) measured and simulated with the fitted parameters. The engine was operated at 10bar IMEP, 1200RPM and 1200bar rail pressure. The different combustion phases with their parameter values are indicated.

5.2.1 Stochastic simulation

For the model simulation, the differential equations were solved recursively with a step equal to the crank angle encoder in the engine, of $0.2CAD$. A trapezoidal method was implemented for each recursion integration. An example of the pressure and heat release simulated with the models fitted to the data is plotted in Figure 5.2.

The simulation of the stochastic models was performed by the Monte Carlo method, where the stochastic results are obtained by repeated random sampling simulation. In this approach, the inputs are randomly generated from their probability description models. The inputs are then taken for the deterministic simulation of the system. The process is repeated a large number of iterations to generate the results, which are then aggregated for the computation of the stochastic output. In the combustion model presented in this thesis, the model includes stochastic inputs i.e., inlet pressure and temperature, injector on-times, rail pressure, injected fuel mass; and stochastic combustion parameters i.e., ignition-delay, combustion efficiency, combustion rate, heat transfer, etc. For

each repetition in the Monte Carlo simulation, the parameters were successively computed as the combustion progressed. The interdependence of the model parameters was indirectly considered by the calculation of the parameters with the realization at that simulation iteration. In this manner, the values of the stochastic realization of the parameters were used for the calculations of the subsequent models.

5.2.2 Intake conditions

The intake conditions are computed for the calculation of the state at inlet valve closing (IVC), determined by the inlet manifold pressure and temperature, fresh air mass and residual gas mass.

Fresh air mass

The fresh air mass is determined by the equivalent air-fuel ratio (λ), which is an operating variable, calibrated for each engine load and speed:

$$m_{air} = \lambda m_f AFR_{st} \quad (5.1)$$

Residual gas mass

The residual gas mass is computed by the state at the exhaust manifold at exhaust valve opening (EVO):

$$m_{res} = \frac{p_{exh} V_{EVO}}{RT_{exh}} \quad (5.2)$$

The total mass at IVC is:

$$m_{IVC} = m_{air} + m_{res} \quad (5.3)$$

Pressure at IVC

A simple experimental model has been derived in this work to determine the pressure at IVC for a given intake manifold pressure and temperature at steady-state conditions:

$$p_{IVC} = k_{in} \cdot p_{intake} \quad (5.4)$$

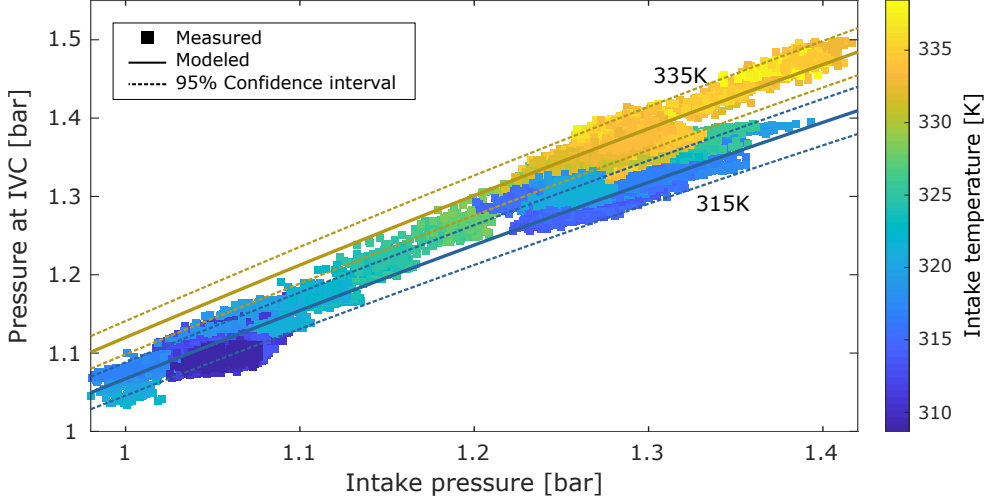


Figure 5.3: Measured and modeled pressure at IVC as a function of the intake pressure for different temperatures. The model 95% confidence interval is indicated.

The correction gain is modeled as a function of the intake pressure and temperature:

$$k_{in} = k_0^{in} + k_1^{in} p_{intake} + k_2^{in} T_{intake} \quad (5.5)$$

The intake manifold geometry, gas flow and heat transfer impact the dynamics of the IVC state and the cylinder-to-cylinder variations. The uncertainty of the correction gain is modeled as a normally distributed variable with a constant standard deviation:

$$\mathbf{k}_{in} \sim \mathcal{N}(k_{in}, \sigma_{k_{in}}^2) \quad (5.6)$$

Temperature at IVC

The temperature at IVC is computed by the ideal gas law, known the pressure and total gas mass at IVC:

$$T_{IVC} = \frac{p_{IVC} V_{IVC}}{m_{IVC} R} \quad (5.7)$$

The range of validity and the model accuracy are summarized in Table 5.1. The model agreement with the calibration data is plotted in Figure 5.3.

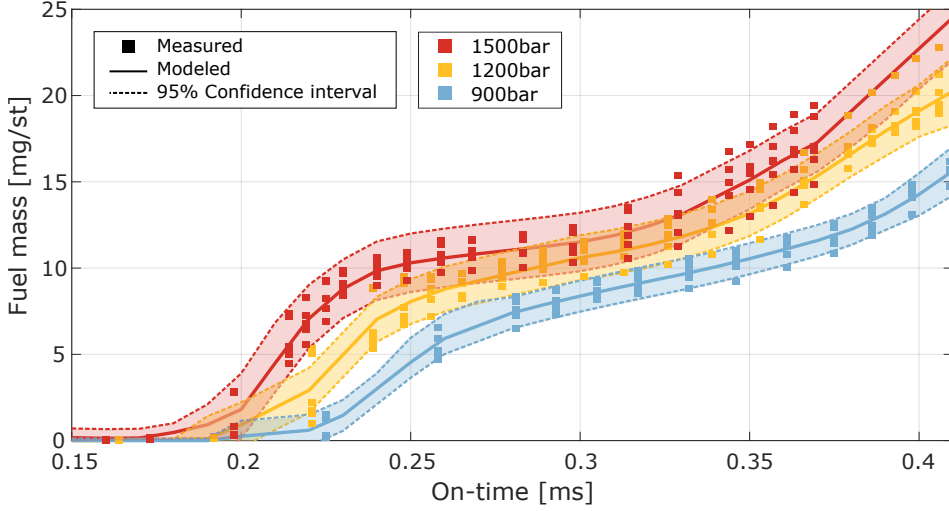


Figure 5.4: Injected fuel mass as a function of the injector's on-time, at different rail pressures. The model and its uncertainty, measured by the 95% confidence interval, are plotted.

Table 5.1: Intake pressure scale factor model accuracy and, inputs and outputs range.

Variable	R^2	RMSE	Range
k_{in}	0.6221	0.0016 [-]	[0.98, 1.15] [-]
$\sigma_{k_{in}}$	0.6144	0.0018 [-]	[0.0053, 0.0054] [-]
p_{intake}			[0.95, 1.45] bar
T_{intake}			[300, 340] K
p_{IVC}			[0.9, 1.5] bar

5.2.3 Fuel injection

The fuel injectors regulate the injected fuel mass by the on-time (t_{inj}) and rail pressure (p_{rail}). For off-line simulations, the non-linear injector calibration was implemented by a look-up table that determines the total injected fuel mass, Eq.(5.8). Other approaches use a third order polynomial (Gupta et al., 2011) or detailed physical modeling of the injector (Seykens et al., 2004).

$$m_{inj} = f(t_{inj}, p_{rail}) \quad (5.8)$$

The model and its uncertainty are plotted in Figure 5.4. The uncertainty of the injected fuel mass is due to injector-to-injector variations, production tolerances, rail pressure oscillations, and the injector opening time, detailed below.

Injection on-time

The on-time uncertainty is motivated by the multiple factors that influence the injection process inside the injectors. These are the electric signals propagation, pressure wave propagation inside the channels, fuel density and viscosity, etc. Therefore, the on-time dispersion is modeled by a normal distribution, which represents the injection-to-injection variations:

$$\mathbf{t}_{inj} \sim \mathcal{N}(t_{inj}, \sigma_{t_{inj}}^2) \quad (5.9)$$

The standard deviation is a function of the nominal on-time and rail pressure:

$$\sigma_{t_{inj}} = k_0^{inj} + k_1^{inj} t_{inj} + k_2^{inj} p_{rail} \quad (5.10)$$

Rail pressure

The variations of the actual injection pressure for each cylinder are generated by the flow turbulence inside the injectors, oscillations within the rail due to the fuel flow, continuous pumping and out flow. To include these effects in the stochastic fuel injection model, the rail pressure dispersion is modeled as normally distributed:

$$\mathbf{p}_{rail} \sim \mathcal{N}(p_{rail}, \sigma_{p_{rail}}^2) \quad (5.11)$$

The standard deviation is modeled as a function of the nominal rail pressure and engine speed:

$$\sigma_{p_{rail}} = k_0^p + k_1^p p_{rail} + k_2^p N_{eng} \quad (5.12)$$

Injectors

The fuel mass dispersion due to injector-to-injector variations is modeled by a normal distribution:

$$\mathbf{m}_{inj} \sim \mathcal{N}(m_{inj}, \sigma_{m_{inj}}^2) \quad (5.13)$$

The standard deviation is a linear function of the nominal on-time and rail pressure:

$$\sigma_{m_{inj}} = k_0^m + k_1^m t_{inj} + k_2^m p_{rail} \quad (5.14)$$

Injection rate

The previous model computes the total injected mass. The fuel injection rate was modeled as constant, computed over the injection on-time:

$$\dot{m}_{inj} = \frac{m_{inj}}{t_{inj}} \quad (5.15)$$

The range of validity of the fuel mass injection model and the model accuracy are summarized in Table 5.2.

Table 5.2: Fuel mass injection model accuracy and, inputs and outputs range.

Variable	R ²	RMSE	Range
m_{inj}	0.99	1.9 <i>mg/st</i>	[0, 300] <i>mg/st</i>
$\sigma_{t_{inj}}$	0.6221	0.0031 <i>ms</i>	[0.0025, 0.0169] <i>ms</i>
$\sigma_{p_{rail}}$	0.6369	0.7838 <i>bar</i>	[4.95, 7.84] <i>bar</i>
$\sigma_{m_{inj}}$	0.656	0.3697 <i>mg/st</i>	[0.376, 2.247] <i>mg/st</i>
t_{inj}			[0, 2.8] <i>ms</i>
p_{rail}			[900, 1500] <i>bar</i>

5.2.4 Pilot combustion

Pilot misfire probability

The transition of the misfire probability from full misfire to full combustion is modeled by a sigmoid function:

$$r_m = \frac{1}{1 + e^{k_{r_m}(m_{pilot} - m_0^r)}} \quad (5.16)$$

where k_{r_m} is the pilot misfire ratio sensitivity. The central transition mass m_0^r is parametrized as a function of the in-cylinder pressure at the pilot SOI:

$$m_0^r = k_m + k_p(p_{SOI} - p_0)^2 \quad (5.17)$$

The misfire probability for a given pilot mass may differ from its nominal value due to random normal variations, as well as different operating conditions and trends not captured by the model. The effect of these uncertainties is modeled

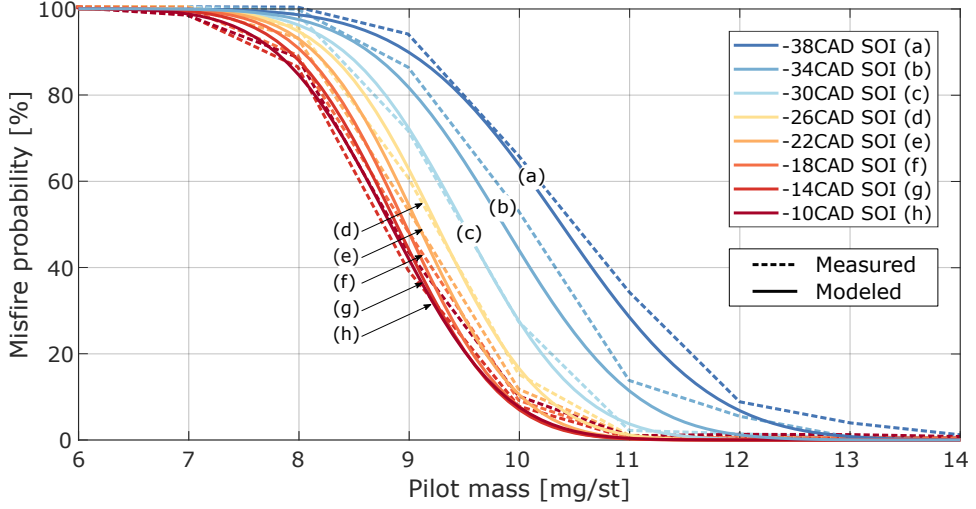


Figure 5.5: Pilot misfire probability as a function of the pilot mass for different pilot SOI. The engine was operated at different loads and engine speeds.

as normally distributed, Eq.(5.18), with a standard deviation modeled as a quadratic function of the nominal misfire ratio, Eq.(5.19):

$$\mathbf{r}_m \sim \mathcal{N}(r_m, \sigma_{r_m}^2) \in [0, 1] \quad (5.18)$$

$$\sigma_{r_m} = k_{\sigma_r} r_m (r_m - 1) \quad (5.19)$$

The correlation between the misfire probability and the pilot mass is exploited in Chapter 6 for the pilot mass estimation. The model and the experimental data for its calibration are plotted in Figure 5.5. The range of validity of the pilot misfire model and its accuracy are summarized in Table 5.3:

Table 5.3: Pilot misfire model accuracy and, inputs and outputs range.

Variable	R ²	RMSE	Range
r_m	0.8824	0.15 [-]	[0, 1] [-]
σ_{r_m}	0.9672	0.0253 [-]	[0 0.4] [-]
m_{pilot}			[0, 30] mg/st
p_{SOI}			[10, 60] bar

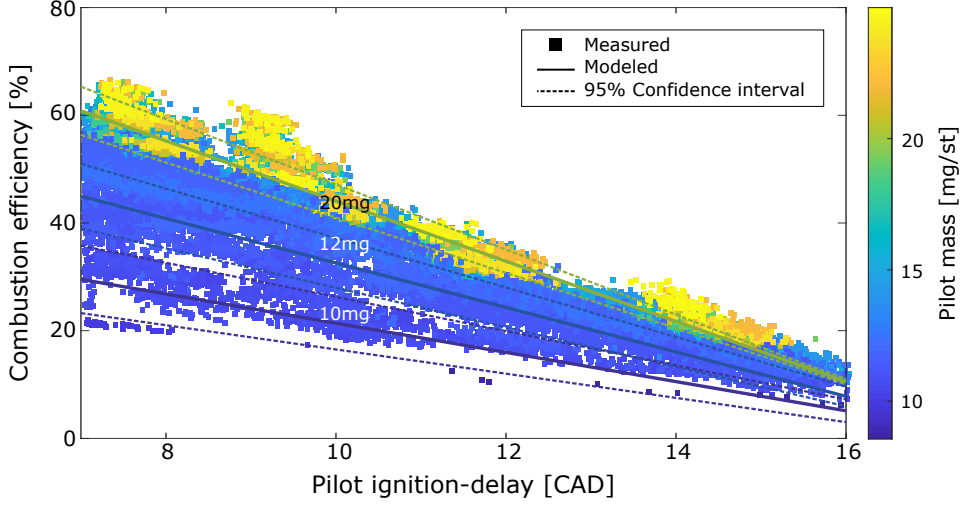


Figure 5.6: Measured and modeled pilot combustion efficiency as a function of the pilot ignition-delay for different pilot masses. The model 95% confidence interval is indicated.

Pilot combustion efficiency

The pilot mass does not burn fully during its own separate combustion, as discussed in Section 4.2.2. The combustion efficiency is described by the empirical model in Eq.(5.20), as a function of the pilot mass and ignition-delay:

$$\eta_{comb}^{pilot} = \frac{1 - k_{ID}\Delta\theta_{ID}^{pilot}}{1 + e^{-(m_{pilot} - m_0^{\eta})}} \quad (5.20)$$

The remaining unburnt fuel from the pilot combustion is added to the main fuel injection. The pilot combustion efficiency variability is modeled by a normal distribution whose standard deviation is a function of the pilot ignition-delay and pilot mass:

$$\eta_{comb}^{pilot} \sim \mathcal{N}(\eta_{comb}^{pilot}, \sigma_{\eta_{comb}^{pilot}}^2) \quad (5.21)$$

$$\sigma_{\eta_{comb}^{pilot}} = k_0^{\eta} + k_1^{\eta}\Delta\theta_{ID}^{pilot} + k_2^{\eta}m_{pilot} \quad (5.22)$$

The pilot combustion efficiency model is included in the pilot misfire detection to increase its robustness, see Section 6.4. The pilot combustion efficiency model and the experimental data for its calibration are plotted in Figure 5.6. The range of validity and the model accuracy are summarized in Table 5.4.

Table 5.4: Pilot combustion efficiency model accuracy and, inputs and outputs range.

Variable	R ²	RMSE	Range
η_{comb}^{pilot}	0.886	0.0412 [-]	[0, 1] [-]
$\sigma_{\eta_{comb}^{pilot}}$	0.6203	0.0195 [-]	[0.04 0.14] [-]
$\Delta\theta_{ID}^{pilot}$			[5, 18] <i>CAD</i>
m_{pilot}			[0, 30] <i>mg/st</i>

5.2.5 Ignition-delay

The ignition-delay in a direct-injection combustion engine depends on physical processes such as fuel atomization, vaporization and the mixing of fuel and air in the cylinder. It also depends on chemically controlled auto-ignition reactions (Heywood, 1988). To reduce the complexity and computational time in simulation, an empirical modeling approach was taken in this work. Empirical ignition-delay models are normally based in correlations following an Arrhenius expression (Assanis et al., 2003), where pressure and temperature are the parameters of greatest influence for a given fuel. A study of different ignition-delay empirical correlations is presented in (Finesso and Spessa, 2014), which the models adopted in this work are based on.

Pilot ignition-delay

The chemical mechanism is dominant for early and short pilot injections (Heywood, 1988). The pressure and temperature at the pilot SOI is only dependent on the compression stroke, which can be easily predicted by means of a polytropic evolution. Based on this discussion, the Arrhenius correlation in Eq.(5.23) was selected to predict the pilot ignition-delay for sufficient accuracy in the simulations:

$$\Delta\theta_{ID}^{pilot} = N_{eng} K_p e^{\frac{\alpha_p}{T_{SOI}}} \quad (5.23)$$

This model describes the experimental trends in Figure 4.3. A comparison of the model and its uncertainty to the measurement data is plotted in Figure 5.7. The dispersion of the model is described as a normal random variable, Eq.(5.24):

$$\Delta\theta_{ID}^{pilot} \sim \mathcal{N}(\Delta\theta_{ID}^{pilot}, \sigma_{\Delta\theta_{ID}^{pilot}}^2) \quad (5.24)$$

The standard deviation is parametrized as a function of the nominal pilot

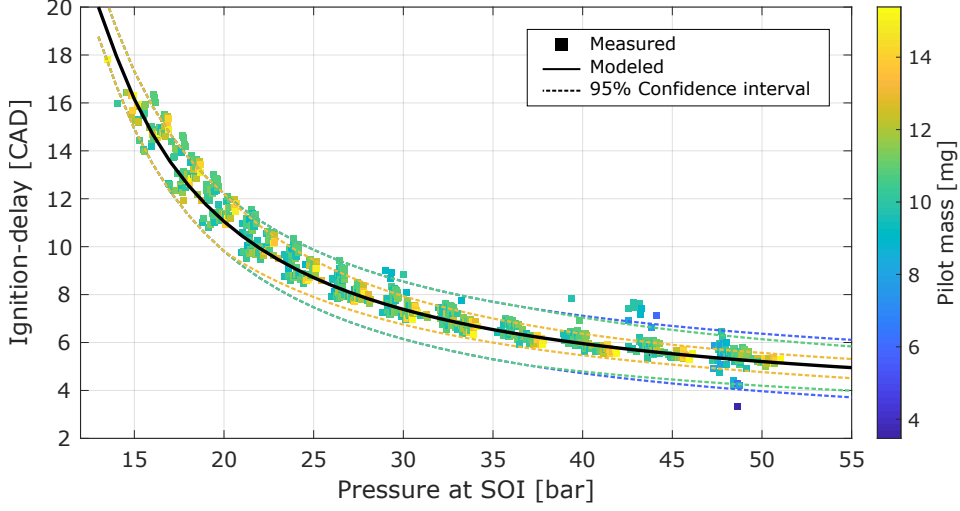


Figure 5.7: Measured and modeled pilot ignition-delay as a function of the pressure at SOI for different pilot masses. The engine was operated at 1200RPM, 1200bar rail pressure. The model uncertainty is represented by the 95% confidence interval for three pilot masses 4mg/st, 8mg/st and 12mg/st.

ignition-delay and the pilot mass by Eq.(5.25). The equation describes an exponential decay in the pilot ignition-delay dispersion as it decreases and the pilot mass increases (see Figure 5.7).

$$\sigma_{\Delta\theta_{ID}^{pilot}} = k_0^p e^{k_1^p \Delta\theta_{ID}^{pilot} + k_2^p m_{pilot}} \quad (5.25)$$

Main ignition-delay

Short ignition-delays, as the ones obtained for the main injection in a conventional Diesel engine, rely more on the physical factors (Heywood, 1988). Furthermore, the pilot combustion has a significant impact on the local temperature, pressure and oxygen concentration of the cylinder chamber when the main injection is introduced (Finesso and Spessa, 2014). Based on the discussion of the study by Finesso and Spessa (2014), a term accounting for the injected fuel and injection pressure is included, which represents the physical contribution to the ignition-delay. In this work, the model is extended to explicitly consider the pilot combustion with a binary variable δ_{comb}^{pilot} . The model is described by Eq.(5.26):

$$\Delta\theta_{ID}^{main} = N_{eng} K_m e^{\frac{\alpha m}{T_{SOI}} + \beta_m \frac{m_{inj}}{p_{rail}} + \gamma_m \delta_{comb}^{pilot}} \quad (5.26)$$

The dynamic variations in the charge thermodynamics and chemical properties

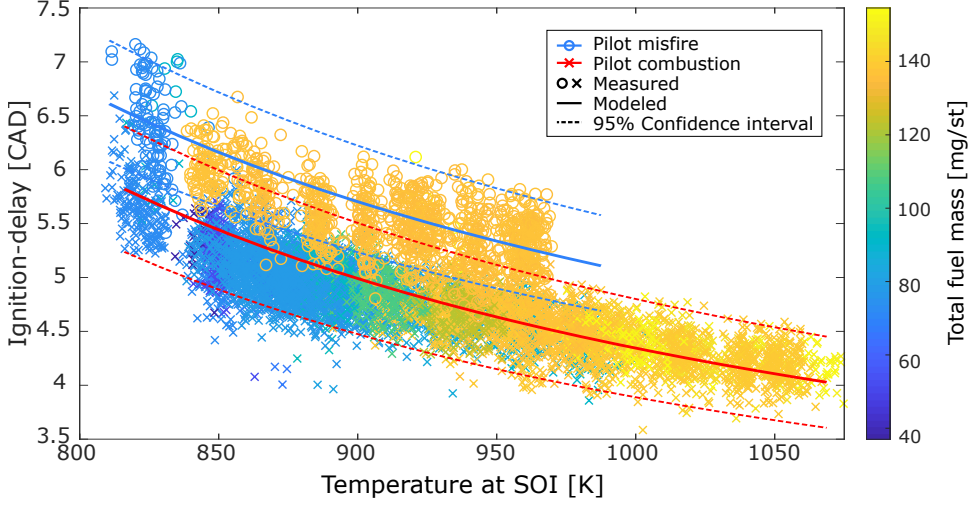


Figure 5.8: Measured and modeled main ignition-delay as a function of the temperature at SOI for different injected masses. The engine was operated at 1200RPM, 1200bar rail pressure. The model uncertainty is represented by the 95% confidence interval for the pilot combustion and misfire cases.

during the compression phase can be included following the Livengood and Wu integral criteria (Livengood and Wu, 1955). However, this increases the computation complexity. A comparison of ignition-delay models of different complexity is found in Turesson (2018), where it is concluded that the higher complexity only resulted in limited improvements on model accuracy.

The dispersion of the main ignition-delay is described as normally distributed, Eq.(5.27). The standard deviation is parametrized as a function of the pressure at SOI, the pilot-main separation and the pilot-main mass ratio, Eq.(5.28):

$$\Delta\theta_{ID}^{main} \sim \mathcal{N}(\Delta\theta_{ID}^{main}, \sigma_{\Delta\theta_{ID}^{main}}^2) \quad (5.27)$$

$$\sigma_{\Delta\theta_{ID}^{main}} = \frac{k_0^m}{p_{SOI}} + k_1^m \frac{m_{pilot}}{m_{main}} + k_2^m \Delta\theta_{pilot-main} \quad (5.28)$$

The pressure at SOI has the most significant effect, explaining up to a 60% of the total dispersion variation. The injected mass ratio has a less significant effect, depending on the operating conditions, with up to a 35% effect.

The main ignition-delay model and the experimental data for its calibration are plotted in Figure 5.8. The pilot and main ignition-delay model accuracy, with the inputs and outputs range, are summarized in Table 5.5.

Table 5.5: Pilot and main ignition-delay model accuracy and, inputs and outputs range.

Variable	R ²	RMSE	Range
$\Delta\theta_{ID}^{pilot}$	0.946	0.361 <i>CAD</i>	[4, 20] <i>CAD</i>
$\Delta\theta_{ID}^{main}$	0.671	0.329 <i>CAD</i>	[3, 8] <i>CAD</i>
$\sigma_{\Delta\theta_{ID}^{pilot}}$	0.8564	0.0025 <i>CAD</i>	[0.04 0.14] <i>CAD</i>
$\sigma_{\Delta\theta_{ID}^{main}}$	0.518	0.008 <i>CAD</i>	[0.1454, 0.257] <i>CAD</i>
T_{SOI}^{pilot}			[600 900] <i>K</i>
T_{SOI}^{main}			[800, 1100] <i>K</i>
m_{pilot}			[0, 30] <i>mg/st</i>
m_{inj}			[40, 150] <i>mg/st</i>
p_{rail}			[900, 1500] <i>bar</i>
δ_{comb}^{pilot}			(0,1) [-]

5.2.6 Heat-release rate

Modeling the fuel combustion rate from first principles is challenging due to its dependency on multiple factors, such as chemical combustion rates, fuel-injection profile and fuel-air mixing rates. A common approach is to describe the combustion in terms of the burnt mass i.e., the AHR. A Wiebe expression is widely used to describe the shape of the AHR (Heywood, 1988). However, the accuracy of a single Wiebe function is limited for the description of Diesel combustion (Miyamoto et al., 1972). Therefore some approaches used double Wiebe functions (Maroteaux et al., 2015) or multiple Wiebe function combinations (Ghojel, 2010). The major drawback is the parameters are not directly physically related, which hinders the model parametrization. A different approach is to model the combustion by the accumulated mass assumption, introduced in (Chmela and Orthaber, 1999). The combustion dynamics are described as a proportional factor of the available fuel mass at a certain instant, which can be delayed to account for intrinsic delays (Catania et al., 2011). The approach is a compromise between a physical-based description of the combustion dynamics and low complexity. The model is divided in the three phases of Diesel diffusive combustion (Arrègle et al., 2003b,a):

$$\frac{dQ_{HR}}{d\theta} = q_{prem} + q_{diff} + q_{decay} \quad (5.29)$$

Following this approach, the combustion model for the stochastic simulation was built in this work. The heat release rate for each phase is detailed in the following sections.

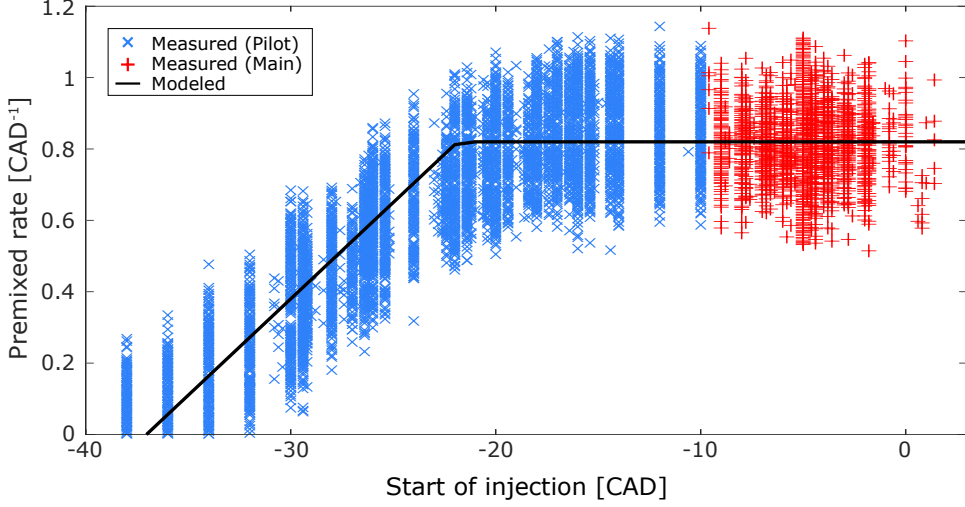


Figure 5.9: Identified and modeled premixed combustion rate gain as a function of the SOI for pilot and main injections.

Premixed combustion

The premixed combustion is modeled as an exponential decay to the fuel impulse response. In the CAD domain, the heat release shape follows Eq.(5.30), starting at the SOC:

$$q_{prem}(\theta) = q_{prem}^{max} e^{\mu_{prem}(\theta - \theta_{SOC})^2}; \quad \theta > \theta_{SOC} \quad (5.30)$$

The rate gain (μ_{prem}) regulates the premixed combustion rate. It is parametrized as a function of the SOI by Eq.(5.31), and limited to a maximum:

$$\mu_{prem} = \min(k_{\mu_0}^{prem} + k_{\mu_1}^{prem} \theta_{SOI}, \mu_{prem}^{max}) \quad (5.31)$$

It represents the correlation between the premixed rate with the fuel-air mixing as the compression advances. The rate gain is plotted in Figure 5.9 as a function of the start of injection for pilot and main injections.

The premixed combustion is scaled according to the maximum premixed heat release (q_{prem}^{max}). For the pilot injection, $q_{prem}^{max}|_{pilot}$ is indirectly determined by the premixed combustion rate (μ_{prem}), as the combustion of a small pilot completes during the premixed phase. This is satisfied when $Q_{prem}^{pilot} = Q_{fuel}^{pilot}$, where Q_{fuel}^{pilot} is the total pilot fuel burnt energy, computed from the pilot combustion efficiency by Eq.(5.20). Q_{prem}^{pilot} has to be computed by numerical integration of q_{prem} , as it has no analytical expression.

For the main injection, the maximum premixed rate is modeled as a function of the main ignition-delay and available oxygen, by Eq.(5.32):

$$q_{pre}^{max}|_{main} = \min(k_q^{prem}(m_{O_2} - m_0)e^{\Delta\theta_{ID}^{main}}, q_{pre}^{lim}) \quad (5.32)$$

The limit of the maximum premixed rate (q_{pre}^{lim}) is determined by the available fuel mass before the main SOC. This is composed by the main injection and the remaining unburnt pilot fuel. The limit on the premixed combustion rate is determined by the numerical integration of q_{pre} , which must verify:

$$Q_{pre}^{main} = Q_{fuel}|_{\theta=\theta_{SOC}^{main}}$$

where Q_{fuel} is the total available unburnt fuel before the main SOC.

The dispersion of the pilot premixed combustion is indirectly included by the dispersion model of its combustion efficiency. For the main injection, the dispersion of the premixed combustion is modeled as normally distributed:

$$q_{pre}^{max}|_{main} \sim \mathcal{N}(q_{pre}^{max}|_{main}, \sigma_{pre}^2) \quad (5.33)$$

The standard deviation is a function of the factors the main premixed combustion is sensitive to, namely the pilot combustion, main ignition-delay and main injected fuel mass:

$$\sigma_{pre} = k_{\sigma_0}^{prem} + k_{\sigma_1}^{prem} \Delta\theta_{ID}^{main} + k_{\sigma_2}^{prem} m_{main} + k_{\sigma_3}^{prem} m_{pilot}^{burnt} \quad (5.34)$$

The main measured and modeled premixed burnt mass, with its uncertainty, are plotted as a function of the main ignition-delay for different oxygen masses in Figure 5.10.

Diffusive combustion

After the premixed combustion, the fuel burns with a constant rate during the diffusive combustion, proportional to the available unburnt fuel. The available fuel increases as more fuel is injected, for a total injected fuel Q_{fuel} , and consumes as it burns during the premixed and diffusive phases, for a total burnt fuel of Q_{pre} and Q_{diff} respectively. The total fuel is computed by the integration of the injection fuel flow with the addition of the unburnt pilot mass:

$$Q_{fuel}(\theta) = Q_{pilot}(1 - \eta_{comb}^{pilot}) + \int q_{inj}^{main}(\theta) d\theta \quad (5.35)$$

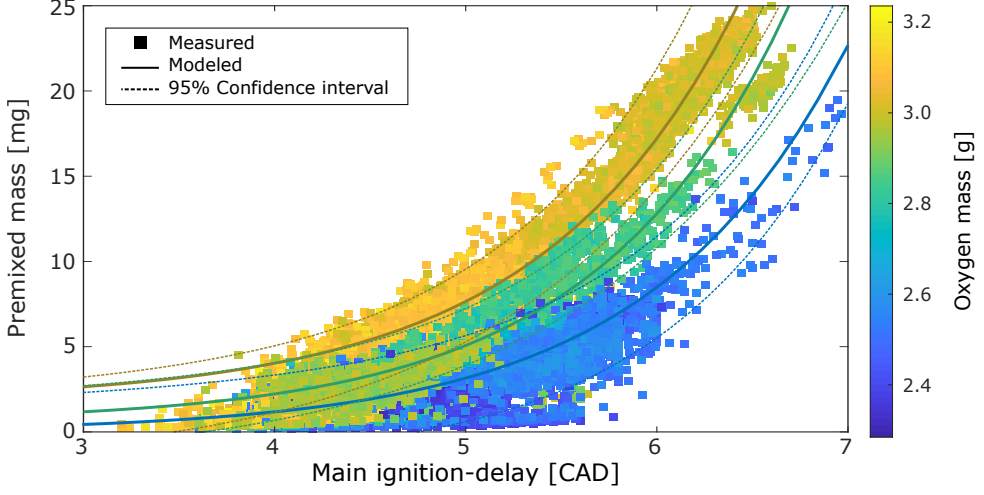


Figure 5.10: Identified and modeled main premixed burnt mass as a function of the main ignition-delay for different oxygen masses. The model 95% confidence interval is indicated.

The differential equation describing the diffusive combustion rate is:

$$q_{diff} = \mu_{diff} (Q_{fuel} - (Q_{diff} + Q_{prem})); \quad \theta_{SOC} < \theta < \theta_{EOI'} \quad (5.36)$$

The diffusive combustion rate gain is modeled as a function of the main ignition-delay:

$$\mu_{diff} = \min \left(k_{\mu_0}^{diff} + k_{\mu_1}^{diff} \Delta\theta_{ID}^{main}, \quad \mu_{diff}^{max} \right) \quad (5.37)$$

The oxygen concentration limits the maximum diffusive rate, determined by the rate gain μ_{diff}^{max} , which relates to the mixing rate of the oxidizer and reducer (see the lower plot in Figure 5.2):

$$\mu_{diff}^{max} = \frac{k_{O_2}^{diff}}{[O_2]} \quad (5.38)$$

The oxygen concentration is computed from the intake oxygen mass and air-fuel ratio as the cycle advances, proportional to the combustion progress (r_{comb}), assuming a complete combustion:

$$[O_2] = \frac{m_{O_2} (1 - \frac{r_{comb}}{\lambda})}{V(\theta)} \quad (5.39)$$

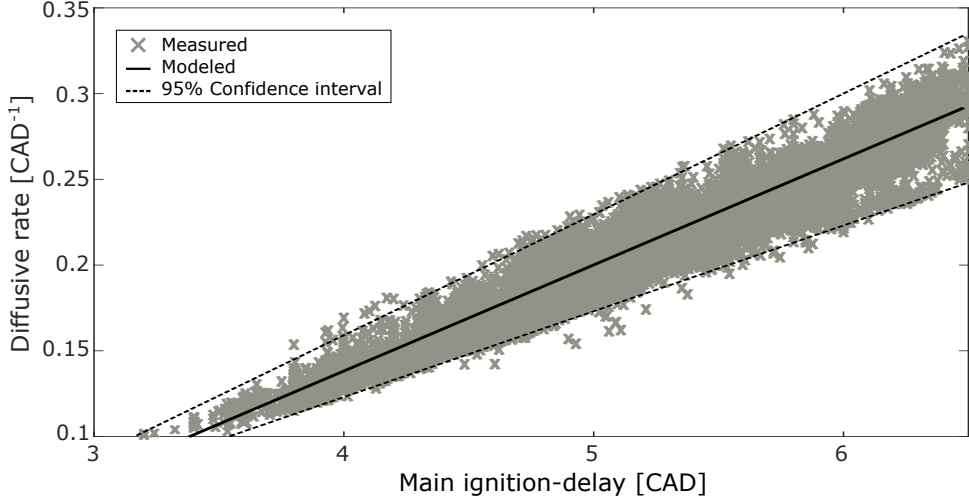


Figure 5.11: Identified and modeled diffusive combustion rate gain as a function of the main ignition-delay. The model 95% confidence interval is indicated.

The diffusive combustion is kept only while the fuel-jet is maintained, until $\theta_{EOI'}$. The ignition-delay is added to represent the time between the EOI is commanded by the electrical signal until the fuel injector closes:

$$\theta_{EOI'} = \theta_{EOI} + k_{EOI} \Delta \theta_{ID}^{main} \quad (5.40)$$

The dispersion of the diffusive combustion rate is modeled as normally distributed, with a standard deviation which is a function of the nominal diffusive rate:

$$\mu_{diff} \sim \mathcal{N}(\mu_{diff}, \sigma_{diff}^2) \quad (5.41)$$

$$\sigma_{diff} = k_{\sigma_0}^{diff} + k_{\sigma_1}^{diff} \mu_{diff} \quad (5.42)$$

The diffusive combustion rate gain and its uncertainty are plotted in Figure 5.11 as a function of the main ignition-delay.

Combustion decay

After the fuel injection ends, the remaining fuel burns with a rate proportional to the available unburnt fuel, resulting in an exponential decay. This follows an Arrhenius process where the remaining fuel finishes its combustion with a

slower rate as the mixing of fresh fuel and oxygen becomes more difficult. The differential equation describing the combustion decay is:

$$q_{decay} = \mu_{decay} (Q_{fuel} - (Q_{decay} + Q_{diff} + Q_{prem})); \quad \theta > \theta_{EOI'} \quad (5.43)$$

The combustion decay rate gain (μ_{decay}) is modeled as constant. However, due to different factors such as turbulence, the stochasticity of the mixing between fuel and air, etc. the total dispersion of the decay rate is increased. Its dispersion is hence modeled as normally distributed, with a constant standard deviation:

$$\mu_{decay} \sim \mathcal{N}(\mu_{decay}, \sigma_{decay}^2) \quad (5.44)$$

The accuracy of the heat release rate parameters, with the inputs and outputs range, are summarized in Table 5.6.

Table 5.6: Heat release rate parameters accuracy and, inputs and outputs range.

Variable	R ²	RMSE	Range
q_{prem}	0.9305	75.4 <i>J</i>	[0, 1278] <i>J</i>
μ_{prem}	0.864	0.035 <i>CAD</i> ⁻¹	[0, 0.82] <i>CAD</i> ⁻¹
μ_{diff}	0.896	0.0252 <i>CAD</i> ⁻¹	[0.1, 0.35] <i>CAD</i> ⁻¹
μ_{decay}	0.964	0.0212 <i>CAD</i> ⁻¹	[0.098, 0.111] <i>CAD</i> ⁻¹
σ_{prem}	0.57	11.19 <i>J</i>	[22.05, 51.41] <i>J</i>
σ_{diff}	0.8876	0.002 <i>CAD</i> ⁻¹	[0.0053, 0.0216] <i>CAD</i> ⁻¹
σ_{decay}	0.845	0.0018 <i>CAD</i> ⁻¹	[0.0091, 0.0106] <i>CAD</i> ⁻¹
T_{SOI}^{pilot}			[600 900] <i>K</i>
T_{SOI}^{main}			[800, 1100] <i>K</i>
m_{pilot}			[0, 30] <i>mg/st</i>
m_{inj}			[40, 150] <i>mg/st</i>
m_{O_2}			[2.3, 3.3] <i>g</i>
θ_{SOI}			[-40, 10] <i>mg/st</i>
$\Delta\theta_{ID}^{main}$			[3, 8] <i>CAD</i>

5.2.7 In-cylinder pressure

The in-cylinder pressure is computed as a single-zone, following the same approach as the heat release in Eq.(2.15):

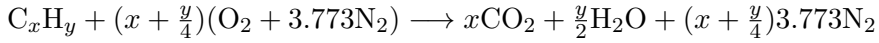
$$\frac{dp}{d\theta} = -\frac{\gamma}{V} p \frac{dV}{d\theta} + \frac{\gamma - 1}{V} \left(\frac{dQ_{HR}}{d\theta} - \frac{dQ_{HT}}{d\theta} \right) \quad (5.45)$$

Cylinder volume

The cylinder volume was estimated by the method described later in Section 6.1.

Specific heat ratio

The ratio of specific heats $\gamma = c_p/c_v$ was computed with the NASA specific heat polynomials as a function of the cylinder gas composition and temperature. The gas composition was interpolated between the unburnt and burnt gas compositions during combustion, using the computed heat release rate, EGR ratio and the stoichiometry of the overall chemical reaction:



The average chemical formula for conventional Diesel fuel is $C_{12}H_{24}$, ranging approximately from $C_{10}H_{20}$ to $C_{15}H_{28}$ (Heywood, 1988). The hydrogen to carbon ratio is therefore about $y = 1.86x$.

Heat transfer

The heat transfer (dQ_{HT}) is computed by Newton's law of cooling, adjusted for its CAD resolution:

$$dQ_{HT} = h_{HT}A(T_{cyl} - T_{wall}) \quad (5.46)$$

The heat transfer coefficient is calculated by the Woschni model in Eq.(2.16), described in Section 2.5.3.

5.3 Predictive Models

The previous models for simulation may not meet the requirements for on-line implementation and execution, see Chapter 11. The models have to be predictive, of low implementation and evaluation complexity, and locally accurate around the nominal operating conditions where the engine is to be regulated. To meet these requirements, the approach taken in this work was to select simple mathematical models, fast to compute and uncomplicated to implement in the FPGA. High accuracy is obtained by the on-line adaptation of the parameters. The model structure used for on-line prediction is described in detail in the

following subsections. The model structure is designed considering the requirements of the linear adaptation algorithms used. This is discussed in Chapter 7, where the prediction accuracy of the models is also addressed.

5.3.1 Ignition-delay

The in-cylinder temperature is an input to the ignition-delay models. However, the in-cylinder temperature is not measured directly and it has to be estimated. The temperature estimation is sensitive to the initial state estimation (total trapped mass, temperature, etc.). This results in higher sensitivity and larger error for the ignition-delay predictions. Therefore, the models are modified by using instead the available measured in-cylinder pressure as an input:

$$\Delta\theta_{ID}^{pilot} = N_{eng} K_p e^{\alpha_p p_{SOI}} \quad (5.47)$$

$$\Delta\theta_{ID}^{main} = N_{eng} K_m e^{\alpha_m p_{SOI} + \beta_m \frac{m_{inj}}{p_{rail}} + \gamma_m \delta_{comb}^{pilot}} \quad (5.48)$$

This permits a faster computation and simpler adaptation of the models. For their adaptation, the equations can be formulated as linear by taking logarithms, which eases the adaptation method.

5.3.2 Injected fuel mass

The implementation of look-up tables complicates the individual cylinder adaptation for each injector. For the region of large injection on-times, over $0.5ms$, the injector characteristics was approximated by Eq.(5.49):

$$m_{inj}^{main} = m_0^{main} + a_m t_{inj} (1 + b_m p_{rail}) \quad (5.49)$$

Despite the non-linearities of the model, it can be formulated for its linear on-line adaptation (discussed in Section 7.2). For the model adaptation, the fuel mass is estimated cycle-by-cycle from the accumulated heat release (Finesso and Spessa, 2015). The unburnt pilot mass that burns together with the main injection combustion is first subtracted. The lower region of the injector on-time is modeled together with the pilot combustion efficiency.

5.3.3 Pilot burnt mass

The pilot burnt mass has to be computed from the injected pilot mass and its combustion efficiency. To avoid the adaptation of two highly non-linear models, an experimental model, combining both of them, was proved to be suitable for in-cycle predictions and on-line adaptation:

$$m_{pilot}^{burnt} = m_0^{pilot} + a_p t_{inj} \left(1 + b_p p_{rail} + c_p (\Delta\theta_{ID}^{pilot})^2 \right) \quad (5.50)$$

The expression includes two main factors. The first is the fuel injection, represented by the on-time (t_{inj}) and rail pressure (p_{rail}). The second factor is the combustion efficiency, which relates to the ignition-delay ($\Delta\theta_{ID}^{pilot}$). From the experimental results in Section 4.2.2, the longer the ignition-delay, the smaller the pilot fuel mass burnt.

5.3.4 Main premixed mass

The main premixed heat release peak was computed for on-line feedback of the in-cycle control algorithms. The previous method in Eq.(5.32) requires the estimation of the oxygen mass. To reduce the sensitivity to estimation errors, the main premixed peak is computed as a function of the main ignition-delay and burnt pilot mass, by Eq.(5.51). These variables can be measured in real-time as the combustion evolves, enabling in-cycle feedback control.

$$HR_{prem}^{main} = HR_0 + \Delta\theta_{ID}^{main} (k_1 + k_2 m_{pilot}^{burnt}) + k_3 (m_{pilot}^{burnt} - m_0)^2 \quad (5.51)$$

5.3.5 In-cylinder pressure

The prediction of the in-cylinder pressure at pilot SOI and main SOI is required for the computation of the ignition-delays. The pressure increase by the polytropic compression and the pilot combustion requires simplifications for its implementation in the FPGA, described below.

Polytropic compression

The NASA polynomials require large resources for their implementation in the FPGA. Furthermore, the pressure has to be integrated iteratively, which enlarges the FPGA resources and computational lag. Instead, the compression is

computed by a polytropic process with a constant equivalent polytropic coefficient. The assumptions are a constant heat capacity ratio, and the ideal gas behavior of the bulk mass inside the combustion chamber:

$$pV^\kappa = p_0V_0^\kappa \quad (5.52)$$

The initial state is selected where the assumptions hold. A good trade-off between an early reference point while having a low variation of the polytropic coefficient was found at -40CAD. The polytropic coefficient is updated on-line to improve the pressure prediction as more pressure measurements are obtained, discussed in Section 6.2.

Isochoric combustion

For the computation of the pressure at the main SOI, the pressure rise from the pilot combustion is modeled as an instantaneous isochoric pressure rise:

$$\Delta p = \frac{\kappa - 1}{V} m_{pilot}^{burnt} Q_{LHV} \quad (5.53)$$

5.3.6 Engine load

The engine load, quantified by the IMEP, is predicted by a simple linear model:

$$IMEP = IMEP_0 + k_m \cdot m_{main} + k_p \cdot p_{inlet} + k_{bp} \cdot m_{pilot}^{burnt} \quad (5.54)$$

5.4 Model Calibration

The model parameters were identified by the minimization of a sum-of-squares model-error cost function $J(f_M, \vartheta)$ over the total number of cycles N , where f_M is the measured output and ϑ is the parameter set:

$$J(f_M, \vartheta) = \sum_{i=1}^N (f_M^i - f^i(\vartheta))^2 \quad (5.55)$$

The parameters of the ignition-delay models were first fitted for all the cycles altogether. By taking logarithms, the problem becomes a linear regression.

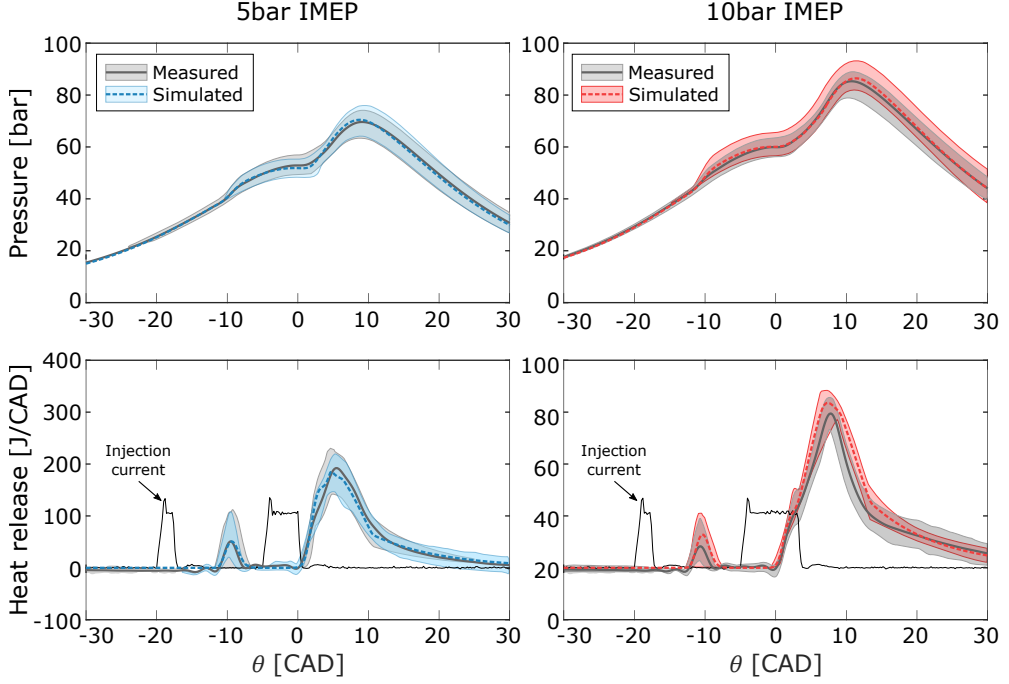


Figure 5.12: Simulated in-cylinder pressure (upper plot), injection current and heat release (lower plot) at 5bar (left) and 10bar IMEP (right), 1200RPM , -20CAD SOI and 10mg pilot, -5CAD main SOI. The measured data (greys) and simulated data (red and blue) are compared. The area represents the range of the cycle-to-cycle variation minimum and maximum values.

For the intake pressure model in Eq.(5.5) and the combustion rate parameters in Eq.(5.30)-(5.43), each cycle must be fitted individually, so the stochastic parameters can be calibrated as well, including the interdependency and cross-correlation of the combustion parameters. For each cycle, the model-error cost function was computed as a weighted average of the sum-of-squares of the pressure (α_P) and heat release (α_{HR}) traces between IVC and EVO:

$$J(f_M, \vartheta) = \sum_{\theta_{IVC}}^{\theta_{EVO}} (\alpha_P(p_{cyl}(\theta) - p_{mod}(\vartheta, \theta))^2 + \alpha_{HR}(Q(\theta) - Q_{mod}(\vartheta, \theta))^2) \quad (5.56)$$

The parametrization of the combustion rate is then fitted minimizing the cost function of Eq.(5.55) for all the identified cycles. The model parameter identification for each cycle permits to calculate the total dispersion of the parameters. The dispersion is parametrized by the models of the standard deviation of the normal distributions. The same sum-of-squares criteria was used for the parametrization of the normal distribution models.

The model was calibrated from the data of Publication I and II, which covered a wide range of operating conditions. An example of the model ability to describe the combustion process and its cyclic dispersion is illustrated in Figure 5.12 for 5bar and 10bar IMEP and 100 measured cycles over the six cylinders.

5.4.1 Model validation

A combination of engine loads, engine speeds, rail pressures, injection timings and pilot masses were used to simulate and validate the model against experimental data outside the calibration points. The test points are summarized in Table 5.7:

Table 5.7: Test points for the model validation.

Test point	Engine load (IMEP) [bar]	Engine speed[RPM]	Rail pressure[bar]	Main SOI [CAD]	Pilot SOI [CAD]	Pilot mass[mg/st]
#1	10	1200	1200	-2	-12	10
#2	10	1200	1200	-7	-17	10
#3	10	1200	1200	-12	-22	10
#4	10	1200	1200	-7	-18	5
#5	15	1200	1500	-5	-15	10
#6	12.5	1200	1350	-5	-15	12
#7	10	1500	1200	-10	-20	10
#8	10	900	1200	-7	-12	15
#9	7.5	1200	900	-2	-6	9
#10	5	1200	1200	-9	-20	14
#11	5	1200	1200	-10	-18	14
#12	2.5	1200	1200	-3	-14	9

The validation results are plotted in Figure 5.13. The simulation model was validated by studying the accuracy of the combustion metrics relevant for the closed-loop combustion control. These are, the pilot and main start of combustion, pilot burnt mass, center of combustion (CA50), engine load, maximum pressure, maximum pressure rise rate and exhaust temperature. The input variables were averaged from the experimental data. The dispersion of the experimental data was computed over 100 cycles and all six cylinders. The simulation model was run 500 iterations.

From the results in Figure 5.13, the average error and the dispersion present similar trends as the experimental data, with a reduced error of the relevant operating variables.

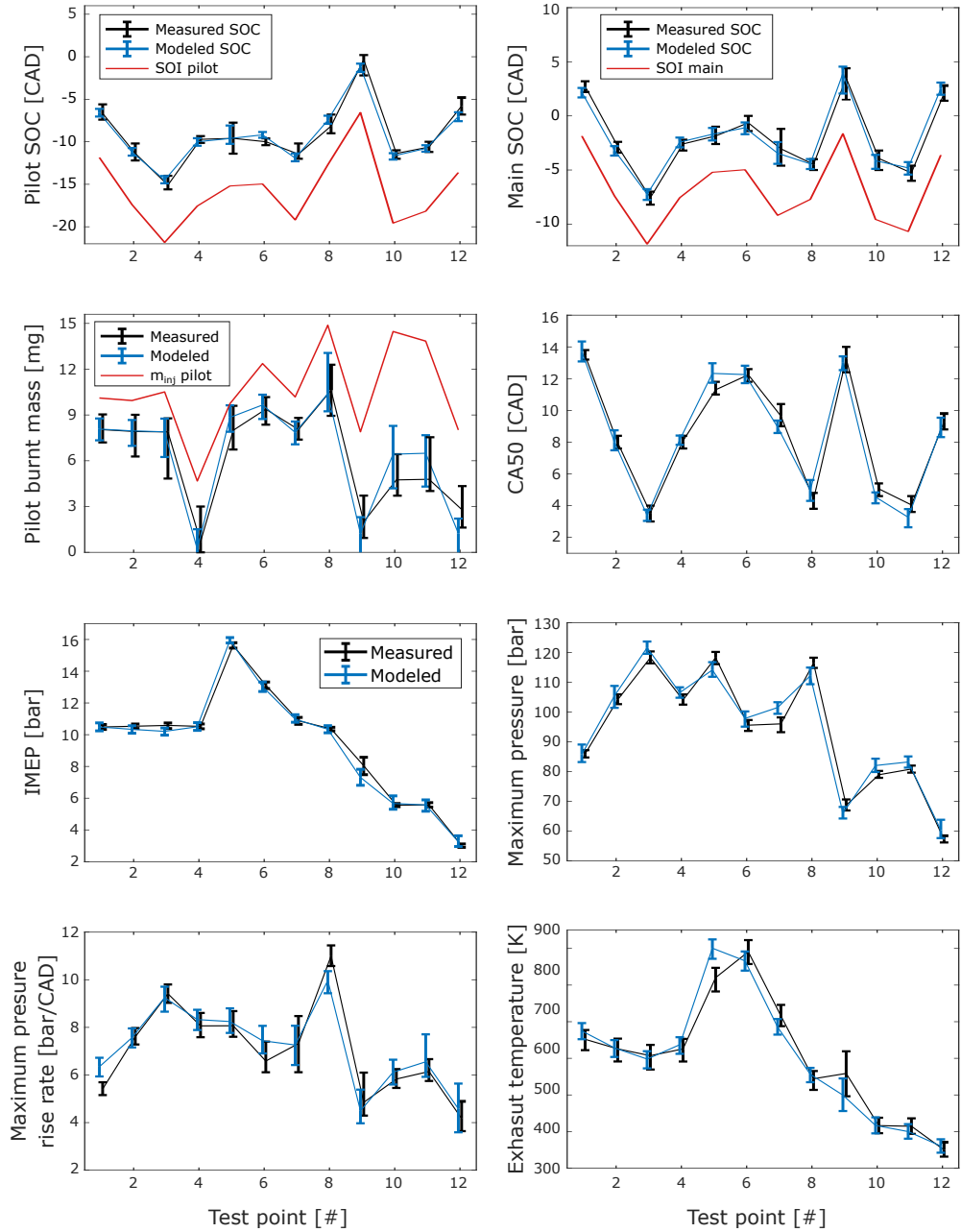


Figure 5.13: Combustion model validation at the test points of Table 5.7. The average and 95% confidence interval of the data dispersion are indicated. The relevant combustion parameters are plotted.

Estimation Methods

This chapter presents the estimation methods used to monitor the progress of the combustion and provide feedback to the in-cycle controller. The cylinder volume estimation accounting for thermal, pressure and mass forces permits to increase the accuracy of the heat release analysis, which is the basis for the rest of the estimation methods. The heat capacity ratio is estimated in-cycle for an accurate pressure prediction. The estimation methods focus on monitoring the progress of the pilot combustion. To determine the pilot combustion, different detector designs for pilot misfire are compared. The start of combustion is detected by an in-cycle model-based method for its early identification. During the pilot combustion, an algorithm for an early in-cycle pilot mass estimation is proposed. Finally, the correlation between the pilot mass and misfire ratio is exploited to increase the pilot mass estimation accuracy for short pilot on-times.

6.1 Cylinder Volume Estimation

During engine operation, the components surrounding the combustion chamber are exposed to thermal forces, pressure forces, and mass forces from the reciprocating components. Due to these forces, the components will deform and the volume of the combustion chamber will deviate from its ideal volume. A com-

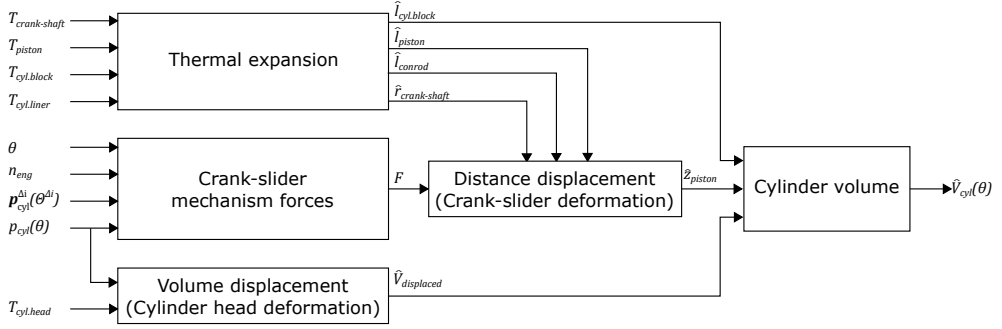


Figure 6.1: Flow-chart diagram of the computational blocks of the method to estimate the volume deformation.

mon assumption is to model the cylinder volume as the nominal, calculated by the geometrical relations of the engine components. However, heat release analysis is sensitive to cylinder volume errors. Based on detailed CFD simulations, a method to estimate the cylinder volume during engine operation was developed in Publication VI. The model for the calculation of the cylinder volume is based on linear approximations of the simulation results.

The model includes deviations from static and dynamic deformations. The summary of the method is in Figure 6.1. The inputs to the model are the crank angle, the engine speed, the in-cylinder pressure and the temperatures. The respective pressures from the cylinders have to be expressed relative to the current cylinder CAD (θ). This is computed using the cylinder offsets, to obtain the absolute CAD for each of the cylinders (Θ^{Δ_i}). A summary of the model is given in this section.

6.1.1 Thermal expansion

The thermal expansions are calculated with the average temperatures of the crankshaft, cylinder block and piston. The lengths are calculated analytically as a one-dimensional free thermal expansion:

$$\epsilon = \alpha \Delta T \quad (6.1)$$

where $\epsilon = \frac{l-l_0}{l_0}$ is the non-dimensional normal strain. The normalized strain is proportional to the coefficient of linear thermal expansion α and temperature difference. The thermal expansion coefficient is a material constant. The initial length is measured at the initial temperature, $20^\circ C$ in this study. It is assumed that the radial clearances will not be affected by the thermal expansion.

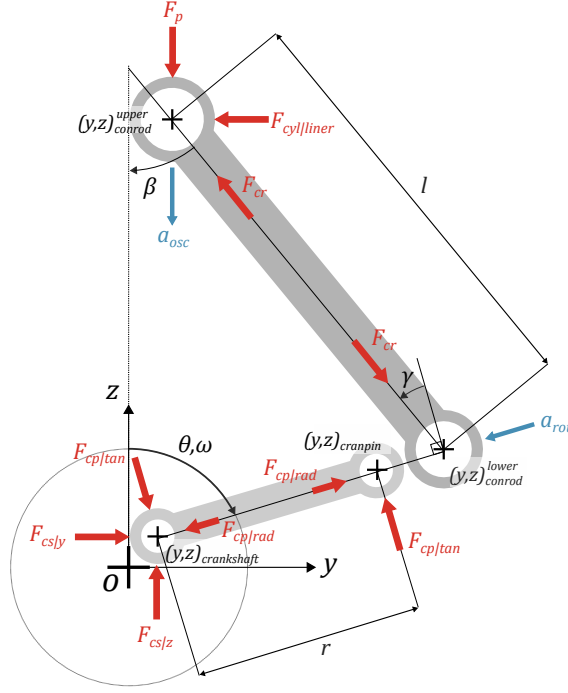


Figure 6.2: Free body diagram of the forces acting on the crank-slider mechanism and notation of coordinates.

The lengths considered are the cylinder block, the crankpin, the connecting rod and the piston. The temperature to compute the thermal expansion of the connecting rod is approximated as the temperature of the crankshaft. For the cylinder liner, the volume is calculated approximately by the radial expansion from the free thermal strain in Eq.(6.1).

6.1.2 Acting forces on the crankshaft mechanism

The forces acting on the crankshaft mechanism are illustrated in Figure 6.2. Based on the crank angle, engine speed and cylinder pressure, the forces and accelerations are calculated. From the angular velocity $\omega = N_{eng} \frac{2\pi}{60}$, the acceleration due to the oscillation bodies in the crankshaft (a_{osc}) and the rotational acceleration (a_{rot}) are:

$$a_{osc} = -r \left(\omega^2 \cos(\theta) + \frac{r}{l} \omega^2 \cos(2\theta) \right) \quad (6.2)$$

$$a_{rot} = -r\omega^2 \quad (6.3)$$

The oscillation and rotational forces are:

$$F_{osc} = m_{osc}a_{osc} \quad (6.4)$$

$$F_{rot} = m_{rot}a_{rot} \quad (6.5)$$

The force on the piston due to the in-cylinder pressure acting on the piston area (A_p) is:

$$F_p = p_{cyl}A_p \quad (6.6)$$

The force on the conrod (abbreviated cr) and its components are:

$$F_{cr|z} = F_{osc} - F_p \quad (6.7)$$

$$F_{cr} = F_{cr|z} \cos^{-1}(\beta) \quad (6.8)$$

$$F_{cr|y} = F_{cr} \sin(\gamma) \quad (6.9)$$

The radial and tangential forces on the crankpin (abbreviated cp) are:

$$F_{cp|rad} = F_{rot} + F_{cr} \sin(\gamma) \quad (6.10)$$

$$F_{cp|tan} = F_{cr} \cos(\gamma) \quad (6.11)$$

Finally, the force components on the crankshaft (abbreviated cs) are:

$$F_{cs|z} = F_{cp|tan} (\cos(\theta) + \sin(\theta)) \quad (6.12)$$

$$F_{cs|y} = F_{cp|tan} (\cos(\theta) - \sin(\theta)) \quad (6.13)$$

6.1.3 Crank-shaft linear deformation

The previous forces are computed to calculate the strain and bending deformations. The components of the crank-slider mechanism have an irregular cross section area. The Hooke's law of normal strain cannot be directly applied based on the modulus of elasticity. Based on the meshed simulations of the actual

geometries, the strain of each component i is modeled as proportional to the force action on that component by a calibrated constant C :

$$\epsilon_i = C_i \times F_i \quad (6.14)$$

For the bending deformation w , the small deflection angle δ is approximated as $\delta \approx \sin(\delta) = \frac{w}{l}$. With this approximation, the angular bending for each component i is calculated proportional to a calibrated constant R :

$$\delta_i = R_i \times F_i \quad (6.15)$$

The force and bending constants C and R are calibrated individually for each component. The calculation of the linear and bending deformations for each of the components are detailed below.

Crankpin

The strain and bending of the crankpin are:

$$\epsilon_{cp} = C_{cp|rad} F_{cp|rad} \quad (6.16)$$

$$\delta_{cp} = R_{cp|tan} F_{cp|tan}^{res} \quad (6.17)$$

The resultant tangential force F^{res} after adding the influence of the other cylinders is computed as:

$$F_{cp|tan}^{res} = F_{cp|tan} + \sum_{i_{cyl}=1}^{n_{cyl}} K^{i_{cyl}} F_{cp|tan}^{i_{cyl}} \quad (6.18)$$

The tangential force of the other cylinders $F_{cp|tan}^{i_{cyl}}$ is calculated with the angular offset, relative to the current cylinder. $K^{i_{cyl}}$ is a factor determining the influence of each of the other cylinders on the resultant tangential force.

Connecting rod

The horizontal displacement of the top of the connecting rod is linearly related to the force in the horizontal direction:

$$\Delta y_{cr} = C_{cr,top|y} F_{cr|y} \quad (6.19)$$

Radial bearings

The radial bearings (abbreviated b) are modeled as a free movement of the shaft. The relative movement of the connection between the crankshaft with the cylinder block, and the crankshaft with the connecting rod, are in the vertical and horizontal directions:

$$\Delta z_b = \frac{F_z}{F_{tot}} \mu_b \quad (6.20)$$

$$\Delta y = \frac{F_y}{F_{tot}} \mu_b \quad (6.21)$$

where F_{tot} is the total force acting on the shaft and (F_z, F_y) its vertical and horizontal components. μ_b is the radial clearance for the main bearing. The oil film behavior is neglected to avoid non-linear mathematical representation of the model, which would be time consuming to solve. The force direction has influence on the displacement of the shaft, but not its magnitude.

Vertical piston position

The vertical piston position is calculated including the deformation of the connecting rod and crankpin, together with the radial clearances. For the crankshaft, the coordinates are:

$$(y, z)_{cs} = -\frac{\mu_b}{F_{cs}} (F_{cs|y}, F_{cs|z}) \quad (6.22)$$

For the crankpin, the coordinates are:

$$(y, z)_{cp} = (y, z)_{cs} + r (\sin(\theta + \delta_{cp|tan}), \cos(\theta + \delta_{cp|tan})) \quad (6.23)$$

where the crankshaft radius and deflection are:

$$r = r_0 + r_0 F_{cp|rad} C_{cp|rad} \quad (6.24)$$

$$\delta_{cp|tan} = r_0 + r_0 F_{cp|rad} R_{cp|rad} \quad (6.25)$$

The lower position of the conrod is:

$$(y, z)_{cr}^{lower} = (y, z)_{cp} - \frac{\mu_b}{F_{cr}} (F_{cr|y}, F_{cr|z}) \quad (6.26)$$

The conrod length is:

$$l = l_0 + l_0 F_{cr} C_{cr} \quad (6.27)$$

Finally, the upper position of the conrod is computed as:

$$y_{cr}^{upper} = F_{cr|y} C_{cr,top|y} \quad (6.28)$$

$$z_{cr}^{upper} = z_{cr}^{lower} + \sqrt{l^2 - (y_{cr}^{upper} - y_{cr}^{lower})^2} \quad (6.29)$$

6.1.4 Cylinder head volumetric deformation

The cylinder head deforms and bulges upwards due to the high in-cylinder pressures during combustion. The change in the cylinder volume is modeled proportional to the cylinder pressure:

$$\Delta V_{head|p} = C_{disp|p} p_{cyl} \quad (6.30)$$

The volume change due to the thermal deformation of the cylinder head is modeled as proportional to the temperature difference, by a calibrated constant to fit the simulations:

$$\Delta V_{head|T} = C_{disp|T} \Delta T_{cyl} \quad (6.31)$$

The temperature difference is computed between the mean cylinder head temperature and the reference temperature at zero deformation.

6.1.5 Cylinder volume estimation

The final cylinder volume is estimated with the corrected dimensions of the crank-slider mechanism and radial expansion of the cylinder liner in Eq.(2.4), and corrected with the displaced cylinder volume in the cylinder head.

6.1.6 Simulation results

The approximations taken for the analytical volume correction in the linear model were fitted and compared to simulation results computed by a fine-mesh CFD and FEM model, see Publication VI for details on modeling and simulation analysis. The absolute and relative volume deformation are plotted in Figure 6.3 for different relative engine loads.

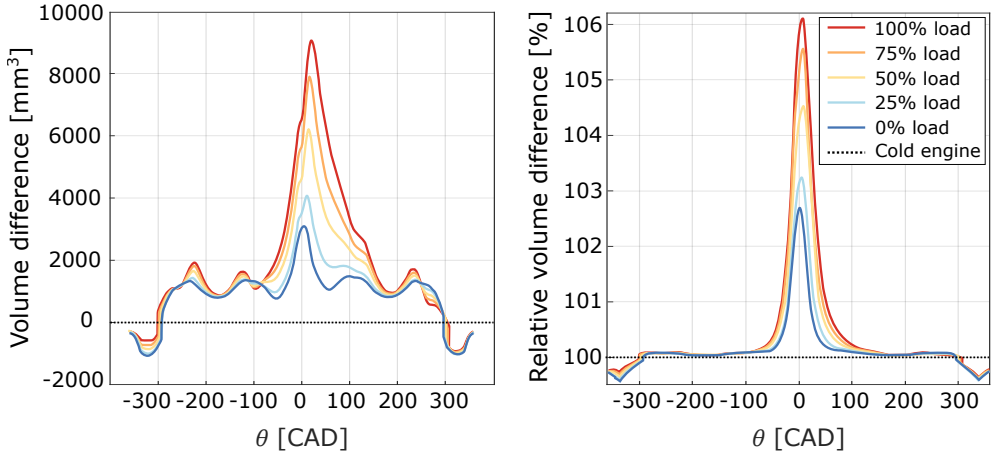


Figure 6.3: Absolute (left) and relative (right) volume displacement for different loads. The loads are expressed relative to the maximum engine brake torque. The engine speed is 1200RPM. The volume difference is expressed relative to the cold engine volume.

Due to static distortion and dynamic deformation, the cylinder volume may deviate up to 6% around TDC. For the cold engine, the deformation of the connecting rod and its horizontal displacement are the largest contribution to the total volume difference. The volume difference decreases as the engine becomes warmer, as deformations due to mass and pressure forces are counteracted by the thermal expansions. By the volume estimation with the proposed method, the error can be reduced below 0.4%. The mechanical tolerances will define the final tolerance of the model. Errors in the volume calculation caused by errors in the in-parameters and errors between the model and the simulations are small compared to the mechanical tolerances.

The computation error of the AHR using the volume estimation method is reduced between 0.5% and 5%, which will increase the estimated thermodynamic efficiency. The heat release metrics (CA_x) error was reduced between 0.0 to $-1CAD$ for CA10, -0.3 to $-1.25CAD$ for CA50 and -2.5 to $-4.25CAD$ for CA90, with an increasing error trend as the load increases. See Publication VI for more details.

6.2 Specific Heat Ratio Estimation

The heat capacity ratio (γ) is estimated for the in-cylinder pressure prediction as an adiabatic process by a polytropic compression. The NASA polynomials used for the off-line computations demand memory resources of the FPGA

for their storage and computation resources for the recursive calculation of the pressure. The simplest approach for the in-cycle pressure prediction is to consider γ as constant (Wilhelmsson et al., 2006). A more accurate approach is to model the polytropic coefficient as a linear function of the in-cylinder temperature (Gatowski et al., 1984). However, the in-cylinder temperature has to be estimated, adding further computations.

A different approach is to identify the exponent during the adiabatic compression (Tunestål, 2009a). The assumption neglects heat or mass energy flows, which is compensated by the adjustment of the exponent. This results in an exponent no longer equal to the heats ratio γ , hence the denotation is changed to κ . For the estimation of κ during the combustion, it is approximated by a linear interpolation between its value before and after the combustion. The identification problem is solved by Newton method for non-linear least squares estimation. This limits its application for real-time computations in the FPGA.

In Zander (2011), the proposed solution to overcome these limitations is to reformulate the estimation problem by assuming an adiabatic compression. The heat release is zero, and Eq.(2.15) is modified for the estimation of κ . The pressure derivative can be evaluated by the logarithm of the pressure, which avoids division, and approximated by a second order Taylor expansion. The drawback of this approach is the pressure measurement noise, which propagates to the estimation of κ and the pressure prediction. The instantaneous computation of the heat release is not significantly sensitive to these errors. However, for the pressure prediction, the uncertainty of κ reduces the prediction accuracy significantly. The approach taken in this work is a recursive estimation of an equivalent κ exponent, assuming an adiabatic compression from a constant initial pressure-volume state:

$$p_i V_i^{\hat{\kappa}_i} = p_0 V_0^{\hat{\kappa}_i} \quad (6.32)$$

The constant initial state reduces the propagation of the pressure noise to the pressure prediction. The assumptions are a constant heat capacity ratio, and the ideal gas behavior of the bulk mass inside the combustion chamber. The polytropic coefficient is estimated by recursive least-squares minimization of one-step ahead pressure prediction. By taking logarithms in Eq.(6.32):

$$\log p_i = \kappa_i (\log V_0 - \log V_i) + \log p_0 \quad (6.33)$$

From the logarithmic pressure evolution ($Y_i = \log p_i - \log p_0$), the one-step ahead prediction is:

$$\hat{Y}_i = \hat{\kappa}_{i-1} (\log V_0 - \log V_i) \quad (6.34)$$

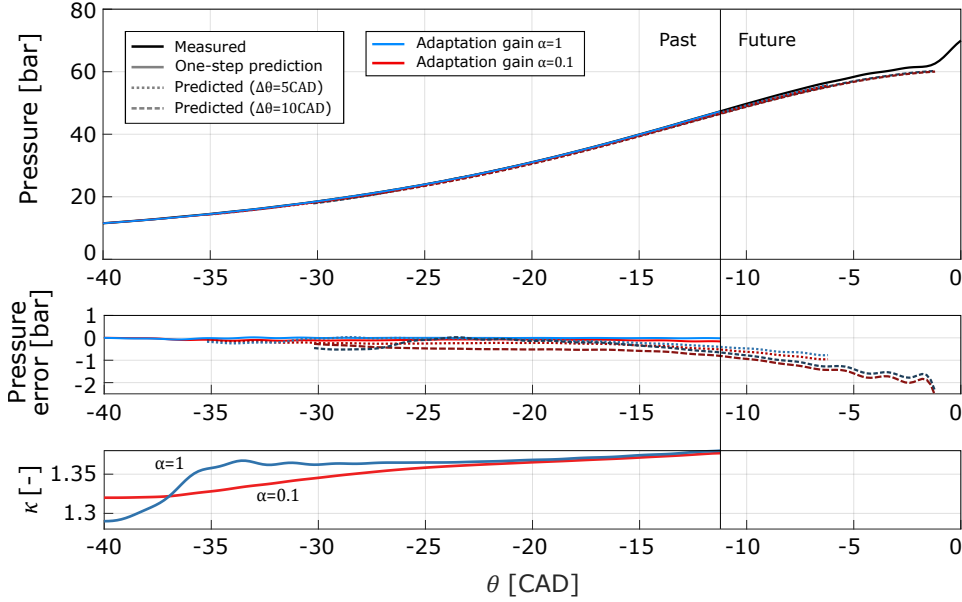


Figure 6.4: Measured and predicted in-cylinder pressure (upper plot), prediction error (middle plot) and equivalent estimated heat ratio (lower plot) for different prediction steps (single-step, 5CAD and 10CAD), with a correction factor of $\alpha = 0.1$ and $\alpha = 1$ and initial guesses of $\kappa_0 = 1.32$ and $\kappa_0 = 1.28$, respectively.

The least-square error minimization for this problem formulation results in a linear recursion. The correction step uses a factor α , which is calibrated as a trade-off between convergence speed and prediction accuracy:

$$\hat{\kappa}_{i+1} = \hat{\kappa}_i + \alpha(Y_i - \hat{Y}_i) \quad (6.35)$$

For the assumptions to be valid, the initial state has to be calibrated and the prediction range limited. A good trade-off for the initial state at an early reference with low variability of the polytropic coefficient was established at $-40CAD$. To speed the estimation convergence and reduce the pressure prediction error, the previous cycle's value of κ can improve the accuracy of the initial guess.

An example of the equivalent κ estimation and the pressure prediction is plotted in Figure 6.4 for different correction factors (α) and initial guesses (κ_0). A larger correction step reduces the convergence time of the estimation despite a large initial error. However, too large values of α may result in oscillations. The one-step prediction error is under $\pm 0.1bar$. Further predictions result in an increased error. For a large correction factor, the prediction error can be kept under $\pm 0.2bar$. The largest error (of about $1.5bar$) is around TDC, when the fuel combustion starts and the estimation assumptions are not valid.

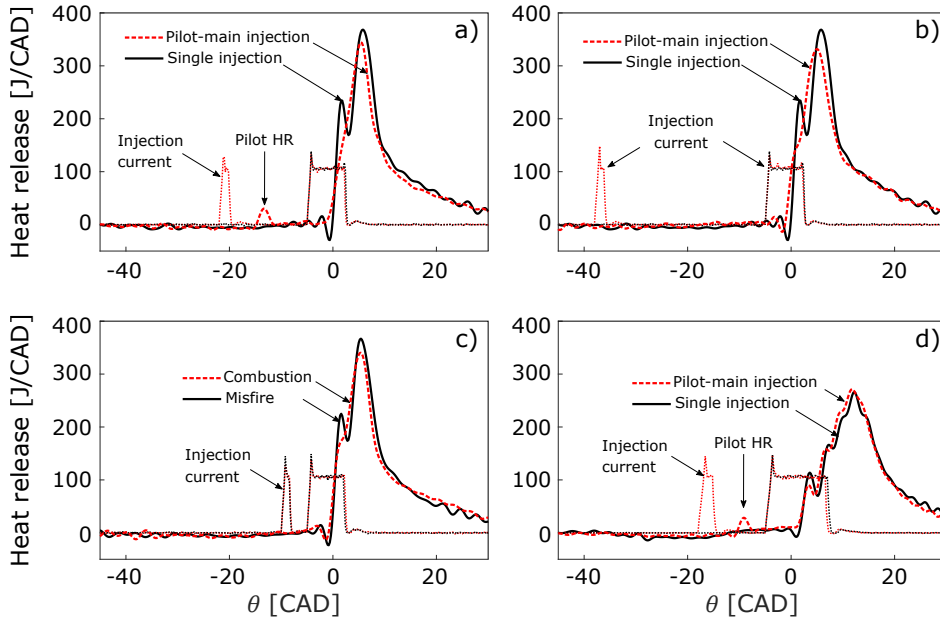


Figure 6.5: Comparison of the heat release between fire and misfire cases. The regular case of pilot combustion is compared to single main injection in the upper left plot (a). In the upper right plot (b), the single injection is compared to the reduction of the premixed peak of the main heat release despite the lack of pilot apparent combustion from the heat release signal. The lower left plot (c) shows when similar pilot heat release has different misfire classification. In the lower right plot (d), the effect of high engine speeds (1600RPM) is illustrated for a single injection (black) and pilot-main injection (red). The oscillations on the heat release rate due to the higher turbulence and faster signal sampling result in a smaller difference on the premixed peak of the main heat release rate for the fire and misfire cases.

6.3 Pilot Misfire Detection

From the definition of pilot misfire given in Section 4.2.1, the in-cycle pilot misfire detector can be understood as a predictor stating if a reduction in the premixed peak of the main combustion will be obtained based on the measured pilot combustion. An example of the challenges for detecting pilot misfire with this definition is illustrated in Figure 6.5.

Previous work based the misfire diagnosis on measurement signals already available on production engines, such as the instantaneous engine speed (Kiencke, 1997; Connolly and Rizzoni, 1994; Eriksson et al., 2013), knock sensor (Lindemann and Filbert, 2002; Chang et al., 2002), accelerometers (Singh et al., 2019; Villarino and Bohme, 2004), and also the spark-plug in SI engines (Fan et al., 2012; Auzins et al., 1995).

For the information to be applicable for the in-cycle adjustment of the upcoming fuel injections in a misfire event, the detector has to diagnose pilot misfire robustly before the main start of injection within the same cycle. To accomplish this requirement, the in-cylinder pressure provides fast measurements for the combustion supervision. This is the signal used for the misfire diagnosis in this work, also used in (Cesario et al., 2006) for SI engines. The methods proposed in the literature do not achieve the real-time diagnosis requirements, as they focus on the legislation demands on the overall combustion misfire detection on a cycle-to-cycle basis (Mohammadpour et al., 2011). Real-time in-cycle pilot misfire diagnosis methods were investigated in Publication VII, which are presented in this section.

6.3.1 In-cycle pilot misfire detection

Available signals for diagnosis

The directly measured variable is the in-cylinder pressure. From it, different variables are estimated and studied for pilot misfire diagnosis. These are the heat release rate (HR), the accumulated heat release (AHR) and the pressure rise over the estimated motoring trace (referred to as pressure rise). This last one has the advantage compared to the AHR of requiring less filtering and processing, as the pressure derivative is not required. The location of the heat release magnitude is also a metric for the expected timing of the pilot combustion. Additionally, the frequency content can be obtained from the in-cylinder pressure trace. However, it was observed that the signal-to-noise ratio is too low for robust diagnosis of pilot misfire.

Detector design

The misfire detector design consists in composing a function $\phi(\mathbf{x}) : \chi \rightarrow (0, 1)$ such that (Kay, 1993) :

$$\phi(\mathbf{x}) = \begin{cases} 1, \text{ misfire} \\ 0, \text{ combustion} \end{cases} \quad (6.36)$$

where \mathbf{x} are the measured or estimated variables. Two approaches for the design of this function were investigated. The first is a deterministic approach, the second is a stochastic approach for the computation of the misfire probability.

Pilot misfire observability

In-cycle pilot misfire observability is measured by the correlation between the measured variables, for the monitoring of the pilot combustion, and the effects on the main premixed heat release. The lack of observability hinders the prediction of the pilot misfire effects on the main injection, hence the in-cycle control. The in-cycle pilot misfire observability is measured by the probability of detection (Kay, 1993) obtained with an optimized constant detection threshold. The threshold is calibrated individually for each steady-state operating condition for the maximization of the detection probability.

6.3.2 Deterministic detector design

The detection function $\phi(\mathbf{x})$ is the comparison of the measured variable x to a threshold γ :

$$\text{Decide misfire : } x > \gamma \quad (6.37)$$

The detection threshold has to be calibrated for a satisfactory detection performance. The baseline for comparison between the different detection algorithms was set by a constant detection threshold, calibrated to maximize the misfire detection ratio for all operating conditions. The optimal threshold is a trade-off between combustion and misfire detection, which is a function of the signal-to-noise ratio of the different operating conditions. To improve the misfire detection performance, the threshold calibration can be based on more advanced methods. The calibration can be adjusted for different operating conditions or adapted on-line, as investigated in Publication VII. The suggested method for the on-line adaptation of the detection threshold is described below.

On-line threshold adaptation

The proposed method in Eq.(6.38) corrects the detection threshold every cycle a diagnosis fails, proportional to a correction gain K :

$$\gamma_{i+1} = \gamma_i + K \frac{\delta_i - \hat{\delta}_i}{\epsilon + |x_i - \gamma_i|} \quad (6.38)$$

The in-cycle misfire diagnosis is represented by the binary variable $\hat{\delta}$. At the end of the cycle, δ is computed, stating if there was pilot misfire. For a faster update, the recursive equation uses the information of the distance to the threshold (γ).

For a correct diagnosis, the distance to the detection threshold is interpreted as an indicator of the diagnosis robustness. For a wrong diagnosis, the distance to the threshold is an indicator of the measurement uncertainty. To reduce the sensitivity to measurement noise, the detection threshold is updated inversely proportional to the threshold distance. The update law is designed in this manner to avoid large threshold updates under noisy measurements. As more data is collected, the measurement uncertainty reduces, and the threshold updates faster. A small constant ϵ is added to avoid division by zero.

6.3.3 Stochastic detector design

The stochastic approach is equivalent to maximizing the detection probability. The decision rule to minimize the average detection error, where x is the measured variable, is:

$$\text{Decide misfire : } P(\text{misfire}|x) > P(\text{combustion}|x) \quad (6.39)$$

The posterior probabilities are computed with two methods. The first is the direct modeling for each measured variable, presented in next subsection. The second is to apply Bayes rule, in Eq.(6.40), to the stochastic models for the heat release, accumulated heat release and pressure rise (introduced in Section 5.2):

$$P(\psi|x) = \frac{P(x|\psi)P(\psi)}{P(x)} \quad (6.40)$$

ψ represents each hypothetical case i.e., combustion or misfire. The total misfire probability ($P(\psi)$ when $\psi \equiv \text{misfire}$) is modeled by Eq.(5.19), computed for the current injection. The measurement probability $P(x)$ is computed by the law of total probability:

$$P(x) = P(x|\text{misfire})P(\text{misfire}) + P(x|\text{combustion})(1 - P(\text{misfire})) \quad (6.41)$$

The first approach for the probability modeling provides a systematic method to calculate a variable threshold on the measured variables with the operating conditions. The second approach simplifies how the probability distributions are updated each cycle, discussed in Chapter 7. The advantage of the first approach is a reduced number of parameters (16) compared to the required number of parameters in the predictive models (32).

Posterior probability modeling

The posterior probability models describe the probability of having a misfire event given a measured heat release, accumulated heat release or pressure rise. The models presented in Publication VII are briefly summarized here. For the heat release (q_{HR}), the posterior misfire probability is:

$$P(\text{misfire}|q_{HR}) = P(q_{HR} < \mathcal{N}(\mu_{HR}, \sigma_{HR}^2)) \quad (6.42)$$

The parameters of the normal distribution are modeled as a function of the pilot-main separation. This variable is introduced to reduce the sensitivity to the oscillations before the main SOC of the filtered pressure signal, which may be confounded with the pilot combustion's heat release rate. The mean and standard deviation parametrization are:

$$\mu_{HR} = \mu_{HR0} + k_{\mu_a} e^{k_{\mu_b} \Delta\theta_{pilot-main}} \quad (6.43)$$

$$\sigma_{HR}^2 = \sigma_{HR0}^2 + k_{\sigma_b} \Delta\theta_{pilot-main} \quad (6.44)$$

For the accumulated heat release (Q_{HR}), the posterior misfire probability is:

$$P(\text{misfire}|Q_{HR}) = P(Q_{HR} < \mathcal{N}(\mu_{AHR}, \sigma_{AHR}^2)) \quad (6.45)$$

The mean and standard deviation are parametrized as functions of the pilot SOI:

$$\mu_{AHR} = \mu_{AHR0} + k_{\mu_a} (\theta_{SOI}^{pilot} - \theta_0)^2 \quad (6.46)$$

$$\sigma_{AHR}^2 = \sigma_{AHR0}^2 + k_{\sigma_a} e^{-k_{\sigma_b} \theta_{SOI}^{pilot}} \quad (6.47)$$

For the pressure rise (Δp), the posterior misfire probability is:

$$P(\text{misfire}|\Delta p) = P(\Delta p < \mathcal{N}(\mu_{\Delta p}, \sigma_{\Delta p}^2)) \quad (6.48)$$

The mean and standard deviation are parametrized as functions of the pilot SOI:

$$\mu_{\Delta p} = \mu_{\Delta p0} + k_{\mu_a} \theta_{SOI} \quad (6.49)$$

$$\sigma_{\Delta p}^2 = \sigma_{\Delta p0}^2 + k_{\sigma_a} (\theta_{SOI}^{pilot} - \theta_0)^2 \quad (6.50)$$

Sensor fusion

The detection performance of the stochastic detector can be improved by combining adequately the information from each measurement. The combination of the indicators should prioritize those ones with the higher detection accuracy. The performance of each indicator can be evaluated on-line for an adaptive combination of them. The investigated combination method is a weighted average of the predicted probabilities of misfire and combustion. The distance between the misfire and combustion probability is also included as a measurement of the robustness of each indicator. For each indicator, the proposed recursion for its weight is:

$$\omega_{i+1} = \omega_i + K \left((2(\delta_i - \hat{\delta}_i) - 1) |P(\text{misfire}|x_i) - P(\text{combustion}|x_i)| \right) \quad (6.51)$$

The weights are increased proportionally to the robustness when the detection is successful i.e., $\delta = \hat{\delta}$, and decreased when it is not. The weights are normalized for the computation of the weighted average. The normalization in matrix form, where bold refers to vectors, is:

$$P(\text{misfire}|\mathbf{x}_i) = \frac{\omega_i}{\sum \omega_i} \times \mathbf{P}(\text{misfire}|x_i)^\top \quad (6.52)$$

6.3.4 Experimental results

The experimental results for the misfire detection for a sweep of pilot on-times, SOI, rail pressures, engine speeds and EGR ratios are plotted in Figure 6.6. To illustrate the detection robustness, the engine was run with HVO, whilst the models were calibrated for Diesel. The results compare the different detection methods using the different indicators. The observability results are discussed based on the theoretical optimal detection threshold. The baseline for comparison is the optimized constant detection threshold in Eq.(6.37). A detailed analysis of the results is discussed in the following subsections.

In-cycle pilot misfire observability

The in-cycle pilot misfire observability is a metric of the correlation between the in-cylinder pressure signal during the expected pilot combustion and the main combustion. The maximum theoretical observability is obtained when all the pilot misfire indicators are combined, reaching 98.83%. The observability of the

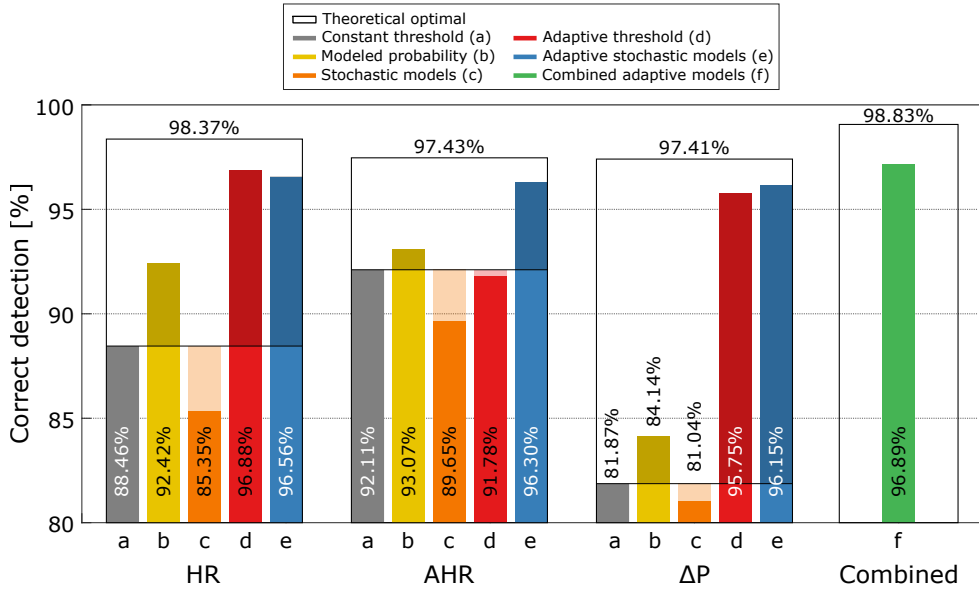


Figure 6.6: Pilot misfire detection performance of the algorithms using the heat release magnitude, the accumulated heat release, the pressure rise over motoring, and the combination of the three by sensor fusion, for HVO. The models were calibrated for Diesel. The relative detection performance of the different algorithms is compared.

individual indicators is lower, of about 98%. The observability is affected by the operating conditions. The minimum observability was obtained at the transition region from pilot misfire to pilot combustion, where the signal-to-noise ratio is minimum. The pilot on-time and SOI affected significantly this transition, with a minimum observability of 94% correct detection. Early pilot SOI, or short pilot-main separations reduced the pilot misfire observability. Early pilot injections burn with reduced combustion efficiency. Short pilot-main separations result in an overlap of the pilot combustion with the main injection. Both have the effect of a reduction in the signal-to-noise ratio. Higher engine speeds decrease the observability as well, due to the higher oscillations and noise in the pressure signal. See Publication VII for a detailed discussion.

Detection performance

The maximum detection performance with a constant threshold is 92% using the accumulated heat release as indicator. The heat release results in a detection performance of 88%, reduced to 82% for the pressure rise. The non-adaptive stochastic detectors can improve the detection performance of a constant threshold. The modeled posterior probability increases the detection per-

formance by up to +4%. Contrarily, the predictive models calibration is sensitive to the fuel, reducing the accuracy and robustness of the detection performance.

The previous limitations are overcome by the adaptive methods, which significantly increase the detection performance up to 96% for both the adaptive threshold and the stochastic detector. Similar detection performance are achieved for all the indicators. However, the exception of improved detection performance is found for the adaptive threshold detector using the AHR. Due to a too large gain for the feedback, the performance is lower than the constant threshold detector. The adaptation gain is therefore sensitive to the fuel and operating conditions for a good adaptation and detection performance. This inconvenience is not found for the stochastic models' adaptation, with a detection performance improvement by +7%_{unit} on average compared to the constant threshold detectors. The sensor fusion of the adapted stochastic models further increases the detection performance by +0.5%_{unit} on average.

The adaptive threshold detector using the heat release magnitude has a good compromise between detection performance and an early detection, if the feedback gain is calibrated adequately. The additional complexity of the adapted predictive stochastic detectors, using sensor fusion, can only be motivated if higher detection performance is required.

Detection sensitivity and robustness

For the sensitivity analysis, a constant error offset was added to the input and measured variables. The sensitivity to input errors is most significant for the detectors based on the predictive stochastic models. The other methods can successfully overcome the input errors, either because they are not dependent on the input variables (for the constant threshold and direct posterior misfire probability-based detector) or because they can adjust to them (adapted threshold detectors and adapted stochastic models). The sensitivity to the measurement error was highly significant for the non-adaptive detectors. The measurement error directly impacts the detector based on that indicator, where the largest sensitivity is obtained. The adaptive methods can overcome the effects of these disturbances successfully. The highest sensitivity was found for the heat release magnitude, with a decrease of -15%_{unit} detection performance for the non-adaptive and -3%_{unit} for the adaptive detectors, for a bias of +10J/CAD. Despite the lower sensitivity of the adaptive detectors, they require few cycles to compensate for measurement errors. Contrary to what would be expected, the adaptive fusion of the detectors is more sensitive than the individual sensors. This is because the disturbances generate erroneous feedback for the weights

update, resulting in increased sensitivity.

The minimum robustness is obtained at operating conditions where the magnitude of the indicator is similar to the signal noise. This increases the difficulty of distinguishing between pilot combustion and pilot misfire. The methods based on previously calibrated models are the least robust ($-3.4\%_{unit}$ detection performance reduction on average), even less than using a constant threshold ($-2.6\%_{unit}$ on average). For the stochastic detectors, the predictive stochastic models present lower robustness than the direct posterior probability models. This is due to the difficulty of having accurate predictive models in all operating conditions for each fuel. Therefore, it is more robust to model the misfire probability directly as a function of the measured variable and operating conditions. The detection robustness can be improved significantly by the adaptive detectors, further increased when the information is combined by sensor fusion. If properly adapted, the adaptive predictive models show the best robustness ($+1.32\%_{unit}$ detection performance increase on average), similar to the detectors that use an adaptive threshold ($+0.89\%_{unit}$ on average).

6.4 Start of Combustion Detection

The start of combustion provides feedback for the in-cycle controllers. It also permits the location of the pilot combustion for its mass estimation and pressure prediction. This requires a robust detection of the SOC in real-time. A summary of on-line SOC detection methods can be found in (Yang et al., 2014). Whereas most of the on-line methods rely on the pressure difference between firing and motoring cycles, this work uses the heat release rate, as done by (Oh et al., 2015). However, the method used in this thesis follows a stochastic approach.

The detection problem is stated as a hypothesis test of a model change at SOC. The null hypothesis \mathcal{H}_0 is the combustion not being triggered. The alternative hypothesis \mathcal{H}_1 is the trigger of the combustion at a certain SOC. The prior knowledge is included by the ignition-delay model in Eq.(5.23) and its uncertainty in Eq.(5.24) in the probability distributions. The uncertainty in the heat release measurements (from the measurement noise) is formulated as an added white noise ν , uncorrelated with the ignition-delay uncertainty. The hypothesis test probabilities are:

$$\begin{aligned} P(\text{SOC} \mid \mathcal{H}_0) &= P(\mathcal{N}(0, \sigma_{HR}^2) \leq 0) \\ P(\text{SOC} \mid \mathcal{H}_1) &= P(\mathcal{N}(0, \sigma_{HR}^2) > 0) \cdot P(\mathcal{N}(\theta_{SOC}, \sigma_{\Delta\theta_{ID}}^2) \geq \hat{\theta}_{SOC}) \end{aligned} \quad (6.53)$$

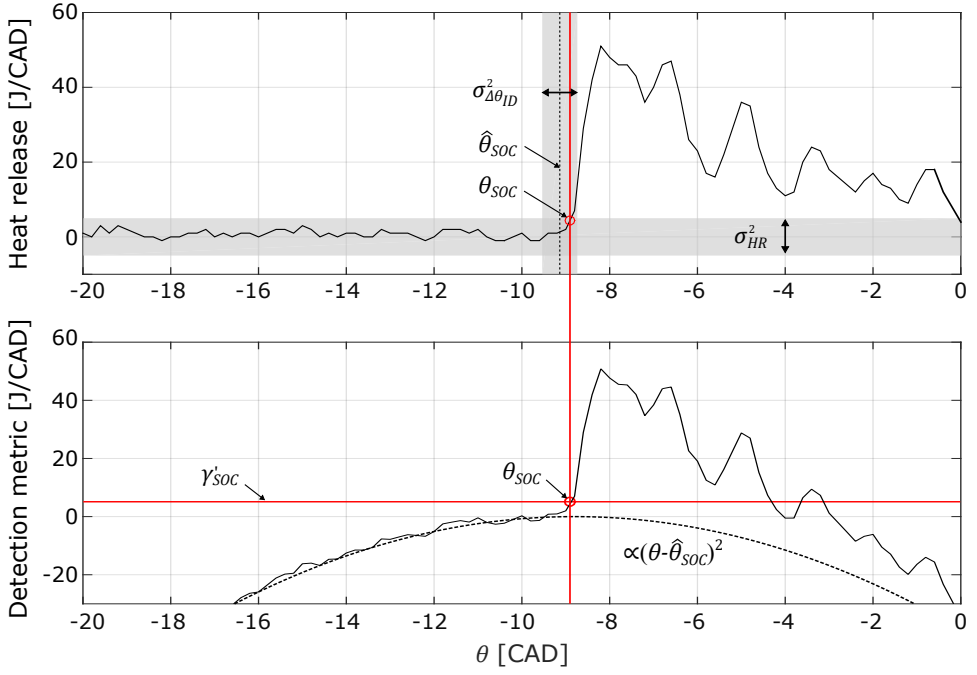


Figure 6.7: SOC detection method. The heat release rate with the modeled uncertainties is in the upper plot. The matched filter terms are in the lower plot. The detected SOC is highlighted.

where σ_{HR}^2 is the measurement noise (ν) dispersion, and $\hat{\theta}_{SOC}$ the model-based SOC prediction by Eq.(5.23). The combustion is detected when the alternative hypothesis is adopted, at which CAD the SOC is determined. Following the Newman-Pearson lemma (Kay, 1993), this is decided when:

$$L(x) = \frac{P(\text{SOC} | \mathcal{H}_1)}{P(\text{SOC} | \mathcal{H}_0)} \geq \gamma_{SOC} \quad (6.54)$$

where the detection threshold γ_{SOC} is calibrated for a satisfactory false alarm probability. Taking logarithms of the exponentials of the normal distribution expression and simplifying, the detection problem solution is the matched filter (Kay, 1993), extended to include the ignition-delay model:

$$q_{HR} - \frac{\sigma_{HR}^2}{2\sigma_{\Delta\theta_{ID}}^2}(\theta - \hat{\theta}_{SOC})^2 > \gamma'_{SOC} \quad (6.55)$$

The detection threshold is updated by the mathematical manipulation of the normal distributions in Eq.(6.53), resulting in γ'_{SOC} . The variances and thresholds can be calibrated to obtain a good trade-off between an early and a robust detection for each operating condition.

A representation of the detection method is illustrated in Figure 6.7. In Publication III, the SOC detection method was applied also for the detection of the start of vaporization.

6.5 In-Cycle Pilot Mass Estimation

The fuel properties and pressure oscillations in the rail disturb the actual injected mass (Tennison and Reitz, 2001) on a cycle-to-cycle basis. In order to compensate in-cycle for deviations of the pilot combustion and its effects on the main injection, the pilot mass has to be estimated before the main SOI. Finesso and Spessa (2015) proposed a fuel mass estimation based on the accumulated heat release, which can be implemented in-cycle. The injected fuel mass is estimated by inverting a combustion model. This method requires the completion of the pilot combustion for its estimation, which reduces the CAD interval for the main injection regulation in-cycle. Furthermore, the combustion efficiency of the pilot is not considered.

An alternative in-cycle estimation method was investigated in Publication III. For the fast in-cycle estimation, the proposed approach is based on the pilot ignition-delay and combustion rate. In Publication III, the vaporization was also included to investigate if an earlier estimation could be achieved. This is omitted here as it was concluded it did not contribute significantly to improve the pilot mass estimation accuracy.

6.5.1 Estimation based on the ignition-delay

The ignition-delay model in Eq.(5.47) is extended with the pilot mass:

$$\Delta\theta_{ID}^{pilot} = N_{eng}(k_m m_{pilot} + K_p e^{\alpha_p p_{SOI}}) \quad (6.56)$$

Assuming all the inputs are measured accurately, the ignition-delay can be inverted for the pilot mass estimation:

$$\hat{m}_{SOC} = \frac{1}{N_{eng}k_m}(\theta_{SOC} - \theta_{SOI}) - \frac{K_p}{k_m}e^{\alpha_p p_{SOI}} \quad (6.57)$$

This formulation allows for an estimation even if the combustion is not triggered yet. To obtain an estimation when the pilot SOC (θ_{SOC}) has not been detected

after the predicted SOC ($\hat{\theta}_{SOC}$), the current CAD is hypothesized to be the current value of the pilot SOC:

$$\theta_{SOC} \equiv \theta, \theta > \hat{\theta}_{SOC} \quad (6.58)$$

The new estimation is used to update the initial pilot mass estimation from the injectors calibrated map. Assuming the injectors uncertainty and the ignition-delay model are uncorrelated, the probabilities in Eq.(5.13) and Eq.(5.24) are used to compute the pilot mass uncertainty:

$$P(m_{pilot}|m_{inj}, \hat{m}_{SOC}) = \mathcal{N}(m_{inj}, \sigma_{m_{inj}}^2) \mathcal{N}(\hat{m}_{SOC}, \sigma_{m_{SOC}}^2) \quad (6.59)$$

where $\sigma_{m_{SOC}}^2$ is computed from the transformation of the variance of the ignition-delay model in Eq.(5.25), evaluated at the nominal injected pilot mass m_{inj} and predicted pilot ignition-delay $\widehat{\Delta\theta}_{ID}^{pilot}$. The estimated pilot mass is computed for the maximization of the pilot mass probability. This results in a weight average of the previous pilot mass estimations, based on each estimation uncertainty:

$$\hat{m}_{pilot} = \frac{\sigma_{m_{SOC}}^2}{\sigma_{m_{inj}}^2 + \sigma_{m_{SOC}}^2} m_{inj} + \frac{\sigma_{m_{inj}}^2}{\sigma_{m_{inj}}^2 + \sigma_{m_{SOC}}^2} \hat{m}_{SOC} \quad (6.60)$$

This estimation will be the initial value for the pilot mass estimation based on the heat release. The uncertainty of the estimation is also required for the combination of the new estimations. As the estimated mass is a linear transformation of two uncorrelated normal distributions, its variance is:

$$\sigma_{\hat{m}_{pilot}}^2 = 2 \frac{\sigma_{m_{inj}}^2 \sigma_{m_{SOC}}^2}{\sigma_{m_{inj}}^2 + \sigma_{m_{SOC}}^2} \quad (6.61)$$

6.5.2 Estimation based on the heat release rate

The pilot heat release is modeled as a premixed combustion with a simplified predictive model to reduce the computational load in the FPGA. The injected mass is normalized so it can be scaled with the pilot mass. The linear system modeling the heat release rate (q_{HR}) dynamics is:

$$\begin{aligned} \begin{bmatrix} d\chi_{vap} \\ d\chi_{prem} \end{bmatrix}_k &= \begin{bmatrix} -\frac{1}{\tau_{vap}} & 0 \\ \frac{1}{\tau_{prem}} & -\frac{1}{\tau_{prem}} \end{bmatrix} \begin{bmatrix} \chi_{vap} \\ \chi_{prem} \end{bmatrix}_k + \begin{bmatrix} \frac{1}{\tau_{vap}} \\ 0 \end{bmatrix} \delta_{inj} \\ q_{HR_k} &= \begin{bmatrix} 0 & m_{pilot} \eta_{comb}^{pilot} Q_{LHV} \end{bmatrix} \begin{bmatrix} d\chi_{vap} \\ d\chi_{prem} \end{bmatrix}_k \end{aligned} \quad (6.62)$$

The input to the system is a unit step δ_{inj} , which represents the start of the pilot injection, but shifted to the pilot SOC. There are two states, the vaporization, and the premixed combustion. The dynamic states $\chi \in [0, 1]$ represent the completeness of the transition from one state to the next one, from the injection, to vaporization, to premixed combustion. The rate constants (τ_{vap}, τ_{prem}) are parametrized as a function of the pilot ignition-delay. Additional variables were included in Publication III, but the effect of these variables can be indirectly considered by the ignition-delay. Furthermore, this parametrization permits an initial estimation of the combustion rates based on the measured ignition-delay.

The pilot mass can be estimated by inverting the output gain:

$$\hat{m}_{pilot} = q_{HR} \left(d\chi_{prem} \cdot Q_{LHV} \cdot \eta_{comb}^{pilot} \right)^{-1} \quad (6.63)$$

However, the solution to this equation is non-linear, as the combustion efficiency is computed by Eq.(5.20). Additionally, it requires division, which is a limitation for its implementability in the FPGA. Furthermore, the model errors and measurement noise are not considered in this solution, which will result in higher sensitivity to measurement error and model uncertainties. The approach suggested in Publication III reformulates this problem as a linear system with a time-variable gain, which can be estimated recursively without division, assuming the model and measurement error can be modeled as added white noise:

$$\begin{aligned} \hat{m}_{pilot}|_{k|k-1} &= \hat{m}_{pilot}|_{k-1} + v \\ \hat{q}_{HR}|_{k|k-1} &= \left(Q_{LHV} \cdot \eta_{comb}^{pilot}|_{k-1} \cdot d\chi_{prem}|_{k-1} \right) \cdot \hat{m}_{pilot}|_{k-1} + \nu \end{aligned} \quad (6.64)$$

The normalized combustion rate $\chi_{prem}|_k$ is computed recursively by the state-space transition matrix in Eq.(6.62) with a discrete CAD step equal to the sampling rate of $0.2CAD$. The combustion efficiency is computed by Eq.(5.20) evaluated with the estimated pilot mass at the $(k-1)^{th}$ cycle. Assuming small variations of the combustion efficiency with the pilot mass, so it can be approximated as a constant, the optimal state estimation of this linear formulation is the Kalman filter (Åström and Wittenmark, 1997). The pilot mass is estimated recursively with the Kalman gain. The correction step is:

$$\hat{m}_{pilot}|_{k|k} = \hat{m}_{pilot}|_{k|k-1} + K \left(q_{HR}|_k - \hat{q}_{HR}|_{k|k-1} \right) \quad (6.65)$$

The Kalman gain K is updated each iteration based on the covariance estimate (Åström and Wittenmark, 1997). The process is iteratively repeated until the EOC is detected. In case stringent implementation constraints are imposed, the

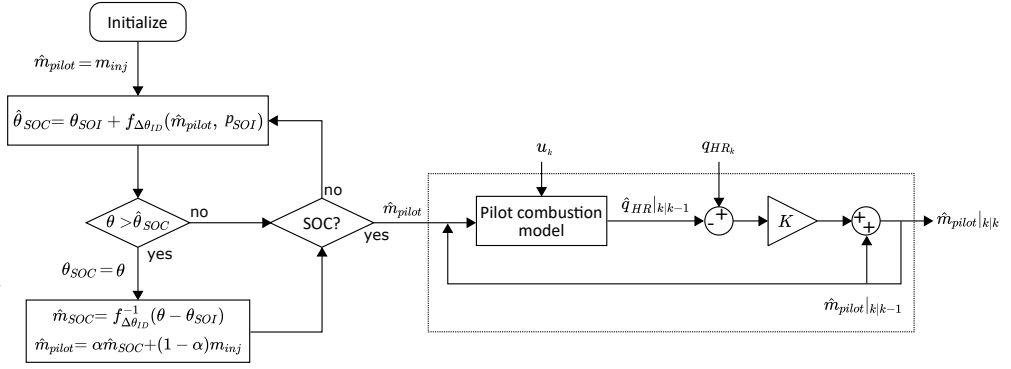


Figure 6.8: Flowchart diagram of the pilot mass estimation. The weights in Eq.(6.60) are represented by α . The Kalman filter gain is K . The ignition-delay function $f_{\Delta\theta_{ID}}$ is computed by Eq.(6.56).

correction gain can be constant. Despite different estimation and convergence properties, the estimation will converge to the average value of the pilot mass. The complete algorithm flowchart is illustrated in the diagram of Figure 6.8.

6.5.3 Experimental results

The combustion parameters were calibrated according to the methodology in Section 5.4. The calibration experiments followed a Box-Behnken design (Andersson, 2012) with the levels in Table 6.1, for a total of 41 operating points:

Table 6.1: Levels of the variables for the Box-Behnken experimental design for the model calibration.

Variable	Values
Engine speed	900, 1200, 1500 [<i>RPM</i>]
Load [IMEP]	5, 10, 15 [<i>bar</i>]
EGR	0, 7.5, 15 [%]
Rail pressure	900, 1200, 1500 [<i>bar</i>]
Pilot SOI	-20, -15, -10 [<i>CAD</i>]
Pilot mass	9, 12, 15 [<i>mg/st</i>]

Intermediate and external points were added for the study of the interpolation and extrapolation accuracy. The validation of the method was tested experimentally. The estimation accuracy was studied by adding a perturbation to the initial pilot mass estimation, with a random error within $\pm 1.5 \text{ mg/st}$. The nominal initial estimation was computed with the average injector calibration.

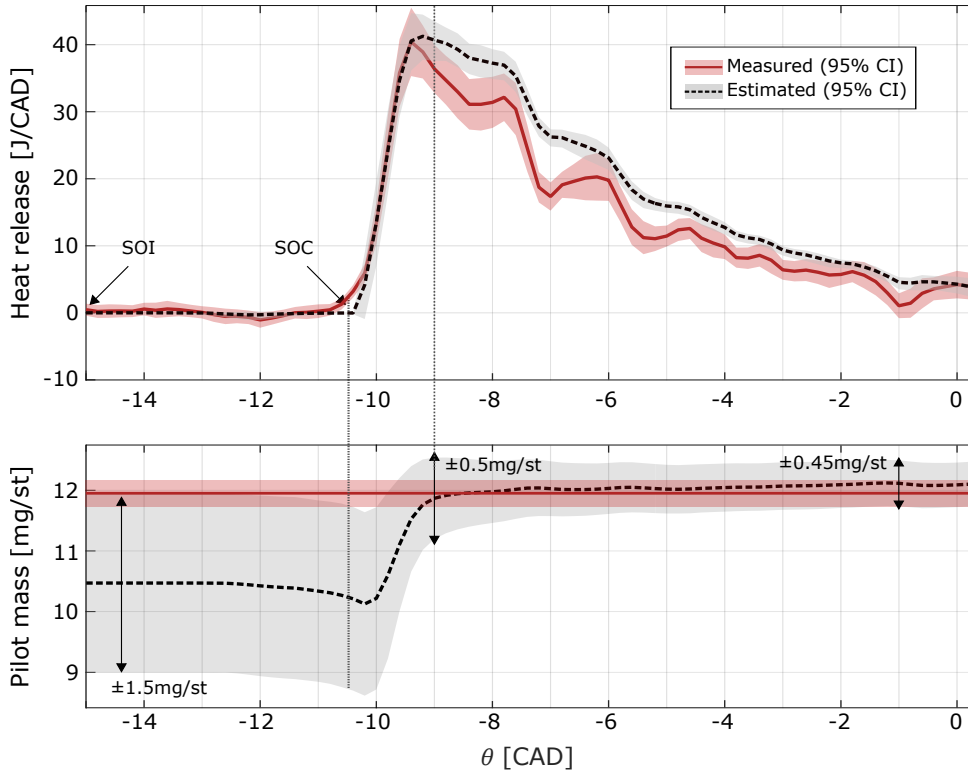


Figure 6.9: Measured heat release (solid lines) and the on-line estimated heat release (dashed lines), upper plot. Comparison between the averaged estimated pilot mass (dashed lines) to the actual injected mass (solid line), lower plot. The data corresponds to cylinder 1 averaged over 100 cycles with the 95% confidence interval area. The engine was operated at 10bar IMEP, 1200RPM, 1200bar rail pressure, -15°CAD SOI pilot and no EGR with a pilot on-time of 0.3ms.

The estimation accuracy was evaluated by comparing the final estimation to the actual injected pilot mass, computed with the individual calibration of the injectors. The final estimation error was investigated as a function of the injection on-time, rail pressure, load, engine speed and EGR. Detailed results can be found in Publication III.

In-cycle pilot mass estimation

An example of the pilot mass estimation is shown in Figure 6.9. The initial error with a 95% confidence interval of $\pm 1.5\text{mg/st}$ is significantly reduced to $\pm 0.5\text{mg/st}$ when the combustion evolution reaches its maximum peak, about 1CAD after the pilot SOC in this example. Compared to the AHR method, the same accuracy is not obtained until the pilot EOC, at around $\theta = 0^{\circ}\text{CAD}$ for

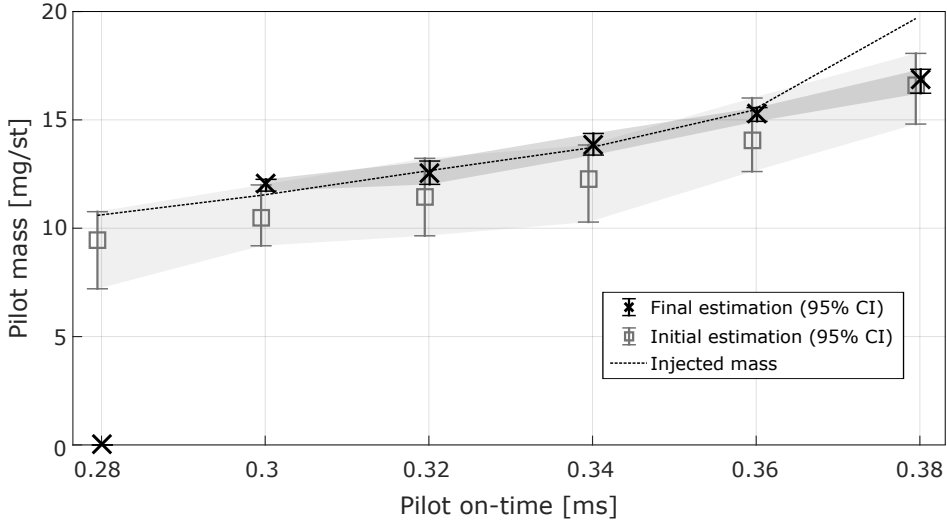


Figure 6.10: Comparison between the actual injected pilot mass and the final pilot mass estimation as a function of the pilot on-times, injected at $-15CAD$ SOI. The results over 100 cycles for cylinder 1 are plotted. The bars represent the 95% confidence interval. The engine was operated at 10bar IMEP, 1200RPM, 1200bar rail pressure, no EGR.

this example. From the HRR-peak at $-9CAD$, the additional iterations permit to improve the estimation uncertainty, down to $\pm 0.45mg/st$. The estimation based on the ignition-delay or the vaporization did not improve significantly the estimation error. These results were exploited to release computational resources in the FPGA. In the proposed simplification, the pilot mass estimation was only based on the heat release magnitude of the pilot combustion, where the estimation accuracy is already improved to similar levels as at the end of the pilot combustion. In this manner, the implementation of the combustion rate dynamic model is avoided. The position of the maximum heat release magnitude determines the minimum pilot-main separation to ensure the observability of the pilot combustion for its mass estimation based on in-cylinder pressure measurements. Other signals to monitor the injected pilot mass would be necessary to overcome this limitation, such as pressure measurements at the injector tip or rail pressure-based methods to estimate the actual injector opening.

Estimation accuracy

The estimation accuracy for different pilot on-times is plotted in Figure 6.10. The injected pilot mass uncertainty is reduced with the proposed in-cycle pilot mass estimation method. The method is only effective when the pilot burns. For short on-times (see the case of $0.28ms$), pilot misfire is interpreted by the

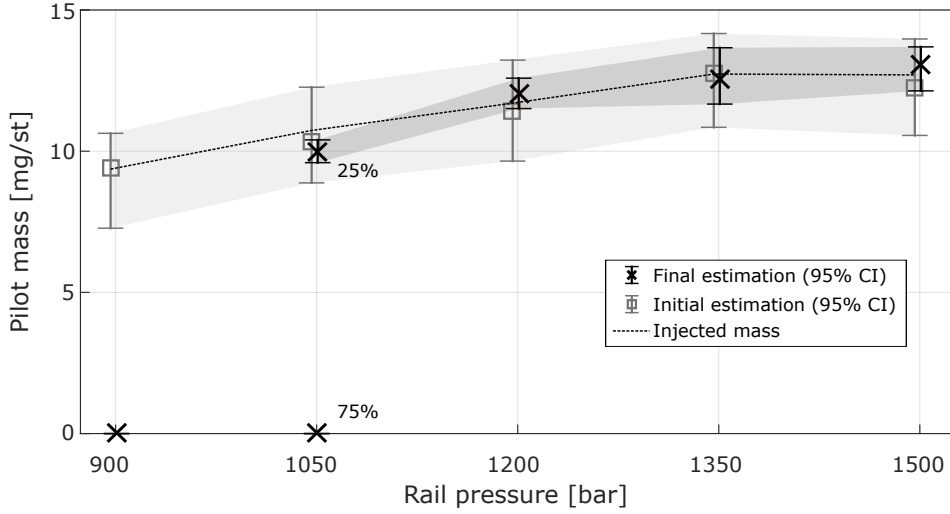


Figure 6.11: Comparison between the actual injected pilot mass and the final pilot mass estimation as a function of the rail pressure. The pilot injection was of $0.3ms$ on-time at $-15CAD$ SOI. The results over 100 cycles for cylinder 1 are plotted. The bars represent the 95% confidence interval. The engine was operated at $10bar$ IMEP, $1200RPM$, no EGR.

estimator as there was no pilot injection. Due to the linear parametrization, the method is effective for the region where the injected pilot mass varies linearly. A more complex parametrization can help to reduce this limitation, such as gain-scheduling or non-linear parametrization.

The estimation accuracy as a function of the rail pressure is plotted in Figure 6.11. The rail pressure affects the misfire probability as well as the injected pilot mass for a constant on-time. The initial pilot mass error is reduced for the burnt cycles. A 75% misfire ratio is obtained at $1050bar$ rail pressure. In those cases, the pilot mass is estimated as there was no pilot injection. The non-linear effects of the model parametrization were not observed for the studied range of rail pressures.

Sensitivity analysis

The sensitivity analysis of the method to measurement and parameter errors is detailed in Publication III. The estimation method is sensitive to the variables whose error propagates through the computation of the model parameters, mostly the inlet pressure. The phase offset between the combustion and its estimation also affected significantly the estimation accuracy. For this reason and for errors in the computation of the heat release rate, the method is sensit-

ive to TDC offset error. The model parameter that affected most significantly the estimation error was the pilot combustion efficiency. The pilot mass and the combustion efficiency are not observable simultaneously, as they cannot be separated linearly. Hence, the error on the combustion efficiency is directly correlated to the pilot mass estimation error.

6.6 Misfire Ratio Based Pilot Mass Estimation

From in-cylinder pressure measurements, the heat release is used to estimate the fuel mass based on the energy released on a cycle-to-cycle basis (Finesso and Spessa, 2015). However, at the region of short pilot injections, the low signal-to-noise ratio of the rail pressure and the heat release rate results in a high uncertainty of the estimations. The stronger correlation of the pilot misfire ratio with the pilot mass (0.8979), compared to the correlation between the nominal injection on-time and pilot mass (0.6957), suggests that the pilot misfire ratio can be exploited to estimate the actual pilot injected mass for a given on-time. A Bayesian approach for the pilot fuel mass estimation, based on the pilot misfire ratio, was investigated in Publication VIII. The advantage of this approach is that the accuracy of other on-line fuel mass estimation methods, with lower estimation accuracy for short pilot on-times, can be improved further using available on-board sensors that can detect pilot misfire.

6.6.1 Pilot mass estimation

Following a Bayesian approach, the likelihood distribution of the pilot mass for a given measured misfire ratio r_m is:

$$P(m_{pilot}|r_m, \overline{m_{inj}}) = \frac{P(r_m|\mu_{r_m})P(m_{pilot}|\overline{m_{inj}})}{\int P(r_m|\mu_{r_m})P(m|\overline{m_{inj}})dm} \quad (6.66)$$

In this equation, $\overline{m_{inj}}$ is the prior nominal estimation of the injected pilot mass, obtained from the map of the injectors or other available calibration. The stochastic variable m represents the probability space of pilot masses that may result from a nominal injected mass $\overline{m_{inj}}$, by its normal distribution in Eq.(5.13). The uncertainty of a measured misfire ratio is described by the conditional probability of its nominal value, $\mu_{r_m} = f_{r_m}(m_{inj})$, which is a function of the yet unknown pilot mass m_{pilot} , by Eq.(5.16).

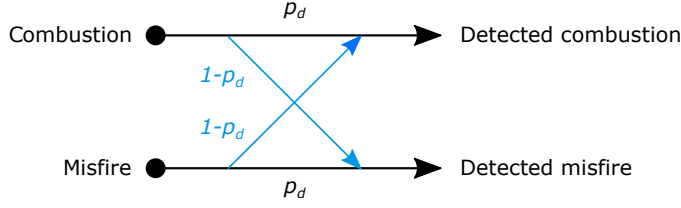


Figure 6.12: Binary symmetric channel with a crossover probability modeling the misfire detector with a correct detection probability p_d (Cover and Thomas, 2006).

The misfire ratio has to be estimated by the n misfire events detected in N samples. Hence, the distribution of the estimated pilot mass is expressed as a function of the estimated misfire ratio \hat{r}_m :

$$P(m_{pilot}|n, N, \overline{m_{inj}}) = \frac{P(\hat{r}_m|n, N, m_{pilot})P(m_{pilot}|\overline{m_{inj}})}{\int P(\hat{r}_m|n, N, m)P(m|\overline{m_{inj}})dm} \quad (6.67)$$

The estimated pilot mass (\hat{m}_{pilot}) is the argument that maximizes the pilot mass likelihood L :

$$L(m_{pilot}|n, N, \overline{m_{inj}}) \propto P(\hat{r}_m|n, N, m_{pilot})P(m_{pilot}|\overline{m_{inj}}) \quad (6.68)$$

$$\hat{m}_{pilot} = \arg \max_{m_{pilot}} (L(m_{pilot}|n, N, \overline{m_{inj}})) \quad (6.69)$$

Pilot misfire ratio estimation

The distribution of the estimated pilot misfire ratio is computed as a function of the pilot misfire ratio r . For a pilot misfire ratio r , the number of misfire events in an experiment is binomially distributed. Its probability mass function, expressing the probability of obtaining n misfire cycles out of N cycles, is:

$$P(r|n, N) = \mathcal{B}_N(r|n, N) = \binom{N}{n} r^n (1-r)^{N-n} \quad (6.70)$$

The actual number of detected misfire events results in a detected misfire ratio of $r_d = \frac{n}{N}$. Its probability is described by a Bernoulli distribution, where the misfire events are detected successfully with a probability p_d . This is the misfire detector accuracy. The detector acts therefore as a binary symmetric channel (Cover and Thomas, 2006), illustrated in Figure 6.12, with a crossover probability $1 - p_d$.

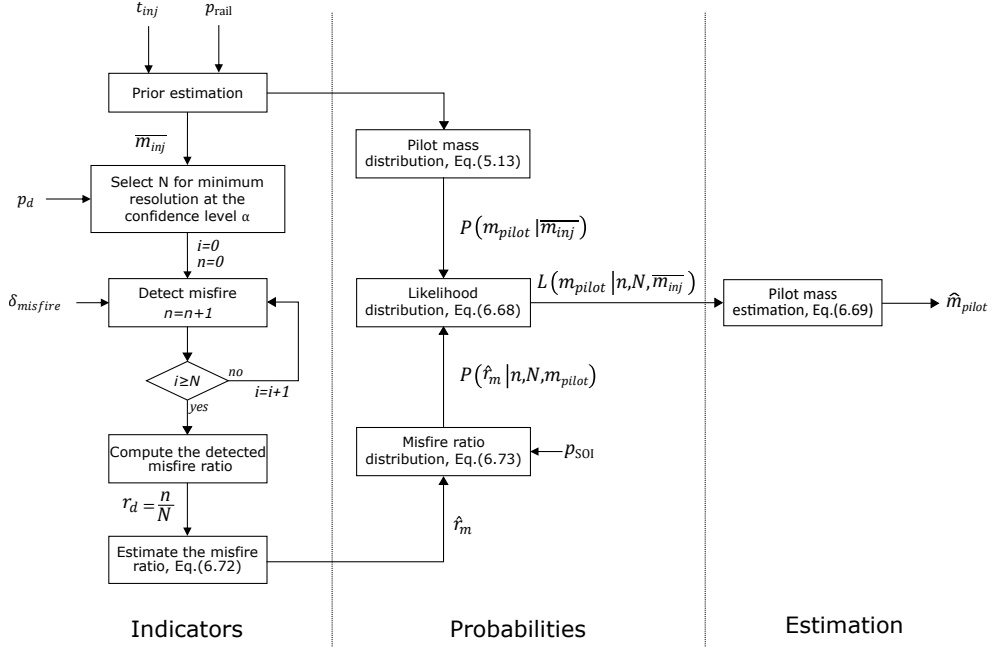


Figure 6.13: Diagram of the algorithm's steps for the pilot mass estimation. The inputs to the algorithm (Injection on-time - t_{inj} , rail pressure - p_{rail} , detection accuracy - p_d , misfire detection - $\delta_{misfire}$ and pressure at pilot SOI - p_{SOI}) are marked. The blocks represent each computation step with its respective output. The final output is the estimated pilot mass \hat{m}_{pilot} .

Note that if $p_d < 0.5$, the detector can swap the output and obtain the equivalent result. Therefore, $p_d \in [0.5, 1]$.

The probability of the detected misfire ratio $P(r_d)$ is computed by the conditional probability of having a misfire event (M), from the misfire ratio r_m , and detecting it (D), with a correct detection accuracy of p_d :

$$P(r_d) = P(r_m) \otimes P_d = \begin{cases} M = 0 | D = 0 & (1 - r_m)p_d \\ M = 0 | D = 1 & (1 - r_m)(1 - p_d) \\ M = 1 | D = 0 & r_m(1 - p_d) \\ M = 1 | D = 1 & r_m p_d \end{cases} \quad (6.71)$$

The result is a new binomial distribution with a detected misfire ratio of $r = r_d$, where the detected misfire ratio is computed as a function of the actual misfire ratio r_m :

$$r_d = r_m(2p_d - 1) - p_d + 1 \quad (6.72)$$

Finally, by the transformation and composition of the probability distributions

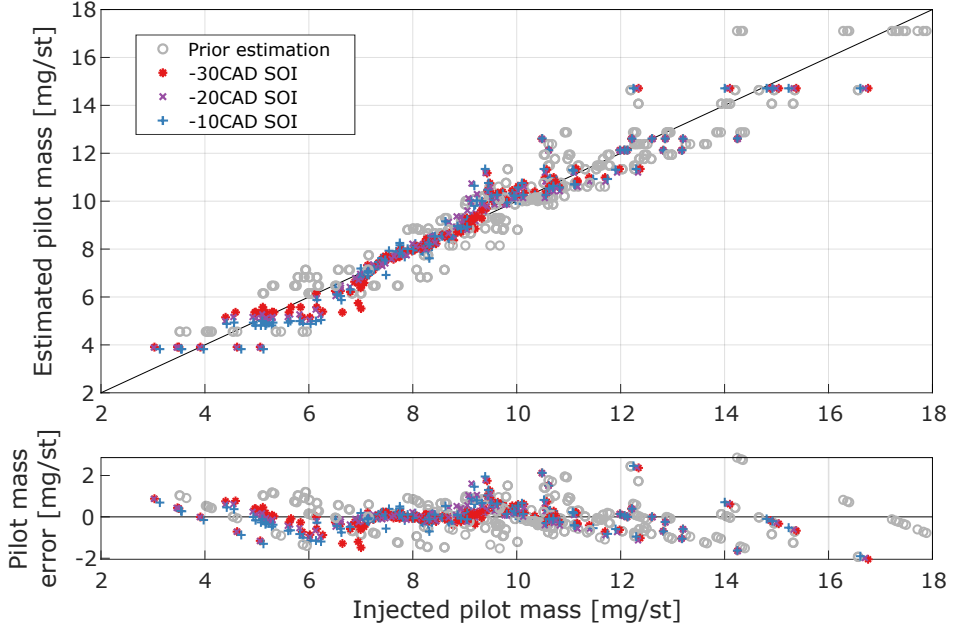


Figure 6.14: Estimated pilot mass as a function of the actual injected pilot mass, for the prior estimation (injector's calibration) and the estimation with the proposed method. Pilot on-times from $0.22ms$ to $0.36ms$ at rail pressures from $800bar$ to $1600bar$ were used. The engine was run at $10bar$ IMEP and $1200RPM$. Three injection timings are shown in the plot. 100 cycles (samples) were collected for each operating point.

describing the misfire detection (Eq.(6.70)) and the misfire ratio uncertainty (Eq.(5.19)), the conditional distribution of the estimated pilot misfire ratio is:

$$P(\hat{r}_m | n, N, m_{pilot}) = \mathcal{B}_N(\hat{r}_m | n, N) \mathcal{N}(\hat{r}_m | \mu_{r_m}, \sigma_{r_m}^2) \quad (6.73)$$

where \hat{r}_m is estimated as a function of the detected misfire ratio by Eq.(6.72). μ_{r_m} is the nominal misfire ratio in Eq.(5.16) expressed as a function of the unknown pilot mass $\mu_{r_m} = f_{r_m}(m_{pilot})$.

A block diagram illustrating the algorithm, with the models used at each step, is devised in Figure 6.13.

6.6.2 Experimental results

For the experimental validation of the proposed estimation method, 100 cycles were sampled from the engine run at $10bar$ IMEP, $1200RPM$, for different pilot on-times, SOI and rail pressures. Based on the misfire detectors, the best detection accuracy of $p_d = 0.98$ was selected. In Figure 6.14, a comparison

of the nominal pilot mass of the prior (from the injector's map) and the final estimation is plotted.

The standard deviation in the pilot mass error is reduced from 0.79mg/st to 0.57mg/st . The method improves the estimation accuracy of the pilot mass estimation in the range of the pilot misfire transition. For the experiments, this occurs for pilot masses between 5mg/st and 12mg/st (see Figure 5.5). In this region, the standard deviation of the error reduces from 0.66mg/st to 0.27mg/st . The error in the estimation is due to modeling errors in the pilot misfire ratio as well as the limited number of samples for its measurement. The estimation uncertainty is also reduced i.e., within which bounds the actual pilot mass is expected. The reduction in the estimation error and uncertainty is more significant for on-times between 0.24ms and 0.34ms , since outside this interval the pilot misfire ratio sensitivity is close to zero. The initial uncertainty of $\pm 1.8\text{mg/st}$ is reduced to $\pm 0.5\text{mg/st}$. Due to the different pilot misfire ratio sensitivity at different SOI for a constant pilot mass, smaller pilot masses are estimated with a smaller error for late SOI.

From the assumptions taken for the derivation of the estimation method, the pilot mass estimation accuracy is improved for operating conditions with a smooth enough pilot misfire ratio transition. The characteristic curve has to be calibrated off-line for the same operating conditions and fuel that is used during the on-line application. For a detailed discussion about the estimation robustness, model error and sampling sensitivity, see Publication VIII.

On-line Model Adaptation

The reduced complexity of the predictive models limits the prediction accuracy required for the in-cycle closed-loop combustion control. On-line adaptation permits to achieve the required prediction accuracy without increasing the model complexity and calibration effort. This chapter presents the formulation and on-line adaptation techniques for the predictive models.

7.1 Model Adaptation

In-cycle closed-loop combustion control relies on accurate model prediction to overcome the intrinsic delay of the measurements. For their implementation and real-time execution, the models were formulated considering the trade-off between model complexity and prediction accuracy. However, the simplifications limit the prediction accuracy of the models over the whole range of operating conditions, component tolerances and system uncertainties. To overcome this limitation, alternative solutions may be higher model complexity, which consumes large implementation resources; or multiple calibrations for each operation condition, which is cumbersome and time consuming to calibrate, and requires a large amount of data. However, even though these options can increase the prediction accuracy, this is not guaranteed under the variations due

to production tolerances and engine aging.

A more robust approach is to adjust the model parameters on-line. The parameters are adapted based on the model prediction performance, evaluated from the measurements. The models were formulated for a reduced complexity and local prediction accuracy. Their low complexity ensures that the models can be implemented in the FPGA. The predictive models were also designed considering their on-line adaptation, which eases the application of adaptation techniques.

Examples of on-line model adaptation are the estimation of the heat capacity ratio and compression ratio (Klein et al., 2004), air/fuel ratio and trapped mass (Tunestål, 2001; Di Leo, 2015), the injected fuel mass (Finesso and Spessa, 2015), or combustion parameters such as the center of combustion (CA50) (Tschanz et al., 2013). In this work, the predictive models for the pilot and main ignition-delay, burnt pilot mass and engine load were adapted on-line.

7.1.1 State estimation

The on-line parameter estimation derives from their formulation as a dynamic system. The state-space model description is (Johansson, 1993):

$$\begin{aligned}\psi_{k+1} &= \psi_k + v \\ \mathbf{z}_k &= f(\psi_k, u_k) + \nu\end{aligned}\tag{7.1}$$

The parameters are assumed to be constant, hence the state matrix is the identity. The prior knowledge of the model is expressed by the parameters uncertainty (v) and the measurement error uncertainty (ν). The uncertainty is modeled as random white noise, assuming the previous and the updated parameter errors are uncorrelated. ψ is a vector containing all the model parameters of each of the cylinders. The predictive model f computes the cylinders output in the vector \mathbf{z} as a function of the model parameters and inputs u each cycle k .

The model parameters are adapted by their on-line identification. For their identification, the parameters are corrected iteratively to reduce the prediction error, computed each cycle from the new measurements. The parameter adaptation consists in the estimation of the states in Eq.(7.1). With a model linear-in-parameters, this is achieved optimally by a Kalman filter (Johansson, 1993). For the model parameter estimation, the output transition matrix is $H_k = u_k$. Hence, the output equation of the linear system is represented as:

$$\mathbf{z}_k = u_k \psi_k + \nu\tag{7.2}$$

The states are estimated in two steps. The algorithm starts with the prediction step, where the error covariance P is projected ahead. Since the state transition matrix is the unity, the projected covariance is equal to the previous with the addition of the state covariance matrix R and the measurement covariance matrix Q :

$$\begin{aligned}\hat{\psi}_{k|k-1} &= \hat{\psi}_{k-1|k-1} + R \\ P_{k|k-1} &= P_{k-1|k-1} + Q\end{aligned}\tag{7.3}$$

The Kalman gain is computed as:

$$K = P_{k|k-1} u_{k-1}^\top (u_{k-1} P_{k|k-1} u_{k-1}^\top + R)^{-1}\tag{7.4}$$

The estimation is performed at the correction step, once the measurements are obtained for the error computation:

$$\begin{aligned}\hat{\psi}_{k|k} &= \hat{\psi}_{k|k-1} + K (z_k - u_k \hat{\psi}_{k|k-1}) \\ P_{k|k} &= (I - K u_k) P_{k|k-1}\end{aligned}\tag{7.5}$$

The system noise can be used as a tuning parameter for the convergence speed.

7.2 Multi-Cylinder Adaptation

The information from each of the cylinders is used for the adaptation of the model parameters. This is referred as multi-cylinder adaptation. Three adaptation strategies were investigated in Publication X. The first is to use the same set of parameters common to all the cylinders. The second is to adapt each parameter individually for each cylinder. The third approach is an intermediate solution, where some of the parameters are adapted individually for each cylinder, and the rest common to all the cylinders. The state-space formulation for the parameter adaptation with each of the strategies is detailed in this section.

Common parameters

Using the same set of parameters common to all the cylinders, the output vector is extended with the predictions of each of the cylinders. The output matrix of

the state-space representation is:

$$\begin{bmatrix} z_1 \\ z_2 \\ \vdots \\ z_{n_{cyl}} \end{bmatrix}_k = \begin{bmatrix} u_1^1 & u_1^2 & \dots & u_1^n \\ u_2^1 & u_2^2 & \dots & u_2^n \\ \vdots & \vdots & \ddots & \vdots \\ u_{n_{cyl}}^1 & u_{n_{cyl}}^2 & \dots & u_{n_{cyl}}^n \end{bmatrix}_k \begin{bmatrix} \psi^1 \\ \psi^2 \\ \vdots \\ \psi^n \end{bmatrix}_k \quad (7.6)$$

Individual parameters

The cylinder-to-cylinder variations reduce the prediction accuracy when the same parameters are used. This can be compensated by adapting the parameters individually for each cylinder. The output matrix of the state-space representation is:

$$\begin{bmatrix} z_1 \\ z_2 \\ \vdots \\ z_{n_{cyl}} \end{bmatrix}_k = \begin{bmatrix} u_1^1 & u_1^2 & \dots & u_1^n \\ u_2^1 & u_2^2 & \dots & u_2^n \\ \vdots & \vdots & \ddots & \vdots \\ u_{n_{cyl}}^1 & u_{n_{cyl}}^2 & \dots & u_{n_{cyl}}^n \end{bmatrix}_k \begin{bmatrix} \psi_1^1 & \psi_1^2 & \dots & \psi_1^n \\ \psi_2^1 & \psi_2^2 & \dots & \psi_2^n \\ \vdots & \vdots & \ddots & \vdots \\ \psi_{n_{cyl}}^1 & \psi_{n_{cyl}}^2 & \dots & \psi_{n_{cyl}}^n \end{bmatrix}_k \quad (7.7)$$

For a model with n parameters and n_{cyl} cylinders, the total number of parameters is $N_{par} = n \cdot n_{cyl}$.

Reduced parameters

The disadvantage of the previous approach is a lower robustness and higher sensitivity to measurement errors. Furthermore, the total number of parameters is proportional to the number of cylinders. For this reason, an intermediate approach was proposed. The parameter vector (ψ) is divided into some cylinder-individual parameters (ξ) and the rest of the cylinder-common parameters (φ). This is referred as a model reduction based on ξ . The final parameter vector is:

$$\psi = \begin{bmatrix} \xi_1 \\ \vdots \\ \xi_{n_{cyl}} \\ \varphi \end{bmatrix} \quad (7.8)$$

In the scope of Publication X, only one parameter was adapted individually.

The output matrix of the state-space representation is:

$$\begin{bmatrix} z_1 \\ z_2 \\ \vdots \\ z_{n_{cyl}} \end{bmatrix}_k = \begin{bmatrix} u_1^1 & u_2^1 & \dots & u_{n_{cyl}}^1 \\ u_1^2 & u_2^2 & \dots & u_{n_{cyl}}^2 \\ \vdots & \vdots & \ddots & \vdots \\ u_1^n & u_2^n & \dots & u_{n_{cyl}}^n \end{bmatrix}_k \begin{bmatrix} \xi_1 & \xi_2 & \dots & \xi_{n_{cyl}} \\ \varphi^1 & \varphi^1 & \dots & \varphi^1 \\ \vdots & \vdots & \ddots & \vdots \\ \varphi^n & \varphi^n & \dots & \varphi^n \end{bmatrix}_k \quad (7.9)$$

For a model with n parameters, n_{cyl} cylinders, and one individually adapted parameter, the total number of parameters is $N_{par} = n_{cyl} + (n - 1)$.

7.2.1 Estimation robustness

The estimation robustness quantifies the sensitivity of the correct parameter estimation despite inputs and measurement errors. The inference of the parameter values from the information of the different cylinders increases the estimation robustness. The robustness of the estimators is studied by adding an input (ϵ_u) and measurement (ϵ_z) error to one of the cylinders:

$$\begin{bmatrix} z_1 + \epsilon_z \\ z_2 \\ \vdots \\ z_{n_{cyl}} \end{bmatrix} = \begin{bmatrix} u_1 + \epsilon_u \\ u_2 \\ \vdots \\ u_{n_{cyl}} \end{bmatrix} \psi \quad (7.10)$$

The added disturbances have to be cycle-to-cycle uncorrelated, as they would be compensated otherwise. In this study, the disturbance ϵ is a random variable with a zero-mean normal distribution of different variance σ_ϵ^2 . The robustness metric Γ is the ensemble of the output error for each realization of ϵ (Christopher Frey and Patil, 2002):

$$\begin{aligned} \Gamma &= \mathbb{E}(z - \hat{z}_\epsilon) \\ \epsilon &\sim \mathcal{N}(0, \sigma_\epsilon^2) \end{aligned} \quad (7.11)$$

7.2.2 Sensitivity analysis

The sensitivity to parameter errors is computed analytically. The sensitivity analysis uses the relative error of the model f as a function of the parameter error Δ_ψ :

$$\epsilon_f = \frac{f(\psi, u) - f(\psi + \Delta_\psi, u)}{f(\psi, u)} \quad (7.12)$$

7.2.3 Design of parameter reduction

The average error obtained with the reduced multi-cylinder adaptation achieves similar values for any selected variable (ξ) for its individual cylinder adaptation. However, the robustness and sensitivity properties of the reduced multi-cylinder adaptation are different. In order to select which parameter base the reduced multi-cylinder adaptation on, a systematic method was proposed in Publication X. The correlation between the difference of the individual and common parameter multi-cylinder model outputs (δ_f), and the adapted values of each parameter (δ_{ξ_i}) is studied. The correlation ρ_i is computed by the Pearson correlation coefficient for each of the individually adapted parameters (i):

$$\rho_i(\delta_f, \delta_{\xi_i}) = \frac{\text{Cov}(\delta_f, \delta_{\xi_i})}{\sigma_{\delta_f} \sigma_{\delta_{\xi_i}}} \quad (7.13)$$

where the difference variables are:

$$\begin{aligned} \delta_f &= f(\psi, u) - f([\xi_i, \varphi], u) \\ \delta_{\xi_i} &= \psi_i - \xi_i \end{aligned} \quad (7.14)$$

ψ_i refers to the common adapted parameter that corresponds to the individually adapted parameter ξ_i . The parameter with the largest correlation is selected for the adaptation reduction. The largest correlation represents which parameter has the strongest impact on the cylinder-to-cylinder error when the parameters are common to all the cylinders. This permits a reduced variance of the rest of the parameters, which reduces the sensitivity to input errors and increases the robustness.

7.3 Adaptation of Predictive Combustion Models

The predictive combustion models were adapted on-line by the proposed method to increase their prediction accuracy. The performance (measured by the error dispersion), robustness and sensitivity of each of the adaptation approaches were studied for the pilot and main ignition-delay, and the pilot burnt mass. Although not included in Publication X, the engine load model was also adapted on-line by these techniques. The non-linear model formulation adapted by the Extended Kalman Filter (EKF) was compared to the linear formulation for their adaptation with the Kalman Filter (KF). For the linear model formulation, the necessary assumption is that the system noise can be represented by white

Gaussian noise after the linear transformation. It was concluded the assumption is valid and the linear formulation of the models provides the required prediction accuracy. The linear transformation of the models for their adaptation and the experimental results are discussed in the following subsections.

7.3.1 Linear model formulation for adaptation

The predictive models are non-linear-in-parameters equations that require a reformulation for the linear adaptation of the parameters. The predictive IMEP model in Eq.(5.54) is linear and can be adapted with the same structure. The linear reformulation of the pilot ignition-delay, main ignition-delay and pilot burnt mass models is detailed below.

Pilot ignition-delay

The pilot ignition-delay model in Eq.(5.47) is reformulated as linear by taking logarithms. In matrix form, the system state-space representation for its adaptation is:

$$\begin{aligned} \begin{bmatrix} \log(K_p) \\ \alpha_p \end{bmatrix}_{k+1} &= \mathbf{I}_{2 \times 2} \begin{bmatrix} \log(K_p) \\ \alpha_p \end{bmatrix}_k + v_k^p \\ \left[\log\left(\frac{\widehat{\Delta\theta}_{ID}^{pilot}}{N_{eng}}\right) \right]_k &= [1 \quad p_{SOI}]_k \begin{bmatrix} \log(K_p) \\ \alpha_p \end{bmatrix}_k + \nu_k \end{aligned} \quad (7.15)$$

Main ignition-delay

The same mathematical manipulation is used for the linear formulation of the main ignition-delay model in Eq.(5.48):

$$\begin{aligned} \begin{bmatrix} \log(K_m) \\ \alpha_m \\ \beta_m \\ \gamma_m \end{bmatrix}_{k+1} &= \mathbf{I}_{4 \times 4} \begin{bmatrix} \log(K_m) \\ \alpha_m \\ \beta_m \\ \gamma_m \end{bmatrix}_k + v_k^m \\ \left[\log\left(\frac{\widehat{\Delta\theta}_{ID}^{main}}{N_{eng}}\right) \right]_k &= \begin{bmatrix} 1 & p_{SOI} & \frac{m_{inj}}{p_{rail}} & \delta_{comb}^{pilot} \end{bmatrix}_k \begin{bmatrix} \log(K_m) \\ \alpha_m \\ \beta_m \\ \gamma_m \end{bmatrix}_k + \nu_k \end{aligned} \quad (7.16)$$

Pilot burnt mass

The pilot burnt mass in Eq.(5.50) is non-linear in parameters. The inputs can be lumped together to reformulate the system as linear. The equation is rewritten as:

$$m_{burnt}^{pilot} = m_0 + a_p t_{inj} + b'_p t_{inj} p_{rail} + c'_p t_{inj} (\Delta\theta_{ID}^{pilot})^2 \quad (7.17)$$

The lumped parameters are $b'_p = a_p b_p$ and $c'_p = a_p c_p$. In matrix form, the system state-space representation for its adaptation is:

$$\begin{bmatrix} m_0 \\ a_p \\ b'_p \\ c'_p \end{bmatrix}_{k+1} = \mathbf{I}_{4 \times 4} \begin{bmatrix} m_0 \\ a_p \\ b'_p \\ c'_p \end{bmatrix}_k + \nu_k^{pm} \quad (7.18)$$

$$\begin{bmatrix} \hat{m}_{burnt}^{pilot} \end{bmatrix}_k = \begin{bmatrix} 1 & t_{inj} & t_{inj} p_{rail} & t_{inj} (\Delta\theta_{ID}^{pilot})^2 \end{bmatrix}_k \begin{bmatrix} m_0 \\ a_p \\ b'_p \\ c'_p \end{bmatrix}_k + \nu_k^{pm}$$

7.3.2 Experimental results

The prediction accuracy, robustness and sensitivity of the on-line adapted models was studied for the different adaptation schemes. Experimental data was collected for individual sweeps of pilot SOI, pilot mass, main SOI, engine loads and rail pressures. The engine was operated at 1200RPM with no EGR. The models were calibrated off-line with engine data fueled with Diesel. The properties of the on-line adaptation were studied by the engine data fueled with Diesel, HVO and RME. The model prediction accuracy adapted with the different strategies was quantified by the cylinder average error and the total error 95% confidence interval over the whole data set.

Parameter reduction

The correlation analysis for the design of the parameter reduction of the models is summarized in Table 7.1. In the case of the pilot ignition-delay model, the correlation value is small for both parameters. Hence, both parameters can be selected for the reduced multi-cylinder adaptation. However, due to the model structure, the adaptation is more robust when the multi-cylinder parameter reduction is based on α_p as the individual cylinder parameter. This is discussed

in more detail in the following subsections. For the main ignition-delay model, $\log K_m$ is selected as the base for the parameter reduction. In the pilot burnt mass model, the higher correlation of the parameter b'_p reveals that it was the combination of the rail pressure and the pilot on-time that have the strongest significance on the cylinder-to-cylinder error. This is in agreement with the physical interpretation that cylinder-to-cylinder variations of the pilot burnt mass are a consequence of the injector-to-injector pilot mass variations. Hence, b'_p is selected as the base for the parameter reduction.

Table 7.1: Correlation analysis for the multi-cylinder adaptation reduction.

Model	Parameter	Correlation coefficient
Pilot ignition-delay	$\log K_p$	0.0578
	α_p	0.002
Main ignition-delay	$\log K_m$	0.2136
	α_m	$3 \cdot 10^{-4}$
	β_m	$2.4 \cdot 10^{-3}$
	γ_m	$2.7 \cdot 10^{-4}$
Pilot burnt mass	m_0	0.03
	a_p	0.01
	b'_p	0.56
	c'_p	0

Prediction accuracy

An example of the prediction accuracy of the models adapted with the different strategies is plotted in Figure 7.1. The results are summarized in Table 7.2. The results indicate that the on-line adaptation of the models increases the prediction accuracy, with a reduced bias and error dispersion. This becomes more relevant when the engine runs with a different fuel than the one used for the model calibration. The results validate the initial assumption of the system noise being approximately linear after the linear formulation of the models. The common multi-cylinder model structure results in a cylinder-to-cylinder error, where the adaptation is a trade-off between the error of all the cylinders. The reduced multi-cylinder adaptation can compensate for the cylinder-to-cylinder error and achieve similar performance as the individual multi-cylinder adaptation, but with a reduced number of parameters. For the pilot ignition-delay, the initial model error with a confidence interval of $[-0.50, 0.57]CAD$ can be reduced to

$[-0.30, 0.30]CAD$ for any of the fuels by the reduced multi-cylinder adaptation. For the main ignition-delay, the initial model error between $[-0.74, 0.40]CAD$ can be reduced to $[-0.3, 0.3]CAD$ for any of the fuels by the reduced multi-cylinder adaptation. For the burnt pilot mass, the initial model error between $[-1.57, 0.51]mg$ can be reduced to $[-0.27, 0.22]mg$ for any of the fuels by the reduced multi-cylinder adaptation.

Robustness and sensitivity

The robustness analysis for each of the models, detailed in Publication X, show that the common or reduced multi-cylinder adaptation increases the robustness of the adaptation to input and measurement errors. By the correlation analysis, the parameter reduction based on the one with the strongest correlation can increase the adaptation robustness. Because of the stronger correlation between the parameter and the cylinder-to-cylinder error, the impact of the errors is reduced by combining the information from the non-faulty cylinders. For the reduced multi-cylinder adaptation, the model structure propagates the errors differently depending on the parameter selected for the reduction. This can be studied by the analytical sensitivity analysis.

Taking as an example the pilot ignition-delay model, the physical interpretation of α_p is the activation energy, and therefore should be equal for all the cylinders. However, the model structure results in $\log(K_p)$ being sensitive to measurement errors but not to input errors. Hence, by the individual adaptation of $\log(K_p)$, the measurement errors are incorrectly compensated, reducing the adaptation robustness. On the other hand, when α_p is individually adapted, the sensitivity of α_p to the inputs (p_{SOI}) avoids its individual adaptation to compensate for measurement errors, as $\log(K_p)$ cannot compensate for an individual measurement error. By exploiting the properties of the model structure, the adaptation robustness is increased.

In the case of the main ignition-delay, except for the pilot misfire, the model has a very low sensitivity to all the input variables. However, even in the case of the pilot misfire, the adaptation of the parameters increases the model robustness. For an erroneous pilot misfire signal, γ_m will converge to zero as the pilot misfire will not result in a significant error improvement of the output signal.

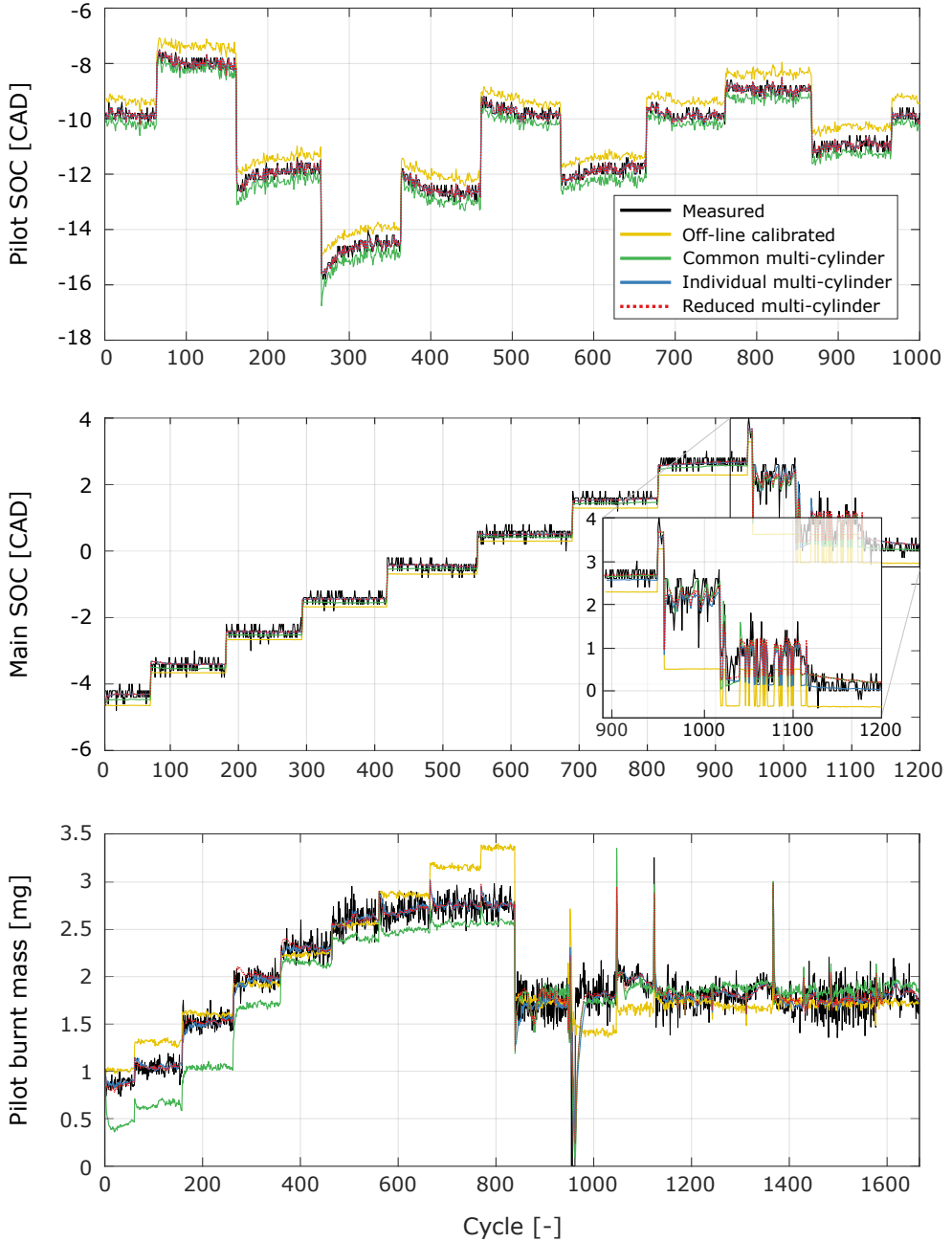


Figure 7.1: Measured and predicted signals of the pilot SOC (upper plot), main SOC (middle plot) and pilot burnt mass (lower plot) adapted by the different strategies. For the pilot ignition-delay, the engine was run at 10bar IMEP, 1200RPM and 1200bar rail pressure, for different pilot SOI. For the main ignition-delay, the engine was run at 1200RPM, 1200bar rail pressure, for different main SOI and engine loads. The peaks around cycle 1000 occur due to the transition of pilot misfire events (zoomed in). For the pilot burnt mass, the engine was run at 10bar IMEP, 1200RPM, for different pilot on-times and rail pressures. The peaks of the pilot burnt mass occur due to the closed-loop controller transient at the rail pressure steps. The engine was fueled with HVO.

Table 7.2: Summary of the pilot ignition-delay, main ignition-delay and pilot burnt mass models prediction accuracy, measured by the total 95% confidence interval and the individual cylinder-averaged error. The engine was operated at steady-state with the different adaptation methods for Diesel, RME and HVO. The total number of model parameters is indicated (#).

Model	Adaptation strategy	#	Fuel	95% CI [CAD]	Cylinder-averaged error [CAD]
Pilot ignition-delay	Off-line calibration	2	Diesel	$[-0.50, 0.57]$	$[0, -0.44, -0.15, -0.14, -0.26, 0]$
			RME	$[-0.50, 0.75]$	$[0.26, -0.4, -0.3, -0.37, 0.7, 0.37]$
			HVO	$[-0.18, 1.36]$	$[0.64, 0.41, 0.80, 0.85, 0.40, 0.91]$
	Common multi-cylinder	2	Diesel	$[-0.37, 0.37]$	$[0.2, -0.16, 0, 0, -0.12, 0.21]$
			RME	$[-0.38, 0.42]$	$[0, -0.14, 0, 0.12, -0.21, 0.21]$
			HVO	$[-0.45, 0.50]$	$[0, -0.21, 0, 0, -0.25, 0.28]$
	Individual multi-cylinder	12	Diesel	$[-0.26, 0.27]$	$[0, 0, 0, 0, 0, 0]$
			RME	$[-0.28, 0.29]$	$[0, 0, 0, 0, 0, 0]$
			HVO	$[-0.30, 0.30]$	$[0, 0, 0, 0, 0, 0]$
	Reduced multi-cylinder	7	Diesel	$[-0.26, 0.26]$	$[0, 0, 0, 0, 0, 0]$
			RME	$[-0.28, 0.29]$	$[0, 0, 0, 0, 0, 0]$
			HVO	$[-0.30, 0.30]$	$[0, 0, 0, 0, 0, 0]$
Main ignition-delay	Off-line calibration	4	Diesel	$[-0.74, 0.40]$	$[0.17, 0.02, 0, -0.17, -0.22, -0.25]$
			RME	$[-2.28, 0.97]$	$[-0.2, -0.3, -0.2, -0.3, -0.4, 0.4]$
			HVO	$[0.1, 0.94]$	$[0.5, 0.59, 0.55, 0.52, 0.44, 0.5]$
	Common multi-cylinder	4	Diesel	$[-0.36, 0.41]$	$[0.24, 0.1, 0, -0.1, -0.14, -0.17]$
			RME	$[-0.37, 0.37]$	$[0.13, 0, 0.12, 0, -0.1, -0.1]$
			HVO	$[-0.32, 0.34]$	$[0, 0.1, 0, 0, -0.1, 0]$
	Individual multi-cylinder	24	Diesel	$[-0.28, 0.27]$	$[0, 0, 0, 0, 0, 0]$
			RME	$[-0.28, 0.33]$	$[0, 0, 0, 0, 0, 0]$
			HVO	$[-0.3, 0.31]$	$[0, 0, 0, 0, 0, 0]$
	Reduced multi-cylinder	9	Diesel	$[-0.28, 0.27]$	$[0, 0, 0, 0, 0, 0]$
			RME	$[-0.3, 0.3]$	$[0, 0, 0, 0, 0, 0]$
			HVO	$[-0.3, 0.31]$	$[0, 0, 0, 0, 0, 0]$
Pilot burnt mass	Off-line calibration	4	Diesel	$[-1.57, 0.51]$	$[-0.7, -0.9, -0.37, 0, -0.3, 0.25]$
			RME	$[-1.66, 0.49]$	$[-0.62, -1, -0.33, 0, -0.3, 0.13]$
			HVO	$[-0.99, 0.76]$	$[-0.3, -0.56, -0.17, 0.29, 0, 0.3]$
	Common multi-cylinder	4	Diesel	$[-0.77, 0.74]$	$[-0.35, -0.59, 0, 0.28, 0, 0.62]$
			RME	$[-0.85, 0.7]$	$[-0.28, -0.68, 0, 0.32, 0, 0.5]$
			HVO	$[-0.68, 0.58]$	$[-0.25, -0.51, 0, 0.38, 0, 0.35]$
	Individual multi-cylinder	24	Diesel	$[-0.19, 0.18]$	$[0, 0, 0, 0, 0, 0]$
			RME	$[-0.24, 0.23]$	$[0, 0, 0, 0, 0, 0]$
			HVO	$[-0.23, 0.21]$	$[0, 0, 0, 0, 0, 0]$
	Reduced multi-cylinder	9	Diesel	$[-0.21, 0.17]$	$[0, 0, 0, 0, 0, 0]$
			RME	$[-0.26, 0.21]$	$[0, 0, 0, 0, 0, 0]$
			HVO	$[-0.27, 0.22]$	$[0, 0, 0, 0, 0, 0]$

Closed-Loop Combustion Controller Design

This chapter gives an overview of the considerations and design process of the in-cycle closed-loop combustion controller. The architecture of the controller, with the multiple time scales, is presented. The controller design is discussed based on the in-cycle closed-loop controllability limitations. The impact of the multi-loop cascade controllers interaction on the combustion control dynamics is discussed. The challenges and solutions to possible stability problems are analyzed.

8.1 In-Cycle Controller Design

The design of the in-cycle controller consist of the selection of the regulated control input to reduce the disturbance effect on the controlled parameter, in order to fulfill the specified system-performance requirements. The system-performance sets the demands on a system state, where a measured output provides information of it. Engine performance requirements relate to efficient, durable and reliable operation subject to emissions and hardware constraints. A system analysis allows for an effective controller design based on the control targets.

8.1.1 Control targets

A number of combustion control targets have been investigated in the literature (see Section 1.2.2 for an overview). The control targets can be classified by the disturbance rejected, the control input and the control strategy, summarized in Table 8.1:

Table 8.1: Summary of in-cycle combustion control targets with their associated variables.

Control target		Variable
Disturbance rejection	Disturbance	p_{IVC} , m_{IVC} , EGR, m_{inj}^i , θ_{SOC}^i ,
	rejection	m_{burnt}^i , HR_{peak} , NO_x , p_{max} , dp_{max}
Control input		θ_{SOI}^i , t_{inj}^i , m_{AdBlue} , θ_{SOI}^{AdBlue} , θ_{IVC} , θ_{EVO} , θ_{SI}
Control strategy	Parameter tracking	θ_{SOC}^i , CA50, $\Delta\theta_{ID}$, CA50 $_{NO_x}$, IMEP
	Trajectory deviation	p_{cyl} , AHR, NO_x
	Constrained optimization	Criteria: η_{th} , NO_x
		Constraints: p_{max} , dp_{max} , T_{exh}^{max} , T_{exh}^{min} , NO_x^{max}

To compensate for a determined disturbance, the controller design selects which system output should be monitored. When the effect of the disturbance is directly correlated between the measured output and control input, the design is straight-forward. For example, the intake disturbance effects on the start of combustion can be compensated by the regulation of the start of injection. However, some other control strategies require a deeper analysis. For example, to select the regulated parameter to achieve the maximum indicated efficiency based on the disturbance effects on the pilot combustion.

Disturbances

The in-cycle disturbances impact the state at the intake valve closing (p_{IVC} , m_{IVC}), the EGR, the fuel mass of the multiple injection (m_{inj}^i) and their corresponding burnt fuel mass (m_{burnt}^i), which includes a possible misfire, the combustion timing of each fuel injection (θ_{SOC}^i), the NO_x formation, maximum pressure (p_{max}) and maximum pressure rise rate (dp_{max}), among other effects. The monitoring of the disturbances is commonly obtained by the estimation of their effects from in-cylinder pressure measurements.

Controlled outputs

The system outputs monitor the effect of the disturbances on the combustion progress and are used for in-cycle feedback to the controller. Depending on the control strategy, different outputs are used for feedback. For control based on parameter tracking, different combustion metrics, such as the start of combustion (θ_{SOC}^i), center of combustion (CA50), ignition-delay ($\Delta\theta_{ID}$) or center of NO_x formation (CA50_{NO_x}) can provide feedback. A more advanced strategy is to control a crank angle resolved variable, such as the pressure (p_{cyl}), accumulated heat release (AHR) or NO_x formation, to follow a prescribed trajectory. Another control strategy is to base the control on a constrained optimization criterion. An example is the indicated thermal efficiency (η_{th}), constrained under the maximum in-cylinder pressure (p_{max}), the maximum combustion noise (dp_{max}), the exhaust temperature (T_{exh}), or exhaust NO_x.

Control inputs

The in-cycle controlled inputs are determined by the degrees of freedom of the combustion system. Typically, the fuel injection pulses θ_{SOI}^i , t_{inj}^i are the controlled parameters. Additional degrees of freedom can be provided by variable valve timings (θ_{IVC} , θ_{EVO}), direct urea injection for NO_x reduction (m_{AdBlue} , θ_{SOI}^{AdBlue}) and in the case of SI engine, the spark-ignition timing (θ_{SI}). Advanced injection systems may allow for rate shaping of the fuel injection. In this thesis, the control inputs were limited to the injection timings and durations of a pilot-main injection.

8.1.2 Controller architecture

Traditionally, the combustion has been regulated in open-loop. By the closed-loop feedback of the measurements to the controllers, the system is more resilient to external disturbances. Depending on the subsystem affected, these are classified as combustion disturbances and engine disturbances. The in-cycle regulator adjusts the control action to compensate for disturbances that affect the combustion process. The cycle-to-cycle regulator compensates for disturbances affecting the combustion process and the engine operation. The monitoring of the disturbance effects is measured and fed back to the controllers.

The closed-loop architecture for the in-cycle combustion control is illustrated in Figure 8.1. Higher position indicates a higher hierarchy level of the conceptual

block. Outer blocks execute on a multi-cycle time basis, intermediate blocks on a cycle-to-cycle, and the center blocks in-cycle. The system is separated in the combustion process and the engine. This architecture permits higher modularity, which eases the controller design to fulfill the demands on the engine operation by the multiple combinations of feedback signals, controllers and inputs.

At the highest hierarchy level, the strategy coordinator adapts the combustion controllers to achieve the power demands under the operational constraints. Different control strategies can be followed depending on the current operating conditions, legislation levels on emissions (depending on the market), performance selected by the user (eco-mode, efficiency-mode, power-mode, etc.) and engine mode (cold start, torque reduction, engine protection, etc.). The strategy coordinator determines the reference variables, feedback signals and controllers depending on the control targets. The set-point reference and feed-forward for the in-cycle controller are set by the cycle-to-cycle controller. The in-cycle controller management supervises changes in the feedback signals and control inputs, adjusting the feedback for the in-cycle controller. This is discussed in detail in Section 9.3. The observer monitors the combustion based on the in-cycle measurements.

8.2 In-Cycle Controllability

In-cycle combustion controllability refers to the ability of the inputs to steer the combustion within the same cycle to a final desired state. In this study, the control inputs are the multiple fuel injections, defined by their timings and durations. Closed-loop in-cycle controllability is the ability of the controller to reach a combustion state (x), inferred from the current measurements (z), by the upcoming fuel injections (u). The concept of reachability is used in this work to study the closed-loop in-cycle controllability. The formal definitions of *reachable state* and *reachable set* are by Pecsvaradi and Narendra (1971). For each of the fuel injections (u_k), there are two states of interest, the initial state, which is a function of the previous inputs (u_{k-1}) and disturbances (ε), and the final reachable state by that injection. The initial set is the ensemble of all possible initial states. Therefore, the initial set $\mathcal{R}_{k|k-1}$ is the reachable set by the system (Φ) from the state after the previous injection (u_{k-1}) with the addition of all possible state disturbances $\varepsilon_x \in \Psi_x$ and input disturbances $\varepsilon_u \in \Psi_u$:

$$\mathcal{R}_{k|k-1} = \{x_{k|k-1} = \Phi(x_{k-1|k-1} + \varepsilon_x, u_{k-1} + \varepsilon_u), \forall \varepsilon_x \in \Psi_x, \forall \varepsilon_u \in \Psi_u\} \quad (8.1)$$

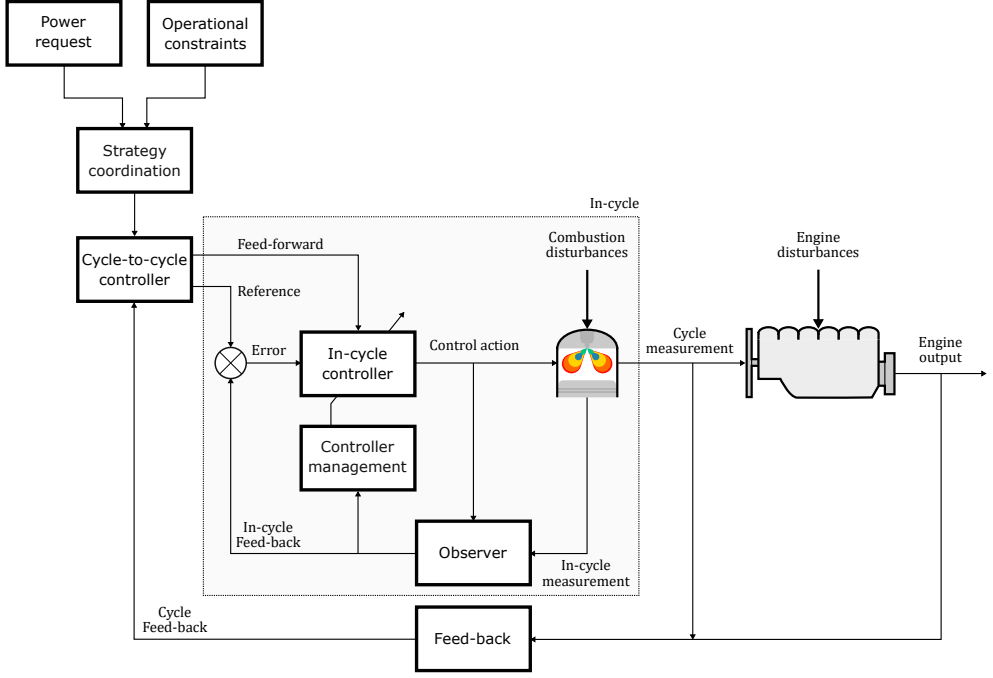


Figure 8.1: Closed-loop architecture for in-cycle combustion control. The shadowed area highlights the blocks executed in-cycle.

Given an initial state ($x_{k|k-1} \in \mathcal{R}_{k|k-1}$), the reachable set $\mathcal{R}_{k|k}$ is the ensemble of all final states that the system can be transferred to by all the possible controlled inputs $u_k \in \mathcal{U}$:

$$\mathcal{R}_{k|k} = \{x_{k|k} = \Phi(x_{k|k-1}, u_k), \forall x_{k|k-1} \in \mathcal{R}_{k|k-1}, u_k \in \mathcal{U}\} \quad (8.2)$$

Depending on the control target, only a subset of the reachable set is of interest. For disturbance rejection problems, closed-loop controllability is obtained when information from the disturbance is within the initial set, and the final set-point reference is within the reachable set of the control input. For the optimization criteria control problem, the control target is to optimize a cost function within the reachable set. The in-cycle closed-loop indicated efficiency controllability is the ability of the controller to reach the maximum indicated efficiency for a given disturbed cycle. This is the maximum reachable efficiency set:

$$\mathcal{R}_k^{\eta_{max}} = \max_{u_k \in \mathcal{U}, x_k \in \mathcal{R}_{k|k}} \eta_{th}(x_k, u_k) \quad (8.3)$$

The closed-loop controllability of the pilot combustion, main combustion and for the efficiency optimization is studied for the design of the in-cycle controllers.

8.2.1 Pilot combustion controllability

Pilot combustion is affected by the charge composition, the thermodynamic state at IVC and its evolution during the compression stroke. The pilot combustion is controlled by its injection. The disturbances affecting the initial state can be monitored, since the pilot injection starts after IVC, ensuring the closed-loop in-cycle controllability of the pilot combustion. The only limitation is imposed by its reachable set. For early pilot SOC references, the pilot combustion efficiency is limited, and even subject to misfire. Hence, the in-cycle closed-loop pilot combustion timing controllability is:

$$\text{Pilot combustion timing controllability : } \theta_{SOC}^{pilot}|_{ref} > \theta_{SOC}^{pilot}|_{min} \quad (8.4)$$

The minimum pilot SOC is imposed by the thermo-chemical chamber conditions. From the experimental results, $\theta_{SOC}^{min} \approx -25CAD$. The in-cycle closed-loop pilot burnt mass controllability is limited by the maximum combustion efficiency:

$$\text{Pilot burnt mass controllability : } m_{burnt}^{pilot}|_{ref} < m_{burnt}^{pilot}|_{max} \quad (8.5)$$

Controllability of pilot disturbances

Controllability of pilot disturbances is provided by the next fuel injection, normally the main injection. For the rejection of pilot combustion disturbances, additional time after the pilot SOC is required for its in-cycle estimation by the method in Section 6.5. As was discussed, good estimation accuracy is obtained at the peak of the heat release rate, about 2CAD after the pilot SOC. To obtain controllability, the next injection SOI (θ_{SOI}) must fulfill:

$$\text{Pilot disturbance controllability : } \theta_{SOI} > \theta_{SOC}^{pilot} + 2CAD \quad (8.6)$$

Pilot misfire in-cycle closed-loop controllability is obtained when the next injection starts after the expected pilot SOC ($\hat{\theta}_{SOC}^{pilot}$):

$$\text{Pilot misfire controllability : } \theta_{SOI} > \hat{\theta}_{SOC}^{pilot} \quad (8.7)$$

Controllability of pilot misfire was investigated in Publication XI. For single pilot injection, Eq.(8.7) determines the minimum main SOI for pilot misfire controllability. In case a second pilot can be injected, in-cycle closed-loop controllability of the second pilot is obtained when the main injection starts after the second pilot expected SOC.

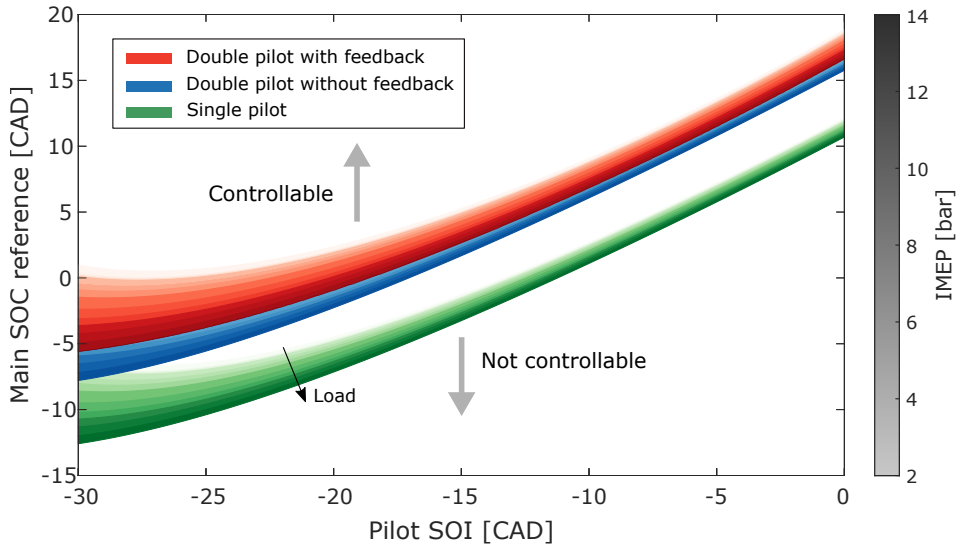


Figure 8.2: In-cycle closed-loop pilot misfire controllability with main and double pilot injection, as a function of the pilot SOI and engine load. Controllability relies on a minimum main SOC reference to guarantee feedback from the expected pilot SOC.

The previous requirements were simulated with the ignition-delay models for different loads, plotted in Figure 8.2. The pilot SOI and engine load are the independent variables. The pilot misfire controllability is a function of the pilot and main ignition-delays. The maximum span determined by the engine load is $\pm 2CAD$. The controllable pilot-main separation is determined by their respective ignition-delays, which saturate for higher in-cylinder temperatures. For double pilot injection strategies, the controllability of the second pilot requires to add its ignition-delay, of about $3CAD$, to the minimum injection separation of $5CAD$ at $1200RPM$. The controllability analysis permits to establish the minimum reference for the main SOC for a given pilot injection and injection strategy. As discussed in Publication XI, references close to the minimum main SOC will challenge the controller to achieve the set-point. The controllers will not be able to compensate possible pilot misfire in the not controllable set. The main injection will be delayed until feedback from the pilot combustion is obtained, increasing the cycle-to-cycle variations further than in open-loop.

8.2.2 Main combustion controllability

In-cycle closed-loop controllability for main combustion disturbance rejection requires that the disturbance effects on the main combustion can be estimated

before the main SOI for its timing regulation and before the EOI for its duration regulation.

Main combustion timing controllability

The main combustion timing is regulated by the main SOI. Depending on the control targets, different parameters can set the reference for the combustion timing regulation. The controllability depends on the sensitivity of the regulated parameter to the main SOI. The related main combustion parameters are:

- **SOC:** it is directly controllable by the main SOI, as long as the required main SOI (θ_{SOI}^{main*}) to reach the reference is in the main reachable set (\mathcal{R}_{main}):

$$\theta_{SOI}^{main*} = \theta_{SOC}^{main}|_{ref} - \Delta\theta_{ID}^{main} \in \mathcal{R}_{main} \quad (8.8)$$

- **CA50:** as the main SOC, it is directly controllable by the main SOI. In this case, the sensitivity is also determined by the shape of the heat release. This is affected by the premixed heat release rate, which is influenced by the combustion of previous injections. It is controllable when:

$$\theta_{SOI}^{main*} = \theta_{CA50}^{main}|_{ref} - \Delta\theta_{CA50-SOC}^{main} \in \mathcal{R}_{main} \quad (8.9)$$

- **Ignition-delay:** it can be regulated by the main SOI. However, the sensitivity is low at high loads. This may result in an unstable controller with large variations of the main SOI to achieve the set-point reference of the main ignition-delay. It is controllable when:

$$\theta_{SOI}^{main*} = \theta_{SOC}^{main} - \Delta\theta_{ID}^{main}|_{ref} \in \mathcal{R}_{main} \quad (8.10)$$

- **Premixed heat release rate:** it is indirectly regulated by the main ignition-delay. The premixed heat release rate has higher sensitivity to previous combustions. Therefore, its controllability by the main SOI regulation is limited. This is specially significant in the case of pilot misfire.
- **Maximum pressure:** the maximum pressure is controllable by the main SOI. The sensitivity is dependent on the heat release shape, cylinder volume and bulk charge mass.
- **Maximum pressure rise rate:** as for the premixed heat release rate, the controllability is limited due to lower sensitivity to the main SOI.

- **Indicated efficiency:** the sensitivity to the main SOI depends on the combustion timing and shape. This is more significantly affected by previous combustions. Therefore, the indicated efficiency controllability relies on the ability of the main SOI to adequately compensate for previous disturbances, estimated from the heat release measurements. In-cycle closed-loop controllability of the indicated efficiency is therefore obtained when:

$$\theta_{SOI}^{main*} > \theta_{SOC}^{pilot} + 2CAD \in \mathcal{R}_{main}^{\eta_{max}} \quad (8.11)$$

where θ_{SOI}^{main*} is the main SOI required to obtain the maximum reachable indicated efficiency of that cycle. This is analyzed in detail in subsection 8.2.3.

With one degree of freedom, only one of the previous parameters can be regulated, limited by the in-cycle closed-loop combustion controllability. Therefore, the in-cycle closed-loop controllability is limited depending on the disturbance.

Main combustion duration controllability

The main combustion duration is regulated to obtain the demanded engine torque i.e., IMEP. The load is directly controllable from the main fuel injection on-time. For the regulation of the main on-time, closed-loop in-cycle controllability is obtained for long enough main injections. Feedback parameters for the main on-time regulation are the main SOC, the ignition-delay and the heat release peak of the premixed combustion. Main SOC feedback provides in-cycle closed-loop controllability when:

$$\text{Main SOC controllability : } \theta_{EOI}^{main} > \theta_{SOC}^{main} \quad (8.12)$$

Main ignition-delay feedback provides in-cycle closed-loop controllability when the ignition-delay is shorter than the injection duration:

$$\text{Main ignition-delay controllability : } \Delta\theta_{inj}^{main} > \Delta\theta_{ID}^{main} \quad (8.13)$$

where $\Delta\theta_{inj}^{main}$ is the injection on-time expressed in crank angle degrees. This expression is equivalent to Eq.(8.12). The premixed rate of the main combustion is monitored at its peak location, which is about 2CAD after the main SOC (see Section 4.3). Therefore, main premixed rate feedback provides in-cycle closed-loop controllability when:

$$\text{Premixed heat release controllability : } \theta_{EOI}^{main} > \theta_{SOC}^{main} + 2CAD \quad (8.14)$$

To attain the engine load demand, the main on-time is controlled to supply the necessary fuel mass. For a given fuel mass demand, the injection duration is inversely correlated to the rail pressure. Therefore, larger rail pressures reduce the injection duration, and hence reduce the in-cycle closed-loop controllability. Even though other factors must be considered for the set-point calibration of the rail pressure e.g., emissions, the in-cycle controllability can also be included. An adequate trade-off between controllability and emissions may increase the overall performance.

If further closed-loop controllability is necessary for the regulation of other parameters e.g., NO_x or AHR, additional degrees of freedom can be obtained by splitting the main injection (Zander et al., 2010b; Muric et al., 2013a), or even by rate shaping of the fuel injection with advanced injection systems.

8.2.3 Indicated efficiency controllability

The in-cycle closed-loop efficiency controllability was investigated in Publication IV by the simulation of the model in Section 5.2. The simulations were computed for a reference case of 13mg/st at -14.2CAD pilot SOI and -5.2CAD main SOI at 10bar IMEP, 1200RPM and 1200bar rail pressure. The model was simulated for a discrete sweep of the pilot injection parameters variance between $[-2\sigma, +2\sigma]$, in steps of 0.5σ , as a representation of the disturbance effects.

Disturbed pilot set

The effect of the disturbances on the indicated efficiency was studied by the computation of the disturbed pilot set. The pilot combustion parameters were swept individually maintaining the main injection constant. The ensemble of the cycles of the disturbed pilot set is plotted in Figure 8.3.

The significance of each of the parameters dispersion on the indicated efficiency, and their interaction, was quantified by ANOVA. The parameters were categorized by their significance level hierarchically. The first to third significance levels are plotted Figure 8.4.

The injected pilot mass has the most significant impact on the indicated efficiency. The mean indicated efficiency as a function of the pilot mass is between 37.9% and 38.8% , which represents 79% of the total efficiency variability. The second most significant variable is the pilot combustion efficiency. The indicated efficiency dispersion explained by the combustion efficiency is up to $\pm 0.5\%_{unit}$,

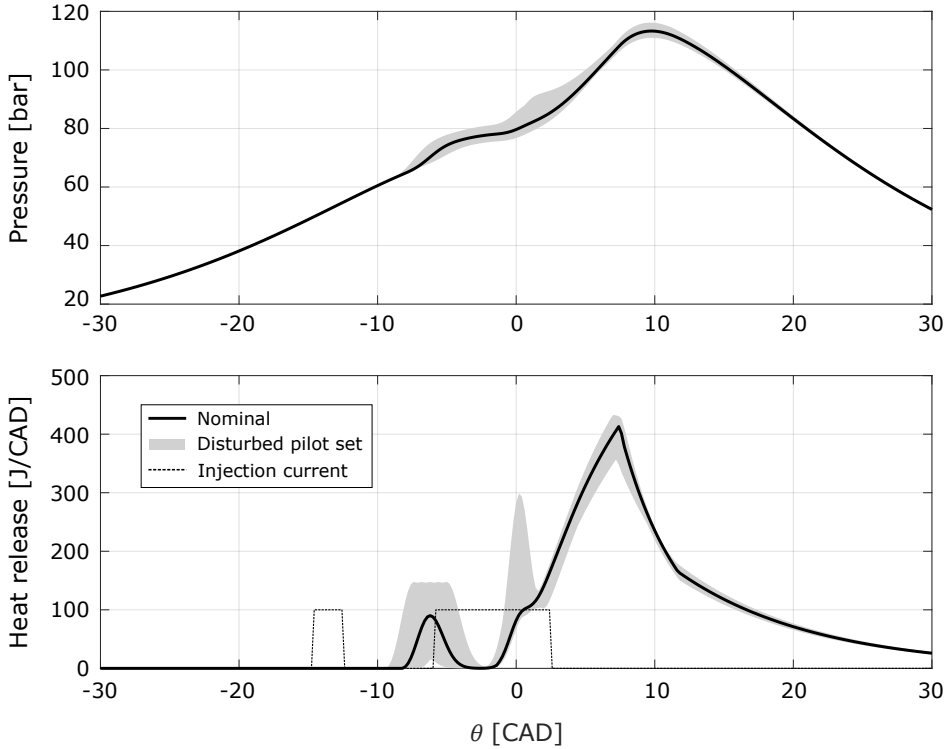


Figure 8.3: Cylinder pressure (upper plot), heat release rate and injection traces (lower plot) of the disturbed pilot set. The simulation was run at 10bar IMEP, 1200RPM, 1200bar rail pressure, no EGR.

depending on the non-linear interaction effects with the pilot mass. Consider the case of 12mg/st , where the interaction has the highest significance, with a variation between between 37.9% and 38.8%. For smaller pilot masses, the interaction is less significant. For example for 11mg/st , the indicated efficiency variation span is between 37.8% and 37.9%. The transition from pilot misfire to pilot combustion is significantly affected by the pilot combustion efficiency. It is therefore the burnt pilot mass the most significant variable to determine the indicated thermal efficiency. The ignition-delay (pilot SOC) represents up to $\pm 0.2\%$ of the indicated efficiency variability.

Maximum reachable indicated efficiency

The reference for the in-cycle closed-loop indicated efficiency controllability is the unconstrained maximum reachable efficiency set (UMRE). The main injection is adjusted to maximize the indicated efficiency under pilot disturbances

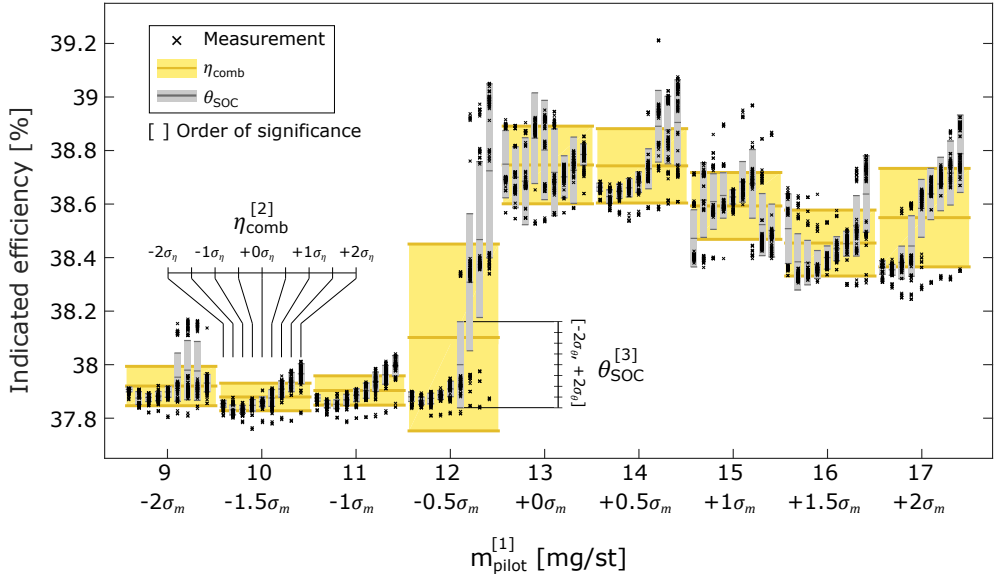


Figure 8.4: Boxplot of the indicated efficiency as function of the disturbed pilot mass, combustion efficiency, and pilot SOC hierarchically sorted by their significance level. The order of significance is indicated with the upper index in brackets. Note the non-linearities by examining the different variation range depending of the variables interaction.

with no observability constraints. The closed-loop controllability is addressed by constraining the main injection to the observable window of the pilot combustion i.e., when the pilot mass can be estimated $2CAD$ after the pilot SOC (see Section 6.5). This conforms the constrained maximum reachable efficiency set (CMRE). The UMRE and CMRE sets compared to open-loop operation are plotted in Figure 8.5.

The results confirm the in-cycle regulation of the main injection can improve the indicated efficiency. The improvement can be achieved in 86% of the total cases, when no controllability restrictions are imposed (UMRE). The improvement is up to $+0.2\%_{\text{unit}}$ net indicated efficiency in most of the cases (75%), and up to $+1\%_{\text{unit}}$ with an average of $+0.3\%_{\text{unit}}$ for the rest. Larger than nominal pilot masses are more easily counteracted (efficiency increased by $+0.7\%_{\text{unit}}$) than pilot masses shorter than nominal (efficiency increased by $+0.3\%_{\text{unit}}$). The maximum improvement of $+1\%_{\text{unit}}$, found for the case of 37.9% nominal indicated efficiency, is representative of a nominal case of pilot misfire. In this cases, disturbances resulting in larger pilot masses, longer ignition-delays but lower combustion efficiencies (instead of misfire), which results in an increased main premixed combustion, are adjusted by the in-cycle regulator with a net increase of the indicated efficiency.

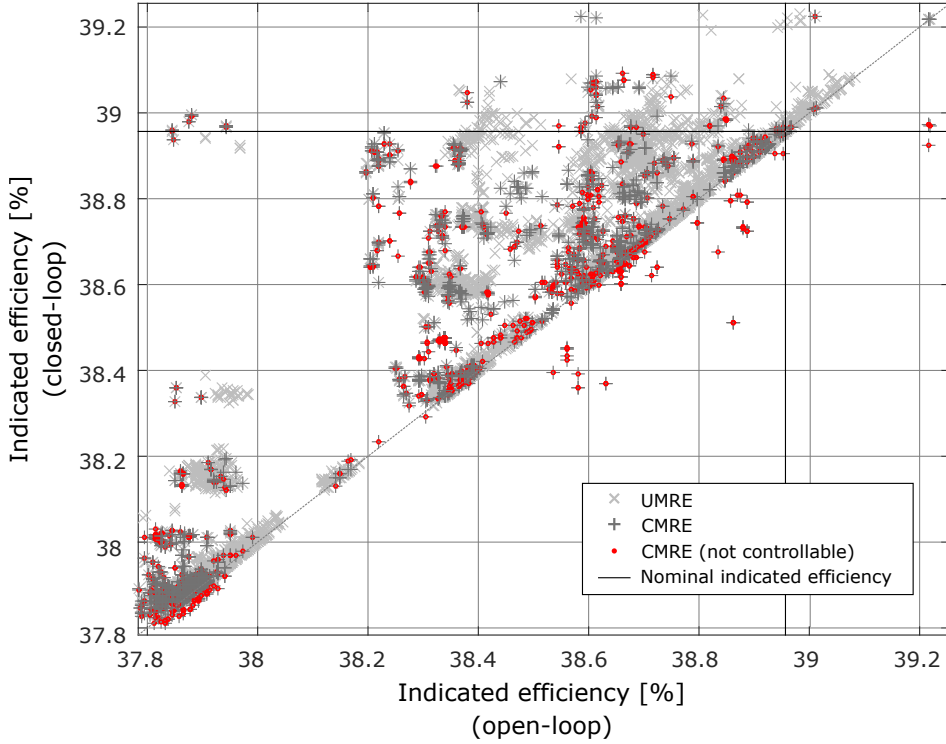


Figure 8.5: Scatter plot of the maximum reachable indicated efficiency by an unconstrained controlled main injection (UMRE) and constrained to in-cycle feedback (CMRE) as a function of the indicated efficiency in open-loop operation. The cases of the CMRE when the main SOI was constrained to the observable window are highlighted with a circle. The crossed lines are the indicated efficiency at nominal conditions.

The maximum reachable efficiency is in-cycle closed-loop controllable in 86.2% of the cases, when the pilot mass estimation constraint is not a limitation, and hence the CMRE matches the UMRE. Even when the observability constraint is imposed, the controllability limitations do not reduce the indicated efficiency significantly ($-0.01\%_{unit}$ on average, with a minimum of $-0.4\%_{unit}$). The largest penalty occurs for the pilot misfire cases of large pilot masses that otherwise burn normally. The in-cycle controller has limited authority to compensate pilot misfire by only adjusting the main injection. However, these cases are unlikely to occur, since the pilot misfire probability reduces as the pilot mass increases (see Section 4.2.1).

From these results, the trade-off between a shorter pilot injection with a larger indicated efficiency, but less robust pilot combustion, is optimized in Section 10.2, considering the limitations of the in-cycle closed-loop controllability.

8.3 Cascade Multi-Loop Interaction

An example of how the cascade multi-loop controller architecture can improve the system performance is by analyzing the IMEP COV. The load regulation is the variable that is more significantly affected by the cycle-to-cycle iterations. This is because the in-cycle controller is fully based on predictions for the load regulation. The load control requires a low error of the initial main on-time value and an accurate IMEP predictive model. The cycle-to-cycle regulator sets the initial value, refined by the in-cycle controller. From the experimental results in Publication V, the IMEP COV was reduced from 3.12% with only the in-cycle controller to 2.6% with the multi-loop cascade controller.

Notwithstanding the improved overall closed-loop control performance, the multi-loop feedback interaction of the cascade controller architecture i.e., cycle-to-cycle and in-cycle, has to be considered for an adequate tuning of the controllers and to avoid unexpected dynamics. The interaction between the multiple feedback loops may generate instabilities, oscillations and longer transients. The dynamics in the multi-loop controller are generated from two main sources. The first is the error of the model-based predictions. The second is the interaction between the cycle-to-cycle and in-cycle regulators.

Model-based prediction errors

The prediction errors are due to the reduced model complexity for their implementation, the stochastic random variations and, measurement error of the feedback variables. Normally, the prediction errors are sufficiently small for an adequate in-cycle regulation that achieves a reduction in the final dispersion. However, larger errors may not only increase the final variance of the regulated metric, but also generate instabilities. Large errors may be induced from too fast adaptation of the models, linearization inaccuracies or large initial errors:

- **Over-fitted adaptation:** the adaptation uses the model inputs and measured outputs for the model parameter inference by the Kalman Filter formulation. The tuning parameters are the model error covariance and measurement error covariance. Fast adaptation occurs when the model error covariance is large compared to the measurement error covariance. This may result in the adaptation algorithm over-fitting the measurements by the fast update of the model parameters. The extrapolation used for the in-cycle prediction results in large prediction errors. The error of the regulated parameter is enlarged, destabilizing the system dynamics.

- **Linearization error:** the nominal point of linearization is set by the cycle-to-cycle controller. However, for large reference steps, the system non-linearities result in large prediction errors from the model-based linear predictions. The cycle-to-cycle controller may overcompensate for the cycle's error, shifting the nominal point. This results in an extrapolation error that grows every cycle, destabilizing the system dynamics.
- **Large initial error:** the cycle-to-cycle control may act as a feed-forward for the in-cycle controller. The in-cycle controller iterates to converge to the reference based on the new measurements and updated predictions each step. For large initial errors, the iterative solver may not converge to the reference before the control action ends, resulting in a large error. The next cycle, the cycle-to-cycle control may overcompensate for this error, setting a large initial error. The process is repeated each cycle, destabilizing the system.

The over-fitted adaptation problem was observed during the calibration of the adaptation algorithms. An adequate tuning of the adaptation parameters avoided the problem. The limitations due to the linearization errors were observed in the linearized controller of Publication XIII. The linearized controller increased further the RMSE of the pilot SOC compared to open-loop due to the discrepancies between the nominal linearization point and the in-cycle prediction error. The limitation is avoided by longer transients, where the linearization error is small, or the use of the complete non-linear models, as will be discussed in Section 9.3.

The large initial error for the iterative convergence to the solution is observed in the results of the predictive controller of Section 9.1. For short pilot-main separations, the main SOC reference tracking starts with an initial error too large to converge with the available iterations before the main SOI. The controller did not converge to the set-point value, increasing the final error and generating a transient response longer than for similar step sizes at different pilot-main separations. The problem can be solved by a feed-forward controller to reduce the initial error.

Multi-loop regulators interaction

In this case, the origin of the instabilities is due to the conflicted control actions between the multi-loop regulators during adaptation transient or too fast multi-loop dynamics. The oscillations or instabilities are generated by the dynamics from the same mechanism as in the model-based prediction errors:

- **Model adaptation transients:** during the model adaptation, the cycle-to-cycle regulator may overreact to compensate for the errors from the in-cycle controller. While the adaptation takes place, the in-cycle controller reduces the set-point error, which is nevertheless increased from the overcompensation of the cycle-to-cycle regulator. The opposite control actions generate oscillations and instabilities during the adaptation transient of the in-cycle predictive models.
- **Fast multi-loop dynamics:** this mechanism is similar to the linearization error. The cycle-to-cycle controller sets the feed-forward for the in-cycle controller, which is modified by the in-cycle controller depending on the control strategy. The system output results in an error for the cycle-to-cycle controller, which may overcompensate it due to a calibration for fast transient response i.e., too aggressive. The in-cycle controller is not able to reduce the initial error, increasing the final error, which results in unstable dynamics.

Due to model adaptation transients, oscillations of the engine load reference tracking were observed at the experiments of the predictive in-cycle controller for the variance reduction (see Section 9.1). Possible solutions to this problem are the adequate tuning of the cycle-to-cycle controller and adaptation parameters, the use of predictive models accurate in a wider range of operating conditions, and more advanced techniques for faster adaptation.

Possible instabilities from conflicted control actions were avoided by an adequate tuning of the controllers. The rule of thumb used for the tuning of cascade controllers is ten times faster in-cycle dynamics than the cycle-to-cycle dynamics. In this context, the in-cycle dynamics must be evaluated by the error at the end of the cycle.

In-Cycle Closed-Loop Combustion Control

The controller design and experimental results of the investigated in-cycle control targets are presented in this chapter. The overall controller strategy follows a model predictive approach. A model-based predictive in-cycle combustion controller is investigated to reduce the effect of external disturbances and uncertainties on the cyclic dispersion of combustion metrics. The controller had limited ability to reduce pilot misfire effects. To extend the predictive controller, the design of an in-cycle controller to compensate for pilot misfire is studied.

Different operating conditions may require different control strategies. Likewise, different operating conditions and set-points may result in different in-cycle controllability. The limitations on observability and controllability determine the applicability of the in-cycle controllers attending to the different control targets. To cover a wide range of operating conditions, a modular approach to handle the transition from different in-cycle controllers is proposed, which increases the overall controller performance in steady-state and transient conditions.

The aggregation of the proposed controller modules permits the design of an in-cycle closed-loop combustion controller to operate with higher robustness for a wide range of operating conditions. This is exploited to optimize the nominal set-point with tighter safety margins for an increased indicated efficiency, whose optimization will be analyzed in Chapter 10.

9.1 Variance Reduction

The cycle-to-cycle variance reduction allows tighter operational margins of the combustion, as investigated in Publication XII. This improves the trade-off for a set-point with a higher indicated efficiency while fulfilling the operational and emissions constraints. The set-point reference may be calibrated off-line or adjusted on-line (see Section 10.2).

9.1.1 Controller design

The stochastic variations of the combustion are a consequence of fluctuations in the inlet conditions (pressure, temperature and gas composition), fueling (rail pressure and injection rate), combustion thermo-chemistry process (ignition-delay and combustion rate), and thermodynamic evolution, affected by the heat transfer. The control target is to compensate for these variations around the reference set-point by the regulation of the fuel injection, so that the stochastic cyclic variations of the combustion are reduced.

To overcome the limitations imposed by the intrinsic delay between the control input (fuel injection) and the measurements (in-cylinder pressure) of their effect on the combustion (heat release), a predictive model controller (MPC) approach was taken. The feedback strategies based on variable trajectories (pressure, heat release or AHR and NOx) have the disadvantage of a control law design based on calibration parameters and heuristic formulations, which have to be tuned for a satisfactory combustion control. The MPC framework provides a systematic approach and abstraction of the system controlled, where only the set-point reference parameters have to be calibrated.

The progress of the heat release is monitored by the combustion metrics. The metrics must be selected to match the degrees of freedom of the injection to fully define the combustion. In this work, the parameters were chosen to correlate directly with the fuel injection timings and durations. Following the combustion sequence, the selected parameters were the pilot start of combustion, the burnt pilot mass, the main start of combustion and the engine load.

9.1.2 Controller structure

The direct correlation between the regulated parameters and the control inputs permits the decoupling of the controllers. Four controllers regulate individually

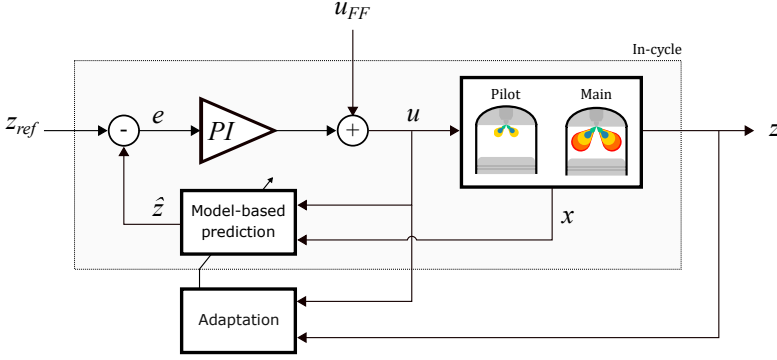


Figure 9.1: Diagram of the in-cycle predictive controller architecture. The controlled output (z) is predicted (\hat{z}) by the model as a function of the measured or estimated outputs x and controlled input u (see Table 9.1). The error e to the reference z_{ref} is reduced by a PI controller that updates the control action from the feed-forward value u_{FF} .

each of the combustion parameters. The outputs are predicted by the models in Section 5.3 as a function of the current combustion progress and the regulated inputs. The combustion progress is monitored by the estimation methods in Chapter 6. The general predictive controller structure is illustrated in Figure 9.1.

The controllers are PI regulators that update the control input to iteratively converge to the reference, continuously updating the prediction with the new measurements. At certain operating conditions and reference set-points, the inputs are not observable while having in-cycle closed-loop controllability. To overcome this limitation, the inputs are predicted by the models. The predicted model inputs are the internal states of the controller. The transition from predictions to measurements may impact the controller performance, which is discussed in Section 9.3. The controller gains are calibrated for a satisfactory trade-off between fast convergence and a possible oscillatory behavior, as discussed in Section 8.3. The inputs and outputs are selected for each of the controllers, detailed in the following subsections, and summarized in Table 9.1.

Pilot SOC controller

The pilot injection is commanded when the SOC prediction ($\hat{\theta}_{SOC}$) finds the SOC reference ($\theta_{SOC|ref}$). The pilot SOC prediction is updated each in-cycle step of $0.2CAD$. To reduce the need for implementation resources, the prediction uses the pilot ignition-delay model in Eq.(5.47) with the current in-cylinder pressure measurement as an input, instead of a pressure prediction. The controller is illustrated in Figure 9.2.

Table 9.1: Reference, inputs, outputs and internal states for the in-cycle closed-loop combustion controller.

Controller	Reference (z_{ref})	Control input (u)	Measured outputs (x)	Estimated states (\hat{x})
Pilot SOC	θ_{SOC}^{pilot}	θ_{SOI}^{pilot}	p_{cyl}	$\widehat{\Delta\theta}_{ID}^{pilot}$
Pilot burnt mass	m_{burnt}^{pilot}	t_{inj}^{pilot}	$\Delta\theta_{ID}^{pilot}, p_{rail}$	\hat{m}_{inj}^{pilot}
Main SOC	θ_{SOC}^{main}	θ_{SOI}^{main}	$p_{cyl}, p_{rail},$ $m_{inj}^{main}, m_{inj}^{pilot},$ δ_{comb}^{pilot}	$\widehat{\Delta\theta}_{ID}^{main}, \hat{p}_{SOI}^{main},$ $\hat{m}_{burnt}^{pilot}, \hat{\theta}_{SOC}^{pilot}$
Load	$IMEP$	t_{inj}^{main}	$p_{inlet}, p_{rail},$ HR_{prem}^{main}	\hat{m}_{inj}^{main}

Early pilot SOI may result in a large pilot ignition-delay prediction, where the pilot auto-ignition is limited by the minimum temperature and pressure to trigger the pilot combustion at the earliest pilot SOC. To ensure the stability of the controller and avoid an early SOI command, the ignition-delay prediction is saturated.

Pilot burnt mass controller

The inputs to the burnt pilot mass model (Eq.(5.50)) are the rail pressure, ignition-delay prediction, computed in the pilot SOC controller, and the pilot on-time. The PI controller adjusts the pilot on-time to converge to the burnt pilot mass reference.

Main SOC controller

The inputs to the main ignition-delay model (Eq.(5.48)) are the rail pressure, cylinder pressure at the main SOI, and the injected fuel mass. The rail pressure is directly measured and the cylinder pressure can be measured after the pilot SOC detection (Section 6.4). The injected fuel mass is calculated from the regulated main mass (by the load controller) and the on-line pilot mass estimation (Section 6.5). The PI controller adjusts the main SOI to converge to the SOC reference. The injection is commanded when the current CAD reaches the regulated SOI.

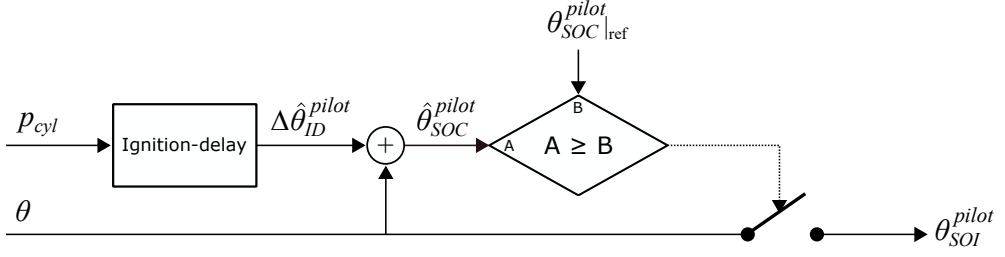


Figure 9.2: Diagram of the in-cycle pilot SOC controller.

Load controller

The load is predicted by the model in Eq.(5.54), extended to include the premixed heat release peak:

$$IMEP = IMEP_0 + k_m \cdot m_{main} + k_p \cdot p_{inlet} + k_{bp} \cdot m_{burnt}^{pilot} + k_{HR} \cdot HR_{prem}^{main} \quad (9.1)$$

The inputs are the measured inlet pressure, burnt pilot mass, the heat release peak for long enough injections, and the regulated main fuel mass. To avoid division in the injector model (Eq.(5.8)), the injection duration is regulated instead of the mass. In case the injection finishes before the main heat release premixed peak, it is predicted by the model in Eq.(5.51), with the predicted or measured main ignition-delay and the measured burnt pilot mass as inputs.

9.1.3 Experimental results

Design of experiments

The experiments were designed to validate the controller performance in steady-state and transient conditions. The engine was run for 100 combustion cycles for a sweep of steady-state reference set-points of each of the controlled metrics. For the set-point tracking transient response analysis, the reference for each regulated variable was varied with different step sizes. The robustness of the controllers was tested by running the engine with HVO and RME, whilst the predictive models were calibrated and tuned for Diesel. The experiments were run with and without on-line adaptation of the models.

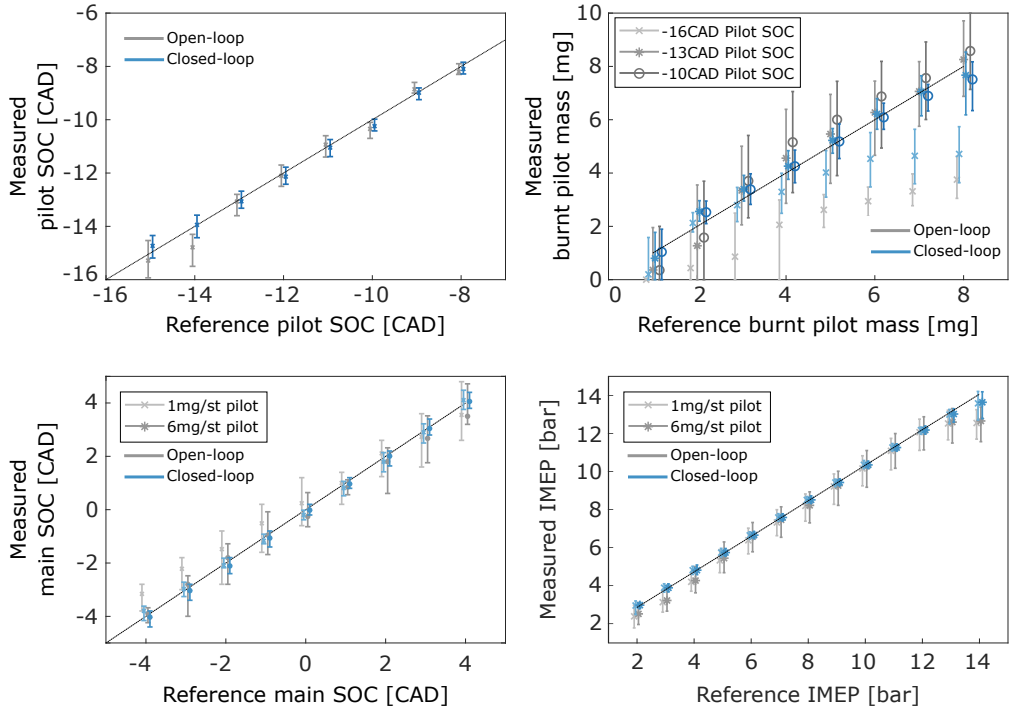


Figure 9.3: Steady-state results at 1200RPM and 1200bar rail pressure. Different pilot set-points are used around the nominal, set at 10bar IMEP, 6mg burnt pilot mass and $-13CAD$ pilot SOC. The bars are the 95% confidence interval.

Steady-state variance reduction

The steady-state results of the reference tracking for the different controlled parameters are plotted in Figure 9.3. The controller is able to reduce the steady-state error and cyclic dispersion of the controlled parameters. The in-cycle control of the pilot SOC (top-left plot) is mostly effective for early SOC references, where the pilot combustion is more sensitive to the intake conditions. The error is reduced from $\pm 1CAD$ to $\pm 0.4CAD$. For later SOC, the pilot combustion is more stable and the in-cycle control does not improve the performance significantly.

The total dispersion of the main SOC dispersion (lower-left plot) is reduced from $\pm 0.4CAD$ to $\pm 0.3CAD$. The reduction is predominantly due to lower cylinder-to-cylinder variations. The cycle-to-cycle dispersion is more significantly reduced at low loads and small pilot masses. In these operating conditions, the pilot combustion has a more significant impact on the main SOC than the random stochastic variations. When the pilot combustion was stable, a similar

dispersion was obtained for open-loop and closed-loop operation.

The burnt pilot mass error (top-right plot) is reduced from $\pm 1.5mg$ to $\pm 0.6mg$. For small pilot masses, the controller can reduce the risk of misfire, see the case of $2mg$. For early pilot SOC ($-16CAD$), there is an offset error due to the limitation of the combustion efficiency. However, the controller is able to reduce the error.

The engine load error (lower-right plot) is reduced from $\pm 0.8bar$ to $\pm 0.2bar$ IMEP. At $2bar$ IMEP, the indicated efficiency was improved from 20.0% to 28.0% due to the higher pilot combustion robustness and the main ignition-delay adjustment when using the in-cycle controller. At low loads, the efficiency was increased from 26.5% to 29.0%. As the load increases, the variations are less significant, reducing the efficacy of the controller. Nevertheless, the efficiency was improved by $+0.37\%_{unit}$.

The controller is particularly effective at operating conditions with high sensitivity to the pilot combustion, such as high EGR rates and early pilot injections. Due to its predictive structure, the use of the in-cycle controller can reduce the dispersion of a cycle-to-cycle regulator in steady-state.

Transient step response

The transient response to different reference step sizes for the different controlled parameters is plotted in Figure 9.4. The pilot SOC reference tracking transient (upper-left plot) takes about 40 cycles. The long transient is to ensure the robustness of the controllers. For early SOC references, the ignition-delay model is more sensitive to the in-cylinder pressure. A number of cycles is required to ensure a robust adaptation without a cycle-to-cycle variance larger than open-loop operation.

The burnt pilot mass reference tracking (upper-right plot) has a short transient of about 5 cycles. The adaptation of the model during negative steps may undershoot and result in misfire cycles. For a positive step from small references, see the case of $1mg$ where only misfire is obtained, to higher masses ($7mg$), the feedback information is missing. This results in a tracking delay until the pilot combustion is triggered at some cycle. An adequate feed-forward controller can overcome this limitation of the investigated in-cycle controller.

The main SOC transient duration (lower-left plot) is about 5 cycles. Instabilities are obtained for short pilot-main separations. The first issue is the lack of direct feedback of the pilot combustion before the main injection, which is not

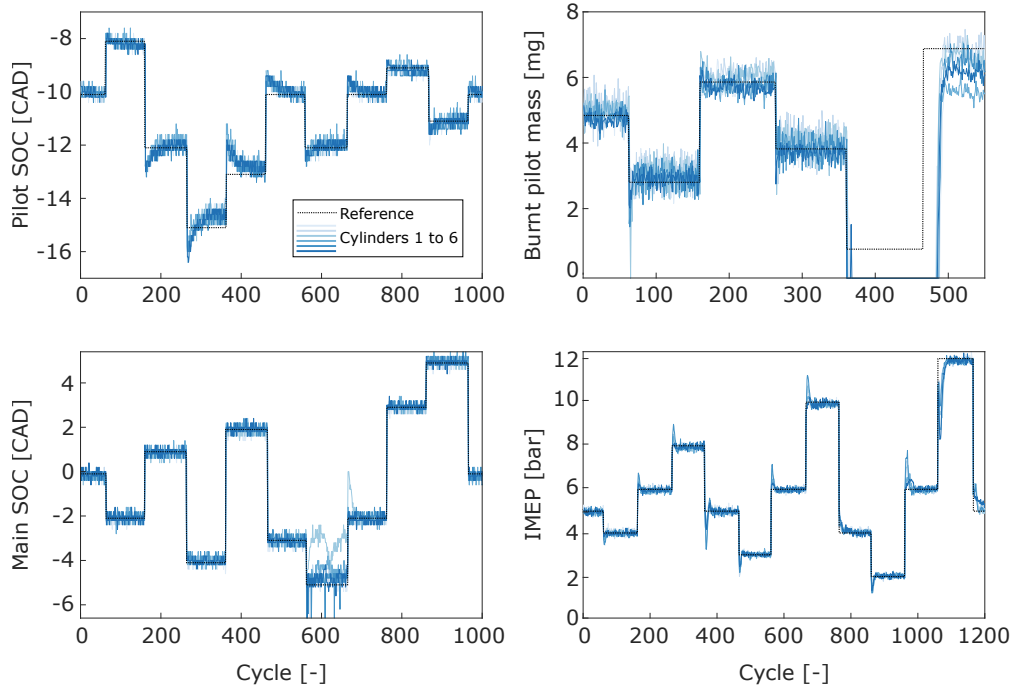


Figure 9.4: Transient response to different reference step sizes. The nominal set-point was at 10bar IMEP, 1200RPM, 1200bar rail pressure, -13CAD pilot SOC and 3mg burnt fuel mass, 0CAD main SOC. The individual sweeps kept the nominal values for the set-point of the other variables.

observable. The second problem is the injector tip does not close fully between the injections, disturbing the injected main mass. To solve this problem, a saturation for a minimum separation is required in the controller.

The load transient (lower-right plot) takes about 20 cycles until steady-state is reached. The reference tracking transient duration and overshoot are caused by the model adaptation transient. A more complex load model with higher accuracy over a wider range can help to reduce the necessity of the model adaptation and reduce the overshoots. The load step change generates transient behaviour for the reference tracking of the other parameters. The pilot SOC required about 40 cycles to update the prediction, mostly sensitive to negative load steps, where the pilot ignition-delay is more sensitive to the intake conditions.

The transients may result in instabilities generated by the combination of the feed-forward and feedback controller (see Section 8.3 for a discussion). This was observed for the pilot combustion at positive load steps. The feed-forward did not account for the transient of the pilot SOC, retarded the pilot SOI to compensate for higher loads, and pilot misfire was obtained. This generated an

oscillation of the load tracking before reaching the reference.

Model adaptation has to be considered in the controller design and calibration. On one hand, to avoid instabilities and saturation in the controlled outputs. On the other hand, to avoid long transients and oscillations. Accurate models over a wider range of operating conditions can overcome the limitations of the proposed models. These results were the motivation for the development of robust multi-cylinder adaptation methods, not yet implemented for these experiments. Moreover, cross-coupling of the controllers is sensitive to the jumps between available measured inputs and estimated inputs for the predictive models. An adequate in-cycle controller management was investigated to overcome these challenges, presented in Section 9.3.

Effect of disturbances and uncertainties

The multi-variate system was decoupled in the four regulated parameters. The cross-coupling of the variables was indirectly included by the inputs of the predictive models. Therefore, the controllers are able to overcome the disturbances of the other variables. Some cross-coupling disturbances were not able to be fully compensated due to the system limitations. The burnt pilot mass was not able to reach large references at low loads and early pilot SOC references due to the limited combustion efficiency. The main SOC controller was not able to fully compensate pilot misfire cycles obtained for small burnt pilot mass references. Even though the average error was reduced from $1.7CAD$ to $1CAD$, there was still a high cycle-to-cycle dispersion ($\pm 0.6CAD$). A controller explicitly dedicated to compensate for pilot misfire is presented in the next section.

The set-point error is directly related to the model accuracy. When the predictive models are adapted, the controller performance is robust against fuel uncertainties. The adaptation of the combustion models for RME and HVO reduced the error of the burnt pilot mass from $\pm 1.2mg$ to $\pm 0.6mg$ on average. The pilot and main SOC error were reduced from $\pm 0.6CAD$ to $\pm 0.3CAD$. The average engine load error was reduced from $\pm 0.7bar$ to $\pm 0.15bar$. The indicated efficiency was improved on average $+0.2\%_{unit}$.

9.2 Pilot Misfire Compensation

In-cycle pilot misfire compensation permits to reduce the nominal pilot mass, which increases the average indicated efficiency. Pilot misfire has a signific-

ant impact on the main combustion timing and shape. The pilot injection fuel mixes with the main injection when it misfires, increasing the available premixed fuel and ignition-delay. Compared to the nominal pilot combustion, this results in a fast premixed heat release rate and shifted combustion timing. The fast premixed combustion generates louder engine-out noise emissions (see Section 4.3.4). Pilot misfire affects also the engine torque, resulting in a reduced comfort and driveability due to higher cylinder-to-cylinder unbalance. Moreover, the different pressure evolution may incur violations of hardware constraints such as maximum pressure limits, and also larger emissions levels of e.g., NO_x. In-cycle pilot misfire control strategies and controller architectures were investigated in Publication XI to overcome the limitations of the previous controller.

9.2.1 Controller target

The controller target is to compensate for the disturbances of pilot misfire on the combustion timing and engine performance. The combustion timing set-point can be determined by any of the timing metrics in Section 2.5.4. In the scope of Publication XI, the main SOC and CA50 were investigated. The injected fuel is determined by the engine load, which is an external demand that must be fulfilled. For the control of the combustion timing, different misfire compensation strategies were investigated. The effect of these strategies on the combustion timing control and engine performance are reviewed in this section.

Misfire compensation strategies

With a pilot-main injection, only one degree of freedom is available for the combustion timing control in case of pilot misfire. To achieve higher controllability, additional degrees of freedom are obtained by a second pilot injection. The two misfire compensation strategies, single pilot-main injection and, double pilot-main injection were investigated.

An example of how each injection strategy compensates for the combustion parameters under pilot misfire is plotted in Figure 9.5. Pilot misfire delays the main SOC and advances CA50 due to the faster combustion (black line). By adjusting the main injection (blue line), the effect of pilot misfire on the main SOC can be counteracted. However, CA50 will be advanced further. The second pilot injection (red line) is able to place both, the main SOC and CA50, at a similar CAD as for pilot combustion.

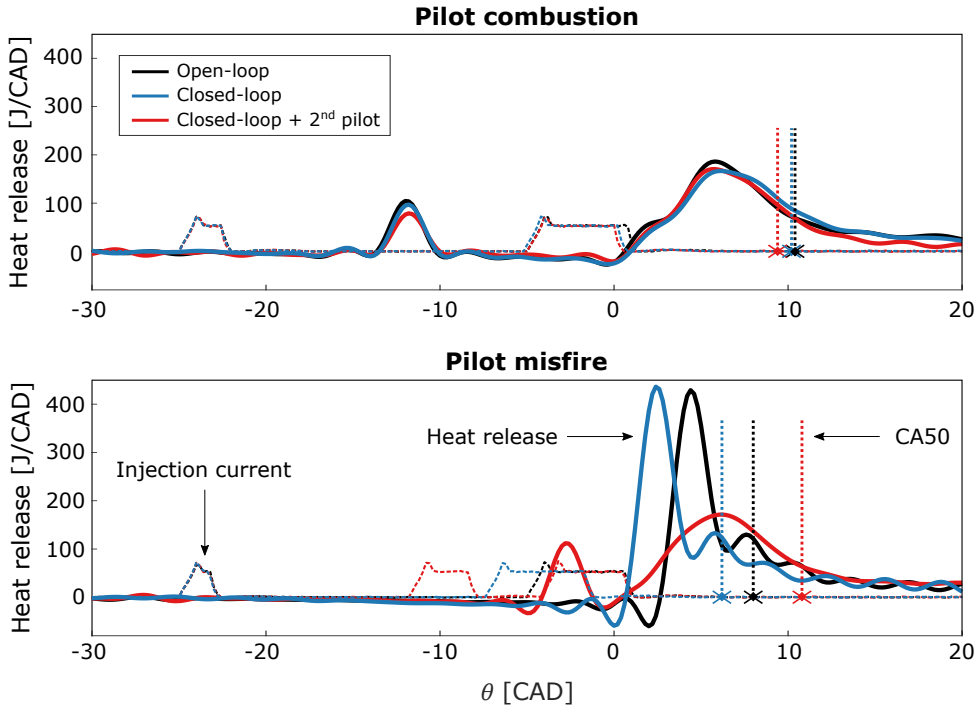


Figure 9.5: Heat release and injection current profiles for the different injection strategies, in open-loop and closed-loop. The upper plot shows the pilot combustion cases. The lower plot shows the pilot misfire cases.

Engine performance metrics

The engine performance metrics of interest affected by pilot misfire are listed below:

- **Indicated efficiency:** the faster premixed combustion due to pilot misfire may increase the indicated efficiency for an adequate combustion timing. However, this should be limited to avoid the violation of hardware and emissions constraints. The indicated efficiency is increased on average by a lower nominal pilot mass while fulfilling the constraints at the same time.
- **Maximum pressure:** the shift in the combustion timing and the faster combustion rate due to pilot misfire may increase the in-cylinder pressure over the constraint limits, which may damage the engine.
- **Maximum pressure rise rate:** the maximum pressure rise rate is an indicator of the engine-out noise. The faster combustion rate due to pilot

misfire increases significantly the engine-out noise to levels that may be over the maximum legislated values (Yoon et al., 2015).

- **Cylinder balancing:** pilot misfire modifies the pressure trace evolution unevenly along the cylinders, increasing the unbalance. The cylinder-to-cylinder variations of the pressure evolution may result in variations of the torque produced by each of the cylinders. Torque variations increase the stress on the crankshaft, engine speed variations, and vibrations (Heywood, 1988). For the cylinder balancing, the fuel injection is adjusted individually for each cylinder (van Nieuwstadt and Kolmanovsky, 2000).

9.2.2 Controller design

The controller is designed attending to the degrees of freedom of the injection strategy and the feedback loop timing i.e., cycle-to-cycle and in-cycle.

The main SOC was selected as the reference for the combustion timing. With the single pilot-main injection strategy, one degree of freedom is available to compensate for pilot misfire by the regulation of the main SOI. Two degrees of freedom (timing and duration) are added by a second pilot to compensate for the first pilot misfire.

Second pilot injection strategy

Two strategies were investigated for the second pilot timing regulation based on the main injection controllability (Section 8.2.1). The first strategy is designed to guarantee the main combustion controllability. The second pilot is injected only if this is assured. This strategy permits the main injection to obtain feedback of the additional disturbances from the second pilot combustion.

The second strategy injects the second pilot as soon as the first pilot misfire is detected, only if there is enough separation to the main injection. This strategy does not guarantee the controllability of the main injection over the second pilot combustion, which may penalize the error on the main SOC reference tracking.

In the scope of this thesis, only the decision of injecting the second pilot, and the regulation of its timing, were investigated. The duration of the second pilot was kept constant and calibrated to guarantee its combustion. To provide basic knowledge for the control of the second pilot on-time, the impact of the second pilot duration on the controller performance was also investigated.

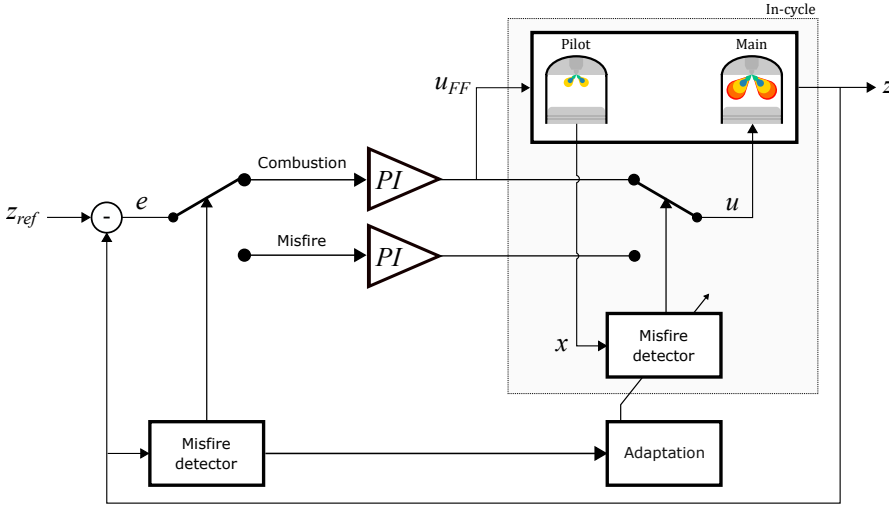


Figure 9.6: Pilot misfire cycle-to-cycle controller with in-cycle switch based on misfire detection.

Controller strategy

Two controller architectures were investigated. The first strategy is cycle-to-cycle based. The main SOI is adjusted each cycle to reduce the main SOC reference error by two PI controllers, for the pilot combustion and misfire cases respectively. The in-cycle controller switches to either control action based on the in-cycle pilot misfire detection. This control strategy uses only the single pilot-main injection strategy. The controller is illustrated in Figure 9.6.

The second strategy is wholly executed in-cycle and based on a predictive model-based controller. The injection parameters are iteratively updated each step from the measurements. The prediction assumes a nominal pilot combustion case. The predictions are updated if pilot misfire is detected. Both injection strategies of the second pilot injection were tested with this control strategy. The controller is illustrated in Figure 9.7.

Set-point reference

Different set-point references of the regulated parameters can be set for pilot combustion and pilot misfire cases. The same set-point reference was used for both cases in the study of Publication XI. Different set-point values were later studied in Publication XII. The constraints fulfillment is not explicitly considered in the controller. The set-point reference to guarantee the fulfillment

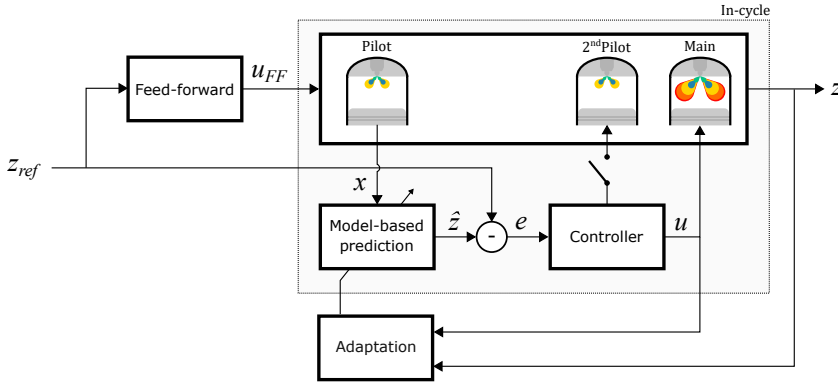


Figure 9.7: Pilot misfire in-cycle controller. The controller may use an optional second pilot injection.

of the constraints under pilot combustion and pilot misfire was also studied in Publication XII.

9.2.3 Experimental results

Design of experiments

The effectiveness and limitations of the different control and injection strategies were addressed experimentally. Pilot misfire was externally induced by small modifications of the pilot injection on-time, with a random offset of $200\mu s$. At each operating point, 100 cycles were collected for each of the cylinders. The ability of the injection strategies to compensate fully for pilot misfire effect was analyzed by studying the shift in CA50. The baseline for comparison of the controller performance is a cycle-to-cycle control without pilot misfire compensation. The effect of the second pilot duration was investigated with an on-time sweep.

Second pilot injection

The two minimum separation strategies to trigger the second pilot injection are designed to test how its observability affects the overall pilot misfire compensation. The injection timings and start of combustion of the multiple injections are plotted in Figure 9.8 for a constant main SOC reference at $5CAD$ as a function of the first pilot SOI. This results in different pilot-main separations and therefore in-cycle controllability. The first strategy (- label) triggers the second

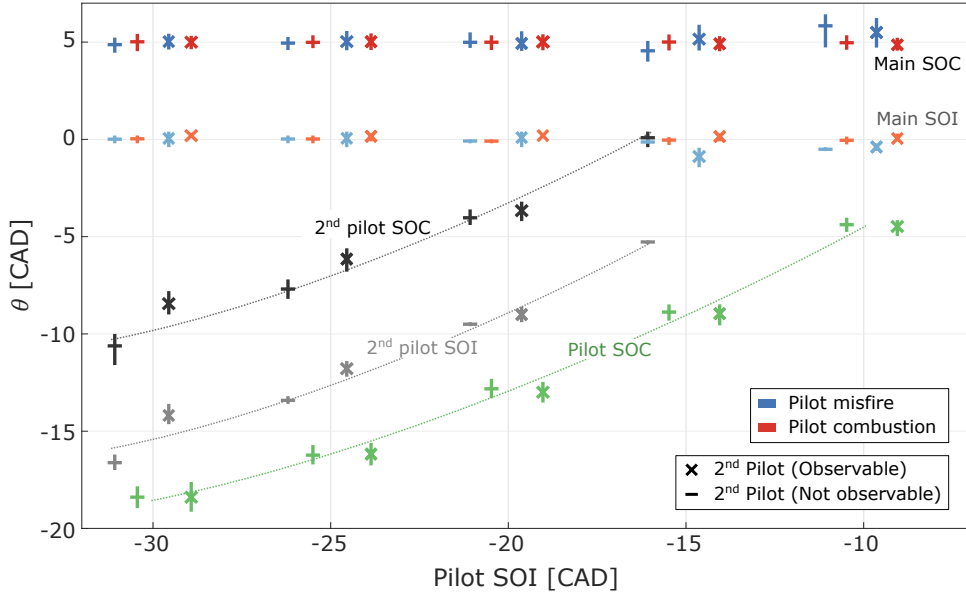


Figure 9.8: Comparison of the two strategies for the trigger of the second pilot injection for different pilot SOI. The main SOC reference was set at $5CAD$. The engine was run at $5bar$ IMEP, $1200RPM$ and $1200bar$ rail pressure. The data was sampled for six cylinders and 100 cycles. The marks are shifted in the X-axis for better readability. The bar length represents the 95% confidence interval.

pilot injection as soon as the first pilot misfire is detected. The second strategy (x label), triggers the second pilot only when the main injection is placed after its combustion.

The long separations at early pilot SOI references permit the trigger of the second pilot with similar results for both strategies. From $-15CAD$ pilot SOI, the second pilot is only triggered for the strategy without main controllability. The control strategy with not observable second pilot combustion permits to compensate for the error on CA_{50} but increases the main SOC error dispersion. On the other hand, the control strategy that ensures the second pilot observability only compensates the first pilot misfire by adjusting the main injection, which reduces the main SOC error, but not the CA_{50} error. For even shorter pilot-main separation (see the case of $-10CAD$ pilot SOI), there is not a large enough window for a second pilot injection. The minimum injection separation offsets the main SOC with an average error of $1CAD$. However, some cycles are compensated, increasing the total error dispersion. This is an example of the limitations due to lack of in-cycle closed-loop controllability.

The effect of the second pilot mass was studied by setting different second pilot on-times. The second pilot was injected as soon as the first pilot misfire was

detected. The error is significantly increased for second pilot masses with sensitive misfire probability (in between the transition from misfire to combustion) and short separations. These effects increase the uncertainty and reduce the observability to counteract for deviations. See Publication XI for more detailed results.

From these results, the strategy selected for the following experiments was to trigger the second pilot injection as soon as the first pilot misfire is detected and if the minimum second pilot-main separation is ensured. The duration of the second pilot is set constant and large enough to ensure its combustion.

Controller performance

For the study of the controller performance, three pilot SOI and main SOC separations were investigated ($25CAD$, $20CAD$, and $15CAD$) at three main SOC references ($-5CAD$, $0CAD$, and $5CAD$). The results of the pilot misfire compensation on the main SOC, CA50 and IMEP are plotted in Figure 9.9 as a function of the engine load, for a pilot SOI placed at $-25CAD$ and the main SOC reference at $0CAD$. This separation guarantees the in-cycle misfire controllability.

Pilot misfire increases the main ignition-delay, resulting in a main SOC error of $2.2CAD$ (upper plot). For controllable pilot-main separations, the in-cycle misfire compensation can reduce the error under $0.5CAD$ on average. The minimum error is limited by the in-cycle controllability, determined by the pilot SOC and main SOI separation. The main SOC average error is similar for the single and double pilot injection strategies. The performance of each controller is quantified by the error dispersion when there is controllability. The dispersion is directly correlated to the main ignition-delay sensitivity to the thermodynamic state. This increases for later main SOC references and lower loads. This trend is observed in the higher delay of the main SOC due to pilot misfire at low loads ($+2CAD$ at $2.5bar$ IMEP) compared to higher loads ($+1.6CAD$ at $10bar$ IMEP). For pilot combustion, the main SOC error dispersion is $\pm 0.7CAD$ using the cycle-to-cycle controller. The error is reduced to $\pm 0.3CAD$ by the in-cycle controllers. Pilot misfire increases the previous error dispersion an additional $0.2CAD$. The dispersion with the second pilot injection is higher than with the single pilot strategy. This is attributed to the higher uncertainty of the second pilot combustion and its effect on the main ignition-delay.

Pilot misfire increases the combustion rate due to the faster premixed combustion. Hence, the total combustion duration is reduced under pilot misfire. As a

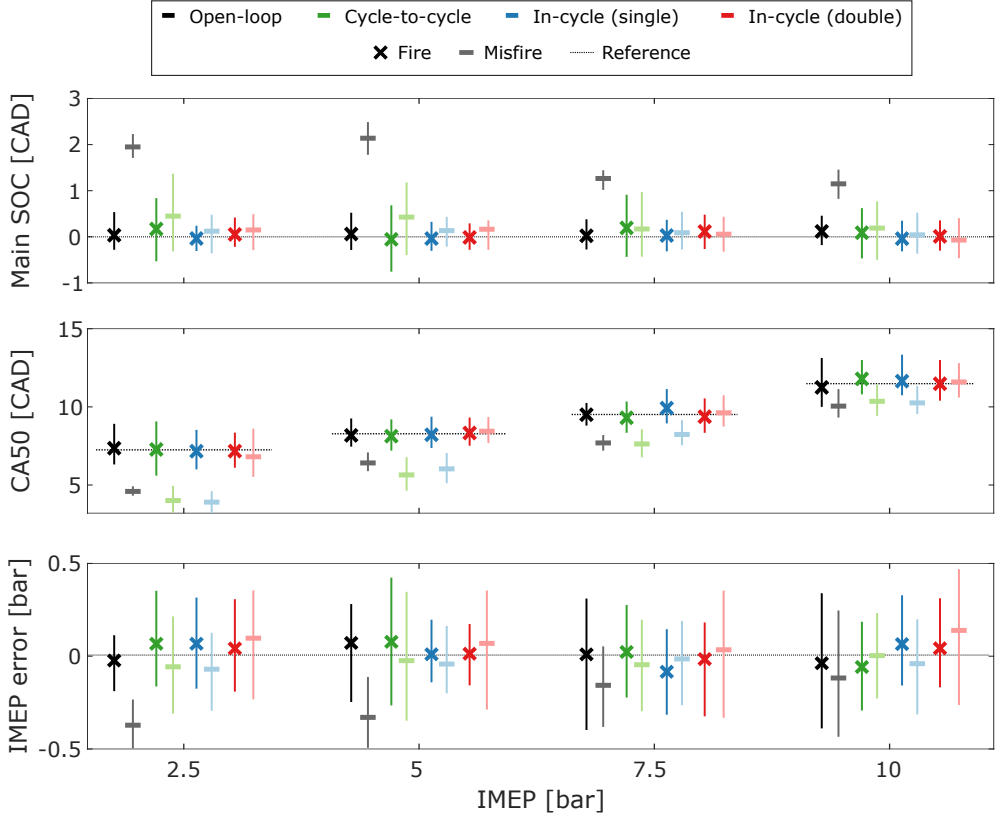


Figure 9.9: Main SOC (upper plot), center of combustion (CA50, middle plot), and engine load (lower plot) error due to pilot misfire for the different controllers. The baseline is the pilot misfire operated in open-loop. The cycle-to-cycle controller, in-cycle controller with single pilot, and in-cycle controller with double pilot injection, are compared. Pilot SOI was placed at -25°CAD . The main SOC reference was set at 0°CAD . The engine was run at 1200RPM and 1200bar rail pressure. The data was sampled for six cylinders and 100 cycles. The bar length represents the 95% confidence interval.

result, the center of combustion (middle plot) is advanced between 2.6°CAD at 2.5bar IMEP and 1.5°CAD at 10bar IMEP. With only the control of the main injection, the error is increased in closed-loop operation to reach the main SOC reference. The cycle-to-cycle controller increases the error, advancing the CA50 an additional 0.5°CAD , and the in-cycle controller an additional 0.6°CAD , compared to open-loop operation. Only with the additional degree of freedom of the second pilot injection the error on CA50 can be effectively compensated for an average 0°CAD error. The error dispersion is similar for the different controllers, about $\pm 1^{\circ}\text{CAD}$. As the controllability is reduced for shorter injection separations, the average error and dispersion are increased. Furthermore, when there is not enough pilot-main separation to allow for a second pilot injection, the error becomes the same as for the single pilot strategy.

Similar trends as the main SOC are obtained for the engine load compensation (lower plot). The lower sensitivity to pilot misfire at higher engine load also reduces the error, from -0.4bar at 2.5bar IMEP to -0.2bar at 10bar IMEP. The average load error for pilot misfire of -0.3bar in open-loop is successfully compensated by the misfire in-cycle controllers, with any of the strategies.

The cycle-to-cycle controller has a load error dispersion of $\pm 0.4\text{bar}$. The in-cycle controller strategy reduces further the error dispersion to $\pm 0.2\text{bar}$ with a single pilot and to $\pm 0.3\text{bar}$ with the second pilot strategy. The cause of the additional error dispersion is the uncertainty in the second pilot fuel mass.

Despite the effects of the engine speed on the combustion timing and shape, the controllers can reduce the pilot misfire effects at any of the studied engine speeds with similar relative performance. However, the engine speed increases the error dispersion in the CAD domain due to the higher sampling rate.

The controller performance was quantitatively similar for all rail pressures. However, a higher rail pressure increases somewhat the dispersion in the main SOC and the engine load. This is believed to be due to higher oscillations and uncertainty in the actual injected fuel mass.

As a main conclusion, the ability of the in-cycle controller to update the prediction within the cycle permits to outperform the cycle-to-cycle architecture. In general, compared to the cycle-to-cycle architecture, the average error is reduced by 50% and the dispersion is reduced by 20% using the in-cycle controller architecture.

Engine performance

The engine performance parameters are plotted in Figure 9.10 for a single operating point. The maximum pressure (upper-left plot) is increased $+2.1\text{bar}$ for pilot misfire due to the advancement of the center of combustion. With the pilot-main injection strategy, controlled either cycle-to-cycle or in-cycle, the maximum pressure is further increased about $+2.8\text{bar}$ for the misfire cases. The second pilot injection strategy reduces the increase of the maximum pressure to $+0.8\text{bar}$. The set-point can be calibrated or controlled differently for pilot combustion or misfire to limit the increase of the maximum pressure and fulfill constraints. The maximum pressure rise rate (lower-left plot) is significantly increased for pilot misfire with the single pilot-main injection strategy and any control strategy. Only the double pilot injection strategy is able to reduce the increase in the maximum pressure derivative, with a level similar to pilot combustion. Pilot misfire does not have a significant impact on the cylinder balancing (upper-right plot). The cylinder-to-cylinder fueling variations have the most significant impact on

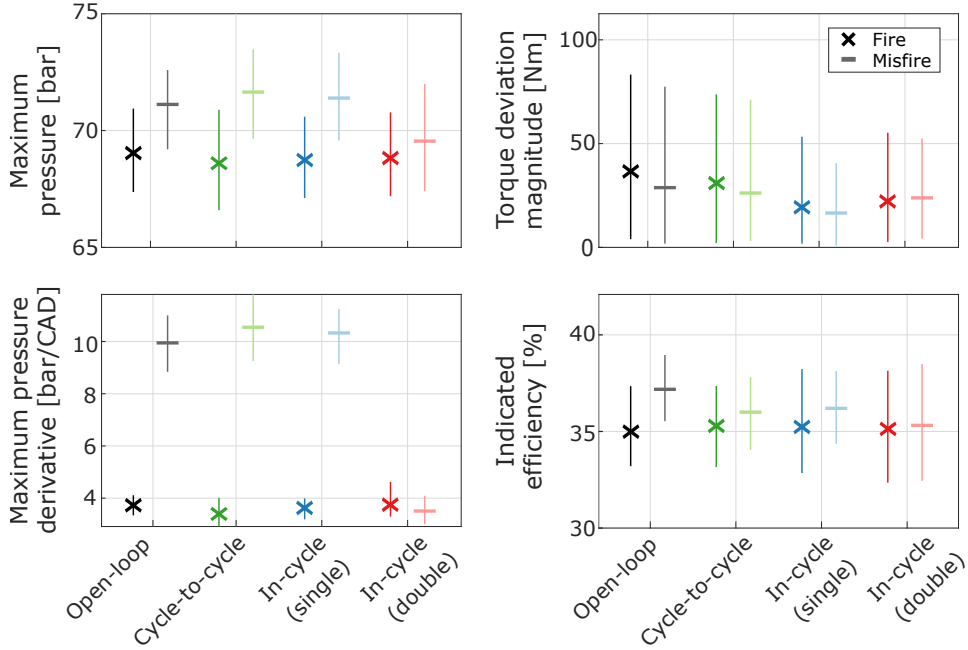


Figure 9.10: Effect of the in-cycle pilot misfire compensation on engine performance metrics for each of the proposed controllers. The engine was operated at 5bar IMEP, 1200RPM , 1200bar rail pressure. The pilot was placed at -25CAD and a constant duration of 0.3ms . The main SOC reference was set at 0CAD . 100 cycles were sampled for each of the six cylinders. The bar length represents the 95% confidence interval.

the cylinder balancing. Hence, the predictive controller structure reaches better performance for the reduction of the cylinder-to-cylinder torque variations. As discussed previously, pilot misfire increases the indicated efficiency (lower-right plot). Hence, the pilot misfire compensation reduces the pilot misfire effects on the indicated efficiency.

9.3 Controller Management

The different in-cycle combustion controllers focus on an effective control at a given operating condition, emission level and fuel. Different feedback information is available at the different operating conditions, and the adjustment of the control action requires different strategies. To cover a wide range of operating conditions, emission levels and fuels with seamless transitions between the controller structures, this section presents how multiple in-cycle closed-loop combustion controllers can be integrated.

An adequate management of the feedback signals and active in-cycle controllers is necessary for an effective combustion control over the whole range of operating conditions. The combinations of control strategies, control actions (i.e., number of injections) and available feedback (i.e., combustion metrics, estimated from in-cylinder pressure measurements), increase the total number of controller variants. A modular controller design approach was suggested in Publication XIII to handle the multiple combinations. This permits the encapsulation of the controller modules, allowing for high flexibility and scalability. The modular solution reduces the design and calibration efforts to support the combustion control solution adequate at each operating condition. Furthermore, incremental improvements in the controller can be easily integrated within this framework.

9.3.1 Modular controller design

Two parallel sequences of events are responsible for the available feedback and control. As discussed in Chapter 8, the control action is established by the number, timing and duration of the fuel injections, which determines the controllability. The pressure and combustion progress of each fuel injection provides feedback to the controllers, which determines the observability. However, different operating conditions result in different interaction modes (see Section 4.3.2) hence the observability and controllability obtained. For a successful control of the combustion, both observability and controllability are required simultaneously (see Section 8.2).

To handle the available feedback and necessary control actions for different control targets (such as the regulation of the combustion timing or NO_x formation), combustion evolution (such as pilot misfire or cold-start), and even combustion modes (such as PPC or HCCI, see Turesson (2018) for control strategies of PPC combustion), different controller designs are required.

To tackle all the different combinations within the controller design, a modular approach is followed. The modularization is achieved by encapsulating each block of the control feedback loop, illustrated in Figure 9.11. Three finite-state machines (FSM) monitor, respectively, the progress of the injection sequence (actuator FSM), the combustion sequence (sensor FSM) and the active regulator (controller FSM). The finite-state machines are illustrated in Figure 9.12.

The transitions are triggered by CAD events (such as inlet valve closing, IVC), actuator events (start of injection, end of injection), internal events (e.g., detection of start of combustion) or external events (when a different finite-state machine transition is triggered). The required modularity is provided by the in-

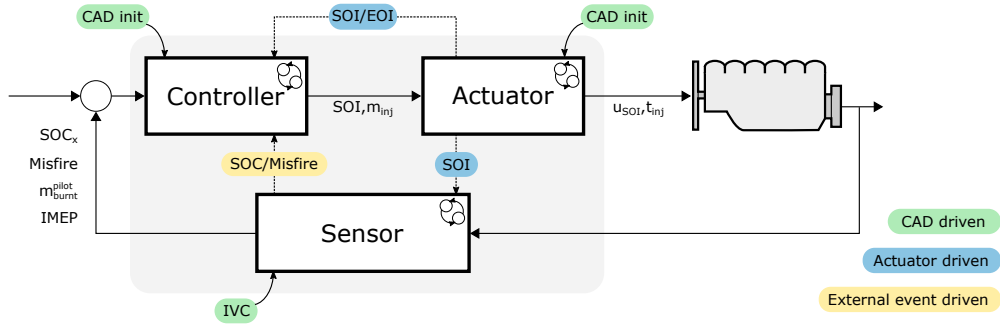


Figure 9.11: Modular closed-loop feedback structure. A finite-state machine supervises the combustion progress with dedicated states for the controller, the actuator and the sensor. The CAD, actuator and external events interconnect the transitions of the FSM.

terconnection of the different finite-state machines through the external events, allowing multiple combinations. The finite-state machines are described below.

Actuator FSM

The actuator FSM supervises the logic of the injection sequence to activate them and prevent a possible overlap. The modular architecture permits to adjust the number of injections if necessary. Each injection is composed by a first state enabling it, followed by a state executing it. The transitions between the states are triggered by the comparison of the current CAD with the continuously regulated SOI and EOI values by the in-cycle controllers. The injection sequence starts after the initialization, at a calibrated CAD. This is normally at the earliest possible crank angle the first injection can start.

Sensor FSM

The sensor FSM provides updated information to the controllers as the cycle advances. Based on the cycle progress, there is a sub state-machine monitoring the compression and a dedicated sub state-machine for each injection combustion.

The combustion state-machine provides continuous feedback to the controllers. Each state for the combustion supervision represents new information (in the form of lumped combustion metrics) to monitor its progress and evolution. The model predictions replace the measurements until they can be directly obtained or estimated. No overlap between the multiple injection combustions is assumed. Otherwise, such event would need to be considered for the combustion sensor's

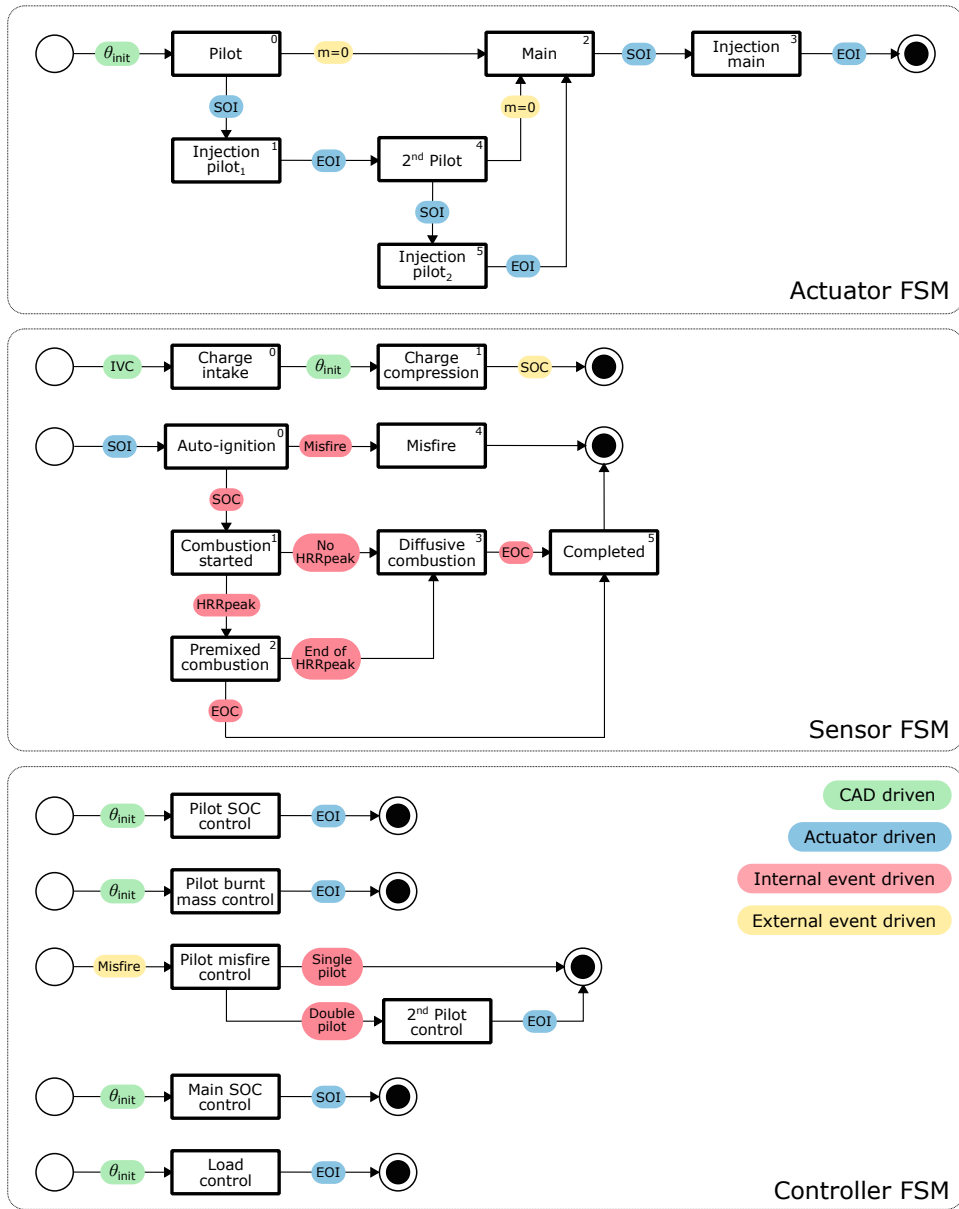


Figure 9.12: Actuator FSM: each injection consists of two phases. A first phase where the controller decides if it is performed, and a second phase where the actuator executes the injection. Sensor FSM: the first supervises the charge compression from inlet valve closing (IVC) until the first combustion starts (SOC). The second is implemented for the supervision of each injection's combustion. Controller FSM: a dedicated FSM is used for each controller, all run in parallel and synchronized by the interconnection of the other FSM's events throughout the closed-loop structure (see Figure 9.11). The transitions are triggered either from CAD, actuator, internal or external events.

finite-state machine.

The decouple between the controllers and feedback allows the use of the same structure in spite of different operating conditions and sequences of events. Furthermore, the modular approach allows that different models and estimations can be selected based on the regulation requirements.

Controller FSM

The controller FSM selects the active controller as the injection and combustion events progress. The feedback is provided by the sensor FSM. The command actions (SOI and on-time) are updated continuously from the initialization CAD, until the actuator commands them. Each dedicated controller is run in parallel. For the investigation of this approach in Publication XIII, the controllers presented in Section 9.1 and 9.2 were implemented. These were, the controller for the main and pilot SOC, burnt pilot mass, pilot misfire and engine load. The misfire controller also decides if a second pilot injection is required or not. Additional controllers can be added easily with the appropriate transitions.

An example of the transitions for each finite-state machine is shown in Figure 9.13. In the first (upper) plot, the progress of the combustion is monitored by the pressure and heat release rate. The state transitions are plotted in the second plot. The third plot is the pilot and main SOC, regulated by the pilot and main SOI. The burnt pilot mass is shown in the fourth plot, regulated by the pilot on-time. The last plot is the engine load and main on-time. The selection of the adequate feedback signals is coordinated by the active states. An early injection adjustment is possible by the replacement of unavailable measurements with the model-based predictions. This is observed in the jumps of the engine load control (lower plot). As the cycle advances, the state-transition updates the information for the load prediction. The continuous update of the relevant signals reduces the magnitude and transient duration after an error update. The early adjustment and the reduction of the initial error minimizes the transient and the final error when the injection is commanded.

9.3.2 Experimental results

Design of experiments

The transition between the available information, control actions and control strategy affects the final combustion behavior. To address the improvement in

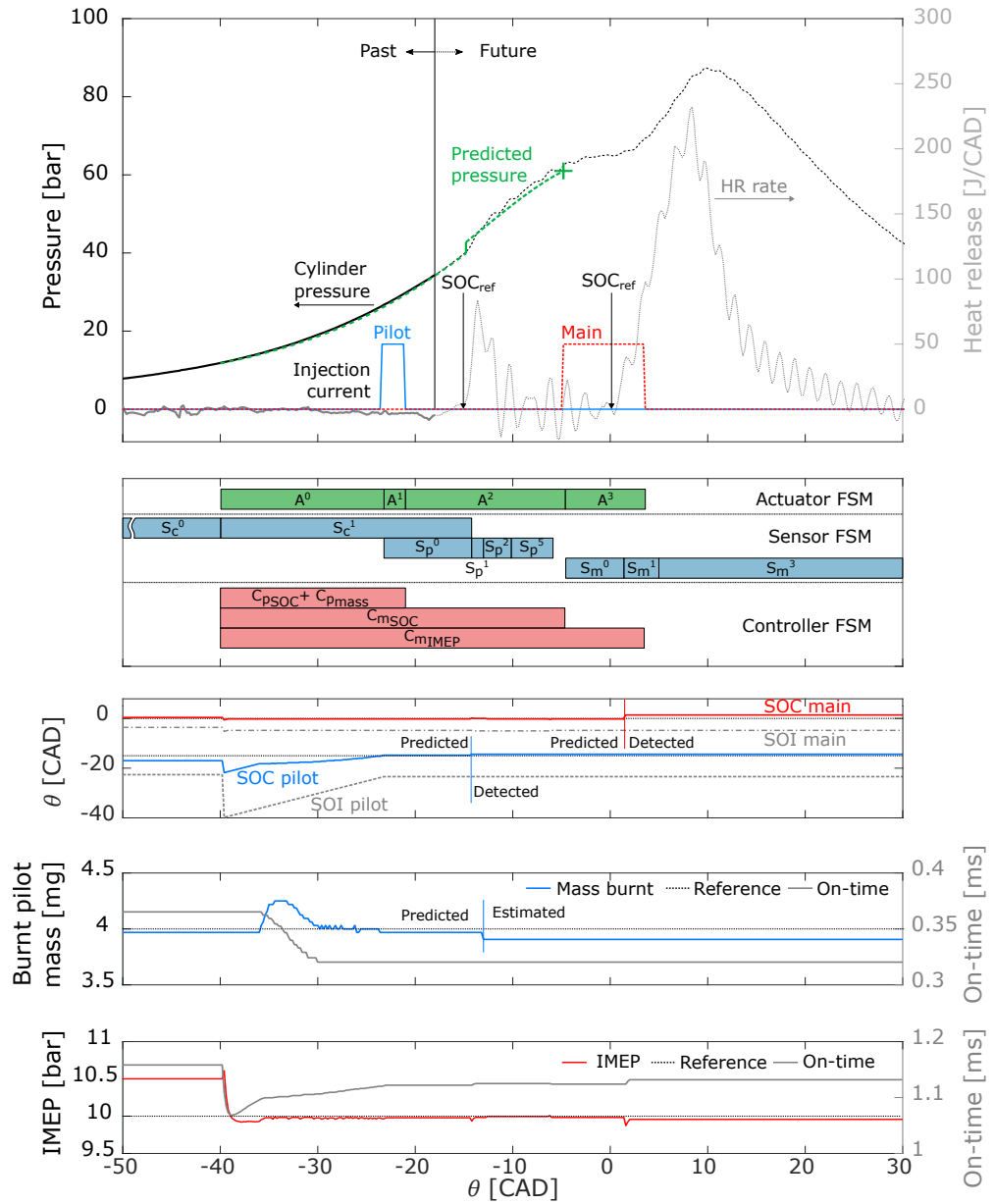


Figure 9.13: Modular in-cycle closed-loop combustion control. The pressure, heat release rate and injection currents are in the upper plot. A line separates the past and the future to illustrate the progress at a given CAD. The second plot illustrates the sequence of the FSM states for the actuator (A), sensor (S) and control (C). The sensor FSM is composed of the compression (c), the pilot (p) and, the main (m) injections observers. The numbers are each of the states in Figure 9.12. The third graph plots the timings of the pilot and main injections, and the start of combustion. The fourth plot is the control of the burnt pilot mass by the pilot on-time. The last plot is the main on-time control for the load regulation. In this example, the engine was run at 10bar IMEP, 1200RPM and 1200bar rail pressure.

the transition between controllers, model-based prediction and available feedback (i.e., interaction modes), the in-cycle predictive controller was compared to a cycle-to-cycle and a linearized in-cycle controller. The cycle-to-cycle controller sets the baseline for comparison with the finer in-cycle regulation of the combustion. The linearized in-cycle controller permits to address the improvement of the modular solution when the transitions from predictions and measurements are included.

For the validation of the proposed approach, operating conditions resulting in different feedback transitions despite a constant combustion timing reference were selected. To cover a significant range of operating conditions where these transitions are found, low and medium loads (from 2.5bar to 12bar) at low and high engine speeds (900RPM to 1500RPM) were run. The engine was operated with three fuels, standard Diesel, RME and HVO. The transient response between different operating points was also tested.

Steady-state results

The main combustion SOC error is plotted in Figure 9.14. for different pilot SOI and 0.5mg burnt pilot mass set-point. The pilot-main separation results in different interaction modes. The low burnt pilot mass reference results in some misfire cycles that require adequate main SOI adjustment.

The cycle-to-cycle controller minimizes the main SOC average error as a weighted-average of the pilot misfire and combustion cycles. The total error dispersion is within the two extremes, at about $\pm 1\text{CAD}$ main SOC error for any pilot-main separation. The in-cycle controllers are able to reduce the error for pilot combustion and misfire. However, the linearized controller reduces its performance for short pilot-main separation (see the pilot SOC reference at -9CAD), as the nominal linearization point has a significant extrapolation error for the binary cases of pilot combustion and pilot misfire. This limitation is overcome by the fully predictive in-cycle controller as long as it has controllability for long enough pilot-main separation. Otherwise, the minimum separation sets the final main SOC error (see the pilot SOC reference at -7CAD).

Similar main SOC and engine load error dispersion were obtained when the feedback to the controllers was consistent (i.e., constant interaction mode). The main SOC error had a dispersion within $\pm 0.35\text{CAD}$ and the engine load was within $\pm 0.5\text{bar}$. As the engine speed increases, the higher CAD resolution increases the error spread and reduces the time separation between the pilot combustion and the main injection. For these cases, and in general for long pilot

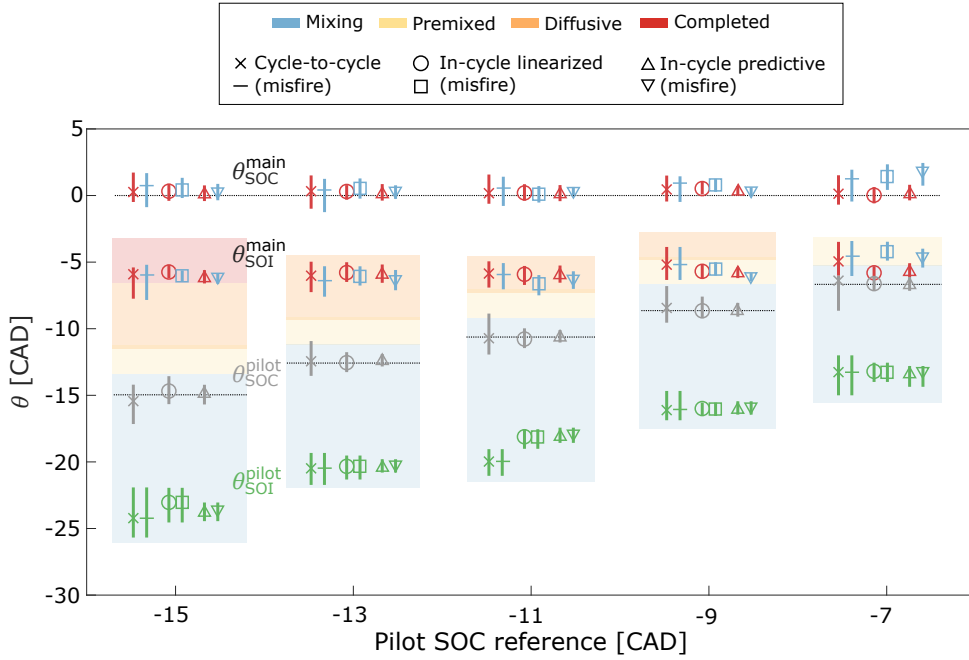


Figure 9.14: Steady-state control of pilot and main SOC, for $0.5mg$ burnt pilot mass and different SOC set-points. The engine was run at $5bar$ IMEP, $1200RPM$ and $1200bar$ rail pressure. The lines indicate the 95% confidence interval. The interaction modes are represented by the color.

ignition-delays, there is no direct feedback from its combustion for the main injection's control. The result is an increased error dispersion of the cycle-to-cycle controller. The main SOC error of $\pm 0.45CAD$ was reduced to $\pm 0.4CAD$ by the predictive in-cycle controller. The higher sensitivity to extrapolation error of the linearized controller increased the error dispersion to $\pm 0.5CAD$. This same trend was observed for the regulation of the engine load. The cycle-to-cycle controller error dispersion within $\pm 0.6bar$, was increased to $\pm 0.7bar$ with the linearized controller. The predictive in-cycle controller achieved a reduction to $\pm 0.5bar$.

The rail pressure impacts the pilot misfire probability and its combustion rate, obtaining different interaction modes, hence available feedback for the main injection's controller. For low rail pressures, the larger pilot ignition-delay increases the error of the cycle-to-cycle and linearized controllers due to the higher cycle-to-cycle variations on one hand, and the lack of direct feedback on the other. At $900bar$, the error dispersion of $\pm 0.45CAD$ with the cycle-to-cycle controller was significantly increased to $\pm 0.6CAD$ with the linearized controller. The predictive in-cycle controller was able to achieve similar results regardless of the rail pressure, with an error dispersion of $\pm 0.35CAD$.

These trends can be derived from the results for the transient response, presented in next subsection. More details are also available in Publication XIII.

Transient response

The transient response to different magnitude set-point steps for the engine load (until cycle 400) and pilot and main combustion timings (from cycle 400) are presented in Figure 9.15. The burnt pilot mass was set constant at $2mg$. The predictive in-cycle controller reduces the transient duration of the engine load regulation compared to the cycle-to-cycle and linearized in-cycle controllers (upper left plot). However, with a similar overshoot due to the model adaptation for large load steps. The transients in the engine speed, rail pressure and intake pressure are produced by the load steps. These can be understood as disturbances to the combustion controllers. These transients affect the temperature evolution and hence the ignition-delay, which is compensated by the controllers (lower left and middle plots). The predictive controller achieves faster transients than the cycle-to-cycle and linearized controllers. The shorter transients improve the driveability and comfort. The IMEP presents smaller error dispersion due to the finer main on-time adjustment (see the left middle plot from cycle 500). For the control of the pilot SOC, the larger error of the linearized controller results in a wider dispersion of the pilot SOC error due to cycle-to-cycle variations (lower middle plot), which determine the linearization points. The result is a larger variability than the cycle-to-cycle and predictive controllers.

Despite not shown in the plot, engine speed transients generated transitions between the interaction modes. The transitions from direct feedback to model-based predictions were handled smoothly with the predictive controller. However, the lack of direct feedback in the cycle-to-cycle and linearized regulators resulted in a wider error dispersion and longer transients.

These results confirm that the proposed modular approach is an effective solution to handle the feedback transitions, and higher control performance can be obtained despite different operating conditions.

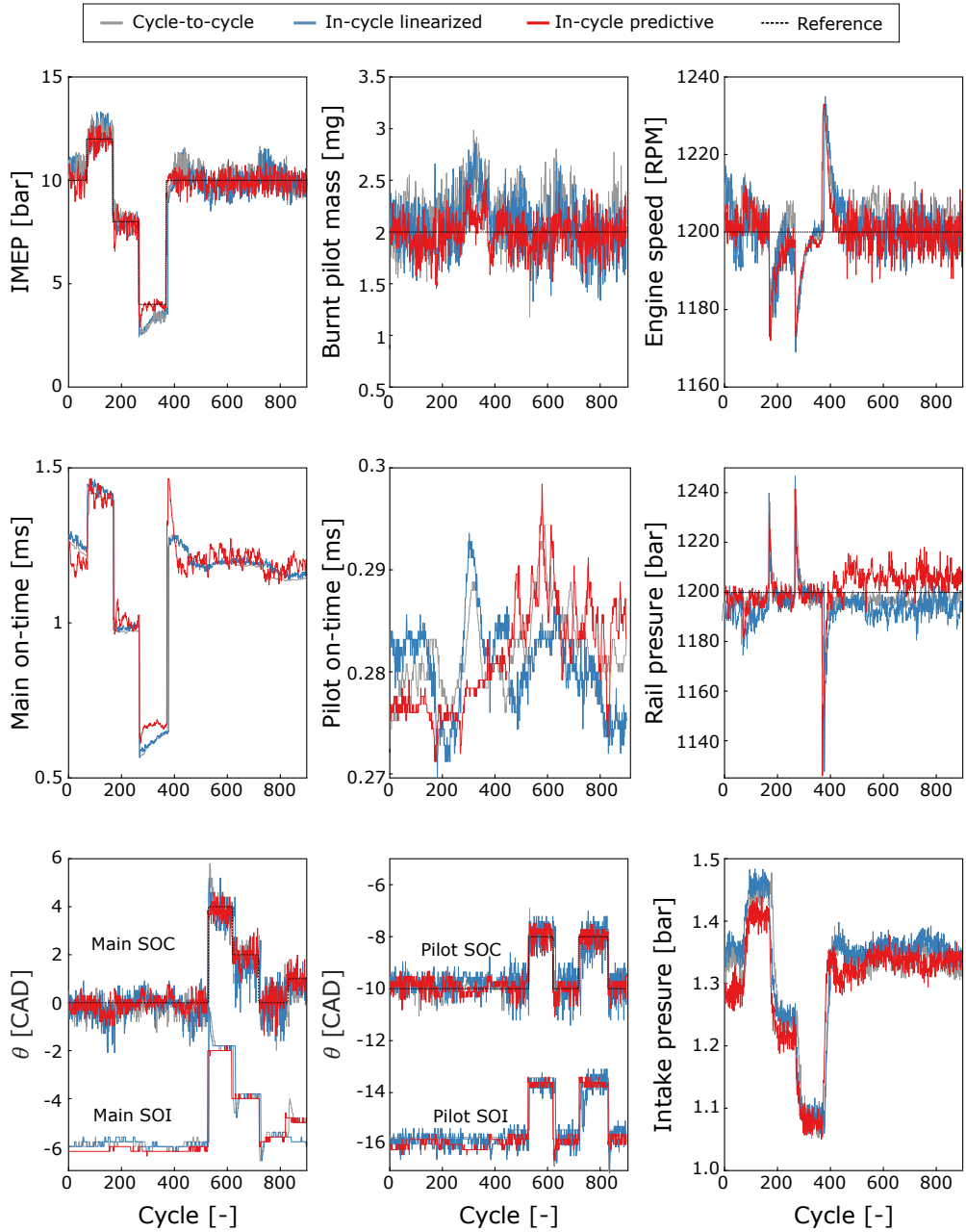


Figure 9.15: Reference tracking of the controlled parameters under transient load and SOC responses. The engine was run at 1200RPM and 1200bar rail pressure. The signals are referred to cylinder 1.

CHAPTER 10

Efficiency Optimization

The goal of in-cycle closed-loop combustion control is to improve the robustness to system and operational uncertainties in order to increase the efficiency. Controller design methods for the direct and indirect maximization of the indicated efficiency are presented in this chapter.

The direct optimization method consists in the design of an in-cycle combustion controller that adjusts the injection to maximize the indicated efficiency of that cycle. The effects of the pilot combustion variations on the indicated efficiency are compensated by the regulation of the main injection. The design of the controller and its experimental validation are reviewed.

The limitations imposed for the real-time on-line computations do not permit to include constraints explicitly in the previous design approach. As an alternative, the indirect optimization method is proposed. The reduced cyclic variations achieved by the controller presented in Chapter 9, including the reduced risk and compensation of pilot misfire, are exploited to optimize the set-point reference for maximum indicated efficiency under different operational constraints. The system is simulated by the stochastic combustion model in Chapter 5 for the off-line efficiency constrained maximization. The optimization of different combustion metrics as the set-point reference is compared and analyzed.

10.1 Direct Efficiency Optimization

The variations of the pilot combustion affect the main injection combustion, as discussed in Section 4.3.4. The effects are the shift of the main combustion timing and shape, which impacts the indicated efficiency. In Publication V, a controller was proposed to counteract the pilot combustion disturbances on the indicated efficiency by the in-cycle adjustment of the main injection. This controller is designed to fulfill higher-level performance targets, whilst the previous controllers in Chapter 9 were designed for the set-point reference tracking.

10.1.1 Controller target

The objective of the controller is to recompute the main injection to achieve the maximum indicated efficiency within the updated reachable set from the measured pilot combustion. The optimal-control problem can be formulated as a model predictive control (MPC). This formulation approach permits to update the combustion evolution based on the current measurements and optimize the indicated efficiency by the regulation of the main injection.

To achieve the controller target, an explicit on-line optimization MPC was derived. An optimization solver requires the indicated efficiency estimation by the prediction of the combustion and pressure evolution. For its on-line real-time execution, the implementation of the combustion model in Section 5.2 is too computationally heavy. For this reason, a more fundamental approach was followed to compute the indicated efficiency directly from the controlled inputs in-cycle, presented below.

10.1.2 In-cycle efficiency optimization

The optimal Diesel combustion timing is a balance between the heat released before TDC, with a faster premixed combustion but larger heat transfer losses, and later combustion with limited expansion ratio (Johansson, 2012). This trade-off was described with a simplified approach. A mixed thermodynamic cycle (Heywood, 1988), composed by an isochoric instantaneous combustion followed by an isobaric process, describes the balance between the premixed and diffusive combustion. The premix ratio r_{prem} determines the share of the isochoric and isobaric processes.

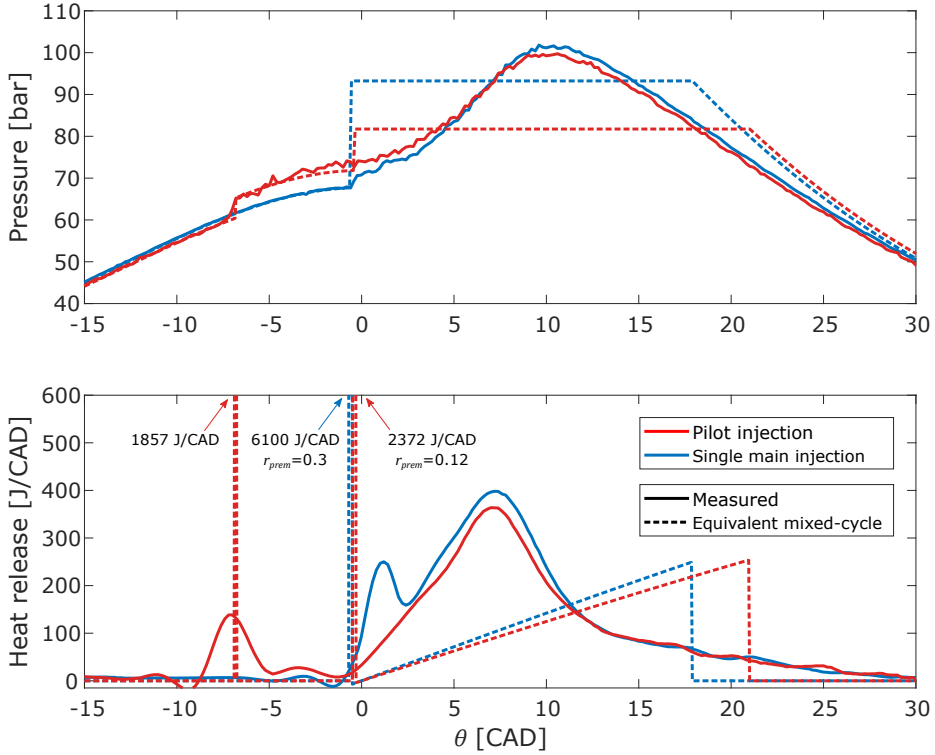


Figure 10.1: Pressure (upper plot) and heat release rate (lower plot) for the equivalent mixed-cycle with and without pilot injection. The y-axis of the lower plot is limited for better resolution.

Premix ratio modeling

For the real combustion process, an equivalent mixed-cycle premix ratio is defined. The equivalent premix ratio (\hat{r}_{prem}) is computed to obtain an equal mean heat release rate (\overline{HR}), starting at the same SOC:

$$\overline{HR} = \frac{Q_{HR}}{\theta_{main}^{main} - \theta_{SOC}^{main}} \quad (10.1)$$

Due to the higher efficiency of the mixed-cycle thermodynamic process, the fuel mass is scaled to achieve the same engine load. An example of the equivalent mixed-cycle computed for single main and pilot-main injections is plotted in Figure 10.1. For the single main injection, the premixed heat release reduces the total combustion duration of the equivalent mixed-cycle. The pilot combustion is totally described as an isochoric process.

The equivalent premix ratio was computed for a sweep of pilot masses and main

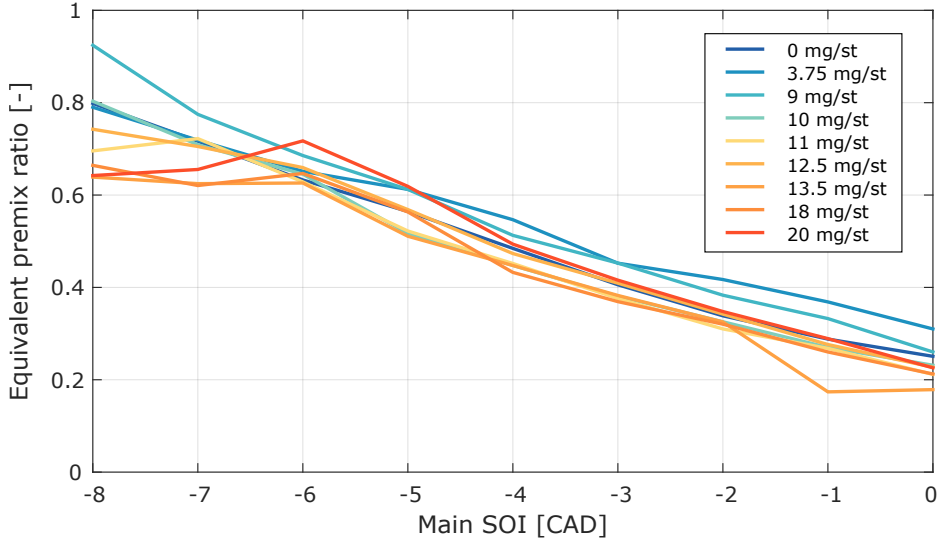


Figure 10.2: Equivalent premix ratio as function of the main SOI for different pilot masses. The pilot SOI was at -16 CAD . The engine was run at 10 bar IMEP, 1200 RPM , 1200 bar rail pressure, no EGR.

SOI at 10 bar IMEP, plotted in Figure 10.2. The equivalent premix ratio can be described as a linear function of the main SOI:

$$\hat{r}_{\text{prem}} = \alpha \cdot \theta_{\text{SOI}}^{\text{main}} + \beta \in [0, 1] \quad (10.2)$$

The data was fitted by a line with a least squares criterion. The ignition-delay is implicitly included in the identification of the equivalent premix ratio as a function of the main SOI and pilot mass. The identified gain (α) and offset (β) are parametrized as sigmoid functions of the pilot mass:

$$\alpha = k_{\alpha_0} + \frac{k_{\alpha_1}}{1 + e^{-k_{\alpha_2}(m_{\text{pilot}} - m_0)}} \quad (10.3)$$

$$\beta = k_{\beta_0} + \frac{k_{\beta_1}}{1 + e^{-k_{\beta_2}(m_{\text{pilot}} - m_0)}} \quad (10.4)$$

The two limits of the sigmoid function describe the saturation of the gain (α) and offset (β) as the pilot injection transitions from pilot misfire to a stable pilot combustion. The intermediate values describe the offset and sensitivity of the equivalent premix ratio to the main SOI for different pilot masses. The root mean-squared error of the equivalent premix ratio model calibration was 0.0637 .

Indicated efficiency maximization

The cylinder pressure of the mixed-cycle combustion was simulated to compute the indicated efficiency for different premix ratio parameters (α, β) . The maximum indicated efficiency is obtained at an optimal main SOI that can be described as a rational function of the gain α and offset β :

$$\theta_{SOI}^{\eta_{max}} = \frac{k_n \alpha}{\alpha^2 + k_d} (1 - \beta) \quad (10.5)$$

The resulting coefficients k_n and k_d are functions of the fuels specific heat ratio and the engine's compression ratio.

10.1.3 Controller design

The controller task is to update the premix ratio function parameters (α, β) from the current measurements and compute the optimal main SOI by Eq.(10.5). The effects of the pilot combustion on the premix ratio parameters are computed for this goal. Disturbances affecting the pilot ignition-delay are modeled as a required shift of the main SOI. The main SOI shift compensates for the difference in the in-cylinder temperature and composition that affect the main ignition-delay. This is computed as an additional offset correction, proportional to the gain α :

$$\Delta\beta_{SOC} = \alpha \cdot \Delta\theta_{SOC_{pilot}} \quad (10.6)$$

Variations in the pilot combustion efficiency affect the main premixed combustion with an inverse correlation. The effects are included with an additional offset in the equivalent premix ratio. The offset is linear, but saturated at the extremes as the pilot combustion converges to misfire or stable combustion. Therefore, a sigmoid function was again selected for the model:

$$\Delta\beta_\eta = \frac{k_{\eta 1}}{1 + e^{-k_{\eta 2}(\eta_{comb} - \eta_0)}} \quad (10.7)$$

The effect of different EGR or intake temperature on the ignition-delay were not explicitly accounted. Instead, the assumption is that their effect can be extrapolated and compensated by the feedback obtained from the modification of the pilot combustion. Summarizing the previous steps, the premix ratio parameters are identified $(\hat{\alpha}, \hat{\beta})$ from the in-cycle heat release measurements,

calculated as a function of the estimated pilot mass (by Eq.(10.3) and Eq.(10.4)), pilot SOC (by Eq.(10.6)), and pilot combustion efficiency (by Eq.(10.7)):

$$\begin{aligned}\hat{\alpha} &= \alpha(\hat{m}_{pilot}) \\ \hat{\beta} &= \beta(\hat{m}_{pilot}) + \Delta\beta_{SOC}(\Delta\theta_{SOC_{pilot}}) + \Delta\beta_{\eta}(\eta_{comb})\end{aligned}\quad (10.8)$$

The main SOI is regulated to obtain the maximum indicated efficiency by Eq.(10.5) from the estimated premix ratio parameters. By substitution, the final expression is a non-linear function. To ease the controller implementation, the assumption is that the optimal main SOI can be approximated as a linear function around the nominal point. The controller gain is obtained from the linearization of the optimal main SOI for each monitored disturbance at the nominal point ($\bar{m}_{pilot}, \bar{\eta}_{comb}^{pilot}, \bar{\theta}_{SOC}^{pilot}$):

$$K_{SOI} = \left[\frac{\partial\theta_{SOI}^{\eta_{max}}}{\partial m_{pilot}}, \frac{\partial\theta_{SOI}^{\eta_{max}}}{\partial \eta_{comb}^{pilot}}, \frac{\partial\theta_{SOI}^{\eta_{max}}}{\partial \theta_{SOC}^{pilot}} \right]_{\bar{m}_{pilot}, \bar{\eta}_{comb}^{pilot}, \bar{\theta}_{SOC}^{pilot}} \quad (10.9)$$

The main on-time controller has to compensate for the disturbances on the indicated efficiency to reduce the error on the engine load set-point. Inverting the maximum indicated efficiency, the required update in the main mass is:

$$\Delta m_{inj}^{main} = - \frac{\Delta\eta_{th}}{\bar{\eta}_{th} + \Delta\eta_{th}} \bar{m}_{inj}^{main} \quad (10.10)$$

The change in the indicated efficiency is approximated as a linear function of the shift for the optimal main SOI ($\Delta\theta_{SOI}^{\eta_{max}}$). The fuel injector model in Eq.(5.49) is included to compute the main on-time as a function of the rail pressure, linearized at the nominal main injection on-time and rail pressure. The final algebraic expression for the main controller is:

$$\begin{bmatrix} \Delta\theta_{SOI}^{main} \\ \Delta t_{inj}^{main} \end{bmatrix} = \begin{bmatrix} k_{SOI}^m & k_{SOI}^{\eta_{comb}} & k_{SOI}^{\theta_{SOC}} & 0 \\ k_{inj}^m + k_{inj}^{\eta_{th}} k_{SOI}^m & k_{inj}^{\eta_{th}} k_{SOI}^{\eta_{comb}} & k_{inj}^{\eta_{th}} k_{SOI}^{\theta_{SOC}} & k_{inj}^{p_{rail}} \end{bmatrix} \begin{bmatrix} \Delta m_{pilot} \\ \Delta \eta_{comb}^{pilot} \\ \Delta \theta_{SOC}^{pilot} \\ \Delta p_{rail} \end{bmatrix} \quad (10.11)$$

The main injection controller architecture to reach the maximum indicated efficiency is illustrated in Figure 10.3.

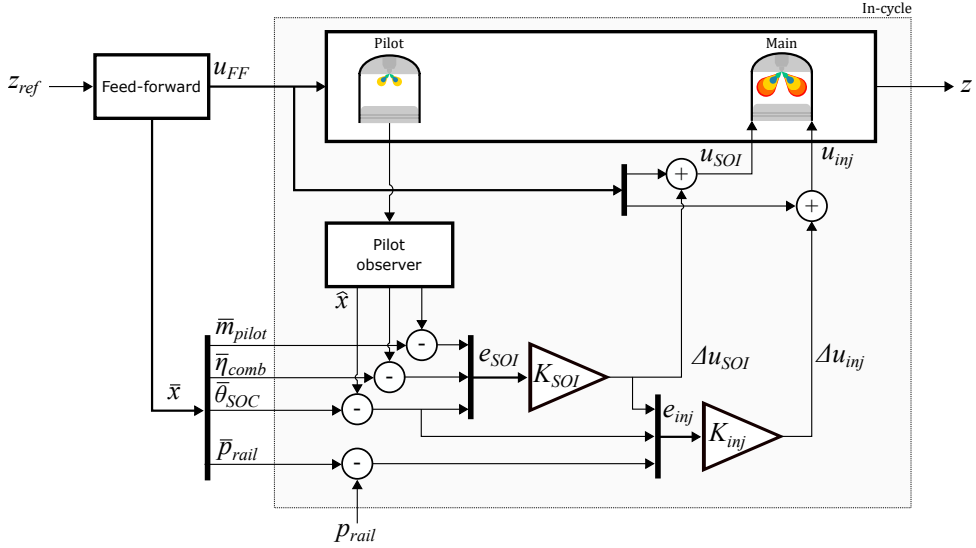


Figure 10.3: Maximum indicated efficiency in-cycle controller.

10.1.4 Experimental results

Design of experiments

The experiments were designed to verify the effectiveness of the in-cycle closed-loop combustion controller to increase the indicated thermal efficiency. The pilot injection was disturbed with a random offset for the on-time and SOI. The on-time offset was between $\pm 200\mu s$, equivalent to $\pm 10mg/st$ at $1200bar$ rail pressure. The pilot SOI was disturbed with a random offset between $\pm 1CAD$. The nominal pilot injection was $13.5mg/st$ at $-16CAD$ SOI. The controller was linearized at this operating condition. The engine was operated for $10bar$ IMEP at $1200RPM$ and $1200bar$ rail pressure. The baseline for comparison of the controller effectiveness was open-loop operation of the main injection.

To verify the increased indicated efficiency by the regulation of the main combustion timing, the in-cycle control of the main injection was compared to open-loop main SOI operation, whilst the engine load was regulated for both cases. The controller was calibrated for Diesel fuel. To test the sensitivity of the proposed controller to modeling uncertainties, the engine was also run with RME.

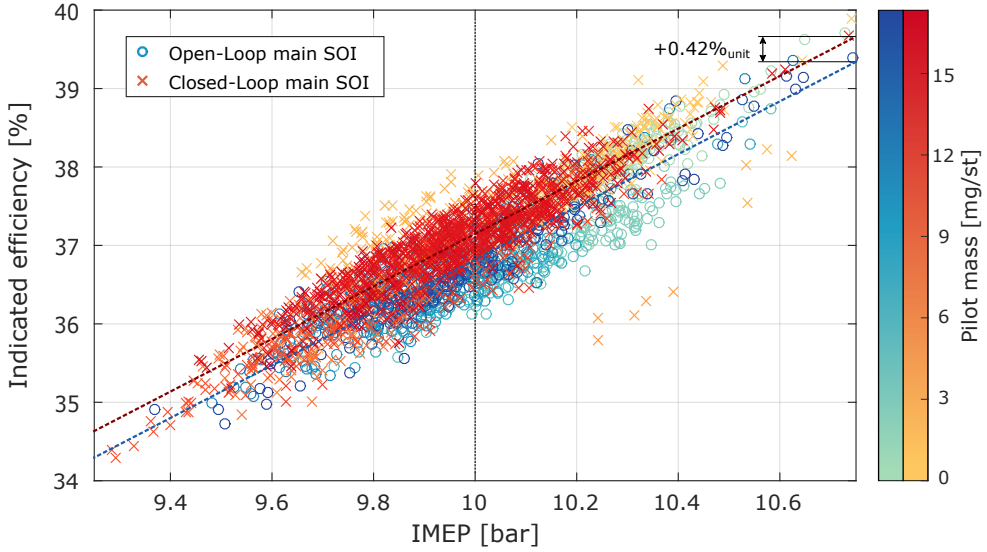


Figure 10.4: Indicated efficiency as a function of the engine load for in-cycle main mass control, with and without main SOI control. The pilot on-time was disturbed randomly, obtaining pilot masses between $0mg/st$ and $16mg/st$. The lines fitted to the data are overlaid to compare the intercepts.

Controller performance

The indicated thermal efficiency is plotted as a function of the engine load in Figure 10.4 for the main on-time controller and the full main controller. Due to the indicated efficiency estimation from the cylinder pressure, there is a linear correlation with the engine load, estimated also from that signal. Hence, the efficiency increase was verified by a hypothesis test over the fitted line. The null hypothesis of both lines having the same intercept was rejected with a p -value close to zero. This validates the increase in the indicated efficiency achieved with the proposed in-cycle control strategy, with a net improvement of $+0.42\%_{unit}$.

The analysis of the controller performance with the full in-cycle controller showed a high sensitivity to small pilot masses. Small pilot masses under $7mg/st$ misfire and were not able to be estimated in-cycle. The engine load error was up to $1bar$ IMEP due to the linearization error of the controller (discussed in the next section). The pilot misfire increased the indicated efficiency due to the faster premixed combustion, as previously discussed, but its effect on operational constraints could not be compensated. More detailed results can be found in Publication V.

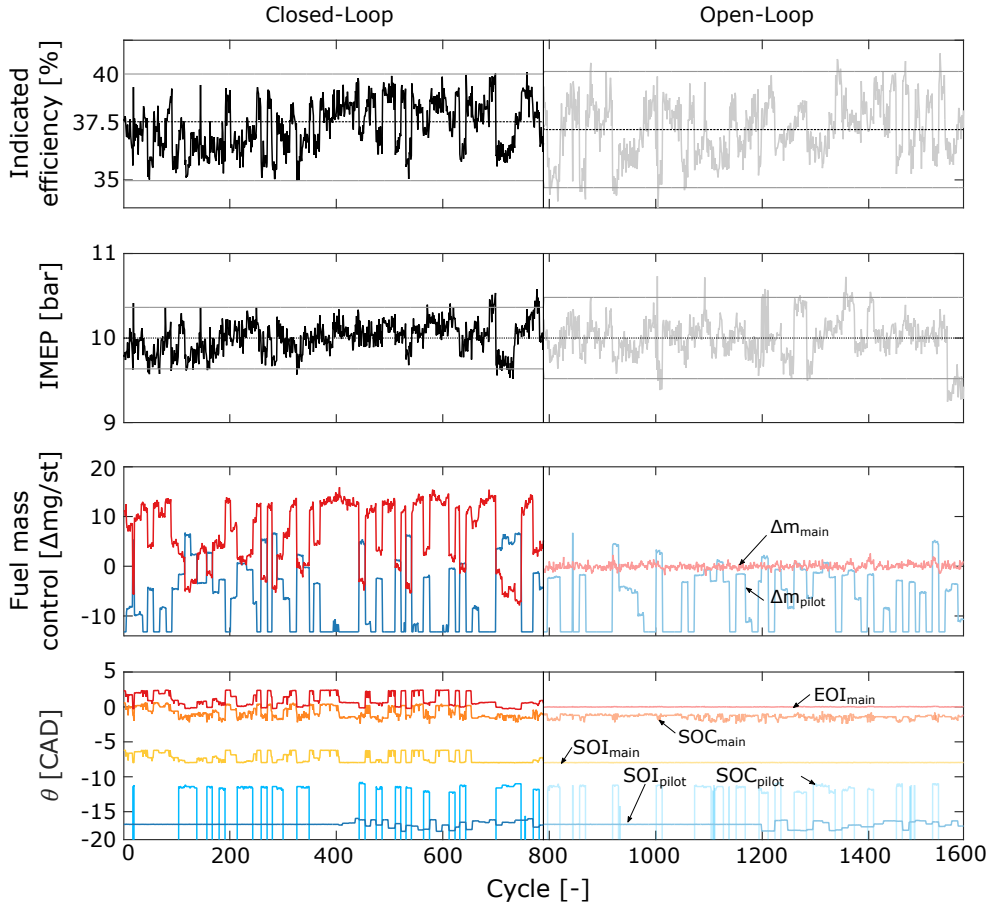


Figure 10.5: Evaluation of in-cycle closed-loop (left, dark) and open-loop (right, light) control. The indicated thermal efficiency, the IMEP, the variation of the pilot and main mass, the pilot SOI and SOC, and the main SOI, SOC and EOI are plotted for a number of cycles. The engine was run at 1200RPM, 1200bar rail pressure and no EGR. The pilot mass was disturbed from the nominal value i.e., $13.5 \pm 10\text{mg/st}$ and a $\pm 1\text{CAD}$ disturbance was added to the pilot SOI. The overlaid lines indicate the average and 95% confidence interval.

Disturbance rejection

The results of the disturbance rejection are illustrated in the plot of Figure 10.5, where the engine is run for a number of cycles with a disturbed pilot injection in closed-loop and open-loop operation. The results confirm the reduced load error and indicated efficiency variance by the in-cycle control of the combustion. Similar indicated efficiency was obtained, around 37.5%, with a small increase in closed-loop operation by the in-cycle controller.

The controller rejects successfully disturbances in the rail pressure. A rail pres-

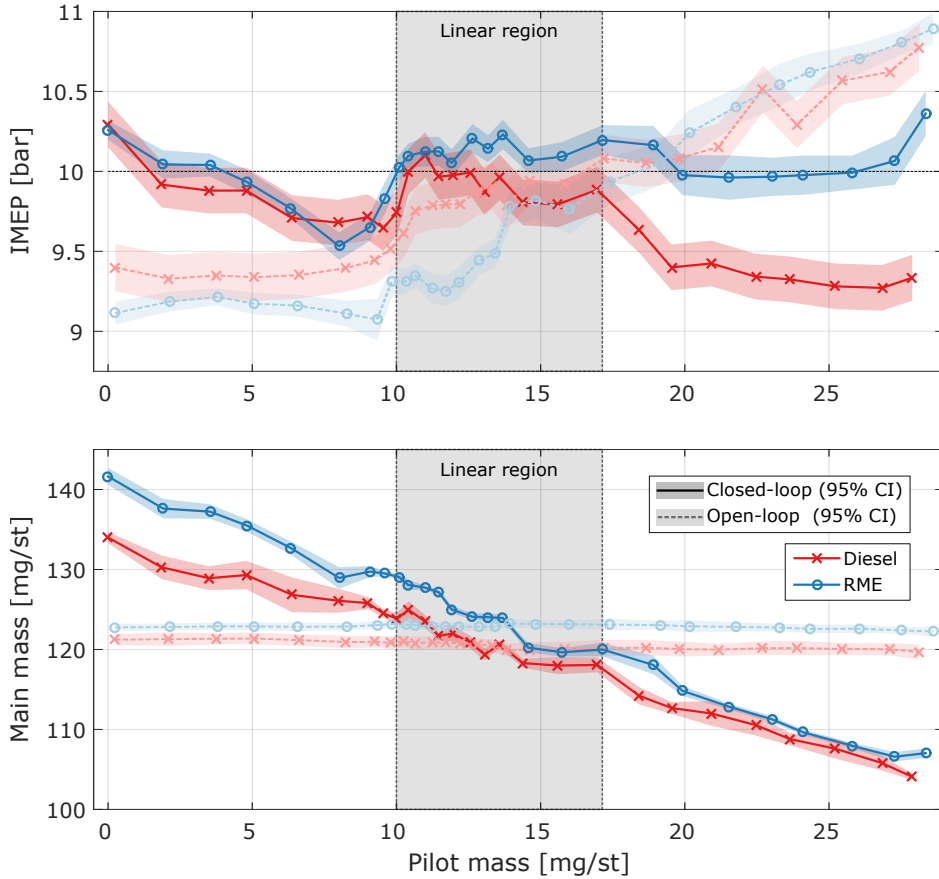


Figure 10.6: Engine load (upper plot) and main injected mass (lower plot) as function of the pilot mass for open-loop and in-cycle closed-loop operation. The engine was run with Diesel and RME. For the study of the non-linear behavior on the linear controller, the nominal pilot mass of 13.5 mg/st was disturbed with an error offset between $\pm 10 \text{ mg/st}$. The 95% confident interval over 100 cycles is overlaid.

sure sweep between 900 bar and 1500 bar resulted in an IMEP range between 7.5 bar and 12.5 bar in open-loop operation. With the in-cycle controller, the load span was reduced between 9.13 bar and 10.92 bar .

Controller limitations

To study the controller limitations due to the linearization, different pilot masses were injected at steady-state while maintaining the nominal point of linearization. The results for open-loop and closed-loop operation of the engine running with Diesel and RME are plotted in Figure 10.6. The non-linear effects can be observed in the open-loop operation. The IMEP in the upper plot is non-linear

for the different pilot masses. The controller is able to reduce the load error due to pilot combustion disturbances in the region within $\pm 3.5 \text{ mg/st}$ around the nominal 13.5 mg/st pilot injection, where the system behaves linearly. The limitations due to the non-linear effects can be reduced by updating the controller linearization on a cycle-to-cycle basis. Nonetheless, the total variation range around the nominal set-point will still be limited.

Out of the linear region, the controller still reduces the effects, but not completely. For small pilot masses, between 5 mg/st and 10 mg/st , the pilot mass estimation is less robust, which increases the final error of the controller. Furthermore, pilot misfire cycles are not fully counteracted. Within the region of large pilot masses, the controller over-compensates the pilot mass disturbance in the case of Diesel but not for RME. Therefore, the non-linear effects are also sensitive to the fuel used. The proposed controller should be calibrated specifically for each fuel or adapted on-line.

A major limitation of the direct optimization method is the possibility to include the operational constraints explicitly in the indicated efficiency optimization problem. This is limited due to the reduced availability of implementation resources required for a constrained on-line optimization solver in the FPGA. However, the indirect efficiency optimization method, presented in next section, can overcome this limitation.

10.2 Indirect Efficiency Optimization

The indirect efficiency optimization method formulates the optimization problem to exploit the reduced dispersion of the pressure trace by operating the engine with the in-cycle controller presented in Chapter 9. Publication XII investigated how the set-point reference should be set and regulated by a higher-level controller to maximize the indicated efficiency under different operational constraints. The operational constraints are related to hardware limitations (maximum cylinder pressure and maximum exhaust temperature), and emission levels (maximum pressure rise rate and minimum exhaust temperature). The maximum pressure rise rate is correlated with the engine-out noise, which has maximum legislated levels as a pollutant. The minimum exhaust temperature is a demand for efficient operation of the after-treatment system. The results of the investigation are presented in this section.

The regulated combustion metrics to reduce the dispersion were the pilot SOC, pilot burnt mass, the combustion timing and IMEP. For the combustion timing,

the main SOC and CA50 were investigated as the combustion timing set-point reference. The effect of the variance reduction on the indicated efficiency was compared in open-loop and closed-loop operation.

The upper bound to evaluate the full potential of the in-cycle controller was computed by adjusting the injection to reach the exact set-point reference. Even though this is only achievable in simulation, it permits to study the impact of the in-cycle controllability limitations on the maximum reachable indicated efficiency. For the pilot misfire compensation, the optimization of a second pilot injection was out of the scope of Publication XII. Hence, only the main injection timing was adjusted.

To represent the whole variation range by the Monte Carlo stochastic method, the simulation was run 500 iterations. As an example, three control strategies (open-loop, main SOC closed-loop and CA50 closed-loop) were simulated and are plotted in Figure 10.7. The cycle-averaged pressure and heat release traces of the different controllers is similar. However, the cyclic dispersion is different for each case. The dispersion determines the worst-case scenario of the engine-out variables, which offsets the indicated efficiency to a smaller or a larger extent when the engine-out variables are constrained.

10.2.1 Stochastic constrained optimization

For the stochastic optimization, the simulations were run for a gridded combination of the fuel injection reference variables, summarized in Table 10.1, at 1200RPM and 1200bar rail pressure. The values of the nominal simulation were used as the set-point reference for the stochastic simulation of the in-cycle controllers at each operating point of the grid. To reduce the quantization error and yet limit the total number of simulation points, the gridded data was interpolated. The efficiency was optimized by selecting the operating point with the maximum indicated efficiency for different constraint levels of the engine-out variables. The optimization problem has multiple optimal solutions. How to select the pilot set-point based on the robustness of the solution by the sensitivity analysis is discussed later.

The risk of pilot misfire and its compensation by the in-cycle controller is included in the indicated efficiency optimization. The overall expected indicated efficiency was calculated by the computation of the indicated efficiency for the pilot combustion and misfire cases, which were weighted average based on the pilot misfire probability. For the calculation of the engine-out constrained parameters, the worst-case scenario was considered.

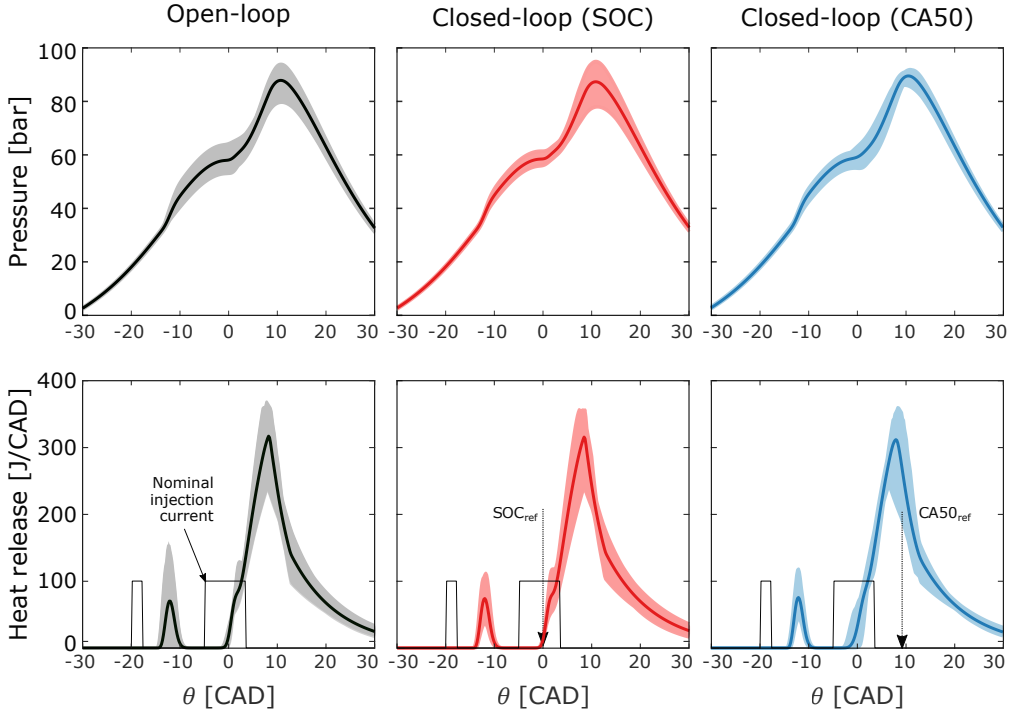


Figure 10.7: Simulation in open-loop control (left), closed-loop control of main SOC (middle) and closed-loop control of CA50 (right). The simulation was run at 10bar IMEP, 1200RPM, 1200bar rail pressure for 500 cycles. The deterministic simulation result is used as the set-point reference for the controllers. The burnt pilot mass reference was computed from the 11mg/st injected pilot mass.

Table 10.1: Gridded operating set-points for the stochastic optimization.

Variable	Range	Step size
Pilot SOI	$[-35, -5]CAD$	$2.5CAD$
Pilot mass	$[9, 14]mg/st$	$0.5mg/st$
Main SOI	$[-14, 4]CAD$	$2CAD$
Engine load (IMEP)	$[2.5, 15]bar$	$2.5bar$

Reference set-point strategy

The maximum efficiency obtained under different engine-out constrained variables is plotted in Figure 10.8 for 10bar IMEP.

The effect of the stochastic cyclic dispersion is studied by comparing the optimization of the nominal and the open-loop stochastic simulations. The deterministic result (nominal case) must be interpreted as the constraint violation when the engine is operated in open-loop and the stochastic variations are not

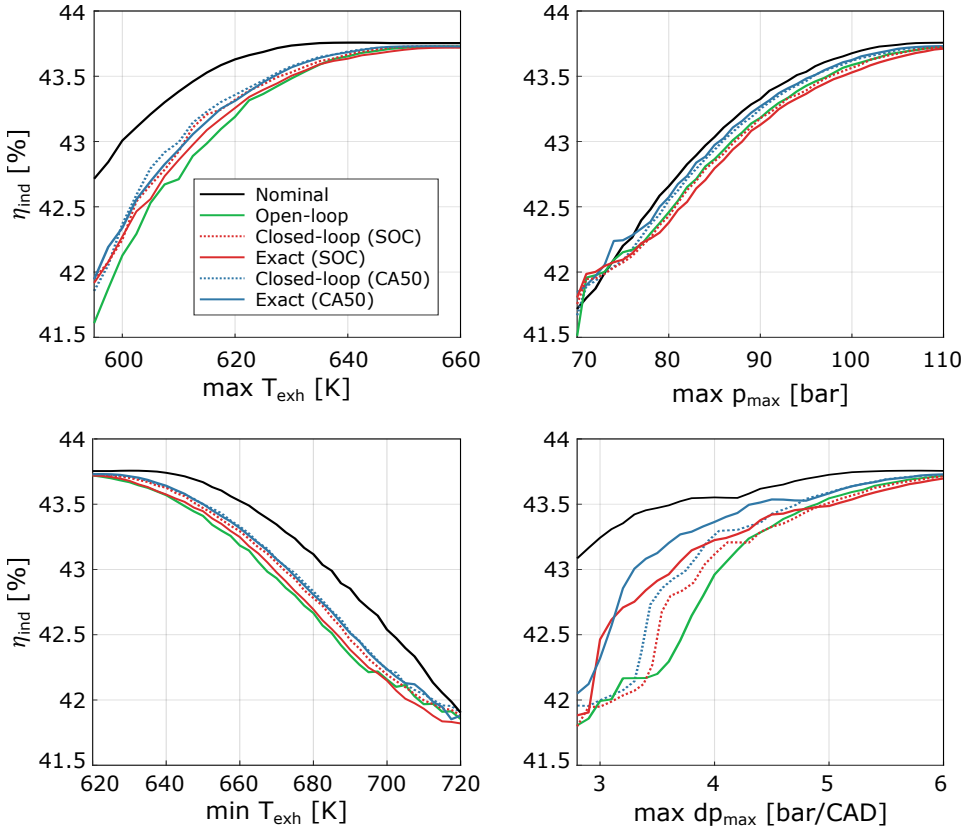


Figure 10.8: Maximum indicated thermal efficiency for maximum exhaust temperature (upper left), minimum exhaust temperature (lower left), maximum pressure (upper right) and maximum pressure rise rate (lower right) constraints. The simulation was run in open-loop for the deterministic and stochastic cases, with the closed-loop control of the main SOC and CA50, and the exact control of the main SOC and CA50.

considered. Take for example the maximum exhaust temperature (upper left plot). When the constraint is set at $620K$, the expected nominal maximum efficiency (black line) would be around 43.5%. However, when the cyclic dispersion is considered, the same efficiency is only achieved for a maximum temperature over $635K$, where the open-loop stochastic operation (green line) reaches the 43.5% efficiency. Hence, the open-loop deterministic optimization may result in constraint violations by up to 6%, and by up to 20% for the maximum pressure rise rate. Furthermore, some constraints based only on the deterministic case may never be fulfilled if too stringent.

The controllability limitations are studied by comparing the exact reference control to the in-cycle closed-loop controllers, based on the regulation of the main SOC and CA50. Consider the case of stringent maximum pressure rise

rate constraints (lower right plot) around $3.5\text{bar}/CAD$. Closed-loop operation is able to increase the indicated efficiency by up to $+1\%_{unit}$, compared to open-loop operation. However, the controllability imposition on the in-cycle controller limits the improvement to $+0.6\%_{unit}$ (compare CA50 for the exact and in-cycle controller). Due to the reduced variance of the constrained variables, the in-cycle combustion control is able to increase the indicated efficiency by about $+0.2\%_{unit}$, compared to open-loop operation. At lower loads, the efficiency is further increased, as at 10bar IMEP the combustion is less sensitive to stochastic variations (see Section 4.3.1). This is discussed in the next section.

The dispersion reduction of CA50 achieves higher indicated efficiencies than the regulation of the main SOC for any of the constrained variables. The main SOC controller does not account for the modification of the combustion rate, which may increase the total dispersion of the constrained variables compared to open-loop operation. This results in a reduced indicated efficiency. It is concluded that higher performance can be obtained by the regulation of the center of combustion, despite the additional complexities of its prediction accuracy compared to the main ignition-delay.

Effect of engine load

The constrained maximum indicated efficiency compared to open-loop operation is plotted in Figure 10.9 for different loads and in-cycle closed-loop control strategies. At low loads, the main combustion is more sensitive to the pilot combustion due to the lower pilot-main mass ratio and lower in-cylinder temperatures, which enlarges the dispersion of the operating variables. Therefore, the variance reduction at low loads increases significantly the maximum indicated efficiency. The constrained values of the maximum exhaust temperature and cylinder pressure do not represent a hardware limitation at low loads. However, the limitations on maximum pressure rise rate and the minimum exhaust temperature of $500K$ are realistic values for engine operation at low loads.

At low and medium loads, the reduction of the exhaust temperature dispersion is exploited for an indicated efficiency increase by up to $+0.7\%_{unit}$.

For engine-out noise limitations over $3\text{bar}/CAD$, the controllers are able to increase the indicated efficiency for any constraint level at low loads, up to $+0.6\%_{unit}$. As the load increases, the effective improvement is set at a smaller range around $3.5\text{bar}/CAD$. Due to the controllability limitations for very stringent constraints on engine-out noise (under $3\text{bar}/CAD$), the in-cycle controllers are not able to improve the indicated efficiency, especially in the case of low

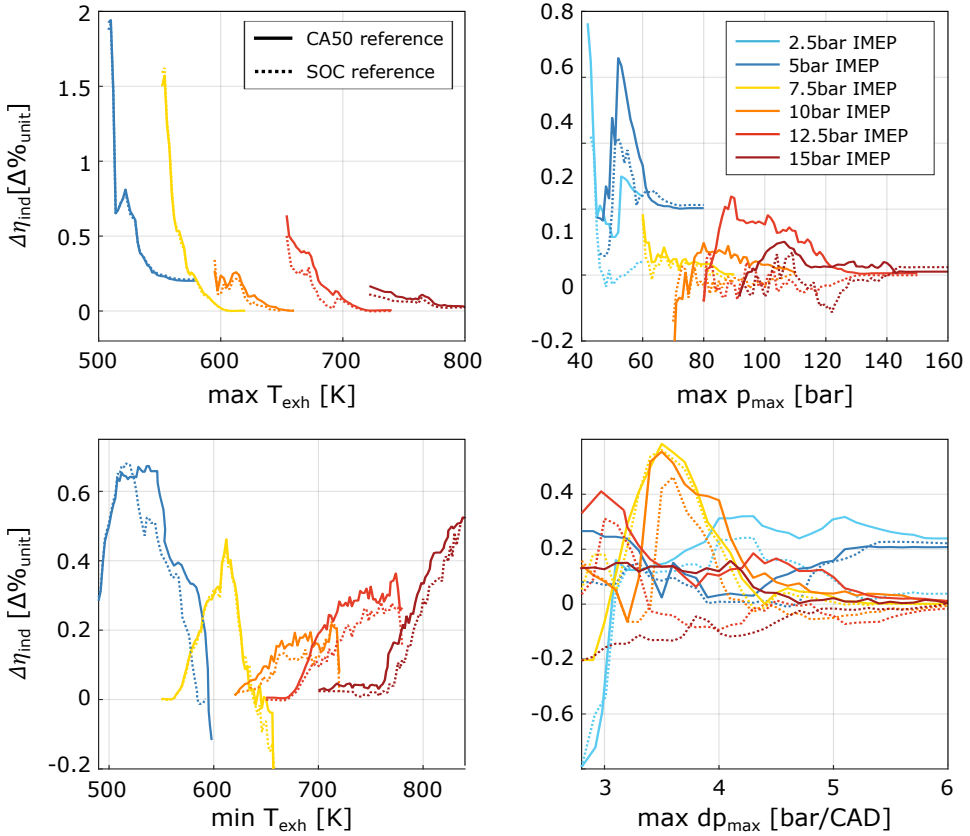


Figure 10.9: Increase of the indicated efficiency by in-cycle closed-loop operation, compared to open-loop operation, for maximum exhaust temperature (upper left), minimum exhaust temperature (lower left), maximum pressure (upper right) and maximum pressure rise rate (lower right) constraints. Loads from 2.5bar to 15bar IMEP are plotted. Note that 2.5bar IMEP is omitted in the exhaust temperature plots.

loads. The penalty is due to the limited observability when the constraint is only fulfilled for short pilot-main separations.

The regulation of CA50 provides higher efficiencies compared to the main SOC regulation, regardless of the engine load. Due to the heat release shape, the difference is smaller at lower engine loads.

Multiple constraint fulfillment

The fulfillment of multiple constraints may be compromised for inversely correlated variables. For the constraints studied, the maximum exhaust temperature is inversely correlated with the others. Hence, a compromise on the constraint

limits must be selected. The variance reduction by the in-cycle combustion controller results in a wider range of limits satisfied on multiple constraints. Moreover, the multiple constraints are attained with a higher indicated efficiency. The regulation of CA50 increases the combination space of constraint limits, as well as the indicated efficiency, compared to open-loop and main SOC closed-loop control. More detailed results can be found in Publication XII.

10.2.2 Reference set-point optimization

This section discusses the set-point reference values for the pilot and main controllers. From the previous results, it is concluded that higher performance can be obtained by the variance reduction of CA50. Therefore, it is selected in this analysis as the combustion timing reference for the in-cycle controller.

Pilot misfire trade-off

The maximum indicated efficiency, compared to open-loop assuming pilot combustion, optimal CA50 and optimal pilot set-point are plotted in Figure 10.10 as a function of the maximum pressure rise rate limit. The simulation was optimized in open-loop and closed-loop control under the assumptions of pilot combustion, pilot misfire, and their combination by the misfire probability ratio. The pilot misfire trade-off is exploited by the set-point optimization when the pilot misfire case is considered and compensated by the in-cycle controller. The range represents the multiple optimal pilot and main set-points.

For open-loop operation, the constraints are fulfilled by reducing the pilot mass set-point and retarding the main combustion. This solution is because the pilot mass variations and the risk of pilot misfire offsets the benefits of the pilot injection. Therefore, when the risk of pilot misfire is considered for the open-loop optimal solution, the indicated efficiency is reduced by $-0.1\%_{unit}$ (see the upper plot in Figure 10.10). As the constraints are relaxed, the pilot mass is increased, where short pilot injections provide the best trade-off. For engine-out noise limits over $4.5bar/CAD$, the set-point is at larger unburnt pilot masses, which burn together with a highly premixed main combustion, and permits to increase the indicated efficiency.

In closed-loop operation, the higher pilot controllability and the ability to compensate for pilot misfire permits to set the optimal set-point at a larger burnt pilot mass reference, without retarding the main injection. This solution increases the indicated efficiency to similar values of the pilot combustion scenario, by up

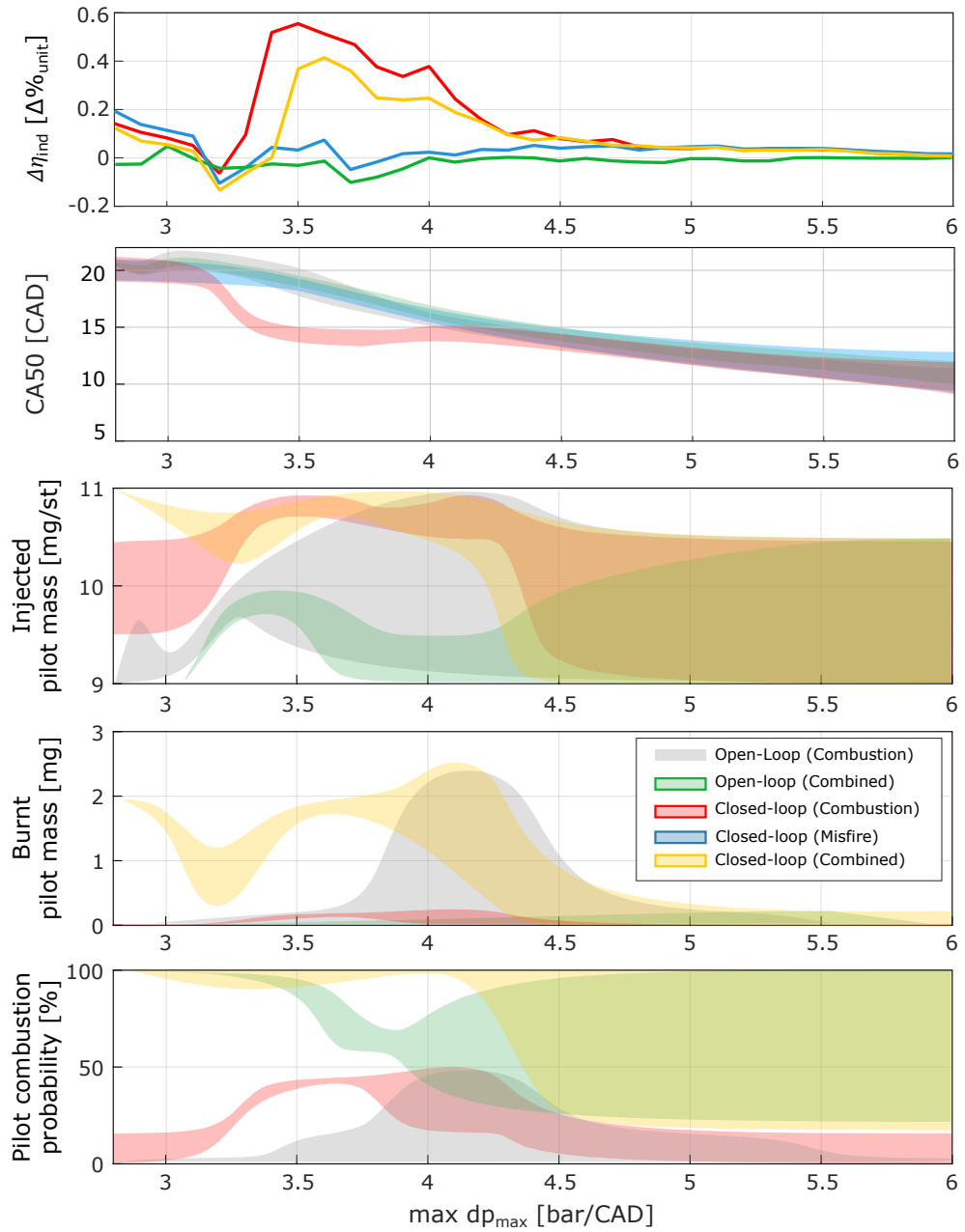


Figure 10.10: Maximum indicated efficiency compared to the stochastic open-loop optimization under pilot combustion (upper plot), CA50 and, pilot injection set-point, as a function of the maximum pressure rise rate constraint. The simulation was at 10bar IMEP, 1200bar rail pressure and 1200RPM. Note that the pilot reference is not shown for pilot misfire. The pilot injection is the same as assuming pilot combustion, but its combustion is undefined in case of misfire.

to $+0.6\%_{unit}$, depending on the active constraint. This is discussed in more detail in the next subsection.

For the rest of the studied operational constraints, the optimal pilot set-point is placed at small burnt pilot masses. This results in small sensitivity to pilot misfire. Hence, the CA50 set-point is similar for both scenarios, pilot combustion or pilot misfire, as will be discussed below.

Optimal CA50

The indicated efficiency (considering the risk of pilot misfire) and optimal CA50 set-point for open-loop and closed-loop (under pilot combustion and misfire) is plotted in Figure 10.11 as a function of the different constraints at 10bar IMEP.

To obtain the maximum efficiency while fulfilling the minimum and maximum exhaust temperatures, CA50 is advanced linearly as the constraints become more stringent i.e., a lower maximum exhaust temperature and a higher minimum exhaust temperature. The correlation to the maximum pressure is the inverse, therefore CA50 is retarded to fulfill increasingly stringent constraints. For the maximum exhaust temperature constraint, the indicated efficiency is increased by up to $+0.3\%_{unit}$, for the minimum exhaust temperature constraint by up to $+0.2\%_{unit}$ and for the maximum pressure by up to $+0.1\%_{unit}$. See Publication XII for more details.

The optimal set-point for the maximum pressure rise rate requires a more detailed study for its understanding. The indicated efficiency is improved from 3.2bar/CAD maximum pressure rise rate (see the upper plot in Figure 10.10). From this point, the in-cycle closed-loop controllability is not a limitation and the controller strategy reaches almost its maximum potential ($+0.6\%_{unit}$). Compared to the pilot combustion scenario, the CA50 reference is delayed in case of pilot misfire (lower subplot). The increase of the pressure rise rate due to the additional main premixed heat release when pilot misfires is compensated by retarding CA50, which limits the maximum achievable indicated efficiency.

In general, the optimal set-point for the combustion timing (main SOC or CA50) is retarded in case of pilot misfire, which ensures the in-cycle closed-loop combustion controllability (see Section 8.2). Therefore, pilot combustion should be the default set-point case, even under high pilot misfire risk scenarios.

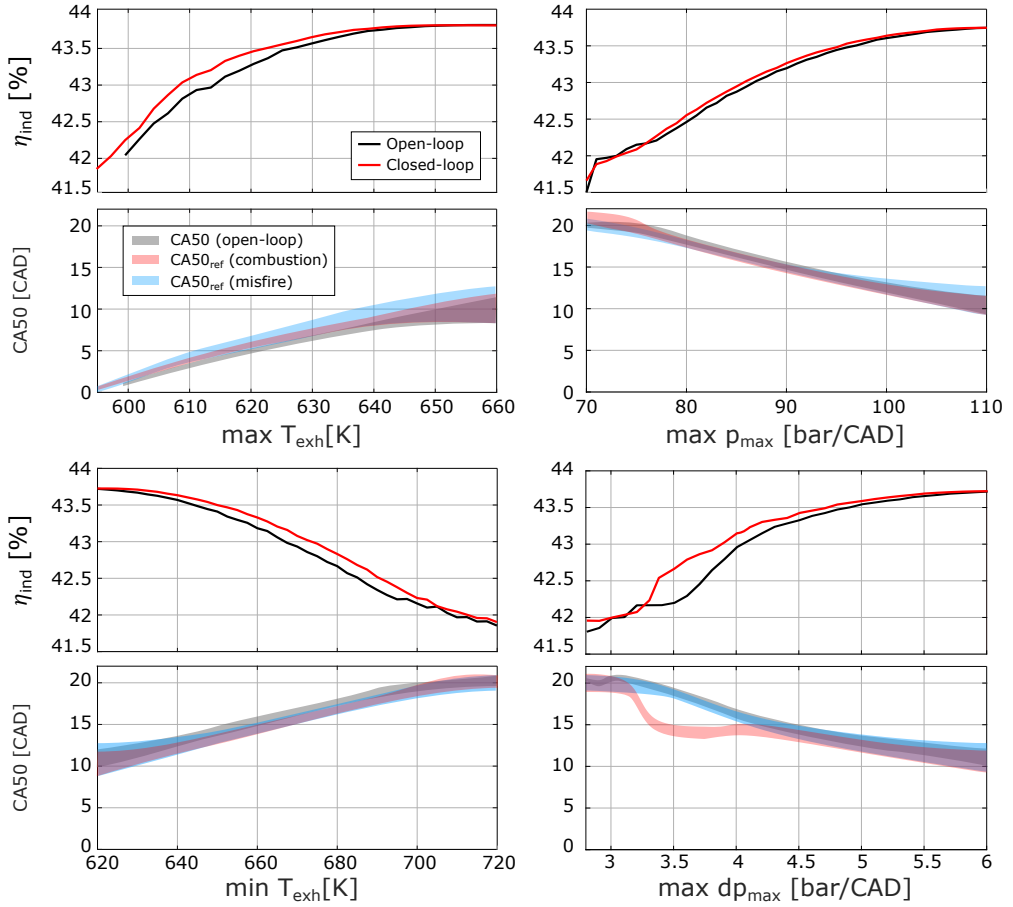


Figure 10.11: Indicated efficiency considering the pilot misfire risk (upper subplot) and CA50 set-point reference (lower subplot) for open-loop and closed-loop operation, under maximum exhaust temperature (upper left), minimum exhaust temperature (lower left), maximum pressure (upper right) and maximum pressure rise rate (lower right). The simulation was at 10bar IMEP, 1200RPM and 1200bar rail pressure.

Nominal set-point robustness

The robustness of the optimal pilot set-point differs between the solutions. This was studied in Publication XII with a sensitivity analysis to pilot mass and SOI errors. The robustness of the indicated efficiency was strongly correlated with errors in the pilot mass, generally reduced by down to $-0.8\%_{unit}$ for most of the pilot nominal masses and SOI when a $+1mg/st$ pilot mass error was added. Larger nominal pilot masses and later injections have higher sensitivity of the constraints, by up to an additional error of 4% for the maximum pressure and 40% for the maximum pressure rise rate. The exhaust temperature is not as sensitive, with an absolute error lower than 1.5%.

Implementation Requirements

The use of an ASIC for the signal processing of pressure signals for the combustion control of an internal combustion engine was first investigated by Wilhelmsson et al. (2006). It was concluded that a virtual heat release sensor can be implemented with very high throughput and negligible latency. Based on this, the in-cycle closed-loop combustion control methods presented in this thesis were all implemented in a FPGA for their real-time execution. The formulation of these methods requires special attention for their efficient implementation, with reduced hardware resources, latency, propagation delay and computational error. The hardware requirements for the real-time execution and implementation of the in-cycle closed-loop combustion control algorithms are presented in this chapter, from the results of Publication XIV.

11.1 Signal Processing Requirements

The signal processing requirements are imposed by the real-time execution of the computations within a fraction of a crank angle degree for the heat release analysis and in-cycle closed-loop control of the combustion. This section reviews the requirements of the digital signal resolution, evaluation rate and the real-time execution of the computations for a successful in-cycle combustion control.

11.1.1 Data acquisition system

The combustion regulation is based on in-cylinder pressure measurements, pegged to the inlet pressure for absolute referencing, and synchronized with the crank angle encoder. The data acquisition system should provide enough measurement and sampling resolution to obtain the required accuracy of the regulated variables, based on the heat release calculations.

The analog-to-digital converter provides the maximum pressure resolution Δp . Assuming an equidistant representation, this is a function of the digital resolution (number of bits, r) and maximum represented value (pressure range):

$$\Delta p = \frac{p_{max} - p_{min}}{2^r} \quad (11.1)$$

The typical range of cylinder pressure sensors is between $0 - 250bar$. With this pressure range and equidistant representation, the required pressure resolution is obtained for digital representations of a minimum of 10-bits, which results in $0.2441bar$ resolution.

The evaluation rate is a demand imposed for the estimation of the heat release. The main benefit of in-cycle closed-loop combustion control is the finer adjustment of the regulated combustion parameters. Hence, the error due to the evaluation rate must be under the dispersion of the regulated parameters in open-loop operation. The total combustion parameters variation range in open-loop are under $\pm 0.3CAD$. Therefore, for an effective in-cycle close-loop combustion control, the evaluation rate should be of $0.2CAD$ or lower.

11.1.2 Real-time execution

The FPGA implementation permits to run the computations in parallel, which is required for the real-time execution. Each parallel block can be isolated to guarantee its real-time execution without adding the complexities of a sequential processor for task prioritization and scheduling at a high clock frequency.

The critical execution time for the combustion control is the CAD evaluation rate, which is the clock the FPGA is synchronized with. The fastest engine speed determines the minimum clock frequency. At $3000RPM$ and $0.2CAD$ evaluation period, the required clock frequency of the FPGA is $90kHz$, which corresponds to $11.11\mu s$. The FPGA used in this project, a Virtex-5 LX110 (Xilinx, 2015), provides up to $40MHz$, which corresponds to a minimum clock

cycle of $25ns$. This means that each tick of the CAD sensor, up to 444 clock iterations are available to complete all the computations.

All the signal processing must be completed each clock step. The limitation is not on the instructions stack, but on the signal propagation delay imposed by the electronic components. The complexity of the FPGA blocks determines the total signal propagation delay (signal lag). In general, this is not a major limitation. However, it must be considered in the design of the computation blocks. National Instruments provides software tools to verify this requirement is fulfilled and the code executed in real-time.

11.2 Algorithm Implementation

The execution timing and hardware resources are directly correlated with the algorithm complexity. With the available hardware, the main limitation is the total number of computational units, rather than the execution time. The algorithm formulation will be focused on how to minimize the total FPGA resources required i.e., slice registers. The considerations for the algorithm implementation are the signal representation, integer arithmetic and pipelining.

11.2.1 Signal representation

The signal resolution is determined by the number of bits for their integer representation in the FPGA. The signal resolution must be selected adequately to reduce the consumption of slice registers. The real-valued signals are scaled for their integer representation. The scaling is done by a power of 2, as it is implemented by a bit-shift operator, which is fast and does not require much resources. The power of the scaling factor $\times 2^\alpha$ determines the number of bits shifted by the *scaling shift* α . Note that for decimal representations, α will be negative. Even for large integer variables, an adequate scaling is necessary to reduce the total FPGA resources. The scaled variable x_α will require less digital resolution while still fulfilling the requirements of the minimum precision and range of variation. To adequately choose the scaling, the minimum precision determines the scaling shift for the maximum representation error ϵ_{max} :

$$\alpha = \left\lceil \frac{\ln(\epsilon_{max})}{\ln 2} \right\rceil \quad (11.2)$$

The resulting precision ϵ_x is:

$$\epsilon_x = 2^\alpha < \epsilon_{max} \quad (11.3)$$

The scaled variable is:

$$x_\alpha = x \cdot 2^{-\alpha} \quad (11.4)$$

The number of bits for the variable representation is determined by the minimum represented range Δx_{min} . The minimum number of bits is:

$$n = \left\lceil \frac{\ln(1 + 2^{-\alpha} \Delta x_{min})}{\ln 2} \right\rceil \quad (11.5)$$

The total range of a variable x shifted by α and represented with n bits is:

$$\Delta x = 2^\alpha (2^n - 1) > \Delta x_{min} \quad (11.6)$$

11.2.2 Integer arithmetic

Intermediate scaling is necessary for an adequate accuracy of the operations and overflow avoidance.

Addition and subtraction

Addition and subtraction require the same signal scaling. The required accuracy for the result will determine if one of the variables is scaled up, the other is scaled down, or an intermediate solution is adopted. To avoid overflow, the range of the result must be considered.

Multiplication

Multiplication adds the scaling of the variables. Therefore, the overflow of intermediate operations must be considered. The required intermediate bit representation of the signal for the multiplication $x \cdot y = z$ to guarantee there is no overflow, assuming x and y are positive, is:

$$n_z \geq \frac{\ln(x_{max} \cdot y_{max})}{\ln 2} + \alpha_x + \alpha_y \quad (11.7)$$

The scaling of z is $\alpha_z = \alpha_x + \alpha_y$. Hence, the dynamic range of z is:

$$\epsilon_z = \frac{2^{n_z} + 1}{2^{\alpha_x + \alpha_y}} \quad (11.8)$$

The intermediate scaling α_x and α_y can be reduced to avoid overflow for a maximum n_z -bits representation and a required dynamic range ϵ_z . However, the rounding loss (ε_z) must also be considered, which is a function of the multiplication:

$$\varepsilon_z = x \cdot y - \frac{\lfloor (x_\alpha \cdot 2^{\alpha_x}) \rfloor \cdot \lfloor (y_\alpha \cdot 2^{\alpha_y}) \rfloor}{2^{\alpha_x + \alpha_y}} \quad (11.9)$$

Division

Division is not a native function of the FPGA. Division by a constant number can be reformulated as a multiplication. For division between two variables, the provided function requires large resources. Instead, the approach was to implement division as a tabulated function with enough resolution. The input and output are adequately scaled to use the same table for any input. The tabulated division operation is:

$$f(x_\alpha) = \left\lfloor \frac{2^{\alpha_T}}{x_\alpha} \right\rfloor \quad (11.10)$$

The result is scaled by 2^{α_T} . The scaling is chosen to obtain enough resolution of the operation with a limited number of elements n_T in the table. To use the same table with different values of x , it is first re-scaled by $\Delta\alpha$ to fit within 2^{n_T} , assuming the maximum value is known:

$$\Delta\alpha = \left\lfloor n_T - \frac{\ln(x_{max})}{\ln 2} \right\rfloor \quad (11.11)$$

The final scaling is:

$$\alpha_f = \alpha_T - (\alpha + \Delta\alpha) \quad (11.12)$$

The proposed approach is able to reduce the necessary FPGA hardware resources, most significantly the required clock cycles, from 18 to only 2.

Other functions

For other mathematical calculations, the only fast approach is to reformulate the required computations and tabulate the non-linear operations. Logarithmic and exponential functions were tabulated in the same manner as division.

11.2.3 Pipelining

The NI blocks modularization alleviates the use of FPGA resources by encapsulating the functions into reusable modules. This is the case for some mathematical operations and models. The modules can be reused along the code with a single hardware implementation. When the modules have to be accessed simultaneously, their re-entrant execution requires multiple physical copies in the FPGA. Sometimes this can be avoided by establishing a sequential execution where the modules do not need to be implemented multiple times i.e., pipelining. This is achieved by the controller manager, implemented with the finite state-machine (see Section 9.3). A compromise between execution speed and FPGA resources is necessary. For the in-cycle closed-loop combustion control, real-time execution is crucial and hence prioritized.

11.2.4 Modules implementation

Following the feedback loop of the in-cycle closed-loop combustion control (see Figure 8.1) the implemented modules are the feedback signals, including the heat release computation, the in-cycle controller, actuator driver and the feedback for adaptation (implemented in the cycle-to-cycle loop).

Feedback signals

The cylinder pressure signals are synchronized with the TDC of each cylinder, filtered and pegged to the intake pressure. For the heat release computation, the pressure derivative is calculated and filtered with a IIR low-pass filter. The cylinder pressure signal is scaled according to the transducer gain to obtain its value in Pascals, with a 32-bit integer resolution and no bit-shift scaling. For the model inputs, the pressure was scaled to bar with a 6-bit shift scaling to obtain the required resolution. These conversions can be avoided as long as there is consistency throughout the model inputs. To be able to reuse the pressure signal processing modules, only the region of interest for the in-cycle combustion control was processed. This is between $[-60, 60]CAD$, where there is no overlap between the combustion among the cylinders for a six-cylinder engine with equally spaced CAD intervals. Two filtering blocks are necessary in total (instead of six) for the pressure pegging. The CAD synchronization module is extended to select the correct cylinder signal at the current CAD. This solution saves 40% of the resources compared to an individual non-reentrant cylinder pressure signal processing running in parallel.

The heat release is computed as a single thermodynamic-zone (see Eq.(2.15)). The terms $\frac{\gamma}{\gamma-1}$ and $\frac{1}{\gamma-1}$ are tabulated as a function of the cylinder temperature, scaled by 8-bit. The cylinder volume and its derivative are tabulated with 22-bit and 28-bit shift scaling respectively. The cylinder temperature is computed with the ideal-gas law, where the initial state is the pressure and volume at IVC. The intermediate calculations are scaled adequately to avoid overflow and reduce round loss error. Finally, the heat release is expressed with a 5-bit scaling, which corresponds to a dynamic representation of $0.03125J/CAD$.

Observer

The in-cycle observer consists of the polytropic estimation, the start of combustion detector and the pilot mass estimation. The intake observer sets the intake volume and temperature, and estimates kappa for the in-cylinder pressure prediction as a polytropic process. The exponential expression is transformed by taking logarithms (see Section 6.2). The logarithms of the pressure and volume are both implemented as tables with a shift scaling of 12-bit and 10-bit respectively. The polytropic coefficient uses a scaling of 15-bit. The pilot mass was represented with a 5-bit shift for a dynamic representation of $0.03125mg$.

Predictive models

The models are composed of linear-in-parameter functions, described in Section 5.3. The implementation is a set of multiplications with adequate intermediate scaling operations for a satisfactory resolution of the model output.

For the estimation of the main ignition-delay, the pressure is predicted until the main SOI in three steps. These are, the compression up to the pilot SOC, the pressure rise due to the pilot combustion (modeled as an isochoric combustion), and the compression until the main SOI. The implementation requires two pressure compression modules running in parallel. However, one can be reused from the pilot combustion module, configured as a non-reentrant, to save FPGA resources.

Controller

The pilot controller is composed of the sub-modules for the prediction, estimation, and regulation of the pilot combustion. These are included in the pilot observer, composed of the pressure compression, ignition-delay and combustion

Table 11.1: Hardware requirements for in-cycle closed-loop combustion control implementation.

Module	Slices	Registers	LUT	RAM	Propagation delay [ns]
Signal processing	1825	4567	3379	0	8.815
Heat release	789	1677	1226	6	11.322
In-cycle control	7036	12154	18099	7	10.863
Adaptation variables	1278	3138	2248	0	4.791
Multi-pulse injection	5220	14925	9574	0	6.791
Other	1844	8606	11967	13	7.26
Total	16816	44330	53371	25	17.376

efficiency predictors, the SOC and the burnt pilot mass estimation. The regulated variables are the pilot SOI, scaled in CAD ticks, and the pilot mass, scaled by 5-bit shift. For the regulation of a second pilot injection, some of the modules can be reused. However, some additional variables specific for the second pilot injection are necessary. The main controller follows the same structure as the pilot, with the corresponding models. The regulated variables are the main SOI, scaled in CAD ticks, and the main on-time, scaled with 12-bit.

Actuator

The actuator is responsible for commanding the control action signals to the injectors, adequately synchronized with the CAD. It includes the translation module for the conversion of the injection current commands to the injector driver and the injector driver itself. The translation module is required for each injection pulse, whilst the injector driver is necessary for each injector.

11.3 Hardware Requirements

By following the previous guidelines to reduce the total FPGA resources, the required modules of the in-cycle closed-loop combustion control were implemented. A summary of the hardware requirements for the different modules is in Table 11.1. The in-cycle control was compiled with support for a single pilot injection. Due to the routing of the signals where all the modules are connected, the total resources are not necessarily the sum of the previous blocks. As some of the RAM memory blocks are re-utilized along the different modules, the total number of RAM blocks is less than the sum of the individual

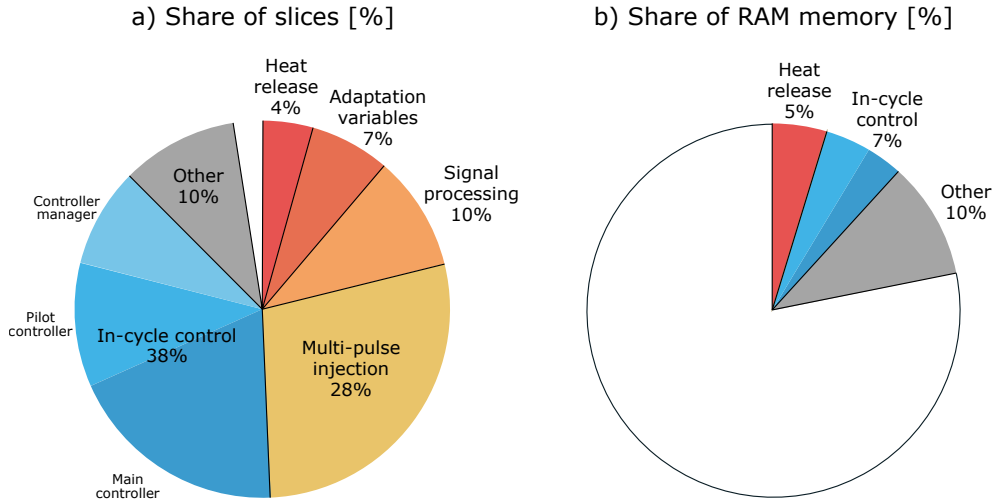


Figure 11.1: Share of slice registers for each module (a) and RAM memory blocks for each module (b), implemented in the Xilinx Virtex-5 LX110.

modules. Additional resources for the implementation of other tasks are also required. These include the A/D conversion, signal buffering and transmission, CAD synchronization and some safety features.

In total, the Virtex-5 LX110 FPGA used in this research has 17280 slice registers (see Section 3.4.1 for the FPGA specifications). The proportion of slices and RAM blocks required for each module are plotted in Figure 11.1. The in-cycle controller is the module that consumes the largest resources. The main controller is the one that represents the largest share. This is because the main controller relies on the pressure prediction, which requires memory blocks as well as many arithmetic operations and logic paths.

The injector drivers require a large share of the total FPGA resources. This is because the modules are implemented as re-entrant for the parallel computation of each cylinder. Furthermore, the module requires a logic for the activation and de-activation of each injection pulse (pilot, main) with a vector of the configuration pulses. The combination of all the logic paths for each entrance in the vector increases the complexity of the logic circuits, which demands a large share of slice registers. This module can be further optimized to alleviate the congestion of the FPGA. Moreover, this module is normally implemented on its own platform. This significantly alleviates the FPGA resources for their use on other tasks focused on in-cycle closed-loop combustion control, such as a module to compute the NO_x emissions. See Publication XIV for more details about this option.

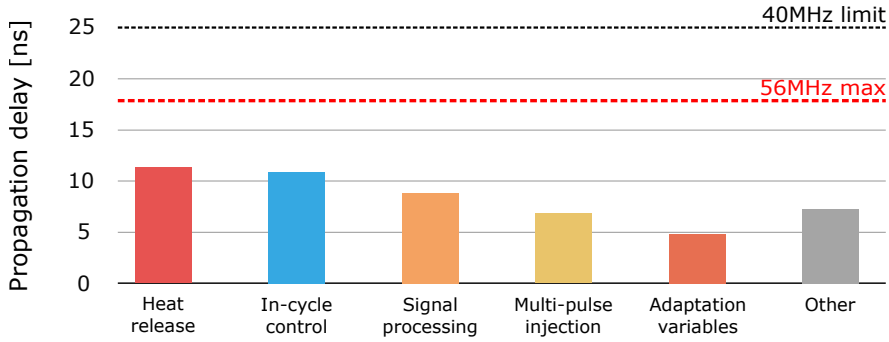


Figure 11.2: Propagation delay of each module implemented in the Xilinx Virtex-5 LX110. The maximum clock frequency allowed by the total propagation delay is indicated.

With the proposed implementation approach for the models, a minimum of 25 RAM blocks are required. The largest share is utilized for additional operations necessary for the correct functioning of the engine, mostly for the buffer to transfer data to the real-time controller. The FPGA in this study provides up to 128 RAM blocks. Therefore, limited slices can be overcome by implementing part of the calculations in memory blocks. This approach can alleviate the use of slices and benefit from the extra memory blocks not used. The implementation of the division operation took advantage of this solution.

The propagation delay of the different modules is plotted in Figure 11.2. The heat release is the module that requires the least hardware resources. However, the heat release has a relatively large propagation delay. This is due to the required intermediate signal scaling together with the look-up tables for the gamma terms in the heat release equation. The computations of the heat release module are required as inputs for the in-cycle controller, which may compromise the total propagation delay in case the in-cycle controller had a larger delay. Improvements of the heat release module implementation for an enhanced pipelining can be investigated in case the total propagation delay becomes a limiting factor.

To select an adequate hardware, the compiled code should not be over the 80% of the hardware resources, as a rule of thumb. Hence, a minimum of 21020 slice registers are necessary with the architecture of the Virtex-5 FPGA family. The Virtex-5 LX155 fulfills this requirement, with additional resources in the LX220 and LX330. The clock frequency should be of a maximum of 56MHz. Otherwise, further optimization in the FPGA code would be necessary.

CHAPTER 12

Summary and Conclusions

This research project has investigated the possibilities and capabilities of the combustion regulation by the in-cycle closed-loop control of multiple injections. The combustion was characterized experimentally to understand the coupling between the injections and how the combustion metrics are affected by the number of injections, injection timings and durations, at different operating conditions. To obtain feedback in real-time, on-line diagnostic methods have been developed for their in-cycle implementation. Due to the intrinsic delay between the controlled actions and measurements, predictive models were proposed along with adaptation methods to obtain accurate prediction of the regulated metrics. Control methods were investigated attending different strategies for the reduction of the combustion variance and misfire compensation. A supervisory control was proposed to modularize the different components and ease the transitions between the control strategies at different operating conditions. The ability of the in-cycle controller to reduce the combustion dispersion and compensate for pilot misfire was exploited to maximize the indicated efficiency under constraints by stochastic simulation methods. An on-line in-cycle controller to maximize the indicated efficiency was also proposed and validated experimentally. Finally, the required hardware to implement the proposed methods was quantified.

A summary of the main conclusions of this thesis is provided below.

Combustion control with multiple injections

The combustion of the pilot injection is significantly impacted by the on-time, rail pressure and chamber thermodynamic state at the start of injection. The risk of pilot misfire is reduced for larger pilot masses, later injections and higher rail pressures. Following this trend, the dispersion of the pilot ignition-delay and AHR are also reduced. For the small pilot masses investigated, the pilot combustion is completed during the premixed combustion phase. This results in a constant heat release duration, with a variable magnitude depending on the pilot mass. The accumulated heat release is a non-linear function of the injected pilot mass and ignition-delay, which set the combustion efficiency. The dispersion of the pilot combustion originates from cycle-to-cycle and cylinder-to-cylinder variations. Furthermore, the combustion of the previous cycle and the pilot combustion are uncorrelated, which is assumed to be due to the high stability and low residuals of Diesel combustion.

The pilot combustion timing impacts the combustion of the main injection. From this result, the *interaction modes* were defined to describe the effects of the pilot combustion on the main combustion and engine-out metrics. Following the pilot combustion sequence, the modes are, mixing, premixed, completed and diffusive mode. As the interaction mode transitions from mixing to completed, the main injection has to be retarded to maintain the center of combustion. This is explained by the shorter main ignition-delay, lower premixed combustion and lower main mass once the pilot combustion is triggered. As a consequence, the maximum pressure rise rate is reduced from premixed combustion mode onwards. The engine-out parameters are most significantly affected by the main combustion timing. However, the interaction mode also impacts the indicated efficiency, maximum pressure, exhaust temperature and NO_x emissions. The indicated efficiency is increased in premixed mode and reduces as the pilot combustion is larger. This same trend is followed by the exhaust temperature and maximum pressure.

To reduce the impact of the pilot combustion on the main combustion, the burnt pilot mass has the most significant effect. This is a combination of the injected pilot mass and combustion efficiency. Hence, the estimation of the burnt pilot mass provides effective feedback for the regulation of the main combustion. In-cycle controllability is obtained for large enough separations between the pilot combustion and the required main SOI to achieve the set-point reference of the main combustion.

Predictive models

To overcome the delay of the feedback signal and the control action, accurate predictive models are required for an effective in-cycle combustion control. The significant system non-linearities demand non-linear models to provide enough accuracy in the whole range of the combustion regulation. However, with the limited resources of the FPGA and the real-time execution demand, this can only be achieved by simplified models. To still achieve the required prediction accuracy, the models were adapted on-line individually for each cylinder. Whilst this increases the total number of parameters, proportional to the number of cylinders, a reduced adaptation method was investigated. In this adaptation structure, some model parameters are adapted individually for each cylinder, and the rest are commonly adapted for all the cylinders. The additional advantage of this solution is an increased robustness. Despite the benefits of a more accurate model-based prediction, adaptation may incur larger transients and even destabilize the system if not adequately calibrated. Over-parametrization of the models may result in instabilities due to the adaptation.

Virtual sensors

The feedback information to the in-cycle regulators is provided by virtual sensors based on in-cylinder pressure measurements. A set of in-cycle diagnostic and estimation methods has been proposed and investigated in this thesis:

- **Cylinder volume:** linear models can increase the accuracy of the cylinder volume estimation. This permits to increase the accuracy of the estimated heat release parameters for more precise control.
- **Heat capacity ratio:** for the in-cycle pressure prediction, it is more effective to estimate the current κ than applying tabulated NASA polynomials. However, it requires an initial CAD interval to be able to obtain an initial estimate.
- **Pilot misfire detection:** for a robust detection, prior knowledge of the expected pilot combustion is required. This can be included following deterministic and stochastic approaches for the models formulation, which require in any case high accuracy. As an alternative, a detection threshold adaptation is an effective manner and a good compromise between detection robustness and low implementation requirements and computations. Pilot combustion observability limits the correct misfire detection to 98%

of the misfire cycles. With the proposed methods, up to 96% of pilot misfires can be detected correctly in real-time.

- **SOC detection:** for fast on-line detection, prior knowledge must be included by predictive ignition-delay and measurement noise models. A real-time accuracy within $\pm 0.3CAD$ error can be obtained.
- **Pilot mass:** the most significant information to infer the injected pilot mass is the peak of the heat release, due to the premixed combustion of short pilot injections. High accuracy can be obtained at this point (of $\pm 0.5mg/st$), and refined as more information is gathered, up to $\pm 0.45mg/st$. An iterative approach increases the robustness, mostly for short on-times where an estimation by the model inversion (division) is very sensitive and may cause large errors. The linear parametrization of the pilot combustion model and the linear approach of the estimation method limit the applicable region for good estimation accuracy. For short pilot on-times, the reduced combustion efficiency increases the uncertainty of the pilot mass estimation based on variables such as the heat release or the rail pressure. Based on the pilot misfire ratio, the accuracy and uncertainty of the initial estimates can be increased by 60%, from $\pm 1.32mg/st$ to $\pm 0.54mg/st$.

In-cycle closed-loop combustion control

The design of in-cycle closed-loop combustion controllers was investigated attending different control targets:

- **Variance reduction:** the in-cycle control of the combustion metrics, based on predictive models, is able to reduced the variations of the pilot SOC from $\pm 1CAD$ in open-loop to $\pm 0.4CAD$ in closed-loop, from $\pm 1.5mg$ to $\pm 0.6mg$ for the burnt pilot mass, from $\pm 0.4CAD$ to $\pm 0.3CAD$ for the main SOC, and from $\pm 0.8bar$ to $\pm 0.2bar$ IMEP for the engine load. The benefits are mostly at lower loads, where the intake conditions and pilot combustion variance are larger. At higher loads, the improvements are less significant as the combustion becomes more robust. To avoid large transients and oscillations, robust adaptation methods are necessary. Controllability limitations have to be included explicitly to avoid instabilities.
- **Pilot misfire compensation:** the proposed in-cycle strategy proved to increase the robustness and performance of the combustion regulation by the pilot misfire compensation. The main SOC error was reduced from

$+1.5CAD$ to $0 \pm 0.4CAD$, and the engine load error was reduced from $-0.5bar$ IMEP to $0 \pm 0.2bar$ IMEP. A second pilot injection is required for a complete compensation of also the center of combustion. In case of limited implementation resources, a cycle-to-cycle controller with an in-cycle switch is also effective for most effects of pilot misfire, although with a reduced performance.

- **Controller manager:** multiple strategies can be easily handled by a modular design of the controllers. A supervisory controller can integrate them for a seamless transition between the different strategies. A finite state-machine was proposed and investigated, where the interdependencies of the feedback signal, control strategy and actuation are encapsulated in individual blocks. This reduces the implementation and calibration effort of the different modules, allowing for high scalability, sequential development and integration of additional controllers. This framework was tested experimentally, where the controller performance, transient response and robustness were improved over a wide range of operating conditions.

Efficiency optimization

The efficiency can be increased by the in-cycle control of the combustion. A direct method, by the in-cycle efficiency maximization, and an indirect method, by the reduction of the cyclic variations, were proposed and investigated for the efficiency optimization:

- **Direct optimization:** the indicated efficiency sensitivity to the pilot combustion efficiency is strongly non-linear and a function of the nominal pilot mass. The largest penalty occurs for pilot misfire, with a reduction of $-1\%_{unit}$. The controllability limitation determines the maximum reachable efficiency set by an in-cycle controller. An in-cycle regulator can compensate in 86% of the cases the impact of pilot combustion variations on the indicated efficiency, increasing it $+0.3\%_{unit}$ and up to $+1\%_{unit}$. Observability constraints do not impact significantly the indicated efficiency controllability, with a penalty of $-0.01\%_{unit}$ and a minimum of $-0.4\%_{unit}$. A mixed-cycle approximation was used for the explicit on-line optimization of the indicated efficiency based on the pilot combustion feedback. The function was linearized for the derivation of the in-cycle controller. The experiments validated this approach, where the indicated efficiency

can be improved by $+0.42\%_{unit}$. However, the linear approximation limits the effectiveness of the controller for a wide range of operating conditions.

- **Indirect optimization:** a simulation model was derived for the stochastic simulation with a Monte Carlo approach. The indicated efficiency was optimized under maximum pressure, maximum pressure rise rate, maximum and minimum exhaust temperature constraints. The optimal set-point took advantage of the pilot misfire probability to obtain a more robust solution and include the reduced dispersion of the in-cycle combustion controllers. The efficiency was maximized effectively by the regulation of the center of combustion. With this approach, the indicated efficiency can be increased by up to $+1.8\%_{unit}$ at low loads and $+0.6\%_{unit}$ at medium loads. The in-cycle regulation of the combustion presented the largest advantage at operating conditions with constrained engine-out noise. To guarantee the in-cycle controllability in case of pilot misfire, the nominal set-point should consider pilot combustion as the default case. By considering the risk of pilot misfire, the indicated efficiency can be increased by an additional $+0.3\%_{unit}$.

Hardware requirements

The in-cycle controllers are implemented in a FPGA for their real-time execution. To reduce the hardware requirements, in-depth analysis of all the operations involved is necessary for an adequate scaling and digital representation. Large resources can be retained by re-using the same modules for all the cylinders, where the computations for the combustion control do not overlap. Resources can be saved by the implementation of re-entrant blocks, which can be reused along the in-cycle computation modules.

CHAPTER 13

Future Work

Suggestions of future work for further in-depth understanding of the presented methods and strategies for in-cycle closed-loop combustion, and possible alternatives, are presented in this chapter. The suggestions are in connection with possible future demands on the combustion control due to hardware modifications and driving conditions, such as fuel properties and alternative combustion concepts. The future work proposals are detailed below for each of the sections of this thesis.

Combustion control with multiple injections

Future work for the combustion characterization should focus on alternative injection patterns with additional injections, and how they impact the combustion metrics and engine performance. The effects of a second pilot injection is a natural progression to investigate how the pilot misfire controller should be derived for the regulation of the second pilot combustion.

The combustion control was limited to a discrete number of injection pulses. However, there are advanced injection systems that permit injection rate shaping. The impact of the additional degrees of freedom on the combustion will be an issue for future research for the design of in-cycle combustion controllers

with the injection rate as the controlled variable.

The main advantage of in-cycle closed-loop combustion control is a more robust and stable combustion, allowing a reduction of the combustion dispersion. A characterization of the combustion metrics dispersion as a function of the fuel injection parameters and operating conditions for different fuels will be an interesting addition to the results presented in this thesis. The investigation will permit to quantify better the benefits of in-cycle combustion control.

The investigation of the in-cycle closed-loop combustion controllability was limited to a pilot-main injection for only one operating condition. Further investigation is necessary to understand the limitations of the combustion controllability including a second pilot injection for a wide range of operating conditions. The effects of the rail pressure on the controllability will expand the knowledge to optimize the controller reference set-point. This knowledge will support which control strategy to follow at the different operating conditions. The number of injections required to regulate the combustion at transitions from low to high loads will provide insights on how the supervisory controller must handle the transitions.

Predictive models

The accuracy of the predictive models determines the final performance of the in-cycle controller. For the engine load regulation, the IMEP is fully regulated relying on the model prediction. Further studies can focus on more complex models for higher prediction accuracy of the engine load over a wider range of operating conditions, which will improve the main mass regulation and reduce the transient effects during the model adaptation for large load steps.

On-line model adaptation

The model adaptation was based on linear methods, where the models had to be formulated as linear-in-parameters. Future research of in-cycle controllers may require more complex models without the possibility of a linear-in-parameters model formulation. Therefore, other adaptation techniques will be necessary to enable the use of non-linear models without the compromise of linearized lumped parameters.

The proposed multi-cylinder adaptation method was used for a robust adaptation of the multiple cylinders. Future research might explore the possibilities of

the reduced multi-cylinder adaptation for the development of on-line diagnosis of the system.

Virtual sensors

The heat capacity ratio was estimated in-cycle for high prediction accuracy of the pressure during compression. This demands an initial interval for the collection of pressure data. An accurate initial estimation can reduce the initial interval for the kappa estimation and increase its accuracy. Further studies can combine the on-line estimation method with other initial estimations, based on e.g., NASA polynomials or other heat capacity ratio cycle-to-cycle estimation approaches, to reduce the required initial interval at the beginning of the cycle.

The pilot mass estimation was based on off-line calibration of the combustion model. Further development includes how the cycle-to-cycle adaptation of the models can increase the in-cycle estimation accuracy and reduce the calibration effort. Additionally, future work should focus on the impact of multiple injections on the estimation accuracy. Further development can improve the estimation accuracy and robustness of the estimation by the combination of additional estimation sources, such as the rail pressure, by sensor fusion methods. This can reduce the sensitivity to measurement errors and model uncertainties.

In-cycle closed-loop combustion control

The predictive controllers assumed the combustion of the multiple injections were decoupled. Further investigation on how the controllers can be designed to handle the overlap of the combustions is suggested for future work. An initial approach was suggested in Turesson (2018). The limitations of the predictive controller were the instabilities generated when unfeasible control actions were commanded, which destabilized the system. Future research can investigate how to explicitly include these constraints in the controller.

For the pilot misfire compensation, the second pilot duration was calibrated and not regulated on-line. A natural continuation of this work should investigate how the second pilot timing and on-time can be regulated for an efficient pilot misfire compensation.

For the supervisory controller strategy, the continuation of the work presented in the thesis will be to include additional controllers, such as the one proposed in (Muric et al., 2013a) for the NO_x regulation. It will be interesting to investigate

how the transition of different control strategies will affect the engine performance, mostly for strategies with conflicting targets, such as the regulation of NO_x and soot or combustion timing and engine-out noise.

Efficiency optimization

The in-cycle controller for the efficiency optimization was linearized. This proved to be a major limitation due to the non-linearities of the system. Future work should include the non-linear implementation of the optimal efficiency controller. How to include the operational and hardware constraints in the controller is an issue for future research to explore.

The set-point of the indicated efficiency was optimized in simulation. The experimental evaluation of the simulation results are required to confirm their validity and quantify their potential.

Future work should include other constraints in the optimization problem, such as NO_x . To this end, stochastic models of NO_x emissions will have to be investigated as well.

Additional control actions can also be included in the optimization problem, such as a second pilot injection for the pilot misfire compensation. A post injection can be an interesting control strategy to handle the minimum exhaust temperature constraint. An additional variable that can impact the controller performance, hence the final indicated efficiency, is the rail pressure. It affects the in-cycle combustion controllability and dispersion, which can have a significant impact on the result of the optimal set-point. Future work can include this variable in the optimization problem.

Future studies can use the same stochastic simulation approach to investigate how the optimal nominal set-point impacts the in-cycle combustion controller designed for the on-line indicated efficiency maximization, and how the set-point has to be defined for its use as the in-cycle controller reference.

The set-point was optimized only at steady-state conditions. Future research can investigate how to adjust the set-point during transients, such as cold-start.

The optimization was run off-line for the derivation of the optimal set-point reference for the in-cycle controller. It will be interesting to study how the stochastic knowledge of the combustion, including the reduction of the dispersion by the in-cycle regulator, can be used by a cycle-to-cycle controller to adjust on-line the set-point reference for the in-cycle controller. Additional suggestions

for future work is to investigate how these results can be integrated in a MPC controller.

The models were calibrated for standard Diesel fuel. Further development includes how the set-point is modified for alternative fuels with different properties and combustion characteristics.

Other suggestions

This investigation was only focused on conventional Diesel combustion. Future research could usefully explore the benefits of the in-cycle control of more unstable combustion concepts, such as PPC and HCCI. In this same aspect, different combustion modes may be used at different operating conditions. How to handle these transitions by an in-cycle controller will be an interesting extension of this work. Investigations that are currently being carried out is how in-cycle combustion control should be designed for spark-ignition engines. The similarities and specific solutions for the systems will be an interesting addition to gather further insights for future work and understand the potential of in-cycle closed-loop combustion control.

For the implementation of the in-cycle combustion control algorithms, the limited resources require that they are employed only when strictly necessary. This was successfully achieved in the code by the non-reentrant implementation of the reusable modules. In this aspect, the signals were evaluated in an equally spaced CAD, even when there was no combustion or the controllers were inactive. A suggestion for future development will be the uneven sampling and reconstruction of the pressure signal, where the CAD intervals are increased as the frequency content of the signal of interest decreases. How to develop a method to optimize the variable evaluation rate is an interesting research area where there is still limited theoretical knowledge.

Future hardware modifications will increase the total degrees of freedom for the control of the combustion, such as variable valve actuation. Research of in-cycle closed-loop methods for the regulation of the combustion by VVA is suggested for future work.

An area not explored in this thesis is the possibility to use additional measurements for in-cycle closed-loop feedback. Some suggestions for future investigation are the variations in the crank angle speed or pressure measurements at the injector tip. In this regard, other signals, such as the ones provided by knock sensors, can be investigated as an alternative to the in-cylinder pressure

transducers or as a hybrid solution to reduce the total cost of the system.

Finally, the evaluation of the proposed methods in real-world conditions will be an important milestone for the assessment of the results presented in this thesis. The in-cycle closed-loop combustion control can be implemented on an engine mounted on a truck. This will permit to evaluate the potential of closed-loop combustion control for the improvement of the engine efficiency, reduction of emissions, increased robustness and the reduction of the development time and calibration effort.

References

- Andersson, Ö. (2012). *Experiment!: planning, implementing, and interpreting*. Wiley.
- Arrègle, J., López, J. J., García, J. M., and Fenollosa, C. (2003a). Development of a zero-dimensional diesel combustion model. part 1: Analysis of the quasi-steady diffusion combustion phase. *Applied Thermal Engineering*, 23(11):1301–1317.
- Arrègle, J., López, J. J., García, J. M., and Fenollosa, C. (2003b). Development of a zero-dimensional Diesel combustion model. Part 2: Analysis of the transient initial and final diffusion combustion phases. *Appl. Therm. Eng.*, 23(11):1319–1331.
- Asad, U. and Zheng, M. (2008). Real-time heat release analysis for model-based control of diesel combustion. In *SAE World Congress & Exhibition*. SAE International.
- Assanis, D. N., Filipi, Z. S., Fiveland, S. B., and Syrimis, M. (2003). A predictive ignition delay correlation under steady-state and transient operation of a direct injection diesel engine. *J. Eng. Gas Turbines Power*.
- Åström, K. and Murray, R. (2008). *Feedback Systems: An Introduction for Scientists and Engineers*. Princeton University Press, Princeton, NJ, USA.
- Åström, K. and Wittenmark, B. (1997). *Computer-controlled systems: theory and design*. Prentice Hall.
- Auzins, J., Johansson, H., and Nytomt, J. (1995). Ion-gap sense in misfire detection, knock and engine control. *SAE Transactions*, 104:1–8.
- Badami, M., Mallamo, F., Millo, F., Rossi, E. E., and Torino, P. (2002). Influence of Multiple Injection Strategies on Emissions, Combustion Noise and BSFC of a DI Common Rail Diesel Engine. *SAE Technical Paper*, (2002-01-0503).

- Badami, M., Millo, F., and D'Amato, D. D. (2001). Experimental Investigation on Soot and NO_x Formation in a DI Common Rail Diesel Engine with Pilot Injection. *SAE Technical Paper*, (2001-01-0657).
- Borgqvist, P. (2013). *The Low Load Limit of Gasoline Partially Premixed Combustion (PPC)-Experiments in a Light Duty Diesel Engine*. PhD thesis, Lund University.
- Bosch (2011). *Automotive Handbook*. Wiley.
- Carlucci, P., Ficarella, A., and Laforgia, D. (2003). Effects of pilot injection parameters on combustion for common rail diesel engines. Number 2003-01-0700. SAE International.
- Catania, A. E., Finesso, R., and Spessa, E. (2011). Predictive zero-dimensional combustion model for DI diesel engine feed-forward control. *Energy Conversion and Management*, 52(10):3159–3175.
- Cesario, N., Tagliatela, F., and Lavorgna, M. (2006). Methodology for misfire and partial burning diagnosis in si engines. *IFAC Proceedings Volumes*, 39(16):1024 – 1028. 4th IFAC Symposium on Mechatronic Systems.
- Chang, J., Kim, M., and Min, K. (2002). Detection of misfire and knock in spark ignition engines by wavelet transform of engine block vibration signals. *Measurement Science and Technology*, 13:1108.
- Chmela, F. G. and Orthaber, G. C. (1999). Rate of Heat Release Prediction for Direct Injection Diesel Engines Based on Purely Mixing Controlled Combustion. *SAE Technical Paper*, (1999-01-0186).
- Chmela, F. G., Pirker, G. H., and Wimmer, A. (2007). Zero-dimensional rohr simulation for di diesel engines – a generic approach. *Energy Conversion and Management*, 48(11):2942 – 2950. 19th International Conference on Efficiency, Cost, Optimization, Simulation and Environmental Impact of Energy Systems.
- Christopher Frey, H. and Patil, S. R. (2002). Identification and review of sensitivity analysis methods. *Risk Analysis*, 22(3):553–578.
- Connolly, F. T. and Rizzoni, G. (1994). Real Time Estimation of Engine Torque for the Detection of Engine Misfires. *Journal of Dynamic Systems, Measurement, and Control*, 116(4):675–686.
- Cover, T. M. and Thomas, J. A. (2006). *Elements of Information Theory*. Wiley-Interscience, USA.

- d'Ambrosio, S., Ferrari, A., and Galleani, L. (2015). In-cylinder pressure-based direct techniques and time frequency analysis for combustion diagnostics in IC engines. *Energy Conversion and Management*, 99:299–312.
- De Cuyper, T., Broekaert, S., Chana, K., De Paepe, M., and Verhelst, S. (2017). Evaluation of empirical heat transfer models using tfg heat flux sensors. *Applied Thermal Engineering*, 118:561 – 569.
- Dec, J. E. (1997). A Conceptual Model of DI Diesel Combustion Based on Laser-Sheet Imaging. *SAE Technical Paper*, (970873).
- Demers D, W. G. (1999). *Guide to exhaust emission control options*. BAeSAME, Bristol.
- Denny, M. (2019). *On the Combustion Characteristics of Closely-Coupled LD Diesel Injection Strategies*. PhD thesis, Lund University.
- Di Leo, R. (2015). Methodologies for air-fuel ratio and trapped mass estimation in diesel engines using the in-cylinder pressure measurement. *Energy Procedia*, 82:957 – 964. 70th Conference of the Italian Thermal Machines Engineering Association, ATI2015.
- Dingle, P. (2010). Fuel injection systems for heavy-duty diesel engines. In *Advanced Direct Injection Combustion Engine Technologies and Development*, volume 2, pages 289 – 317. Woodhead Publishing.
- Egnell, R. (1998). Combustion Diagnostics by Means of Multizone Heat Release Analysis and NO Calculation. *SAE Technical Paper*, (981424).
- EIA (2005). Europe's environment: The third assessment. Technical report, European Environment Agency.
- Eriksson, D., Eriksson, L., Frisk, E., and Krysander, M. (2013). Flywheel angular velocity model for misfire and driveline disturbance simulation. *IFAC Proceedings Volumes*, 46(21):570 – 575. 7th IFAC Symposium on Advances in Automotive Control.
- Eriksson, L. and Nielsen, L. (2014). *Mean Value Engine Modeling*, chapter 7, pages 143–210. John Wiley & Sons, Ltd.
- Eriksson, L. and Thomasson, A. (2017). Cylinder state estimation from measured cylinder pressure traces - a survey. *IFAC-PapersOnLine*, 50(1):11029 – 11039. 20th IFAC World Congress.

- European Union (2007). Cleaner trucks and buses: tighter limits for nitrogen oxides and particulate matter (Euro VI). Technical report, Press release, IP/07/1989.
- Fan, Q., Bian, J., Lu, H., Tong, S., and Li, L. (2012). Misfire detection and re-ignition control by ion current signal feedback during cold start in two-stage direct-injection engines. *International Journal of Engine Research*, 15:37–47.
- Farooq U., Marrakchi Z., M. H. (2012). *FPGA Architectures: An Overview*. Springer, New York, NY.
- Finesso, R. and Spessa, E. (2014). Ignition delay prediction of multiple injections in diesel engines. *Fuel*, 119:170–190.
- Finesso, R. and Spessa, E. (2015). A control-oriented approach to estimate the injected fuel mass on the basis of the measured in-cylinder pressure in multiple injection diesel engines. *Energy Conversion and Management*, 105:54–70.
- Foster, D. E. (1985). An Overview of Zero-Dimensional Thermodynamic Models for IC Engine Data Analysis. (852070).
- G. W. Johnson, R. J. (2006). *LabVIEW Graphical Programming, 4th Edition*. McGraw-Hill USA.
- Gatowski, J. A., Balles, E. N., Chun, K. M., Nelson, F. E., Ekchian, J. A., and Heywood, J. B. (1984). Heat Release Analysis of Engine Pressure Data. *SAE Technical Paper*, (841359).
- Ghojel, J. I. (2010). Review of the development and applications of the Wiebe function: A tribute to the contribution of Ivan Wiebe to engine research. *Int. J. Engine Res.*, 11(4):297–312.
- Gupta, V. K., Zhang, Z., and Sun, Z. (2011). Modeling and control of a novel pressure regulation mechanism for common rail fuel injection systems. *Applied Mathematical Modelling*, 35(7):3473 – 3483.
- Guzzella, L. and Onder, C. (2004). *Introduction to Modeling and Control of Internal Combustion Engine Systems*. Springer.
- Han, J.-S., Lu, P.-H., Xie, X.-B., Lai, M.-C., and Henein, N. A. (2002). Investigation of diesel spray primary break-up and development for different nozzle geometries. *SAE Technical Paper*, (2002-01-2775).
- Heider, G. Woshni, G. and Zeilinger, K. (1998). 2-zonen rechenmodell zur vorausrechnung der no-emission von diesemotoren. *MTZ Motortech Z*, (59).

- Heywood, J. (1988). *Internal Combustion Engines Fundamentals*. McGraw Hill Education, New York, 6th edition.
- Höckerdal, E., Frisk, E., and Eriksson, L. (2018). Real-time performance of DAE and ODE based estimators evaluated on a diesel engine. *Science China Information Sciences*, 61(7).
- IEA (2017a). The future of trucks: Implications for energy and the environment. Technical report, International Energy Agency.
- IEA (2017b). Technology roadmap - delivering sustainable bioenergy. Technical report, International Energy Agency.
- IEA (2020a). Energy technology perspectives. Technical report, International Energy Agency.
- IEA (2020b). Tracking transport. Technical report, International Energy Agency.
- IEA (2020c). World energy outlook. Technical report, International Energy Agency.
- Iorio, B., Giglio, V., Police, G., and Rispoli, N. (2003). Methods of pressure cycle processing for engine control. In *SAE Technical Paper*, number 2003-01-0352. SAE International.
- IPCC (2014). Climate change 2014: Synthesis report. contribution of working groups i, ii and iii to the fifth assessment report of the intergovernmental panel on climate change. Technical report, IPCC.
- Isermann, R. (2016). *Engine Modeling and Control: Modeling and Electronic Management of Internal Combustion Engines*. Springer Berlin Heidelberg.
- Ishida, M., Chen, Z.-L., Luo, G.-F., and Ueki, H. (1994). The effect of pilot injection on combustion in a turbocharged d.i. diesel engine. *SAE Transactions*, 103:1740–1749.
- Johansson, B. (2012). *Combustion Engines*. LTH, Lund.
- Johansson, R. (1993). *System Modeling and Identification*. Information and system sciences series. Prentice Hall.
- Jorques Moreno, C., Stenlås, O., and Tunestål, P. (2018). In-Cycle Closed-Loop Combustion Control with Pilot-Main Injections for Maximum Indicated Efficiency. *IFAC-PapersOnline*, 51:92–98.

- Jorques Moreno, C., Stenlång, O., and Tunestål, P. (2020a). In-Cycle Closed-Loop Combustion Control for Pilot Misfire Compensation. *SAE Int. J. Adv. & Curr. Prac. in Mobility*, 3:299–311.
- Jorques Moreno, C., Stenlång, O., and Tunestål, P. (2020b). Predictive In-Cycle Closed-Loop Combustion Control with Pilot-Main Injections. *IFAC-PaperOnline*, 53:14000–14007.
- Jung, D. and Assanis, D. N. (2001). Multi-Zone DI Diesel Spray Combustion Model for Cycle Simulation Studies of Engine Performance and Emissions. *SAE Technical Paper*, (2001-01-1246).
- Kahn Ribeiro, S., S. Kobayashi, M., Beuthe, J., Gasca, D., Greene, D. S., Lee, Y., Muromachi, P. J., Newton, S., Plotkin, D., Sperling, R., Wit, P., and Zhou, J. (2007). Transport and its infrastructure. Technical report, In Climate Change 2007: Mitigation. Contribution of Working Group III to the Fourth Assessment Report of the Intergovernmental Panel on Climate Change.
- Källkvist, K. (2011). *Fuel Pressure Modelling in a Common-Rail Direct Injection System*. PhD thesis.
- Kay, S. M. (1993). *Fundamentals of statistical signal processing: Detection Theory*. Prentice-Hall PTR, 1998.
- Kiencke, U. (1997). Engine misfire detection. *IFAC Proceedings Volumes*, 30(18):645 – 650. IFAC Symposium on Fault Detection, Supervision and Safety for Technical Processes (SAFEPROCESS 97), Kingston upon Hull, UK, 26-28 August 1997.
- Kiencke, U. and Nielsen, L. (2000). *Automotive Control Systems: For Engine, Driveline and Vehicle*. Springer-Verlag, Berlin, Heidelberg, 1st edition.
- Klein, M., Eriksson, L., and Åslund, J. (2004). Compression ratio estimation based on cylinder pressure data. *IFAC Proceedings Volumes*, 37(22):299 – 304. IFAC Symposium on Advances in Automotive Control 2004, Salerno, Italy, 19-23 April 2004.
- Kolbeck, A. (2011). Closed Loop Combustion Control - Enabler of Future Refined Engine Performance Regarding Power, Efficiency, Emissions and NVH under Stringent Governmental Regulations. *SAE Technical Paper*, (2011-24-0171).
- Kosaka, H., Aizawa, T., and Kamimoto, T. (2005). Two-dimensional imaging of ignition and soot formation processes in a diesel flame. *Int. J. Engine Res.*, 6(1):21–42.

- Kumar, P., Sharma, M., and Dwivedi, G. (2014). Impact of biodiesel on combustion, performance and exhaust emissions of diesel engines. *Journal of integrtaed science and technology*, 2:57–63.
- Kuon, I., Tessier, R., and Rose, J. (2008). FPGA Architecture: Survey and Challenges. *Electron. Des. Autom.*, 2(2):135–253.
- Lakshminarayanan, P. A. and Aghav, Y. V. (2010). *Modelling Diesel Combustion*. Springer.
- Lee, K., Yoon, M., and Sunwoo, M. (2008). A study on pegging methods for noisy cylinder pressure signal. *Control Engineering Practice*, 16(8):922 – 929. Special Section: IFAC Conference on Analysis and Design of Hybrid Systems (ADHS’06).
- Lindemann, M. and Filbert, D. (2002). Methods of misfire detection using knock sensors. *MTZ worldwide*, 63.
- Livengood, J. C. and Wu, P. C. (1955). Correlation of autoignition phenomena in internal combustion engines and rapid compression machines. In *Symp. Combust.*
- MacMillan, D., La Rocca, A., Shayler, P., Morris, T., Murphy, M., and Pegg, I. (2009). Investigating the effects of multiple pilot injections on stability at cold idle for a dl diesel engine. *SAE International Journal of Engines*, 2:370–380.
- Majewski, W. A. and Khair, M. K. (2006). *Diesel Emissions and their Control*. SAE International.
- Manente, V. (2010). *Gasoline Partially Premixed Combustion - An Advanced Internal Combustion Engine Concept Aimed to High Efficiency, Low Emissions and Low Acoustic Noise in the Whole Load Range*. PhD thesis, Lund University.
- Maroteaux, F., Saad, C., and Aubertin, F. (2015). Development and validation of double and single Wiebe function for multi-injection mode Diesel engine combustion modelling for hardware-in-the-loop applications. *Energy Conversion and Management*, 105:630–641.
- Minami, T., Takeuchi, K., and Shimazaki, N. (1995). Reduction of Diesel Engine NOx Using Pilot Injection. *SAE Technical Paper*, (950611).
- Miyamoto, N., Muruyama, T., and Fukazawa, S. (1972). Studies on Low Compression Ratio Diesel Engine : 3rd Report, Relation between Combustibility and Performances. *Bull. JSME*, 15(90):1603–1616.

- Mohammadpour, J., Franchek, M., and Grigoriadis, K. (2011). A survey on diagnostics methods for automotive engines. In *Proceedings of the 2011 American Control Conference*, pages 985–990.
- Monmasson, E. and Cirstea, M. (2007). FPGA Design Methodology for Industrial Control Systems - A Review. *IEEE Trans. Ind. Electron.*, 54(4):1824–1842.
- Muric, K., Stenlås, O., Tunestål, P., and Johansson, B. (2013a). A Study on In-Cycle Control of NO_x Using Injection Strategy with a Fast Cylinder Pressure Based Emission Model as Feedback. *SAE Technical Paper*, (2013-01-2603).
- Muric, K., Tunestål, P., and Stenlås, O. (2013b). A Fast Crank Angle Resolved Zero-Dimensional NO_x Model Implemented on a Field-Programmable Gate Array. *SAE Technical Paper*, (2013-01-0344).
- Oh, S., Min, K., and Sunwoo, M. (2015). Real-time start of a combustion detection algorithm using initial heat release for direct injection diesel engines. *Appl. Therm. Eng.*
- Olsson, J.-O. and Johansson, B. (2001). Closed-Loop Control of an HCCI Engine. *SAE Trans.*, Engines:1076–1085.
- Osuka, I., Nishimura, M., Tanaka, Y., and Miyaki, M. (1994). Benefits of new fuel injection system technology on cold startability of diesel engines - improvement of cold startability and white smoke reduction by means of multi injection with common rail fuel system (ecd-u2). (940586).
- Pecsvaradi, T. and Narendra, K. S. (1971). Reachable Sets for Linear Dynamical Systems. *Inf. Control*, 19:319–344.
- Pickett, L. M. and Siebers, D. L. (2004). Non-Sooting, Low Flame Temperature Mixing-Controlled DI Diesel Combustion. *SAE Technical Paper*, (2004-01-1399).
- Powell, J. D. (1993). Engine Control Using Cylinder Pressure: Past, Present, and Future. *J. Dyn. Syst. Meas. Control*, 115(2B):343.
- Randolph, A. L. (1990). Methods of processing cylinder-pressure transducer signals to maximize data accuracy. In *SAE Technical Paper*, number 900170. SAE International.
- Regulation (EU) 2019/1242 (2019). CO₂ emission performance standards for new heavy-duty vehicles and amending Regulations (EC) No 595/2009 and (EU) 2018/956. Technical report, European Parliament and of the Council of 20 June 2019.

- Reşitoglu, b., Altinisik, K., and Keskin, A. (2014). The pollutant emissions from diesel-engine vehicles and exhaust aftertreatment systems. *Clean Technologies and Environmental Policy*, 17:15–27.
- Reitz, R. D. and Duraisamy, G. (2015). Review of high efficiency and clean reactivity controlled compression ignition (rcci) combustion in internal combustion engines. *Progress in Energy and Combustion Science*, 46:12 – 71.
- Rugland, C. and Stenlaas, O. (2018). Knock sensor based virtual combustion sensor signal bias sensitivity. *SAE Technical Paper*, (2018-01-1154).
- Saracino, R., Gaballo, M. R., Mannal, S., Motz, S., Carlucci, A., and Benegiamo, M. (2015). Cylinder pressure-based closed loop combustion control: A valid support to fulfill current and future requirements of diesel powertrain systems. *SAE Technical Paper*, (2015-24-242).
- Schnorbus, T., Stefan Pischinger, Thomas Körfer, Matthias Lamping, Dean Tomazic, and Marek Tatur (2008). Diesel Combustion Control with Closed-Loop Control of the Injection Strategy. *SAE Technical Paper*, (2008-01-0651).
- Seykens, X., Somers, L., and Baert, R. (2004). Modelling of common rail fuel injection system and influence of fluid properties on injection process. *Proceedings of the international conference on vehicle alternative fuel systems and environmental protection, VAKSEP 2004, 6-7 July 2004, Dublin, Ireland*, pages 72 – 77.
- Shahroudi, K. E. (2008). *Robust Design Evolution and Impact of In-Cylinder Pressure Sensors to Combustion Control and Optimization: A Systems and Strategy Perspective*. PhD thesis, Massachusetts Institute of Technology.
- Shi, Y. and Reitz, R. D. (2010). Multi-dimensional Modelling of Diesel Combustion. pages 207–246. Springer, Dordrecht.
- Sims, R., Schaeffer, R., Creutzig, F., Cruz-Nuñez, X., D’Agosto, M., Dimitriu, D., Meza, M. F., Fulton, L., Kobayashi, S., Lah, O., McKinnon, A., Newman, P., Ouyang, M., Schauer, J., Sperling, D., and Tiwari, G. (2014). Transport. Technical report, Climate Change 2014: Mitigation of Climate Change. Contribution of Working Group III to the Fifth Assessment Report of the Intergovernmental Panel on Climate Change.
- Singh, S., Potala, S., and Mohanty, A. R. (2019). An improved method of detecting engine misfire by sound quality metrics of radiated sound. *Proceedings of the Institution of Mechanical Engineers, Part D: Journal of Automobile Engineering*, 233(12):3112–3124.

- Solsjö, R. (2014). *Large Eddy Simulation of Turbulent Combustion in PPC and Diesel Engines*. PhD thesis, Lund University.
- Steffen, T., Stobart, R., and Yang, Z. (2012). Challenges and potential of intra-cycle combustion control for direct injection diesel engines. *SAE 2012 World Congress & Exhibition*, (2012-01-1158).
- Szekely, G. A., Solomon, A. S., and Tsai, P.-H. (2004). Optimization of the stratified-charge regime of the reverse-tumble wall-controlled gasoline direct-injection engine. *SAE Technical Paper*, (2004-01-0037).
- Tanaka, T., Ando, A., and Ishizaka, K. (2002). Study on pilot injection of DI diesel engine using common-rail injection system. *JSAE Rev.*, 23(3):297–302.
- Tennison, P. J. and Reitz, R. (2001). An Experimental Investigation of the Effects of Common-Rail Injection System Parameters on Emissions and Performance in a High-Speed Direct-Injection Diesel Engine. *J. Eng. Gas Turbines Power*, 123(1):167.
- Tschanz, F., Amstutz, A., Onder, C. H., and Guzzella, L. (2013). Feedback control of particulate matter and nitrogen oxide emissions in diesel engines. *Control Engineering Practice*, 21(12):1809–1820.
- Tsurushima, T., Kunishima, E., Asaumi, Y., Aoyagi, Y., and Enomoto, Y. (2002). The effect of knock on heat loss in homogeneous charge compression ignition engines. *SAE Technical Paper*, (2002-01-0108).
- Tunestål (2009a). Self-tuning gross heat release computation for internal combustion engines. *Control Eng. Pract.*, 17(4):518–524.
- Tunestål, P. (2001). *Estimation of the In-Cylinder Air/Fuel Ratio of an Internal Combustion Engine by the Use of Pressure Sensors*. PhD thesis, Dep. Heat Power Eng. Lund Institute of Technology.
- Tunestål, P. (2009b). Model based TDC offset estimation from motored cylinder pressure data. In *IFAC Proc. 26 ed.*, volume 42, pages 241–247.
- Tureson, G. (2018). *Model-Based Optimization of Combustion-Engine Control*. PhD thesis, Lund University.
- van Nieuwstadt, M. J. and Kolmanovsky, I. V. (2000). Detecting and Correcting Cylinder Imbalance in Direct Injection Engines. *Journal of Dynamic Systems, Measurement, and Control*, 123(3):413–424.

- Villarino, R. and Bohme, J. (2004). Pressure reconstruction and misfire detection from multichannel structure-borne sound. In *2004 IEEE International Conference on Acoustics, Speech, and Signal Processing*, volume 2, pages ii–141–4 vol.2, Los Alamitos, CA, USA. IEEE Computer Society.
- Wang, X., Westerdahl, D., Hu, J., Wu, Y., Yin, H., Pan, X., and Max Zhang, K. (2012). On-road diesel vehicle emission factors for nitrogen oxides and black carbon in two chinese cities. *Atmospheric Environment*, 46:45 – 55.
- Wick, M., Bedei, J., Gordon, D., Wouters, C., Lehrheuer, B., Nuss, E., Andert, J., and Koch, C. R. (2019). In-cycle control for stabilization of homogeneous charge compression ignition combustion using direct water injection. *Applied Energy*, 240:1061–1074.
- Widd, A., Tunestal, P., Akesson, J., and Johansson, R. (2012). Single-zone Diesel PPC modeling for control. *Am. Control Conf. (ACC), 2012*, pages 5731–5736.
- Wilhelmsson, C., Tunestål, P., and Johansson, B. (2006). FPGA Based Engine Feedback Control Algorithms. *FISITA 2006 World Automot. Congr. JSAE*.
- Willems, F. (2018). Is Cylinder Pressure-Based Control Required to Meet Future HD Legislation? *IFAC-PapersOnline*, 51:111–118.
- Woschni, G. (1967). A Universally Applicable Equation for the Instantaneous Heat Transfer Coefficient in the Internal Combustion Engine. *SAE Technical Paper*, (670931).
- Wu, C. (2007). *Thermodynamics and Heat Powered Cycles: A Cognitive Engineering Approach*. Nova Science Publishers.
- Xilinx (2015). *Virtex-5 Family Overview*. Xilinx. Rev. 5.
- Yang, F., Wang, J., Gao, G., and Ouyang, M. (2014). In-cycle diesel low temperature combustion control based on SOC detection. *Appl. Energy*, 136:77 – 88.
- Yang, T., Yin, L., Ingesson, G., Tunestal, P., Johansson, R., and Long, W. (2017). Control-Oriented Modeling of Soot Emissions in Gasoline Partially Premixed Combustion with Pilot Injection. *SAE Technical Paper*, (2017-01-0511).
- Yates, R. (2007). *Fixed-Point Arithmetic: An Introduction*.

- Yoon, S. J., Park, B., Park, J., and Park, S. (2015). Effect of pilot injection on engine noise in a single cylinder compression ignition engine. *International Journal of Automotive Technology*, 16(4):571–579.
- Zak, Z., Emrich, M., Takats, M., and Macek, J. (2016). In-cylinder heat transfer modelling. *Journal of Middle European Construction and Design of Cars*, 14.
- Zander, C.-G. (2011). *Single-Cylinder Diesel Engine Experiments, Modeling and In-Cycle Control with Heat-Release Emphasis*. PhD thesis, Lund University.
- Zander, C.-G., Stenlås, O., Tunestål, P., and Johansson, B. (2010a). Study of a Heavy Duty Euro5 EGR-Engine Sensitivity to Fuel Change with Emphasis on Combustion and Emission Formation. *SAE Technical Paper*, (2010-01-0872).
- Zander, C.-G., Tunestål, P., Stenlås, O., and Johansson, B. (2010b). In-Cycle Closed Loop Control of the Fuel Injection on a 1-Cylinder Heavy Duty CI-Engine. *ASME ICEF2010*, 35100:405–414.
- Zhang, L. (1999). A Study of Pilot Injection in a DI Diesel Engine. *SAE Technical Paper*, (1999-01-3493).
- Zheng, M., Mulenga, M. C., Reader, G., Wang, M., Ting, D., and Tjong, J. (2008). Biodiesel engine performance and emissions in low temperature combustion. *Fuel*, 87:714–722.
- Zheng, M., Tan, Y., Reader, G. T., Asad, U., Han, X., and Wang, M. (2009). Prompt Heat Release Analysis to Improve Diesel Low Temperature Combustion. *SAE Technical Paper*, (2009-01-1883).